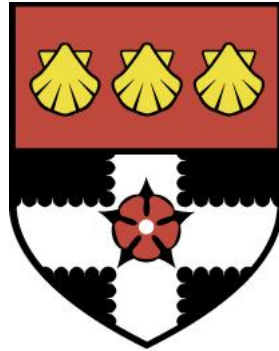


UNIVERSITY OF READING

Department of Meteorology



**Characterisation of industrial
thermal plumes discharged into
coastal waters using remote
sensing and simulation techniques**

AGNIESZKA FAULKNER

A thesis submitted for the degree of Doctor of Philosophy

September 2020

Declaration

I confirm that this is my own work and the use of all material from other sources has been properly and fully acknowledged.

Agnieszka Faulkner

Abstract

Coastal power stations use sea water as a coolant. The cooling waters discharges released by nuclear power stations, referred to in this thesis as thermal plumes, result in locally raised temperatures of the surrounding environments in the coastal regions. Since raised temperatures can impact aquatic flora and fauna, there are environmental permits and policies describing the limits for the allowed maximum temperatures of the discharged thermal plumes. It is therefore of paramount importance that we can characterise the industrial thermal plumes to a sufficient extent. Achieving this using traditional methods has been challenging due to high cost of the field campaigns, high dependence on weather and no repetition of the measuring campaigns. Access to freely available high-resolution satellite imagery has opened up a potentially viable way of characterising surface thermal plumes through satellite remote sensing. Such observations present an opportunity to study sea surface temperature (SST) distributions in the vicinity of the power stations at spatial resolution of 30 m - 100 m and temporal resolution of up to 16 days. To evaluate the potential of high resolution remote sensing, a methodology for thermal plume detection is developed. Thermal plumes observed by the satellite imagery show high dependence on the tidal conditions for the majority of the investigated sites. The plumes have been found to be embedded within the tidal stream and their direction of dispersion followed the direction of the tidal currents. The observed surface thermal gains were highest in the summer months and lowest in the winter months. In order to gain understanding of plume dispersion subsurface, high resolution three dimensional (3-D) simulations coupled with satellite observations were used. Plume dispersion was modelled for an inter-tidal area during the ebb and the flood tide using FLOW-3D software. The simulated plume was found to raise to the surface and spread depending on the strength and direction of the tidal currents, with limited area of raised temperatures at the seabed concentrated close to the discharge pipes. Available satellite data was used to compare with the simulation outputs and gain validation of the high resolution 3-D model of the plume. Despite the potential of high resolution satellite data sets and 3-D simulations in understanding industrial thermal plumes, a thorough evaluation of their capabilities, limitations and a consideration of routine use of such techniques and scientific advances compared to traditional methods have not been fully explored in previous studies. This work provides a detailed comparison of thermal plume characterisation methods, their limitations and recommendations for future set-up.

Acknowledgements

I would like to thank my supervisors, Chris Merchant and Claire Bulgin for the support and guidance throughout this PhD. Thank you for giving me a lot of independence, which helped me gain confidence as a researcher, but also for being there for me when I needed you.

I would also like to thank my Monitoring Committee members: Remi Tailleux and Michaela Hegglin for showing interest in my work and asking me thought-provoking questions and reinstalling faith in me when I doubted myself.

Thank you to EDF Energy for sponsoring this PhD project, and in particular to Hugo Winter and Angus Bloomfield for supervising this project on the industrial part and providing part of the data that was used in this project. I appreciate having had the experience of working for industry and joining the meetings at EDF.

I would like to thank my friends for making this experience fun. Thank you for the running, the coffee breaks and brunch and cinema weekends.

I would also like to thank my husband Ryan. Thank you for supporting me every day on this adventure (and others). I really appreciate everything you've done for me and how understanding you were in the last few weeks of write-up. I couldn't have done it without you!

Contents

Declaration	i
Abstract	iii
Acknowledgements	iv
Table of contents	v
List of Figures	viii
List of Tables	xviii
List of Acronyms	xx
Glossary of terms	xxii
1 Introduction	1
1.1 Motivation	1
1.2 How does a nuclear power plant work?	2
1.3 Why does a power stations need cooling water?	3
1.4 Cooling water as a thermal plume	3
1.5 Why study industrial thermal plumes?	4
1.6 Monitoring thermal plumes through field surveys	5
1.7 Satellite observations of thermal plumes	6
1.8 Modelling of thermal plumes	7
1.9 Combining methods to characterise thermal plumes	9
1.10 Nuclear power generation in UK - background	9
1.11 EDF Energy installations for power generation	9
1.11.1 Dungeness	12
1.11.2 Hartlepool	13
1.11.3 Heysham	13
1.11.4 Hinkley	14
1.11.5 Hunterston	16
1.11.6 Sizewell	16
1.11.7 Torness	17
1.11.8 General hydrographic properties at estuarine locations	19
1.12 Thesis objective and science questions	20
2 Satellite remote sensing data and methods	22
2.1 High resolution satellite imagery	22
2.1.1 Landsat 8	22
2.1.2 Landsat 8 known problems	24
2.1.3 ASTER	26

2.1.4	ASTER known problems	27
2.2	Obtaining satellite data	28
2.3	Satellite data pre-processing	30
2.3.1	Georeferencing the pixels	30
2.3.2	Radiance, Reflectance and Brightness Temperature Calculations	30
2.3.3	Regridding the data	32
2.4	Water detection in coastal imagery	33
2.4.1	Water detection for daytime imagery	33
2.4.2	Water detection for nighttime imagery	36
2.5	Optimal estimation for SST retrieval	37
2.5.1	Comparison of other SST retrieval methods	39
2.6	Thermal plume detection	46
2.7	Summary	47
3	Satellite observations of industrial thermal plumes	48
3.1	Statement of publication status	48
3.2	Abstract	49
3.3	Introduction	49
3.4	Methods	52
3.5	Results	58
3.5.1	Heysham as example of intertidal embayment	58
3.5.2	Sizewell as example of open water exposure	61
3.6	Extended results	63
3.6.1	Hinkley as example of location within an estuary	65
3.6.2	Torness as example of open water exposure	67
3.6.3	Dungeness as example of cusped foreland	69
3.6.4	Hunterston as example of area surrounded by islands	71
3.6.5	Hartlepool as example of estuary location	73
3.7	Discussion	74
3.8	Conclusions	77
4	Simulations of thermal plumes	78
4.1	Statement of publication status	78
4.2	Abstract	79
4.3	Introduction	79
4.4	Methods	81
4.4.1	Satellite observations of thermal plumes to validate simulations	81
4.4.2	FLOW-3D software for flow simulations	82
4.4.3	Setting up thermal plume simulations	86

4.4.4	Density as function of temperature-only vs density evaluated as function of temperature and salinity	90
4.5	Results	93
4.5.1	Simulations of thermal plume dispersion for ebb tide	93
4.5.2	Simulations of thermal plume dispersion for flood tide	95
4.5.3	Simulations with assumed maximum volume discharge	97
4.5.4	Comparing surface SST distribution from simulations with satellite observations	100
4.6	Discussion	103
4.7	Conclusions	108
5	Comparing remotely sensed observations to traditional field campaigns	110
5.1	Statement of publication status	110
5.2	Introduction	111
5.3	Traditional ways of monitoring thermal plumes	111
5.4	Characterising thermal plume through satellite imagery	113
5.5	Comparing thermal plumes characterised through traditional field campaigns and remote sensing of thermal plumes	114
5.5.1	Hunterston power station	115
5.5.2	Heysham power station	127
5.5.3	Assessment of the plume impact on the environment	133
5.6	Conclusions	138
6	Conclusions and future work	139
6.1	Conclusions	139
6.2	Future Work	143
6.3	Closing remarks	147
	References	148

List of Figures

1.1	Schematic of coastal power station coolant system. Black arrows symbolise the direction of the water flow. Sea water is marked in blue, Water and steam used for generation in grey, reactor in yellow and generators in brown.	3
1.2	Locations of EDF Energy power stations around the British coast symbolised by the red pins with names of places in white rectangles.	10
1.3	Bathymetry map of the area in the vicinity of the Dungeness power station (marked as a red square). Lighter colours symbolise shallow waters and darker colours - deeper waters. Depth contours are marked every 2m. . .	12
1.4	Bathymetry map of the area in the vicinity of the Hartlepool power station (marked as a red square). Lighter colours symbolise shallow waters and darker colours - deeper waters. Depth contours are marked every 2m. . .	13
1.5	Bathymetry map of the area in the vicinity of the Heysham power station (marked as a red square). Lighter colours symbolise shallow waters and darker colours - deeper waters. Depth contours are marked every 2m. . .	14
1.6	Bathymetry map of the area in the vicinity of the Hinkley power station (marked as a red square). Lighter colours symbolise shallow waters and darker colours - deeper waters. Depth contours are marked every 2m. . .	15
1.7	Bathymetry map of the area in the vicinity of the Hunterston power station (marked as a red square). Lighter colours symbolise shallow waters and darker colours - deeper waters. Depth contours are marked every 2m. . .	16
1.8	Bathymetry map of the area in the vicinity of the Sizewell power station (marked as a red square). Lighter colours symbolise shallow waters and darker colours - deeper waters. Depth contours are marked every 2m. . .	17
1.9	Bathymetry map of the area in the vicinity of the Torness power station (marked as a red square). Lighter colours symbolise shallow waters and darker colours - deeper waters. Depth contours are marked every 2m. . .	18
2.1	Image taken from Zanter [2019] . Landsat 8 TIR Band 10 over Lake Superior with visible banding (lighter and darker bands of pixels) across the scene highlighted by the red arrows.	25

2.2	Image taken from Zanter [2019] . Landsat 8 TIR Band 10 over clean calm water with visible striping (lighter and darker columns of pixels resembling stripes) across the scene.	26
2.3	Example search for ASTER instrument for Heysham site	29
2.4	Sketch of the original Landsat 8 image grid at a 30 m resolution (marked in black) and the common grid used for data regridding at a 50 m resolution (marked in red).	33
2.5	Modified Normalised Water Difference Index for Heysham on an example day. MNDWI values for the cross-section line of the scene with 0.8 and 0.9 threshold values marked in red and orange respectively (upper plot). MNDWI composite bands: band 3 (Green, left) and band 6 (SWIR, right) reflectance values for the whole scene with the cross-section, for which the MNDWI was calculated, marked in black (lower plot).	35
2.6	Modified Normalised Water Difference Index for Dungeness on 20 April 2016. (upper) MNDWI values for the cross section line of the scene with 0.8 and 0.9 threshold values marked in red and orange respectively. (lower left) MNDWI values obtained from Xu et al (2006) algorithm for the whole scene with the cross section marked in black. (lower right) RGB image of the corresponding scene with corresponding cross section only satisfying the MNDWI 0.8 threshold marked in purple. Land and cirrus cloud visible on RGB fail the MNDWI threshold and hence there is no purple line in those areas of the cross-section.	36
2.7	Mean SST across detected water regions for a sample of scenes using MCSST (marked as red circles and blue squares) and NLSST (marked as black stars and green triangles) algorithms compared to SST retrieved using OE (x axis). The data has been binned by OE SST. In orange is circled an example scene that is later shown in Figure 2.8	40
2.8	Differences in SST across an example Sizewell scene for different retrieval algorithms, Multi-Channel SST (MCSST) in middle panel and Non-Linear SST (NLSST) in bottom panel, compared to SST retrieved using Optimal Estimation (OE) in top panel. Land and clouds are masked in white. Black box indicates the location of the thermal plume and white box indicates the box of ambient waters. Largest positive SST differences are highlighted by dark red colour and large negative SST differences are in dark blue. . .	42

2.9	Differences in ambient SST compared to prior SST from ESA CCI L4 for different retrieval algorithms. The values of prior SST are on the x axis. SST differences Multi-Channel SST (MCSST) algorithms are marked by red circles and blue squares, Non-Linear SST (NLSST) algorithms are marked by the black stars and green triangles, Optimal Estimation (OE) algorithm is marked as magenta diamond.	43
3.1	(a) Location of Morecambe Bay, with Heysham power plant marked as a red square, with land elevation obtained from ASTER GDEM and bathymetry obtained from EMODnet datasets. (b) Close-up of the ROI, with detailed bathymetry with contours at 2 m depth intervals obtained from EMODnet dataset. Lighter colours represent shallower waters and darker colours deeper waters.	52
3.2	(a) Location of East Anglia, with Sizewell power plant marked as a red square, with land elevation obtained from ASTER GDEM and bathymetry obtained from EMODnet datasets. (b) Close-up of the ROI, with detailed bathymetry with contours at 2 m depth intervals obtained from EMODnet dataset. Lighter colours represent shallower waters and darker colours deeper waters.	52
3.3	Workflow plan. Data used are presented in the oval shapes. Yellow ovals represent generated products, purple ovals - existing datasets. Methods applied are presented as green rectangles and decisions as red diamonds. netCDF data format mention in the plan is the Network Common Data Form.	57

- 3.4 (a) Probability density map of thermal plume location and reach during ebb tide with darker colours presenting higher probability and lighter colours lower probability. On some occasions the sands are exposed (see b), while on other occasions the sands are not exposed to the same extent. The plume follows the same direction, along the deeper water channel, independent of the amount of sands exposed. (b) Corresponding RGB composite of an example daytime scene during ebb tide with waters visible in dark blue and green colour, exposed sands visible in light brown colour, land in dark green, and harbour and built-up areas in white. The arrows represent the currents based on the data from MET Norway. During the ebb tide, weaker flow is represented by smaller arrows and stronger flow is represented by bigger arrows. (c) Probability density map of thermal plume location of reach during flood tide with darker colours presenting higher probability and lighter colours lower probability. (d) Corresponding RGB composite depicting example daytime scene during flood tide with waters visible as dark blue colour, land in dark green, and harbour and built-up areas in white. The arrows represent the direction of flow during flood tide with weaker flow being represented by smaller arrows and stronger flow being represented by bigger arrows. 60
- 3.5 (a) Probability density map of thermal plume location and reach during ebb tide with darker colours presenting higher probability and lighter colours lower probability. (b) Corresponding RGB composite of an example daytime scene during ebb tide with waters visible in dark blue and green colour, exposed sands visible in light brown colour, land in dark green, and harbour and built-up areas in white. The arrows represent the currents based on the data from The Norwegian Meteorological Institute. (MET Norway). During the ebb tide, weaker flow is represented by smaller arrows and stronger flow is represented by bigger arrows. (c) Probability density map of thermal plume location of reach during flood tide with darker colours presenting higher probability and lighter colours lower probability. (d) Corresponding RGB composite depicting example daytime scene during flood tide with waters visible as dark blue colour, land in dark green, and harbour and built-up areas in white. The arrows represent the direction of flow during flood tide with weaker flow being represented by smaller arrows and stronger flow is represented by bigger arrows. 62

- 3.6 (a) Probability density map of thermal plume location and reach during ebb tide with darker colours presenting higher probability and lighter colours lower probability. (b) Corresponding RGB composite of an example daytime scene during ebb tide with waters visible in dark blue and green colour, land in dark green. The arrows represent the currents based on the data from The Norwegian Meteorological Institute. (MET Norway). During the ebb tide, weaker flow is represented by smaller arrows and stronger flow is represented by bigger arrows. Strongest flow is highlighted as yellow arrows. (c) Probability density map of thermal plume location of reach during flood tide with darker colours presenting higher probability and lighter colours lower probability. (d) Corresponding RGB composite depicting example daytime scene during flood tide with waters visible as dark blue colour, land in dark green. The arrows represent the direction of flow during flood tide with weaker flow being represented by smaller arrows and stronger flow is represented by bigger arrows. 66
- 3.7 (a) Probability density map of thermal plume location and reach during ebb tide with darker colours presenting higher probability and lighter colours lower probability. (b) Corresponding RGB composite of an example daytime scene during ebb tide with waters visible in dark blue and green colour, land in dark green. The arrows represent the currents based on the data from The Norwegian Meteorological Institute. (MET Norway). During the ebb tide, weaker flow is represented by smaller arrows and stronger flow is represented by bigger arrows. (c) Probability density map of thermal plume location of reach during flood tide with darker colours presenting higher probability and lighter colours lower probability. (d) Corresponding RGB composite depicting example daytime scene during flood tide with waters visible as dark blue colour, land in dark green. The arrows represent the direction of flow during flood tide with weaker flow being represented by smaller arrows and stronger flow is represented by bigger arrows. 68

- 3.8 (a) Probability density map of thermal plume location and reach during ebb tide with darker colours presenting higher probability and lighter colours lower probability. (b) Corresponding RGB composite of an example daytime scene during ebb tide with waters visible in dark blue and green colour, land in dark green. The arrows represent the currents based on the data from The Norwegian Meteorological Institute. (MET Norway). During the ebb tide, weaker flow is represented by smaller arrows and stronger flow is represented by bigger arrows. (c) Probability density map of thermal plume location of reach during flood tide with darker colours presenting higher probability and lighter colours lower probability. (d) Corresponding RGB composite depicting example daytime scene during flood tide with waters visible as dark blue colour, land in dark green. The arrows represent the direction of flow during flood tide with weaker flow being represented by smaller arrows and stronger flow is represented by bigger arrows. 70
- 3.9 (a) Probability density map of thermal plume location and reach during ebb tide with darker colours presenting higher probability and lighter colours lower probability. (b) Corresponding RGB composite of an example daytime scene during ebb tide with waters visible in dark blue and green colour, land in dark green. The arrows represent the currents based on the data from The Norwegian Meteorological Institute. (MET Norway). During the ebb tide, weaker flow is represented by smaller arrows and stronger flow is represented by bigger arrows. (c) Probability density map of thermal plume location of reach during flood tide with darker colours presenting higher probability and lighter colours lower probability. (d) Corresponding RGB composite depicting example daytime scene during flood tide with waters visible as dark blue colour, land in dark green. The arrows represent the direction of flow during flood tide with weaker flow being represented by smaller arrows and stronger flow is represented by bigger arrows. 72
- 3.10 Close-up of the Hartlepool power station (marked as red square), with detailed bathymetry with contours at 2 m depth intervals obtained from EMODnet dataset. The probability density map of thermal plume location and reach is overlaid on top of the bathymetry. Darker colours present higher probability and lighter colours lower probability of the plume location. 73

4.1	Bathymetry for the region of Heysham, eastern part of the Morecambe Bay based on a dataset from European Marine Observation and Data Network (EmodNET). Darker colours mark deeper regions and lighter colours correspond to shallower bathymetry. Land is represented by the dark green colour with the power station marked as a red square. Simulation domains are marked as black and blue rectangles for ebb and flood simulations respectively.	87
4.2	Changes in water density (y axis) with rise in temperature (x axis) based on the McCutcheon et al. (1993).	90
4.3	Changes in water density (y axis) with rise in temperature (x axis) based on the McCutcheon et al. (1993) represented by the green line and on the TEOS-10, with average water practical salinity chosen as 32, represented by the red line.	93
4.4	Horizontal cross sections of the simulated thermal plume during ebb tide at different depths. Land is marked in dark grey. The area of the plume is marked by the black line, with other coloured lines signifying different temperature contours within the plume. Higher temperatures are shown in red.	95
4.5	Horizontal cross sections of the simulated thermal plume during flood tide at different depths. Land is marked in dark grey. The area of the plume is marked by the black line, with other coloured lines signifying different temperature contours within the plume. Higher temperatures are shown in red.	97
4.6	Horizontal cross sections of the simulated thermal plume during ebb tide for maximum volume outfall at different depths. Land is marked in dark grey, while water in blue colours. Plume's area is marked by the black line, with other coloured lines signifying different temperature regions within the plume. Higher temperatures are in light and dark red.	99
4.7	Horizontal cross sections of the simulated thermal plume during ebb tide for maximum volume outfall at different depths. Land is marked in dark grey, while water in blue colours. Plume's area is marked by the black line, with other coloured lines signifying different temperature regions within the plume. Higher temperatures are in light and dark red.	100

4.8	Observed (left) and simulated (right) surface plume during mid-ebb tide for Heysham. The exposed sand banks are represented by the light brown colour and land by the dark green with the power station marked as a red square. Bathymetry is marked in thin black lines. The plume’s temperature contours are thick lines marked also on the colour bar.	101
4.9	Observed (left) and simulated (right) surface plume during mid-flood tide for Heysham. The exposed sand banks are represented by the light brown colour and land by the dark green with the power station marked as a red square. Bathymetry is marked in thin black lines. The plume’s temperature contours are thick lines marked also on the colour bar.	102
4.10	Simulated (marked in red) and observed (marked in yellow) thermal plume dispersing during mid-ebb tide (left panel) and mid-flood (right panel) for Heysham. The exposed sand banks are represented by the dark grey colour and land by the black colour. The common area, where the plume appears in the observations and the simulations is marked in dark brown.	103
5.1	Horizontal plume mapping for Hunterston power station during spring tide (A) and neap tide (B) taken from <i>Briggs</i> [2008] (not publicly available). Temperatures within the plume are marked by green, yellow, orange and red polygons, with green being the lowest temperature gain (0.5 °C - 2 °C) and red bring the highest temperature gain (7 °C - 8 °C). Power station is marked as a red square with black stripes.	117
5.2	Close-up of the Hunterston power station (marked as red square), with detailed bathymetry with contours at 2 m depth intervals obtained from EMODnet dataset. The probability density map of thermal plume location during ebb tide (left) an flood tide (right) and reach is overlaid on top of the bathymetry. Darker colours present higher probability and lighter colours lower probability of the plume location.	119
5.3	Maximum differences between the surface plume temperature and ambient SST for all satellite observations for Hunterston power station. The differences are grouped according to season with green dots representing differences in SST captured during March, April, May, yellow dots - during June, July, August, red dots - during September, October, November, blue dots - during December, January, February.	120

5.4	A timeseries of volume flow rates and temperature gains for the Heysham power station measured over the period of ~ 19 years by the Heysham power station. Same correlation is observed for other EDF Energy power stations.	121
5.5	Location of sensitive habitats in the vicinity of the Hunterston power station. In yellow are marked Marine Consultation Areas around two Cumbrae Islands. In brown are marked sensitive waters, where the shellfish populations are located. Pink stripes represent a Site of Special Scientific Interest, which are the Hunterston Sands. Power station is marked as the red square.	123
5.6	Location of sensitive habitats in the vicinity of the Hunterston power station with thermal plume detected in satellite imagery during different tidal stages. Plume dispersing during ebb tide is in top left, during slack water - top right, slack water changing into flood tide - bottom left and during flood tide - bottom right. Plume's temperature is described as difference from ambient water temperature.	126
5.7	Horizontal plume mapping during neap tide (A) and spring tide (B) taken from <i>Briggs and Taylor</i> [2008] (not publicly available). Temperatures within the plume are marked by green, yellow, orange and red polygons, with green being the lowest temperature gain ($0.5^{\circ}\text{C} - 2^{\circ}\text{C}$) and red bring the highest temperature gain (above 8°C). The power station area is marked in red with black stripes.	129
5.8	Probability density maps for the surface plume extent during ebb tide (left) and flood tide and slack water (right) based on Landsat 8 and ASTER imagery, with lighter color representing lower chance of plume extent and darker colours represent higher probability of plume extent. All plumes were detected based on criterion of 1.5°C warmer than ambient water temperature.	131
5.9	Maximum differences between the surface plume temperature and ambient SST for all satellite observations. The differences are grouped according to season with green dots representing differences in SST captured during March, April, May, yellow dots - during June, July, August, red dots - during September, October, November, blue dots - during December, January, February.	132

- 5.10 Location of sensitive habitats in the vicinity of the Heysham power station. Boulder and cobble skear is marked in brown, mussel beds in grey, cockle beds in yellow. Left panel shows location of all communities, middle panel - boulder and cobble skear and right panel mussel and cockle beds. Distance away from the outfall pipes is marked by different sized circles with the radius written for each circle, ranging from 1 km to 5 km. 135
- 5.11 Location of sensitive habitats in the vicinity of the Heysham power station with thermal plume detected in satellite imagery during different stages. Plume dispersing during flood tide is in top left, during slack water - top right, slack water changing into ebb tide - bottom left and during ebb tide - bottom right. Plume's temperature is described as difference from ambient water temperature. Distance away from the outfall pipes is marked by different sized circles with the radius written for each circle, ranging from 1 km to 5 km. 137

List of Tables

1.1	Nuclear power stations currently operated by EDF Energy	11
2.1	Landsat 8 Operational Land Imager (OLI) and Thermal Infrared Sensor (TIRS) channels with their spatial and spectral resolution.	23
2.2	ASTER VNIR, SWIR and TIR channels with their spatial and spectral resolution.	27
2.3	Landsat 8 and ASTER scenes used for further processing	30
2.4	MCSST and NLSST algorithms presented by <i>Jang and Park</i> [2019]. T_{11} represents BT at 10.8 micron, T_{12} is BT at 12 micron, T_{OSTIA} is the prior known SST from OSTIA data set, a_1 , a_2 , a_3 and a_4 are constants.	39
2.5	Differences in surface temperature of the thermal plume for different retrieval algorithms compared to OE. First column shows the date of the satellite observation, the second column is the maximum gradient across the plume, the third column is the average temperature of the plume for OE retrieval, the latter columns are the differences in the plume average temperature using MCSST and NLSST algorithms compared to OE. Highlighted in orange is the data for Figure 2.8.	45
2.6	Differences in surface temperature of the ambient waters for different retrieval algorithms compared to OE. First column shows the date of the satellite observation, the second column is the maximum gradient across the plume, the third column is the average temperature of the ambient waters (chosen $5\text{ km} \times 5\text{ km}$ area) for OE retrieval, the latter columns are the differences in the average ambient temperature using MCSST and NLSST algorithms compared to OE. Highlighted in orange is the data for Figure 2.8.	45
3.1	Summary of findings on the thermal plume characteristics for different power stations based on Landsat 8 and ASTER imagery.	64
4.1	Summary of plume characteristics from the ebb time and flood tide simulations	102
4.2	Summary of skill scores for the chosen ebb tide and flood tide days	103
4.3	Summary of conditions for the chosen ebb tide and flood tide days	104

4.4	Summary of excess surface heat fluxes for the simulated ebb and flood tides caused by the thermal plume	108
5.1	Comparison of satellite observations and field campaigns to characterise thermal plumes.	115

List of Acronyms

Acronym	Definition
ASTER	Advanced Spaceborne Thermal Emission and Reflection Radiometer
BT	Brightness Temperature
CCI	Climate Change Initiative
DEM	Digital Elevation Model
DN	Digital Number
ECMWF	European Centre for Medium-Range Weather Forecasts
EDF	Électricité de France
ERA Interim	ECMWF Reanalysis - Interim
ESA	European Space Agency
HDF	Hierarchical Data Format
IR	Infra-Red
MCSST	Multi-Channel SST
MET Norway	Norwegian Meteorological Institute
METI	Ministry of Economy, Trade and Industry
MNDWI	Modified Normalized Difference Water Index
MODIS	Moderate Resolution Imaging Spectroradiometer
NASA	National Aeronautics and Space Administration
NWP	Numerical Weather Prediction
NDVI	Normalised Difference Vegetation Index
NDWI	Nomalised Difference Water Index
NetCDF	Network Common Data Form
NIR	Near Infra-Red
NLSST	Non-Linear SST
OE	Optimal Estimation
OLI	Operational Land Imager
OSTIA	Operational Sea Surface Temperature and Sea Ice Analysis
ROI	Region Of Interest
SAC	Special Area of Conservation
SPA	Special Protection Area
SSSI	Site of Special Scientific Interest
SST	Sea Surface Temperature

List of Acronyms

Acronym	Definition
SWIR	Short Wave Infra-Red
TEOS-10	Thermodynamic Equation Of Seawater - 2010
TIR	Thermal Infra-Red
TIRS	Thermal Infrared Sensor
TOA	Top of Atmosphere
UK	United Kingdom
USGS	United States Geological Survey
UTM	Universal Transverse Mercator
VNIR	Visible and Near Infra-Red
WGS	World Geodetic System
WRS	Worldwide Reference System

Glossary of terms

Rip current - Rip current, also known as riptide; a narrow band of water, which flows in a direction normal or nearly normal to the coastline. The riptide flows occasionally seaward for several minutes and is not related to the tidal cycle. [[Encyclopaedia Britannica, 2007](#)]

Stokes drift – Stokes drift is known as the the difference between the Lagrangian and the Eulerian averages of a given flow field and it plays an important role in the oceanic flows. It appears as a property of the wave only and corresponds to the averaging of wave effects on the mean flow. Stokes drift is a term reserved for the velocity differences and stands for the difference in wave-averaged velocity following a particle (Lagrangian reference frame) and in a stationary reference frame (Eulerian reference frame). Combining the Lagrangian and Eulerian averages, Stokes drift transports heat, pollution or salts in the upper ocean layer. [[Van Den Bremer, TS and Breivik Ø, 2018](#)]

Universe Transverse Mercator – Universe Transverse Mercator, UTM, is a horizontal position representation. It is similar to the traditional method of latitude and longitude in the sense that it disregards altitude and treats the earth as a perfect ellipsoid. UTM is a plane coordinate grid system named after the Transverse Mercator map projection, which it is based on. The Earth projected in the UTM system is divided into 60 zones, each 6-degrees of longitude in width. [[The United States Geological Survey, 2021](#)]

World Geodetic System – World Geodetic System, WGS, is a standard used in: cartography, geodesy, satellite navigation and GPS. This standard is responsible for defining the fundamental and derived constants of the coordinate system, as well as a current list of local datum transformations. The latest revision of the WGS is the WGS-84 (other names include: WGS 1984, EPSG:4326). WGS-84 has an Earth-centered terrestrial reference system with Cartesian coordinates (X, Y, Z), which is consistent with the International Terrestrial Reference Frame (ITRF), and a geodetic datum. [[Lohmar, 1988](#)]

Chapter 1:

Introduction

1.1 Motivation

With constantly developing countries, rising population density and technological developments, there has been an increase in demands for energy production [[Markandya and Wilkinson, 2007](#)]. Due to concerns over the effects of greenhouse gas emissions and limited supply of non-renewable fossil fuels, people turn to alternative energy generation methods, such as renewable energy coming from wind or solar or nuclear generation. Nuclear generation has an advantage of being able to generate more power than their carbon-based fuel generation from the same volume of fuel [[Ernst and Ernst, 2000](#)], making this type of generation very efficient.

All nuclear power plants use water, coming from rivers, lakes or seas, for cooling purposes. The intake water is used to cool various installation components, then it is released back into the environment at higher temperature due to the heat exchange that occurred. The released effluent will have a local impact on the environment, possibly affecting the aquatic flora and fauna. Therefore, prior to licensing a power station into operation, in-depth environmental impact studies are carried out in the region of interest, which focus on any possible zones of protection or special areas of conservation, as well as technical details of future power generation such as discharge location, volume flow rates, excess temperature of the outfall. Such studies are based on hydrodynamical models, such as TELEMAC-MASCARET [[Janin et al., 1992](#)] or FLOW 3D [[Barkhudarov, 2004](#)].

After putting the power station into generation, it is possible to carry out a field campaign and collect needed data using profilers and a survey vessel. Field campaigns are very costly, limiting the observations in most cases to a single day with no possibility of repeating observations on a regular basis. Moreover, the measurements can only be

carried out during certain days with good atmospheric conditions. This PhD project looks into alternative ways of characterising temperature fields of cooling water outflows in the vicinity of industrial power plants. High-resolution satellite sensors provide a unique opportunity to study thermal distributions in the vicinity of power stations. Despite the temporal trade-off associated with the satellite repeat-time coverage, remote sensing information has the advantage of high spatial resolution observations, providing a basis for resolving thermal stresses in space and time. Satellite imagery can be integrated with three dimensional (3-D) simulations to infer the subsurface development of the plume and its 3-D structure.

1.2 How does a nuclear power plant work?

Power stations produce electricity using water in their reactors, which undergoes phase changes following a Rankine Cycle (see Figure 1.1). Rankine Cycle is an idealised thermodynamic cycle, where heat is transformed into mechanical work [*Turnpenny et al., 2010*]. In order to change liquid water into vapour, heat is provided, usually from burning gas or from the controlled nuclear fission [*Turnpenny et al., 2010*]. Permanent heating in the reactor vessel brings the water to boiling and allows some part of the water to be converted into steam through latent heat of evaporation. Boiling water, that turns into steam, causes turbines to turn and hence generate electricity. In order to turn the turbines, the steam loses its thermal energy and increases kinetic energy, which is changed into work. Unused steam, that passed through the turbines, is converted back into water. At the end of the turbines the steam meets a cold condensing surface, where it transfers the heat onto the cold surface and condenses back into water. That condensed water can be used again to generate electricity and is then pumped back into the boiler and the whole cycle repeats.

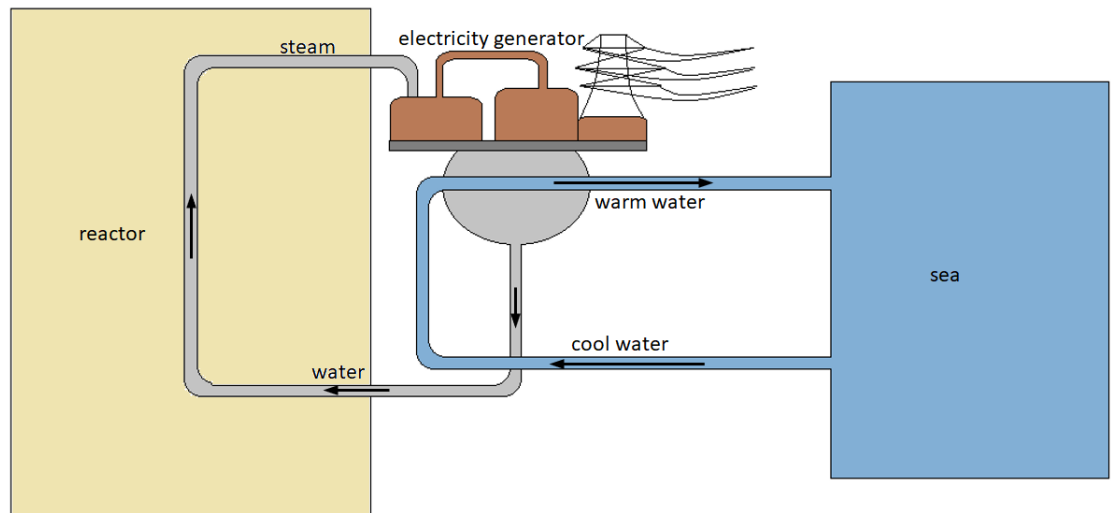


Figure 1.1: Schematic of coastal power station coolant system. Black arrows symbolise the direction of the water flow. Sea water is marked in blue, Water and steam used for generation in grey, reactor in yellow and generators in brown.

1.3 Why does a power stations need cooling water?

It is important that the condensing surface remains cool enough to condense the water and that any heat transferred by the steam is removed. In order to achieve this, cooling water, pumped in from the outside is needed to act as a coolant. The cooling water is taken from cool coastal or river waters, near which the plant is built and after it's gone once-through cooling system, it is ejected back into the environment (see Figure 1.1). The amount of cooling water needed is dependent on the amount of steam that needs to be condensed back into water to start another cycle.

Due to the heat exchange, the cooling water becomes warmer and can no longer act as a coolant. It is therefore ejected back into the sea. A new portion of ambient water is taken in to cool the next portion of steam and the whole process is repeated.

1.4 Cooling water as a thermal plume

The cooling water ejected back into the environment is of temperature higher than ambient, and therefore here after will be named a *thermal plume* [Cunningham *et al.*, 1998]. Langford [1990] provides a definition of a thermal plume, as a *disposal of heat from a man-made heat exchange* and notes that the great part of thermal discharges is related

to the energy generation sector. Thermal plumes leave the outfall pipes in a stream-like flow into the aquatic environments (i.e. rivers, lakes, sea). After some dynamic mixing, due to positive buoyancy, they rise to the surface. Thermal plumes can be localised or spread away from the source pipes up to a few kilometres depending on the conditions, such as: thermal stratification in the water body, currents, winds, bathymetry.

1.5 Why study industrial thermal plumes?

In the 1970s a study looking into 16-year temperature data series did not find any solid evidence of the thermal plume impact on aquatic ecosystems. There were no conclusive trends between the temperature fluctuations and the variations in species communities observed seasonally and annually. The study suggested, however, revisiting the site a few years later and revising the measurements [*Hillman et al., 1977*]. Since then, multiple studies have investigated the relationship between elevated temperatures and species diversities in the aquatic habitats [*Langford, 1990; Hung et al., 1998*]. *Langford [1990]* discussed potential ecological effects of thermal discharges on the aquatic ecosystems, suggesting that a change in temperature distributions in natural ecosystems impacts the ecosystem's flora and fauna.

Warmer waters released to the environment lead to an increase in anaerobic bacteria and lower oxygen content [*Issakhov and Zhandaulet, 2019*]. *Laws [2017]* observed a 20% reduction of the soluble oxygen for every 10°C rise in temperature, which further influences the rate of photosynthesis, eutrophication, metabolic rate of fish [*Punetha, 2018*]. One study found that the water temperature increases of > 3°C caused by industrial thermal plumes during the summer season, when the ambient waters are already warm, would hinder the development of fish species and their diversity [*Jiang and Hou, 2015*].

A Chinese national summary of characteristics for power stations noted that the entrainment of the thermal plume in the ambient waters was affecting marine ecosystems, limiting habitat areas and decreasing biodiversity [*Huang et al., 2016*]. Temperature rises caused by industrial thermal plumes in southern Taiwan were related to coral bleaching and anomalies in fish development [*Hung et al., 1998*]. Comparing environment variables, such as temperature and salinity, sampled in the vicinity of a power station to the communities compositions has indicated differences between intake and outfall regions [*Chuang et al., 2009; Teixeira et al., 2009*] with decreased fish population and benthic cover in the area affected by the thermal plume [*Teixeira et al., 2009*]. The biggest effects of thermal plume on the aquatic ecosystem were noticed close to the outfall where the temperature

rise was the highest, whereas sites further away noted smaller temperature rise [Teixeira et al., 2012, 2009]. The impact of thermal plumes on the environment is not always the same and rather depends on the habitat composition and the temperature tolerances of species located in the environs of the power station. The temperature rises will affect organisms with lower temperature tolerances, while species with high thermal tolerances will not be affected by the thermal plume [Teixeira et al., 2012].

Thermal contamination became a major ecological concern in many river or coastal estuarine ecosystems around the world, in many cases involving nuclear power plants [Poornima et al., 2005; Chuang et al., 2009; Teixeira et al., 2009, 2012]. Due to their ecological impacts, the thermal plumes should be monitored and, in order to keep the power stations thermally efficient, the possible recirculation of the thermal plume to the intake point should be minimized [Langford, 1990]. Monitoring of the industrial thermal plume has typically been done through field campaigns including boat surveys [Hung et al., 1998; Anupkumar et al., 2005] and point measurements [Chuang et al., 2009; Teixeira et al., 2009; Madden et al., 2013].

1.6 Monitoring thermal plumes through field surveys

Field measurements were one of the early methods to monitor thermal plume discharges in terms of chemical and physical characterisation. Field campaigns usually involve a survey vessel taking point measurements in the vicinity of the power plant outfall pipes. The surveying campaign usually lasts between one and two full days [Briggs and Taylor, 2008; Briggs, 2008], trying to capture thermal distributions through a series of profiles and interpolate between the point measurements. Since the field campaigns take measurements at the water temperature at the surface and at depth, they provide information on the three dimensional (3-D) nature of the plume. Boat surveys in shallow coastal regions have shown that the thermal plume dispersion was influenced by the tides and the plume was carried by the sea currents [Briggs and Taylor, 2008; Briggs, 2008], with differences between the surface plume and the plume at depth [Anupkumar et al., 2005].

Despite providing a sufficient description of the thermal plume, field campaigns are expensive and can only be carried out during certain months with fair weather conditions. Any issues with the measuring probes or sudden weather changes cause the campaign to be cancelled or postponed, which generates new costs. Some studies suggested that mapping discharge temperatures in point location is insufficient to evaluate the effect of the plume

on the aquatic ecosystems [*Madden et al.*, 2013].

1.7 Satellite observations of thermal plumes

With recent advances in technology, alternate ways of plume monitoring are emerging. High-resolution remote sensing observations provide good insight into spatial distributions of the sea surface temperatures (SSTs) in the vicinity of the industrial power stations [*Chen et al.*, 2003; *Huang et al.*, 2014; *Dai et al.*, 2016; *Wang et al.*, 2016a; *Ma et al.*, 2017; *Faulkner et al.*, 2019; *Tang et al.*, 2003; *Davies and Mofor*, 1993; *Ahn et al.*, 2006]. These observations provide a snapshot in time of the SST distribution during specific atmospheric and tidal conditions and outfall values from the power plant, which help characterise surface thermal plumes [*Ahn et al.*, 2006; *Chen et al.*, 2003; *Dai et al.*, 2016; *Wang et al.*, 2016a; *Ma et al.*, 2017; *Huang et al.*, 2014; *Xu et al.*, 2014].

A quantitative analysis of SST distribution of coastal waters proved that satellite instruments with better spatial resolution, calibration and reduced noise provide improved detection of thermal plumes [*Chen et al.*, 2003]. High spatial resolution satellite sensors capture the SST variations better than medium-resolution sensors and therefore are more useful for thermal plume analysis and capturing thermal features [*Wang et al.*, 2016a; *Ma et al.*, 2017; *Chen et al.*, 2003] since thermal plume impacts are localised. They are useful in determining the area and the shape of the surface thermal plume and its dispersion direction [*Wang et al.*, 2016a; *Muthulakshmi et al.*, 2013]. Combining observations from multiple satellite sensors extends the data records for the operational lifetime of the power station. In case of newly built power stations, long observational records provide good comparison of SST distributions before and after opening of the power station [*Dai et al.*, 2016], which enables the interpretation of the surface temperature rise related to the thermal discharges.

Thermal plume extent and the associated temperature rise can have seasonal variations, which will be visible over longer observational periods [*Zoran*, 2011; *Muthulakshmi et al.*, 2013]. Seasonal variations in the thermal plume temperature were associated with increased air-sea heat transfer during winter months [*Ahn et al.*, 2006] and water stratification throughout the year [*Tang et al.*, 2003]. The extent and direction of the observed thermal plume have been attributed to underlying terrain, power station capacity [*Dai et al.*, 2016; *Ma et al.*, 2017], tides [*Dai et al.*, 2016; *Huang et al.*, 2014; *Ma et al.*, 2017] and sea currents [*Ahn et al.*, 2006]. The impact of the latter two is evident in the shallow coastal locations, where the proximity of the thermal plume to the shore depends on the

direction of the tidal currents [*Huang et al., 2014*].

Observed plumes have highest temperatures nearest to the discharge point, thus the impact of the thermal plume on the environment will decrease with distance away from the discharge point [*Huang et al., 2014*] as the plume will become more diluted. When the plume area is confined to a limited area [*Dai et al., 2016; Wang et al., 2016a; Muthulakshmi et al., 2013; Wang et al., 2016b*] the impact on the aquatic habitats can be very low and not break any national regulations for the water quality [*Wang et al., 2016a*]. However, if the plume is discharged close to sensitive ecosystems, despite the small area, it will affect the biodiversity of the species [*Dai et al., 2016*]. The impact of the plume is very context-sensitive and potentially depends on the plume behaviour, which is not well understood from limited in-situ surveys.

1.8 Modelling of thermal plumes

Although good for understanding surface processes, satellite observations are not representative of the subsurface development of the thermal plume and hence its possible impact on the benthic environment. In order to gain a broader understanding of the possible impacts of industrial thermal plumes, numerical models are used to simulate thermal plume dispersion [*Cardoso-Mohedano et al., 2015; Jiang and Hou, 2015; Salgueiro et al., 2015; Durán-Colmenares et al., 2016; Dvornikov et al., 2017; Thai and Tri, 2017; Issakhov, 2018; Issakhov and Zhandaulet, 2019; Wang et al., 2019*].

Calibrated numerical simulations have opened the opportunity to reproduce a specific instance of a thermal discharge [*Durán-Colmenares et al., 2016; Issakhov, 2018*], analyse multiple scenarios of thermal plume dispersion [*Cardoso-Mohedano et al., 2015; Salgueiro et al., 2015; Thai and Tri, 2017*], or predict possible future thermal pollution prior to building a power station [*Dvornikov et al., 2017*]. Shallow-water models, due to lower computational costs, are often used to investigate temperature distribution and thermal plume dispersion into river [*Issakhov and Zhandaulet, 2019*] or coastal environments [*Jiang and Hou, 2015*]. Three dimensional (3-D) modelling is used for deep reservoirs [*Wang et al., 2019*] or to obtain a more detailed analysis of thermal discharge into coastal environment [*Salgueiro et al., 2015*].

The area and the direction of the simulated thermal plume depend on multiple prescribed factors, such as: power station capacity [*Salgueiro et al., 2015*], discharge velocity [*Issakhov and Zhandaulet, 2019*], sea currents [*Thai and Tri, 2017*], wind speed [*Thai*

and Tri, 2017; Durán-Colmenares et al., 2016; Salgueiro et al., 2015], tidal conditions [Salgueiro et al., 2015]. In order to understand the plume behaviour and its possible effects, it is worthwhile to conduct multiple simulations with changing conditions and relate outfall temperature to the intake one. Due to long run times and simulation costs, modelling studies often need to focus on a few controlling variables that influence thermal plume dispersion.

The thermal plumes released into stagnant environments tend to rise to the surface and spread at the surface depending on the volume outfall rate, minimising the impact on the bottom temperatures [Ali, 2011]. For such sites it is worthwhile to run a set of simulations with varying discharge rate and power station capacity. Thermal plumes ejected into larger water bodies tend to be more reactive to winds [Issakhov, 2016; Fossati et al., 2011] and tides [Fossati et al., 2011], with plume dispersion driven by tides [Salgueiro et al., 2015], wind speed and direction rather than operational capacity [Issakhov, 2016]. For those locations performing simulations with different current strengths and directions or varying wind speeds is of advantage. Literature in the past has mentioned the random wave action leading to dispersion of pollutants through the induced Stokes drift, with suggested same significance as tidal and wind effects [Giarrusso et al., 2001; Caratelli et al., 2011]. A study looking into estuarine coastal dispersion and the effect of waves looked at the components of the currents and their interaction with waves. One of the components, Stokes drift, was said to add to the advection terms [Delpy et al., 2014], leading to intensified rip current velocities near the surface [Haas and Svendsen, 2002; Reniers et al., 2009]. However, experiments combined with analytical derivation have proven that Stokes drift by itself should not have a dispersive effect on the substances floating at the surface [Huang and Law, 2018]

Once the impact of the thermal plume is well understood, the simulations can become a tool for the mitigation strategy planning for existing power stations. In case the plume is found to critically impact the environment, future developments to decrease the impact of the plume, such as: barriers [Wu et al., 2001], relocation of the discharge pipe [Abbaspour et al., 2005] or building an extra discharge pipe [Issakhov and Zhandaulet, 2019], can be simulated before undertaking any engineering works. In order to assess the effectiveness of proposed mitigation strategies and find the most cost-effective solution, thermal plume simulations before and after the mitigation development can be compared.

1.9 Combining methods to characterise thermal plumes

Validating thermal plume simulations against observations is essential for ensuring their usefulness [Abbaspour *et al.*, 2005], because simulation results can disagree with observations [Ali, 2011; Hamrick and Mills, 2000], particularly in regions further away from the discharge point [Suh, 2001].

Validation of numerical simulations can be performed using long records of field measurements or remotely sensed observations, as they provide better spatial resolution than point measurements and cover a larger area than field campaigns. Combining calibrated spatial observations over a longer period of time with numerical simulations provides detailed analysis of thermal plume behaviour at the surface as well as its development in 3-D, which is of great importance for plume monitoring. Hence, quite often field campaigns are combined with remote sensing techniques [Tang *et al.*, 2003] or a hydrodynamic model [Cardoso-Mohedano *et al.*, 2015] to infer more about the behaviour of the plume and its impact on the environment.

1.10 Nuclear power generation in UK - background

Currently there are 15 operational reactors, within 8 power stations generating energy to the National Grid for the UK. All of them are owned and operated by EDF Energy. EDF Energy is an energy company that produces low-carbon electricity and gas in the United Kingdom. It is part of Electricite de France (EDF) and was formed in 2002 after merging different energy companies in the UK. In 2009 EDF took control of British Energy, and became one of the largest energy suppliers. British Energy operated 8 nuclear plants around the coastline of the UK, that after the acquisition by EDF became part of the EDF Energy (see Table 1.1). Producing electricity is called by EDF Energy the generation business. Electricity produced by the power stations goes directly into the National Grid to be distributed across the UK. Apart from producing energy, EDF Energy deals with customer supply business. It means that the company is buying gas and electricity from the wholesome market and selling it later to customers.

1.11 EDF Energy installations for power generation

All power stations (see Table 1.1) are located around the British coast, and intake the water for cooling purposes from the North Sea, the Irish Sea, the Bristol Channel,

the English Channel, and Firth of Clyde (Fig. 1.2). The type of their geographical location varies between inter-tidal embayments, channels and open water exposure. Varied bathymetry, as well as tides, sea currents and atmospheric conditions influence the dispersion of the once-through-system coolant waters. This provides a good range of case studies for analysing thermal contrasts spatially and temporally.



Figure 1.2: Locations of EDF Energy power stations around the British coast symbolised by the red pins with names of places in white rectangles.

Table 1.1: Nuclear power stations currently operated by EDF Energy

Power stations list		
Name and location	Operating time	Short description
Dungeness B, south coast of England	1983 - 2028	the first Advanced Gas-cooled reactor to begin construction in the UK
Hartlepool, north east coast of England	1983 - 2024	capable of supplying electricity to over 2 million UK homes
Heysham 1, north west coast of England	1983 - 2024	one of the two currently operating power stations on the same EDF Energy site
Heysham 2, north west coast of England	1988 - 2030	one of the two currently operating power station located on the same EDF Energy site
Hinkley Point B, near Bridgwater in Somerset	1976 - 2023	the first Advanced Gas-cooled Reactor to generate electricity to the grid in the UK
Hunterston B, west coast of Scotland	1976 - 2023	capable of supplying electricity to approximately 1.7 million UK homes
Sizewell B, Suffolk coast	1995 - 2035	UK's only Pressurised Water Reactor
Torness, east coast of Scotland	1988 - 2030	capable of supplying electricity over 2 million UK homes

1.11.1 Dungeness

Dungeness headland in the south England is the location of the Dungeness power station. In the past there were two power stations, Dungeness A and Dungeness B, producing energy. The Dungeness A power station ceased to produce energy in 2006, after which only Dungeness B (50.91 N , 0.96 E) stayed in operation and is the currently operating power station. The coastline is forming a triangular-shaped headland called a cusped foreland (see Figure 1.3). The pebble beaches near Dungeness, called a shingle, are some of the largest in Europe and therefore the area is protected by several conservation laws. The waters on both sides of the foreland are shallow with a gentle slope in bathymetry. There is a sudden steep drop in the seabed depth almost perpendicular to the tip of the foreland. The coolant water is discharged on the south west side of the foreland into the shallow coastal waters (see Figure 1.3).

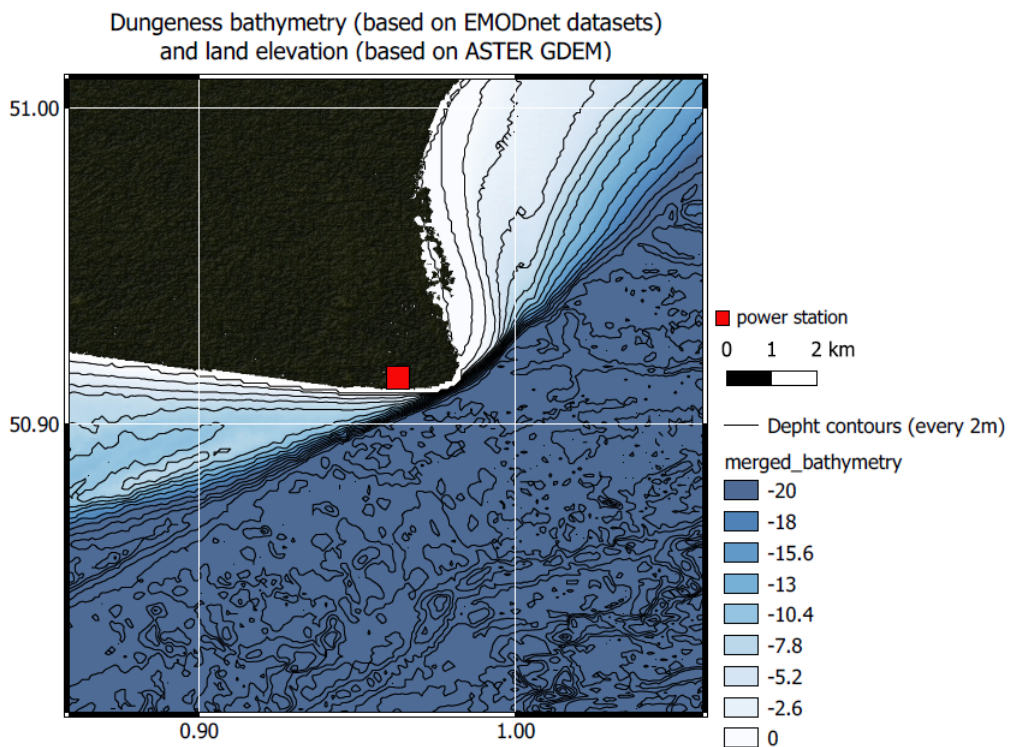


Figure 1.3: Bathymetry map of the area in the vicinity of the Dungeness power station (marked as a red square). Lighter colours symbolise shallow waters and darker colours - deeper waters. Depth contours are marked every 2m.

1.11.2 Hartlepool

Hartlepool power station (54.63 N, -1.18 E) was one of the first power stations to be built near a large urban area. It is located in the estuary of the river Tees, bordering the North Sea, south of the town of Hartlepool, in north east England. The intake of the cooling water is located onshore, deeply into the quayside [Turnpenny *et al.*, 2010]. The Tees estuary is shallow and the water depth is increasing offshore, at a gentle slope.

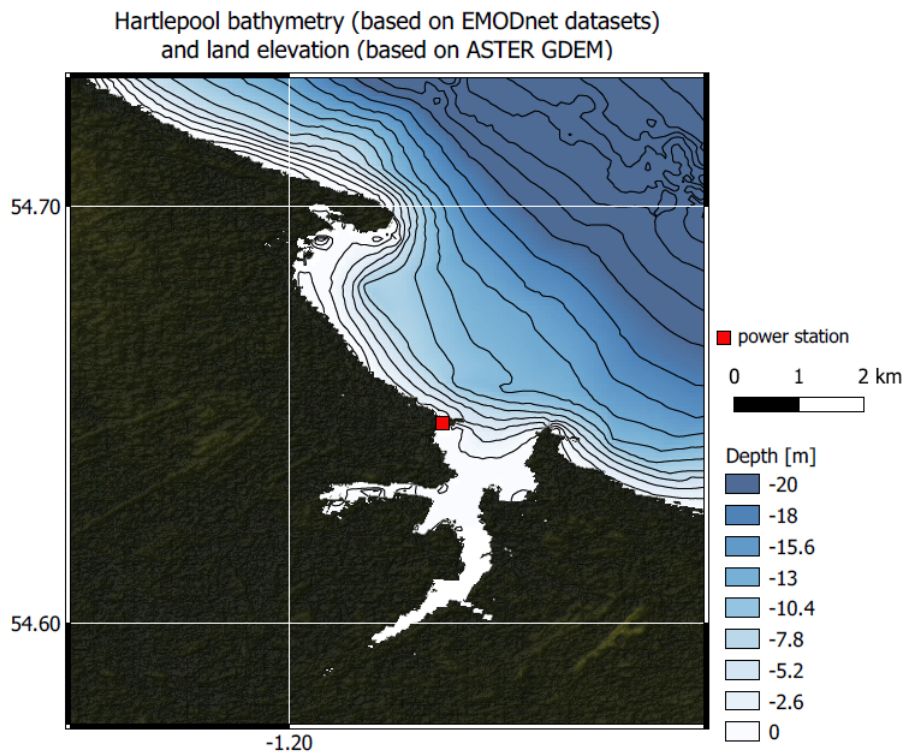


Figure 1.4: Bathymetry map of the area in the vicinity of the Hartlepool power station (marked as a red square). Lighter colours symbolise shallow waters and darker colours - deeper waters. Depth contours are marked every 2m.

1.11.3 Heysham

Heysham is EDF Energy's only site in the UK with two operating power stations, generating electricity from a total of four nuclear reactors between them. Heysham power stations (54.03 N, -2.92 E) are located in the Morecambe Bay, in the western part of the UK. The area has a relatively shallow bathymetry with multiple estuaries scattered around the bay. The deep water channel is stretching south-westward. The Morecambe Bay is one of the largest intertidal areas in the country with dynamically changing land-water boundary and periodically exposed sand- and mudflats during the ebb tide and low

water slack tide [Mason *et al.*, 2010]. Because Heysham is located in the intertidal area, the tides influence the water location. Therefore the discharge points used to release the once-through cooling water back into the sea are built as two long parallel channels, which allows the power station to eject the water back into the sea rather than on the exposed sandflats during low water events.

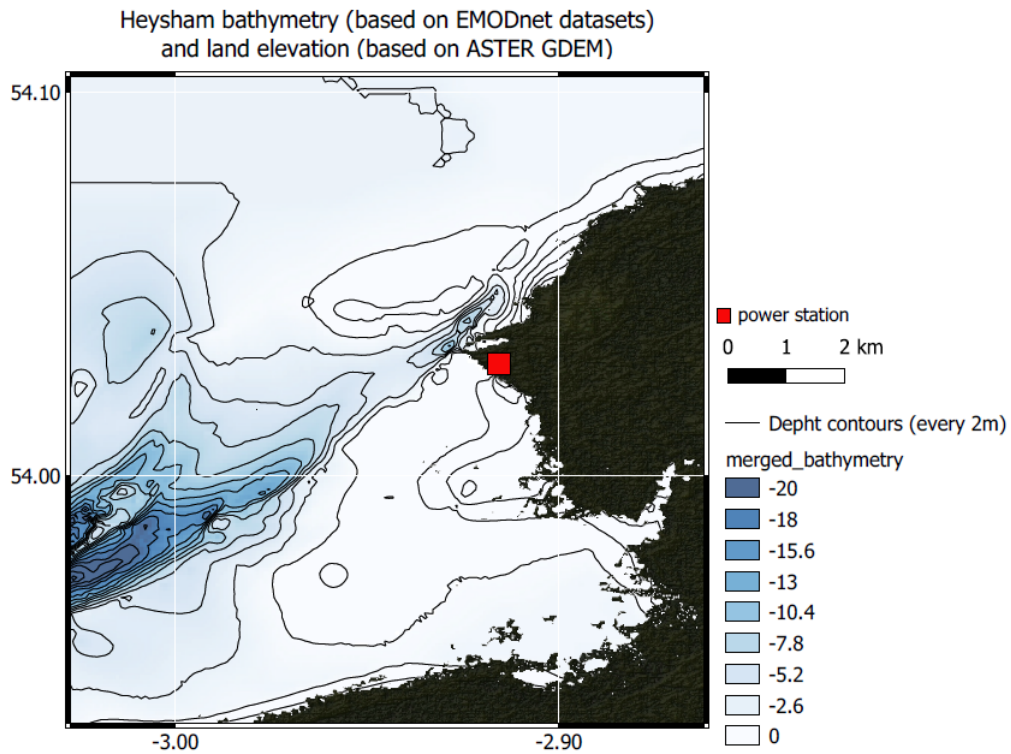


Figure 1.5: Bathymetry map of the area in the vicinity of the Heysham power station (marked as a red square). Lighter colours symbolise shallow waters and darker colours - deeper waters. Depth contours are marked every 2m.

1.11.4 Hinkley

Hinkley power stations (51.21 N, -3.13 E) are located on the south bank of the Severn Estuary, south west England. Hinkley point A is no longer operating while Hinkley point B is still in operation and the construction of Hinkley point C began in 2018. The intake and outfall of the cooling water are situated in the Severn Estuary, both on the seabed [EDF Energy, 2010b]. The waters are shallow close to the shore and gradually deepen further offshore and westward, in the direction of the Bristol Channel and the open water. Similar to Heysham, Hinkley has a large tidal range and strong tidal currents [EDF Energy, 2010b], having a dominant effect especially in shallow waters. The estuary is composed of sandflats mudflats and rock platforms [EDF Energy, 2010b], which provide

habitats for multiple intertidal species. Hence the area is protected by several regulations and conservation directives. Moreover, the power stations are located in the vicinity of Bridgewater Bay, which is a Site of Special Scientific Interest.

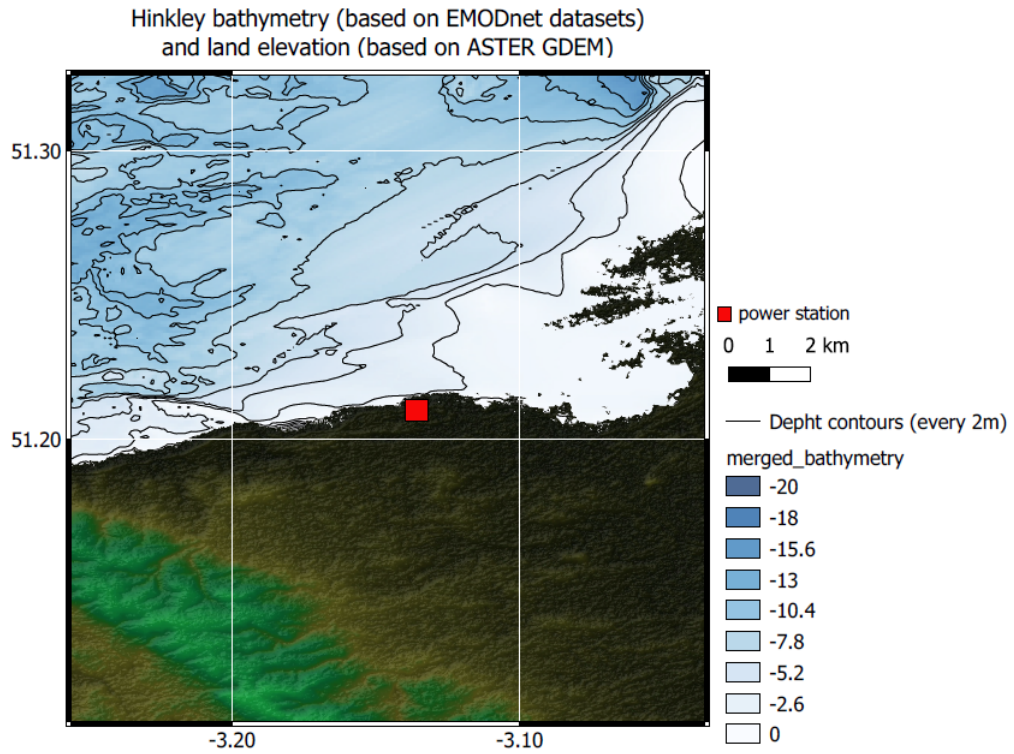


Figure 1.6: Bathymetry map of the area in the vicinity of the Hinkley power station (marked as a red square). Lighter colours symbolise shallow waters and darker colours - deeper waters. Depth contours are marked every 2m.

1.11.5 Hunterston

Hunterston power stations (55.72 N, -4.90 E) are located in the Firth of Clyde, Scotland. Hunterston A was in operation from 1964 until 1990. Currently only Hunterston B is in operation and its cooling water is discharged into Clyde Estuary. The surrounding area in the vicinity of the power station is called Hunterston Sands and is composed of shallow waters (between 2 m and 5 m deep). Beyond the shallow Hunterston Sands the bathymetry drops steeply to about 50 m depth. The Firth of Clyde area is surrounded by Cumbrae Islands, which might be a factor limiting the extent of the discharged coolant water. In 2018 the power station was shut down due to maintenance issues and the energy production renewed in 2019 with one out of two reactors operating.

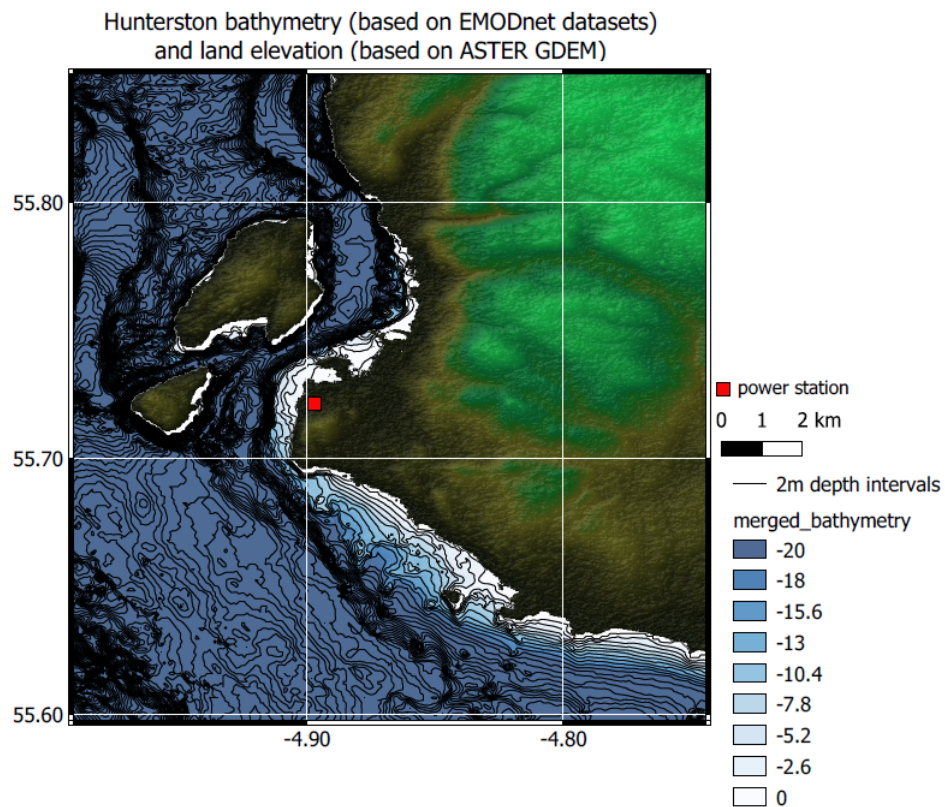


Figure 1.7: Bathymetry map of the area in the vicinity of the Hunterston power station (marked as a red square). Lighter colours symbolise shallow waters and darker colours - deeper waters. Depth contours are marked every 2m.

1.11.6 Sizewell

Sizewell power station (52.21 N, 1.62 E) is located on the Suffolk coast in the eastern part of the UK and is an example of open water exposure. The bathymetry is shallow close to coast with the depth gradually increasing offshore. This part of UK is also located

about 100 km away from an amphidromic point [*Sinha and Pingree, 1997*], which is a point where the tidal constituent amplitude is zero. It has an impact on the pattern of the water flow over different tidal cycles with tidal currents flowing parallel to the coastline. In the vicinity of the power station, parallel to the coast are located narrow underwater sandbanks, called Sizewell-Dunwich Banks. These sandbanks were created naturally by wave energy, sea currents and sediment transport [*Lees, 1983*]. Even though the sandbanks are not high enough to be exposed during low water events, their presence can impact how far offshore the discharged coolant waters disperse.

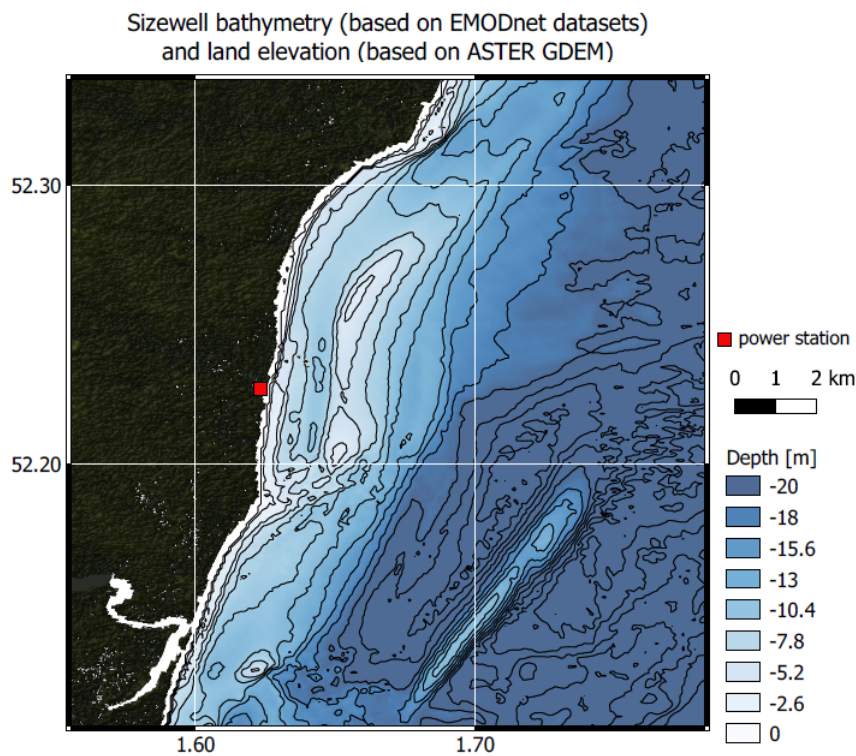


Figure 1.8: Bathymetry map of the area in the vicinity of the Sizewell power station (marked as a red square). Lighter colours symbolise shallow waters and darker colours - deeper waters. Depth contours are marked every 2m.

1.11.7 Torness

Torness is the second EDF Energy power station located in Scotland, near Dunbar (55.97 N, -2.40 E). The waters are shallow close to the coast, but in contrast to Hunterston, the bathymetry is sloping gently into the deep sea [*Davies and Neves, 2012*] with the depth contours increasing parallel to the coastline. The intake of the cooling water is located offshore, away from the main flow. The power station had challenges during its operation related to seaweed and jellyfish blocking the inlet point, which reduced water intake. The

once-through cooling water is ejected back into the coastal environment through an open channel. In order to prevent the ejected water from recirculating into the intake point, there is a breakwater construction [Davies and Neves, 2012].

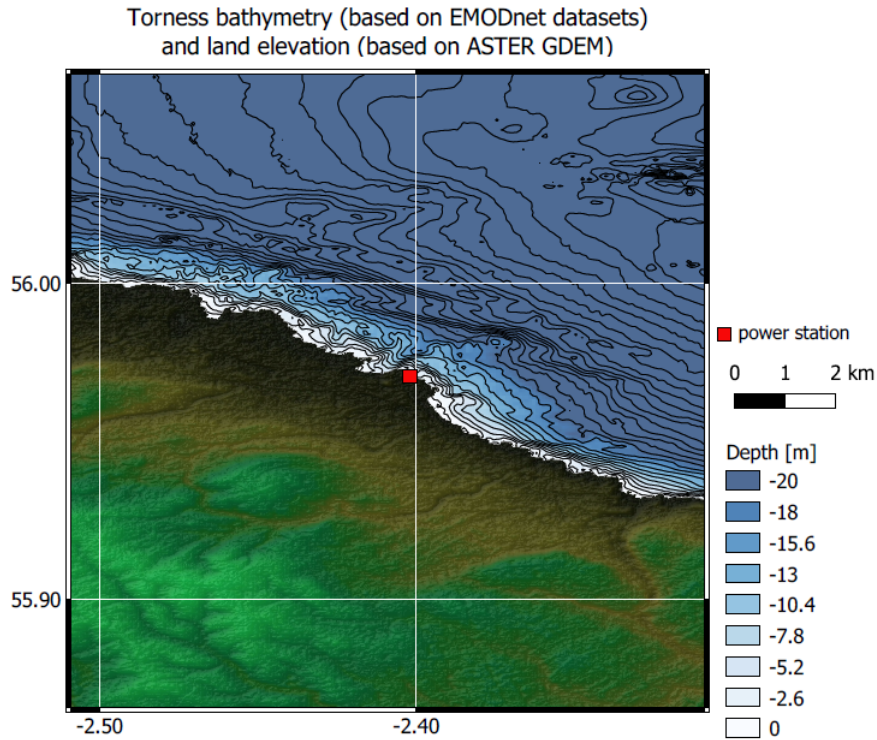


Figure 1.9: Bathymetry map of the area in the vicinity of the Torness power station (marked as a red square). Lighter colours symbolise shallow waters and darker colours - deeper waters. Depth contours are marked every 2m.

1.11.8 General hydrographic properties at estuarine locations

Most often estuaries are defined in geo-morphological terms, which means that such forms might not be related to the salinity gradients. However, real estuarine locations are areas, where the marine waters with high salinity mixes with river outfalls with low salinity [Telesh and Khlebovich, 2010]. As such, estuaries can be defined as transitional ecosystems [Telesh and Khlebovich, 2010; Cloern et al., 2017], where a salinity gradient appears due to the mixing of two types of waters: freshwater and seawater, both characterised by different salinities [Telesh and Khlebovich, 2010; Cloern et al., 2017; Stoker, 1992].

The salinity distribution in the estuaries has two main influences - it acts as an external ecological factor, but it also acts on the internal physiological characteristics, separating the invertebrae communities into freshwater and marine faunas [Telesh and Khlebovich, 2010]. Apart from that, the salinity determines the water density of water in the estuaries. This is different to sea waters, where the density is controlled by mainly temperature [Cloern et al., 2017]. The density difference between the freshwater and the seawater results in strong vertical stratification in estuarine waters [Cloern et al., 2017].

The salinity the the sea waters is relatively stable, related to the ion ratio. However, in estuaries the salinity can change as the ion ratio changes depending on the sea water to the freshwater outfall ratio [Telesh and Khlebovich, 2010]. Hence, the salinity in estuaries is not constant [Stoker, 1992]. Since the salinity variations in the estuaries depend on the mixing of the freshwaters from river outfalls and the seawater, throughout the year the salinity will have different ranges seasonally and areally depending on the ratio of both [Stoker, 1992].

When the river feeds freshwater into the estuary, it is the source of buoyancy and momentum. That momentum input drives internal circulation [Fischer, 1976] The estuarine circulation, or the gravitational circulation, is driven by the density gradients [Fischer, 1976; Cloern et al., 2017]. The freshwater from the river outfalls, having lower density, is advected seaward over a denser, saline seawater flowing landward [Cloern et al., 2017; Stoker, 1992]. The stratification established by the estuarine circulation can have seasonal variations. The seasonality of the stratification has been attributed to the seasonality in the freshwater discharges from the rivers as sources of bouyancy [Cloern et al., 2017].

Apart from the gravitational circulation, in the estuaries there is transverse mixing present due to shoreline irregularities [Fischer, 1976]. This type of mixing has been found to correspond to the tidal patterns and tidal velocity [Fischer, 1976].

The Baltic Sea can be an example of a tide-less estuary. The highly reduced impact of tides results in nearly stable isohalines and smooth salinity gradients [*Telesh and Khlebovich, 2010*]. The isohalines around UK are influenced by the salinity gradients and the tidal conditions, unlike in the example of Baltic Sea. The tides, through the interaction with the underlying bathymetry, create residual and transient currents, which influence the mixing [*Fischer, 1976*].

Moreover, the salinity in estuarine areas depends on the distance from freshwater sources (increased distance from river outfalls will increase the salinity). Therefore, even salinity at fixed points (locations) will fluctuate on a daily basis. The reason for this are the tidal phases and the resulting ebb and flood tidal currents [*Stoker, 1992*]. During the flood tide the salinity increases as saline waters are pushed into the estuary, while during the ebb tide the salinity decreases as the ebb currents carry these more saline waters back out of the estuary [*Stoker, 1992*]. Other studies (e.g. [*Vaz and Dias, 2008*]) have also closely related the salinity distribution to the tidal propagation.

To summarise, in cases of no salinity gradients, the mixing and dispersion is linked mostly due to transverse circulation [*Fischer, 1976*]. When introducing salinity, the transverse circulation is superimposed on the vertical mixing and the dispersion was attributed partly to the gravitational circulation [*Fischer, 1976*]. The amount of vertical mixing is controlled by the changes in stratification [*Scully et al., 2005*]. The estuarine behaviour adjusts dynamically to the two main driving forces: the river outflow and the sea level changes, which determine the thermohaline distribution [*Vaz and Dias, 2008*].

However, mixing and dispersion in estuaries is not solely related to the gravitational circulation, but also determined by the bathymetry [*Fischer, 1976*] and tidal mixing [*Scully et al., 2005*]. Some models have shown that the gravitational circulation has less of an impact in shallow water regions and tidal propagation and mixing acts as a main transport mechanism [*Vaz and Dias, 2008*].

1.12 Thesis objective and science questions

High resolution satellite imagery provides a unique opportunity to look at SST distributions in the vicinity of the power stations from space. It can be used to validate 3-D models, which opens up possibilities of characterising plumes subsurface. The primary objective of this thesis is to present the capabilities of remote sensing observations and modelling as complimentary methods of the thermal plume monitoring to traditional field

campaigns. To address this, three science questions were posed.

Science question 1. What remote sensing methodology enables us to characterise thermal plumes quantitatively?

Firstly, to evaluate the potential of high resolution satellite imagery for thermal plume monitoring, and to investigate the requirements to analyse the surface plumes spatially and temporally, a remote sensing methodology is developed. The description of the satellite data used, their caveats and the methodology are described in Chapter 2. Chapter 3 discusses thermal plumes observed in satellite imagery and the impact of bathymetry and tides on surface plume location.

Science question 2. What complimentary information can 3-D simulations provide in characterising thermal plumes?

Secondly, satellite observations provide information over long periods of time, but the temperatures obtained are valid at the surface, not below. To provide insights into subsurface thermal plume dispersion, a set of numerical simulations is created to model three dimensional (3-D) plume dispersion for a chosen EDF Energy site. In order to validate numerical simulations, satellite observations of surface plumes are used. 3-D simulations present thermal plume dispersion in the vertical and its plausible extent at the seabed. Such information is useful in any ecological assessment of the plume's impact on benthic organisms. Chapter 4 presents 3-D simulations of thermal plumes for different tide and volume outfall scenarios.

Science question 3. Do satellite observations and 3-D simulations provide a feasible complimentary method to traditional ways of thermal plume monitoring?

Thirdly, plume characterisation approaches presented in this PhD are compared to traditional field campaigns, looking at temporal and spatial resolutions and the financial cost. Traditionally EDF Energy characterise thermal plumes through a field campaign with a survey vessel collecting measurements. Those measurements focus on plume characteristics and possible impact on sensitive habitats nearby. High cost of such campaigns is very often the factor limiting the duration as well as repeatability of the field campaigns. Hence, another aim of this thesis is to compare and assess the usefulness of the new plume characterisation techniques proposed in this thesis compared to traditional methods. Chapter 5 compares traditional methods of plume monitoring with remote sensing and modelling techniques. Chapter 6 provides the summary and discussion of possible future work.

Chapter 2:

Satellite remote sensing data and methods

This chapter describes the data and methods used throughout this PhD project to characterise thermal plumes observed at different EDF Energy sites. Satellite data used for characterising surface thermal plumes comes from the Landsat 8 and the Advanced Spaceborne Thermal Emission and Reflection Radiometer (ASTER) observations. Observations are provided over an >10 year period of time at a high spatial resolution, which presents a good opportunity to study the sea surface temperature (SST) distributions in the vicinity of the power stations and analyse detected industrial thermal plumes. Observational data processing methods, as well as the limitations, are described in Sections 2.1 - 2.6.

2.1 High resolution satellite imagery

2.1.1 Landsat 8

Landsat 8 is a satellite funded by a joint project between the National Aeronautics and Space Administration (NASA) and the United States Geological Survey (USGS) and provides high resolution, multi-spectral imagery with a 16-day repeat time. Landsat 8 collects most of the data during daytime (10:30 am local time), with over 99.9% of daytime scenes collected between 57°N and 57°S collected [*The United States Geological Survey, 2020*]. Night scenes are acquired only after a request has been made prior to the flight. The success rate of acquiring the nighttime data depends on priority and cloud cover thresholds assigned [*The United States Geological Survey, 2020*]. There are two

instruments on-board Landsat 8, which have been collecting data since February 2013: the Operational Land Imager (OLI) and the Thermal Infrared Sensor (TIRS). The OLI instrument has a spatial resolution of 30 m (with one panchromatic band collecting data at 15 m) (see Table 2.1), and the TIRS instrument collects thermal data at a spatial resolution of 100 m (see Table 2.1). Before the data becomes available for download, the thermal data from Landsat 8 is regridded onto a regular 30 m grid, using cubic convolution oversampling [Roy *et al.*, 2014]. All channels from a single observation are available to download as GeoTIFF files.

Table 2.1: Landsat 8 Operational Land Imager (OLI) and Thermal Infrared Sensor (TIRS) channels with their spatial and spectral resolution.

channel number	spatial resolution at nadir	spectral resolution	description or typical use
1	30 m	0.43 - 0.45 μm	coastal aerosol
2	30 m	0.45 - 0.51 μm	visible - blue
3	30 m	0.53 - 0.59 μm	visible - green
4	30 m	0.64 - 0.67 μm	visible - red
5	30 m	0.85 - 0.88 μm	near infra-red
6	30 m	1.57 - 1.65 μm	short wave infra-red
7	30 m	2.11 - 2.29 μm	short red infra-red
8	15 m	0.50 - 0.68 μm	panchromatic
9	30 m	1.36 - 1.38 μm	cirrus detection
10	100 m	10.60 - 11.19 μm	surface temperature
11	100 m	11.50 - 12.51 μm	surface temperature

NASA provides each Landsat 8 scene projected in a Universe Transverse Mercator (UTM) map projection, with a north-up orientation, and World Geodetic System 84 (WGS 84) datum. Information in each image pixel is stored as a 16-bit, 55,000 grey-level digital number (DN). The DN can be converted to top of atmosphere (TOA) radiance, reflectance and at-satellite brightness temperature (BT) using equations available in Landsat 8 User's Guide [Zanter, 2016]. All data files are accompanied with a Metadata file, which provides detailed information about the observation, including the sun elevation angle and all radiometric and thermal conversion coefficients. The band-specific multiplicative rescaling factors are used to calculate reflectances and radiances for the visible and near infra-red (NIR) bands and the thermal conversion constants are used to calculate at-satellite BT for the thermal infra-red (TIR) bands. Detailed description of of the

satellite data processing is described in Section 2.3.2.

2.1.2 Landsat 8 known problems

While the number of problems on Landsat 8 is lower compared to previous Landsat satellites, there remain some that shall be considered [Barsi *et al.*, 2017; Levy *et al.*, 2017]. Those problems will impact the retrieved temperature, which is vital when trying to characterise thermal contrasts at the surface. In case of possible non-linearity, they could affect the differences in observed temperatures.

Known limitations related to the TIRS instrument affect thermal retrievals. Despite the TIRS instrument being within the range of uncertainty stated in the requirements for noise and stability, a study investigating the radiance values found that they were overestimated when compared to in-situ measurements [Zanter, 2016]. Some of the observed differences are related to the season with larger differences observed during the summer period, when the land near the calibration sites was hotter [Zanter, 2016]. Comparisons were made before and after recalibration of the thermal channels. The initial results showed that data collected by the TIRS instrument exhibited higher values than the temperatures observed by the buoys, with the error of - 2.1 K for Band 10 (10.8 μm) and - 4.4 K for Band 11 (12.0 μm). After the calibration in February 2014 the bias error was reduced and the residual variability remained 0.87 for Band 10 and 1.67 K for Band 11 at 300 K [Barsi *et al.*, 2014].

Part of the TIRS data is also affected by stray light entering the optical path of the instrument [Zanter, 2016]. The first problem is banding, a variation in signal across the image, even while observing homogeneous regions. The stray light adds additional incident energy onto the detectors causing contiguous columns of pixels to show up as "bands" of stronger signal (see Figure 2.1). The larger the amount of stray light coming in, the greater the amount of banding [Zanter, 2016].

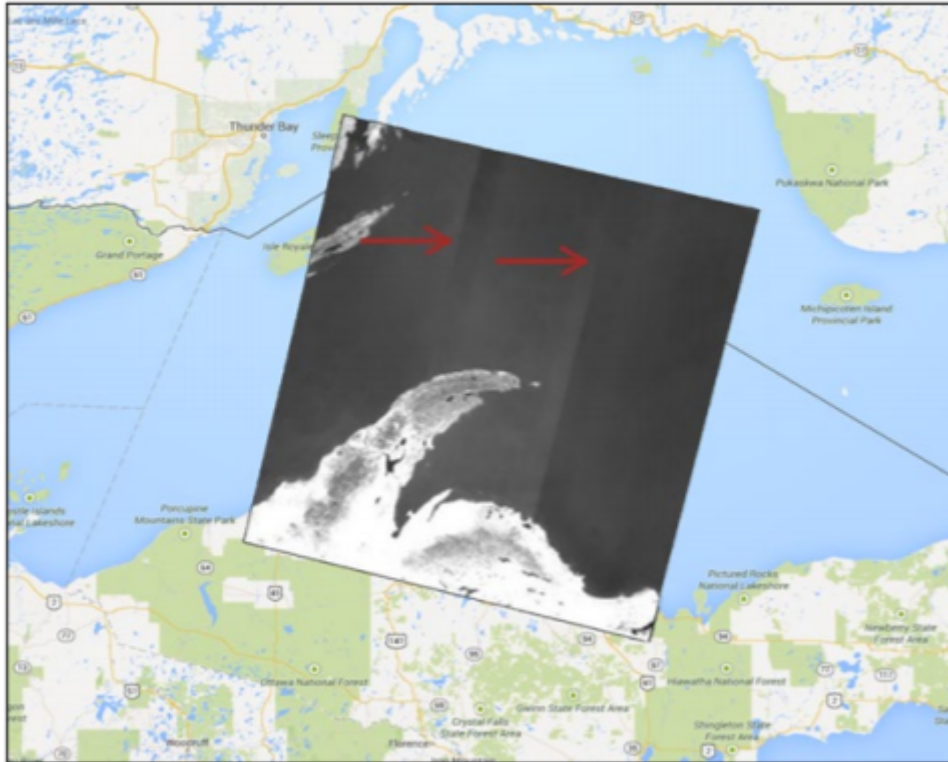


Figure 2.1: Image taken from [Zanter \[2019\]](#). Landsat 8 TIR Band 10 over Lake Superior with visible banding (lighter and darker bands of pixels) across the scene highlighted by the red arrows.

Another problem related to stray light is striping, which is similar to banding. It appears as columns of pixels that are regularly lighter or darker in a single band (see [Figure 2.2](#)). Striping occurs when a part of image is looked at by multiple detectors. In case of overlapping of adjacent sensor aggregates, an artifact that looks like striping is created.

Both striping and banding are often related to flawed calibration of detectors with respect to one another. Most of the banding and striping in the Landsat imagery can be reduced through radiometric processing [[Gerace and Montanaro, 2017](#)]. In 2017 the uncertainties occurring in the thermal bands were reduced on average from -2.1 K at 300 K with no correction to 0.3 K with the stray light correction for Band 10 and from -4.4 K to 0.19 K for Band 11. Variability of the uncertainty is reduced as well, from 0.87 K to 0.52 K at 300 K for Band 10 and from 1.67 K to 0.91 K at 300 K for Band 11 [[Gerace and Montanaro, 2017](#)].

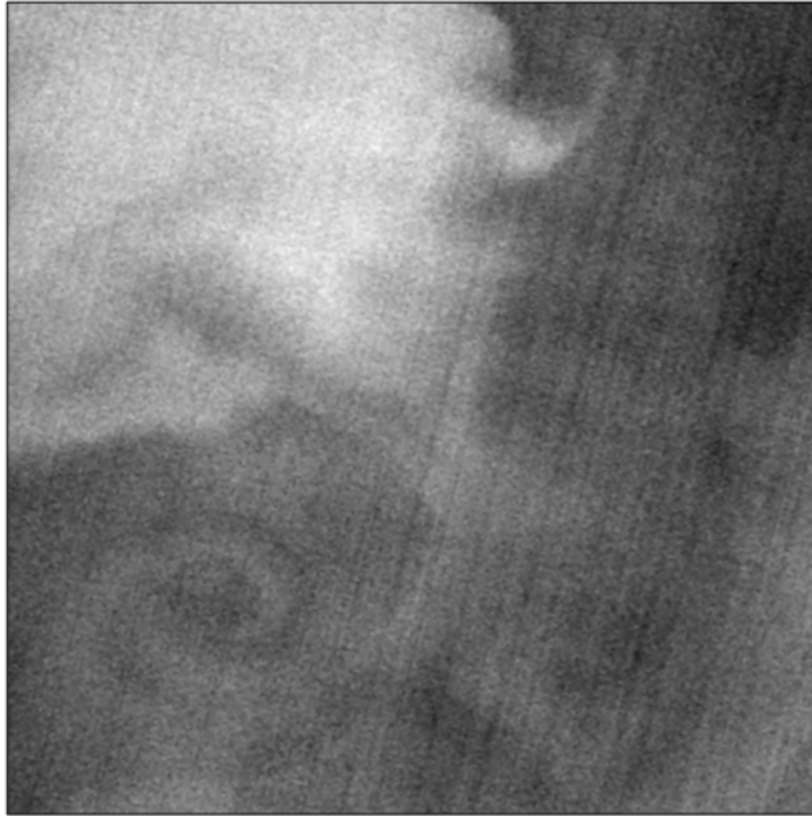


Figure 2.2: Image taken from [Zanter \[2019\]](#). Landsat 8 TIR Band 10 over clean calm water with visible striping (lighter and darker columns of pixels resembling stripes) across the scene.

2.1.3 ASTER

The Advanced Spaceborne Thermal Emission and Reflection Radiometer (ASTER) is an instrument on-board the Terra satellite, launched as a joint mission between NASA and Japan's Ministry of Economy, Trade and Industry (METI). Terra satellite, with ASTER instrument onboard, is in sun-synchronous orbit, which means that ASTER observes the Earth during the same local mean solar time, for daytime imagery near 10:30 AM and for nighttime imagery near 10:30 PM local time at most latitudes [[Crippen et al., 2007](#)]. ASTER provides high resolution (15 m - 90 m) images of Earth by collecting data over 14 wavelengths, ranging from visible to TIR. ASTER is equipped in three sensors: VNIR, SWIR, and TIR, that collect the data at visible and NIR, short wave-IR (SWIR), and TIR respectively (see [Table 2.2](#)). Due to its very high resolution (15 m for the visible channels) and the ability to change viewing angle, ASTER is able to generate stereoscopic images, which are used to produce a digital elevation model (DEM) of the terrain [[Abrams et al., 2002](#)]. ASTER thermal subsystem is comprised of five channels with a spatial resolution of 90 m and a radiometric resolution of less than 0.3 K at 300 K [[Barreto et al., 2010](#)].

ASTER data are projected onto a map rotated to path oriented coordinates (ranging from -180.0° to 180.0°) and saved as a Hierarchical Data Format (hdf) format. Each hdf file contains complete scene data from the available channels with appropriate adjustment for the positioning of the SWIR and TIR detectors. The metadata, containing radiometric and geometric coefficients, is saved in the same hdf file as the collected observational data for each scene [Abrams *et al.*, 2002].

Table 2.2: ASTER VNIR, SWIR and TIR channels with their spatial and spectral resolution.

channel number	spatial resolution at nadir	spectral resolution	description or typical use
1	15 m	0.52 - 0.60 μm	visible - green
2	15 m	0.63 - 0.69 μm	visible - red
3N	15 m	0.76 - 0.86 μm	near infra-red nadir
3B	15 m	0.76 - 0.86 μm	near infra-red backward
4	30 m	1.60 - 1.70 μm	short wave infra-red
5	30 m	2.14 - 2.18 μm	short wave infra-red
6	30 m	2.18 - 2.22 μm	short wave infra-red
7	30 m	2.23 - 2.28 μm	short red infra-red
8	30 m	2.29 - 2.36 μm	short wave infra-red
9	30 m	2.360 - 2.430 μm	short wave infra-red
10	90 m	8.12 - 8.47 μm	surface temperature
11	90 m	8.47 - 8.82 μm	surface temperature
12	90 m	8.92 - 9.27 μm	surface temperature
13	90 m	10.25 - 10.95 μm	surface temperature
14	90 m	10.95 - 11.65 μm	surface temperature

2.1.4 ASTER known problems

Similar to Landsat, there are a couple of issues on ASTER that need to be considered prior to using the data. ASTER is an on-demand instrument, which means that data are

only acquired and downloaded to the ground segment over a given location provided that a request has been submitted to observe that area prior to the scheduled flight [[NASA JPL, *asterweb.jpl.nasa.gov*, 2017](#)]. Most scenes available for the UK nuclear power station sites are night-time scenes since previous requests covered mainly nighttime data. This results in the VNIR instrument being switched off and the collected data is available only for the SWIR and TIR channels. Having no observations in the visible spectrum available does not permit applying reflectance-based water detection techniques, since these are based on a combination of bands including the visible channels [[Xu, 2006](#); [McFeeters, 1996](#)]. Alternate approach to detect water in the nighttime scenes had to be chosen, which is further described in Section 2.4.2.

Another issue affecting the number of channels available for data processing is limited availability of the SWIR data caused after an incident in 2008. The cryo-cooler in the SWIR subsystem was failing to maintain the temperature of that subsystem, which resulted in the SWIR channels generating over-saturated images [[Liang, 2017](#)]. Since the data obtained by the SWIR subsystem was no longer reliable, the subsystem was switched off. This reduced the number of observations available during night-time to TIR channels.

Lastly, the information on cloud cover provided as part of the metadata is not be sufficient for the purpose of assessing cloud contamination of a chosen scene. The algorithm used for cloud detection was based on a combination of channels including one SWIR channel, which after the failure of the cooling system, could no longer be used. Though, the cloud detection algorithm was performing satisfactory during day-time, it was reported as not accurate during night-time [[Hulley and Hook, 2008](#)]. The cloud contamination for ASTER images has been reviewed by using MODIS, another instrument on-board the Terra satellite. Currently, the information on the cloud contamination is given for 4 quadrants of the image and the total cloud cover over the scene is presented as an average over the four quadrants [[lpdaac.usgs.gov, LP DAAC - Land Processes Distributed Active Archive Center, 2017](#)] I used that information for obtaining the ASTER scenes, however, it limited the number of observations useful for the purpose of thermal plume monitoring.

2.2 Obtaining satellite data

High resolution Landsat 8 and ASTER data sets were obtained from the United States Geological Survey (USGS) Earth Explorer website through a Machine-to-Machine access using the USGS and EROS JSON API. Using a Python interface facilitates the

download of the large data volumes, while using the website interface would be more time-consuming. The Python interface was created by Dr. Sam Doolin from the Institute of Environmental Analytisc (IEA) as an aid in Phase I of a precursor EDF/University of Reading/IEA project to investigate thermal plumes released by nuclear power plants.

The Landsat 8 and ASTER datasets were located on the USGS portal by specifying coordinates of the Region of Interest (ROI) and permissible cloud cover over the scene. Cloud cover for each scene has been specified as percentage of the area with identified cloudy pixels compared to the area of the whole image, with numbers from 0 to 9 representing fractions of the cloud cover from <10% cloud cover to <100% cloud cover respectively, as increments of 10%.

Since very cloudy scenes are not useful for surface temperature retrieval, it was important to choose scenes with low cloud cover or clear-sky. The allowed cloud cover over each scene was set to less than 50%. This criterion was chosen because the size of a single satellite scene is larger than the size of the ROI and therefore with moderate cloud contamination over the scene, the clouds present in the image might not be located over the ROI. I investigated the obtained scenes manually to determine that no clouds were present in the vicinity of the power station.

Figure 2.3 presents an example search command for scenes with cloud cover under 10% obtained by ASTER over the Heysham power station from 01.01.2017. Heysham location is specified by the *-bb-centre* giving both latitude and longitude of the location, while *-bb-length* specifies the allowed distance (in kilometers) away from the given coordinates.

```
usgs search--create ASTER_L1T mysearch.json
--bb-centre 54.028889,-2.916111
--bb-length 30
--start-date 2017-01-01
--max-cloud-cover 10
```

Figure 2.3: Example search for ASTER instrument for Heysham site

After running the search command, all scenes fulfilling conditions specified in the search will be listed and downloaded in bulk. The downloaded satellite scenes were then manually revised in terms of cloud contamination. Due to poor cloud cover assessment for the ASTER observations (quadrant cloud cover - [lpdaac.usgs.gov, *LP DAAC - Land Processes Distributed Active Archive Center*, 2017]), many of the ASTER images had to be discarded. The number of scenes for both Landsat 8 and ASTER are shown in Table 2.3. The images were obtained for the instruments' operational period of time, 2013 -

2019 for Landsat OLI and TIRS and 2000 - 2019 for ASTER.

Table 2.3: Landsat 8 and ASTER scenes used for further processing

site	Landsat 8 scenes	ASTER scenes
Dungeness	50	2
Hartlepool	36	5
Heysham	44	2
Hinkley	37	3
Hunterston	42	1
Sizewell	47	1
Torness	44	5

2.3 Satellite data pre-processing

Prior to using the satellite data for the purpose of thermal plume detection, the downloaded data had to be pre-processed. I have geo-referenced the satellite images and regrided them onto a common grid, with the power station coordinates set as the centre of the image.

2.3.1 Georeferencing the pixels

In order to be able to locate the power station in each obtained image, each image pixel had to be geolocated. The metadata file provided information on the geographical coordinates of the four corner coordinates in the upper left, upper right, lower left, lower right corners of the image. I interpolated between the corner coordinates values from the metadata, taking into account the image size. I then reprojected the data onto the WGS84 coordinate system, which is a geographic coordinate system based on a spheroid. After transforming the points, each pixel from the image had corresponding latitude and longitude values. I verified those values against the spatial resolution of the data, converting from metres into degrees.

2.3.2 Radiance, Reflectance and Brightness Temperature Calculations

Since the data are provided as DNs For both Landsat and ASTER thermal bands, those values needed to be translated into physically meaningful units that can be used for further processing. Reflectance from visible and SWIR channels is essential for water detection while BT from thermal channels will be used as input for retrieving sea surface

temperature (SST).

2.3.2.1 Conversion to Reflectance

Deriving reflectance values for Landsat 8 is straightforward and were obtained directly from the DN, as follows:

$$\rho = \frac{M_\rho \cdot DN + A_\rho}{\cos(\theta_{SZ})} \quad (2.1)$$

where DN is Digital Number of a pixel, M_ρ is multiplicative rescaling factor of a specific band, A_ρ is the additive rescaling factor and θ_{SZ} is the local solar zenith angle provided in the metadata file.

For ASTER, reflectance values are based on radiances and hence, first the DN had to be converted into radiance space using:

$$L = ucc \cdot DN - ucc \quad (2.2)$$

where ucc is Unit Conversion Coefficient, which depends on gain information of each band. The values of the ucc are found in the metadata. The obtained radiances were transformed into reflectances using:

$$\rho = \frac{\pi \cdot L \cdot d^2}{E_{irr} \cdot \cos(\theta_{SZ})} \quad (2.3)$$

where L is radiance, d is Earth-Sun distance considered a constant, E_{irr} is mean solar exo-atmospheric irradiance and θ_{SZ} is the local solar zenith angle, both available from the metadata file.

2.3.2.2 Conversion to BT

The BT for each thermal channel is based on the radiance values so firstly radiance had to be derived from the scaled data. Equation 2.2 describes the conversion between DN and radiance for ASTER. For Landsat 8 data, the equation to convert from the DN to radiance of the pixels is:

$$L = M_l \cdot DN + A_l \quad (2.4)$$

where DN is Digital Number of a pixel, M_l is multiplicative rescaling factor of a specific band and A_l is the additive rescaling factor for a specific band obtained from the metadata file.

The radiance values were converted into BT using the following formula:

$$BT = \frac{K_2}{\ln\left(\frac{K_1}{L} + 1\right)} \quad (2.5)$$

where K1 and K2 are constants found in the metadata file. This formula can be applied to both ASTER and Landsat data.

2.3.3 Regridding the data

Regridding the data onto a common grid facilitates comparison of observations from different sensors. The thermal and visible images obtained on the same day can then be compared against each other, so that land/beach/cloud pixels in the visible and SWIR channel can be used to mask corresponding BT pixels.

The size of the common grid is 20 km by 20 km with geographical coordinates of the nuclear power station set as the centre. The resolution is 50 m, which is reasonable to investigate coastal features and distinguish between e.g. the beach and water areas and sensible compared to the native resolution of the observations.

I used the nearest neighbour algorithm to regrid the data onto the common grid. In the NASA-distributed Landsat 8 product the thermal channels have already been down sampled to a 30 m visible grid, sometimes more than one Landsat product grid cell will fall into one common grid cell (see Figure 2.4). However, the thermal bands originally collect data at 100 m resolution so regridding onto a larger common grid does not reduce the real resolution. In case of ASTER, the thermal bands come at their native resolution (90m) and therefore had to be interpolated onto a smaller resolution of the common grid. After regridding ASTER data using the nearest neighbour algorithm, I calculated missing points using a 2-D linear interpolation.

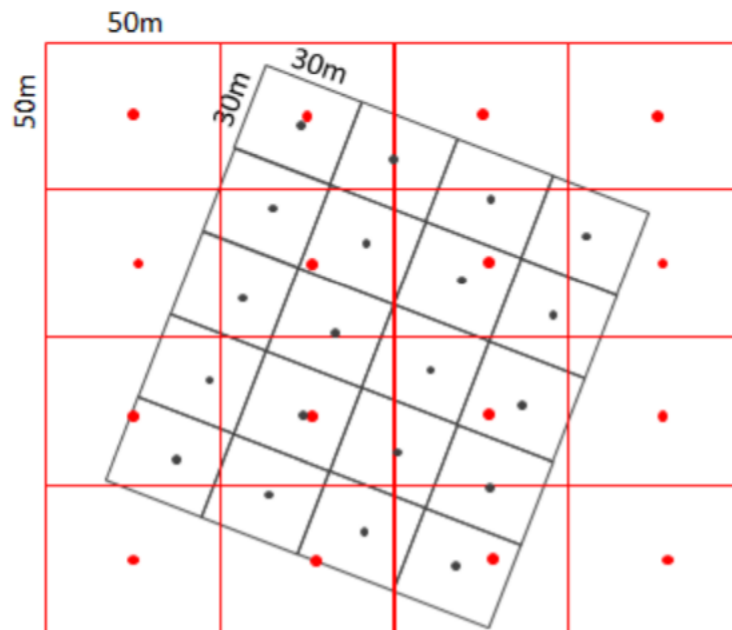


Figure 2.4: Sketch of the original Landsat 8 image grid at a 30 m resolution (marked in black) and the common grid used for data regridding at a 50 m resolution (marked in red).

2.4 Water detection in coastal imagery

In order to detect surface thermal plumes released into coastal environments, it is necessary to properly detect water regions in each image. Inaccurate water detection might lead to classifying hot parts of land as part of the plume or misreading the ambient water temperature in case of any undetected cloud contamination. Coastal environments very often have a dynamic land-water boundary and hence using a land mask product would be insufficient as it would not allow for masking of temporarily exposed sand- and mudflats or clouds. Therefore, because most images were daytime observations, I applied threshold-based water detection algorithms.

2.4.1 Water detection for daytime imagery

[Boschetti et al. \[2014\]](#) provides a review of existing water indices and how they can be used in water detection algorithms. Typically, a combination of visible, NIR and SWIR bands is used. The values are normalised, ranging from 0 to 1, which permits setting a threshold value to separate water from the rest of the image. Since all known water detection algorithms use visible channels, this methods can only be used for the daytime images.

For the purpose of detecting water features, the Normalised Difference Water Index (NDWI) [McFeeters, 1996] is useful. While using green and NIR bands, water tends to have larger index values than vegetation, which makes it easier to differentiate between water and vegetation. However, Xu [2006] demonstrates the limitations of the McFeeters' NDWI as it fails to fully distinguish between built-up land areas and water. He proposed a Modified Normalised Difference Water Index (MNDWI), which has been found to perform better for mixed pixels [Xu, 2006] and highlighting water features without detecting other land features [Szabó *et al.*, 2016].

MNDWI uses values from two reflectance bands, green (0.53 - 0.59 μm) and SWIR (1.57 - 1.65 μm), to determine the index value for each pixel:

$$MNDWI = \frac{green - SWIR}{green + SWIR} \quad (2.6)$$

To test the accuracy of the MNDWI method for my data, a set of pixels, with prior known land cover, has been compared against the MNDWI. To create a known set, I looked at the scenes manually and extracted the pixels based on the RGB composites. The set included pure land pixels, vegetation, clouds, beaches, pure water pixels and mixed pixels from several Landsat 8 observations. For water regions, where there was over 95% of pure water in the pixel, the MNDWI was very high with values oscillating between 0.7 and 1.0. Land, vegetation and clouds had lower MNDWI and hence this index has been verified to be good in highlighting water features.

In order to delineate water from other land covers in each scene, an appropriate MNDWI threshold needed to be chosen. Determining a suitable threshold is challenging, since the ratios of same (or similar) band combinations will yield different values, depending on the instrument and the satellite. Hence there is no one universal threshold for water detection that could be used for different satellites. Liu *et al.* [2012] has shown that very minor changes in the best threshold can exist on a daily basis. Moreover, the MNDWI values depend also on sub-pixel components, such as land, water, vegetation, sand, which is in relevance to coastal areas.

Xu [2006] proposed two MNDWI threshold values for distinguishing between water features and surrounding area: 0.44 for open water surfaces and 0.9 for areas near the shore. The higher threshold was proposed for close-to-coast areas because the use of 0.44 would cause mixed pixels to be identified as water as well. However, Xu [2006] focused on lakes and rivers and used Landsat Thematic Mapper (TM) observations, so the need to revise the thresholds for Landsat 8 was expected. I have tested the MNDWI thresholds

over a sample of clear-sky and partly cloudy scenes during high and low tide events.

Figures 2.5 and 2.6 show the MNDWI values calculated for a cross section of data from the image highlighted as a black line on the satellite images. As suggested by literature, the index has high values for water regions and much lower for urban / vegetation canopy. However, in Figure 2.5, the MNDWI values over the water oscillate around 0.9 and choosing a 0.9 threshold, which was a suggested value by [Xu, 2006] for areas near the shore, would not allow for proper water detection. In the second example (see Figure 2.6), the threshold of 0.9 would not pick up any sea water pixels. Lowering the threshold to 0.8 results in detecting water pixels without reducing accuracy. The cirrus cloud seen in the RGB (see Figure 2.6) is correctly identified as non-water and has lower MNDWI values than 0.8 between pixels 120 and 170. Hence, it was concluded that a threshold of 0.8 proved most fitting in detecting water regions in the coastal areas.

For any ASTER daytime imagery collected after 2008, due to lacking information from the SWIR instrument, the NDWI [McFeeters, 1996] algorithm for water detection was used with appropriately set threshold.

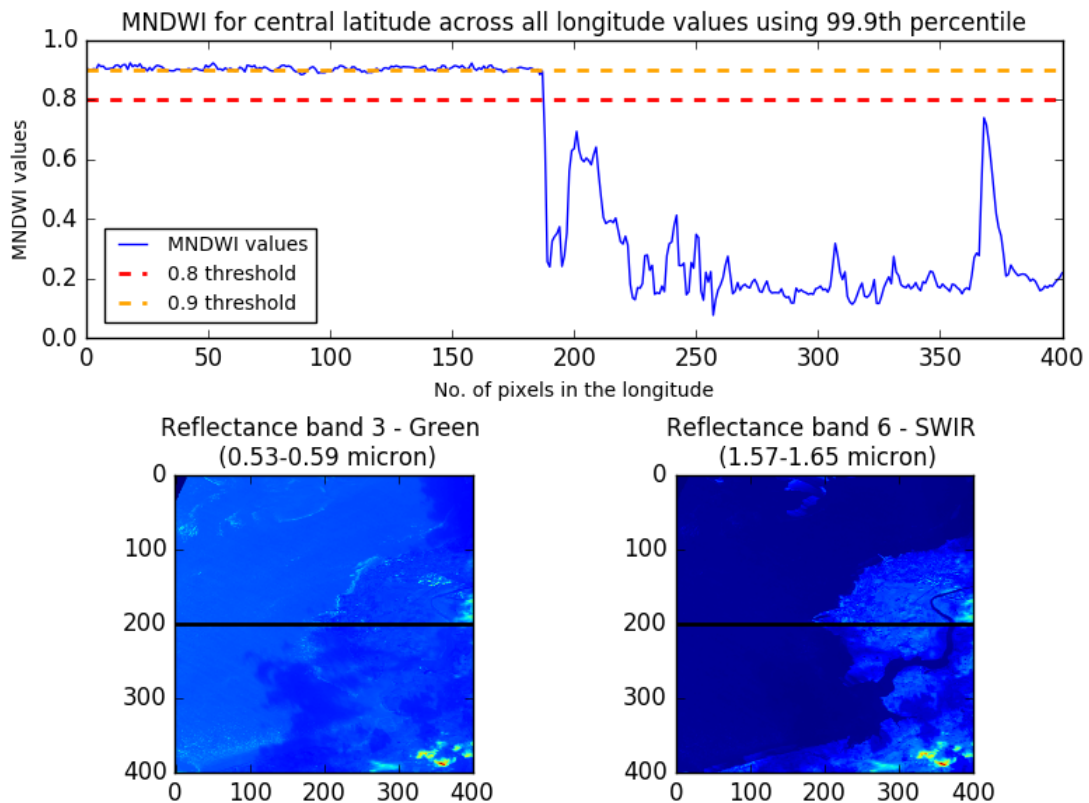


Figure 2.5: Modified Normalised Water Difference Index for Heysham on an example day. MNDWI values for the cross-section line of the scene with 0.8 and 0.9 threshold values marked in red and orange respectively (upper plot). MNDWI composite bands: band 3 (Green, left) and band 6 (SWIR, right) reflectance values for the whole scene with the cross-section, for which the MNDWI was calculated, marked in black (lower plot).

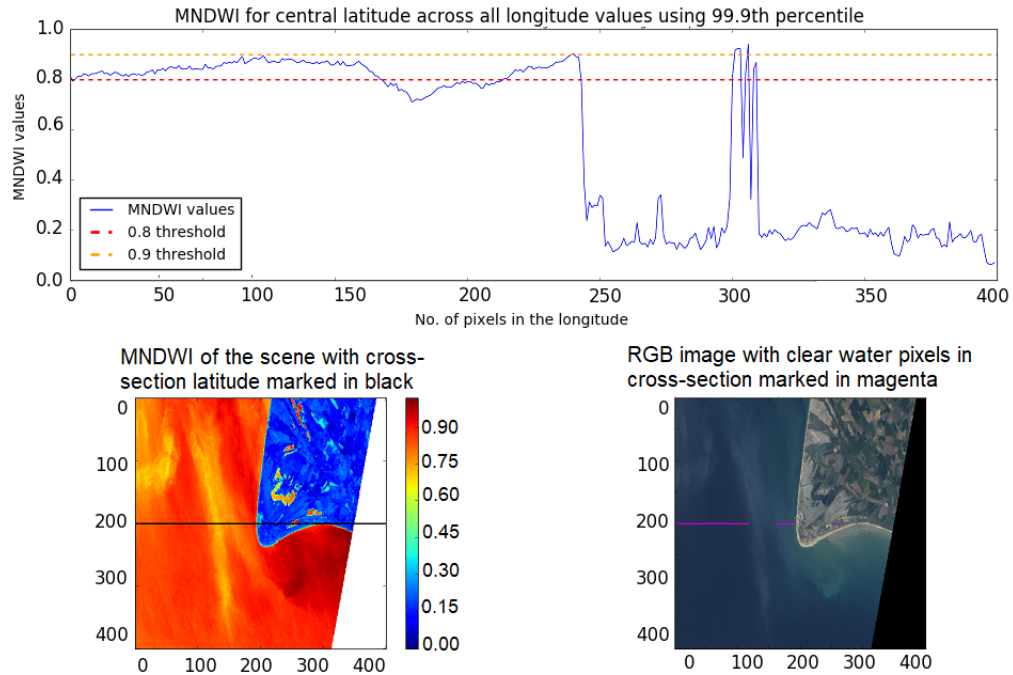


Figure 2.6: Modified Normalised Water Difference Index for Dungeness on 20 April 2016. (upper) MNDWI values for the cross section line of the scene with 0.8 and 0.9 threshold values marked in red and orange respectively. (lower left) MNDWI values obtained from Xu et al (2006) algorithm for the whole scene with the cross section marked in black. (lower right) RGB image of the corresponding scene with corresponding cross section only satisfying the MNDWI 0.8 threshold marked in purple. Land and cirrus cloud visible on RGB fail the MNDWI threshold and hence there is no purple line in those areas of the cross-section.

2.4.2 Water detection for nighttime imagery

The satellite dataset used for thermal plume characterisation has been expanded by adding night time imagery from the ASTER sensor. The product contains only thermal channels, which makes it impossible to apply any of the water detection algorithms described for the daytime scenes. In order to differentiate between land and water, I created a land mask derived from the daytime MNDWI values. Clouds or inter-tidal areas were not included in creating the land mask as their presence and location in each image is different. Because the number of nighttime scenes was low, the images were reviewed by eye after applying the land mask. After the eye inspection, the land mask proved to be sufficient for regions with no inter-tidal sand- and mudflats. For sites such as Heysham, using a land mask was inadequate in most cases as it did not mask any of the exposed inter-tidal areas. For images where the BTs of the exposed flats were similar to the ones of coastal waters and the thermal plume, it was impossible to set a reliable threshold to distinguish between the warm exposed sands and the surface thermal plume. Hence,

those images could not be included in further analysis.

The images with successfully masked land had to then be screened for cloud cover. Since the cloud information in ASTER product is provided only for each quartile of the image, it is difficult to ascertain that the observed thermal plume is not obscured by any clouds. In order to mask out the clouds in the nighttime imagery, I applied a threshold of 276 K on the brightness temperature (BT) from 10.8 micron channel. Every region of contiguous pixels with BT below the 276 K threshold was classed as clouds or cold beaches. This threshold was sufficient for the small geographical region that was looked at. This threshold might not work for other locations and there can be cases of missed warm clouds. Due to the low number of scenes, they could be inspected by eye. The chosen threshold allowed for successful masking of cold clouds and some parts of the exposed cold beaches.

The nighttime sample was used to expand the dataset for thermal plume monitoring. Though it allowed for expansion of the dataset by several images, this method is not feasible for large data volumes as it cannot guarantee that no clouds will be overlooked without visual inspection. In case of a larger volume of nighttime ASTER data available, a different cloud screening algorithm would have to be applied. However, it is worth noting that the thermal plumes observed in the nighttime imagery are not expected to behave differently from the plumes in the daytime imagery.

2.5 Optimal estimation for SST retrieval

To look at the thermal contrasts in the vicinity of the power stations, BT observed by the satellites had to be converted into SST. The chosen sea surface temperature (SST) retrieval method was optimal estimation (OE) as described further in [Merchant et al. \[2008\]](#). OE allows for calculation of the best estimates of the state variables (SST and water vapour), given the initial estimate, with corresponding simulated observations and prior observations. [Rodgers \[2000\]](#) provides an in-depth description and the derivation of the equations for the optimal linear inverse methods, used in the OE algorithm. The SST is retrieved, after [Rodgers \[2000\]](#), using:

$$\hat{x} = x_a + S_a K^T (K S_a K^T + S_\epsilon)^{-1} (y - K x_a) \quad (2.7)$$

where \hat{x} is the retrieved SST, x_a is the initial estimate vector of the total column water vapour (TCWV) and the SST, S_a is the 2×2 diagonal matrix of squared uncertainties

of the SST and the TCWV, K is the matrix of partial derivatives for the reduced state vector, S_{ϵ} is the 2×2 diagonal matrix combining the measurement uncertainty and the radiative transfer model (RTM), y are the BT values observed by the satellite and Kx_a is the simulated BT.

OE requires simulation of observations as part of the retrieval process, for which I used the numerical weather prediction (NWP) atmospheric profile and daily, averaged, gridded, gap-filled SST from the European Space Agency Climate Change Initiative (ESA CCI). The NWP profiles were downloaded from the ECMWF website from the ERA Interim reanalysis dataset [Dee et al., 2011]. ERA Interim is a global atmospheric reanalysis from 1979 and covers the operational lifetime of both Landsat 8 and ASTER. ERA Interim provides the SST values as well, however, the SST is provided on a larger grid ($0.75^\circ \times 0.75^\circ$). Therefore I used the ESA CCI level 4 SST instead as its resolution ($0.05^\circ \times 0.05^\circ$) allowed me to get closer to the coast and the ROI. The CCI level 4 SST is provided at depth of 20 cm and hence a skin-to-bulk correction was used after Donlon et al. [2002]:

$$T_{skin} = T_{bulk} - 0.17 \quad (2.8)$$

To get the best estimate of state variables, an RTM is used, here RTTOV version 11.3 [Saunders et al., 2013; Hocking et al., 2014]. RTTOV is a fast RTM used to simulate the top of atmosphere radiances (and hence BTs) using knowledge of a prior state obtained from numerical weather prediction (NWP) atmospheric profiles. The BTs simulated by the RTTOV can be defined as a function of SST, averaged over a gridbox, and one NWP profile as:

$$BT_{simulated} = f(\langle SST \rangle, NWP) \quad (2.9)$$

I compared the simulated BTs with the BTs observed by the satellites. I used BT observations from 2 channels from Landsat 8 TIRS ($10.6 \mu\text{m} - 12.51 \mu\text{m}$) and from 5 channels from the thermal subsystem of ASTER ($8.12 \mu\text{m} - 11.65 \mu\text{m}$). The BT observed by the satellite (top of atmosphere BT) is defined as a function of the actual SST at a defined point (x,y) and an actual state of the atmosphere:

$$BT_{observed} = f(SST(x, y), Atmosphere) \quad (2.10)$$

It is important to note that the two BTs are compared on the assumption that the

simulated BT (averaged over a gridbox) is approximately equal to the averaged observed BT:

$$BT_{simulated} \sim \langle BT_{observed}(x, y) \rangle \quad (2.11)$$

The observed BT was compared to ESA CCI SST L4 product. ESA CCI SST L4 product comes at a spatial resolution of 0.05 °, but the low resolution of the actual observations means that it is only feasible to use the single SST observation near the ROI. Since I am using only one prior SST per every satellite scene, it will not include the temperature variations across the scene caused by the thermal plume. Hence, the uncertainty in the prior SST was assumed to be the biggest temperature difference across the scene (i.e. biggest difference between the plume and ambient waters in each scene) and after investigation this was set to 8 K.

2.5.1 Comparison of other SST retrieval methods

With the recent publication of *Jang and Park* [2019] on SST retrievals from Landsat 8, towards the end of the PhD different SST retrieval methods have been compared. The methods for SST retrieval suggested by *Jang and Park* [2019] are coefficient-based algorithms that vary depending on the source of the prior SST and including of the satellite zenith angle (see Table 2.4). *Jang and Park* [2019] concluded that the non-linear SST (NLSST) algorithms, which included a prior SST value, performed better than the multi-channel SST (MCSST) retrievals.

Table 2.4: MCSST and NLSST algorithms presented by *Jang and Park* [2019]. T_{11} represents BT at 10.8 micron, T_{12} is BT at 12 micron, T_{OSTIA} is the prior known SST from OSTIA data set, a_1 , a_2 , a_3 and a_4 are constants.

Algorithm	Number	Equation
MCSST	MCSST1	$SST = a_1 T_{11} + a_2 (T_{11} - T_{12}) + a_3$
	MCSST2	$SST = a_1 T_{11} + a_2 (T_{11} - T_{12}) + a_3 (T_{11} - T_{12})(\sec\theta - 1) + a_4$
NLSST	NLSST2	$SST = a_1 T_{11} + a_2 T_{OSTIA} (T_{11} - T_{12}) + a_3$
	NLSST5	$SST = a_1 T_{11} + a_2 T_{OSTIA} (T_{11} - T_{12}) + a_3 (T_{11} - T_{12})(\sec\theta - 1) + a_4$

The prior for NLSST2 and NLSST5 used by *Jang and Park* [2019] comes from the Operational Sea Surface Temperature and Sea Ice Analysis (OSTIA) dataset [*Donlon et al., 2012*]. To compare the SST retrieval algorithms, I have used ESA CCI L4 SST instead of OSTIA SST to keep consistency between the prior used in the OE retrieval and the prior used in the NLSST retrievals. ESA CCI SST and OSTIA SST have a similar processing algorithm and hence it is a suitable substitute. For a well designed retrieval algorithm

the prior value should have minimal impact on the results.

Figure 2.7 shows the mean SST calculated over the detected water region across a sample of scenes. The SST has been calculated using 4 algorithms proposed by *Jang and Park [2019]* and compared with the SST retrieved using OE. The MCSST1 algorithm (marked as a red circle) uses only coefficients to retrieve the SST from two Landsat 8 thermal channels. MCSST2 (marked as a blue square) is a modification of the first algorithm and it accounts for the satellite zenith angle as well. The NLSST algorithms (marked as black star and green triangle) include a prior known SST from the ESA CCI L4 dataset. NLSST5 (marked as a green triangle) accounts for the satellite zenith angle as well. SSTs obtained from the MCSST algorithms were found to have marginally higher values compared to SSTs obtained from NLSST algorithms (see Figure 2.7). The OE algorithm tends to produce warmer SST compared to the other algorithms (7 out of 10 scenes), with differences ranging from $-2.2\text{ }^{\circ}\text{C}$ to $+1.3\text{ }^{\circ}\text{C}$ across the whole scene.

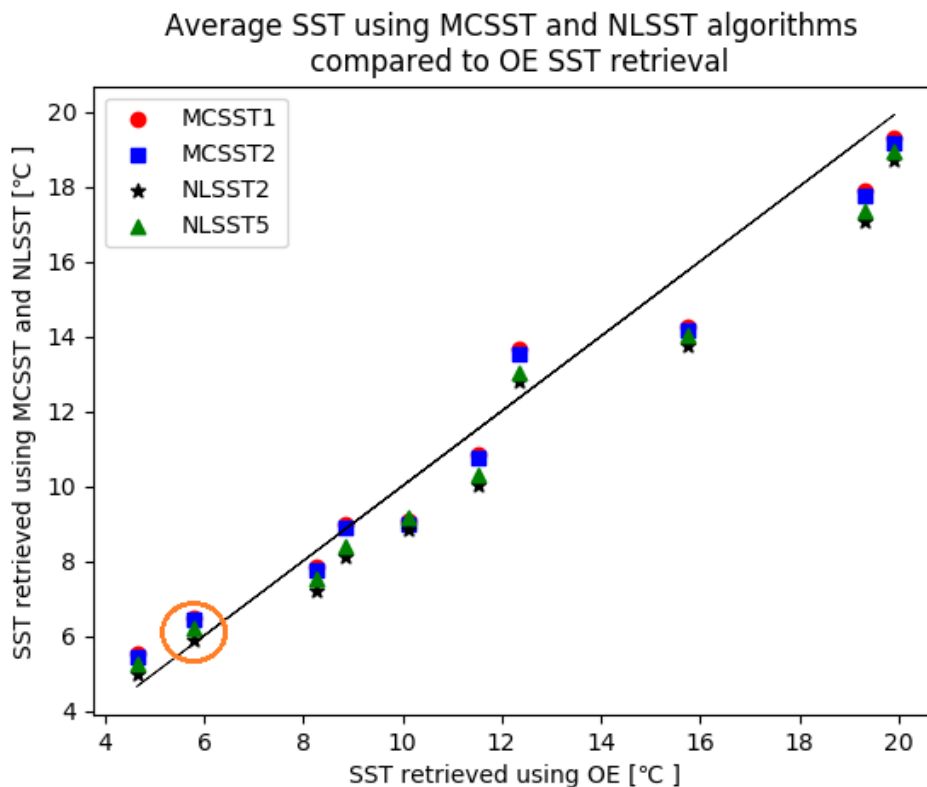


Figure 2.7: Mean SST across detected water regions for a sample of scenes using MCSST (marked as red circles and blue squares) and NLSST (marked as black stars and green triangles) algorithms compared to SST retrieved using OE (x axis). The data has been binned by OE SST. In orange is circled an example scene that is later shown in Figure 2.8.

Figure 2.8 shows the difference in SST values for MCSST and NLSST retrieval methods compared to OE for an example scene circled in orange in Figure 2.7. The box of water with the plume seen in the OE retrieval has been marked as the black square and the box of ambient waters used as ambient waters have been marked as a white square. The MCSST methods yield differences of a 1.0 °C across the whole scene, with highest differences (1.50 - 1.75°C) observed in the right part of the image. The ambient waters in the white box were warmer than in the OE by 0.50°C for MCSST1 and 0.43°C for MCSST2. The plume was also warmer in both MCSST algorithms. The visible striping is associated with the banding observed in both thermal channels. Landsat 8 scenes with SST derived using the MCSST algorithms observed the most amplified banding and striping from all algorithms tested. The NLSST derived scenes had smaller banding and striping across the scene and a more uniform SST across the scene. It can be seen that in the region, where OE observed a region of cooler SST, the NLSST algorithms observed temperatures higher by about 0.75°C, which results in a more uniform SST across the scene. The NLSST2 algorithm was closest to the OE retrieval in the ambient water region with only 0.08°C difference. However, both NLSST algorithms yielded a cooler plume (-0.45°C for NLSST2) compared to the plume seen using the OE method (see the region marked by a black square in Figure 2.8). Warmer ambient waters and cooler plume resulted in lower thermal contrast across the scene. The other scenes have been looked at as well and they exhibited similar SST patterns, where the temperature difference between the plume and the ambient waters was smaller than the one observed by the OE. The three patterns that have been observed, when compared to OE, were:

- the whole ROI was warmer than in the OE retrieval, the ambient waters had a larger temperature increase and the plume had a smaller temperature increase;
- the whole ROI was cooler than in the OE retrieval, the ambient waters had a smaller temperature decrease and the plume has a larger temperature decrease;
- the average SST over ROI was similar to the OE retrieval, the ambient waters had an increase in temperature and the plume seemed cooler than in the OE retrieval.

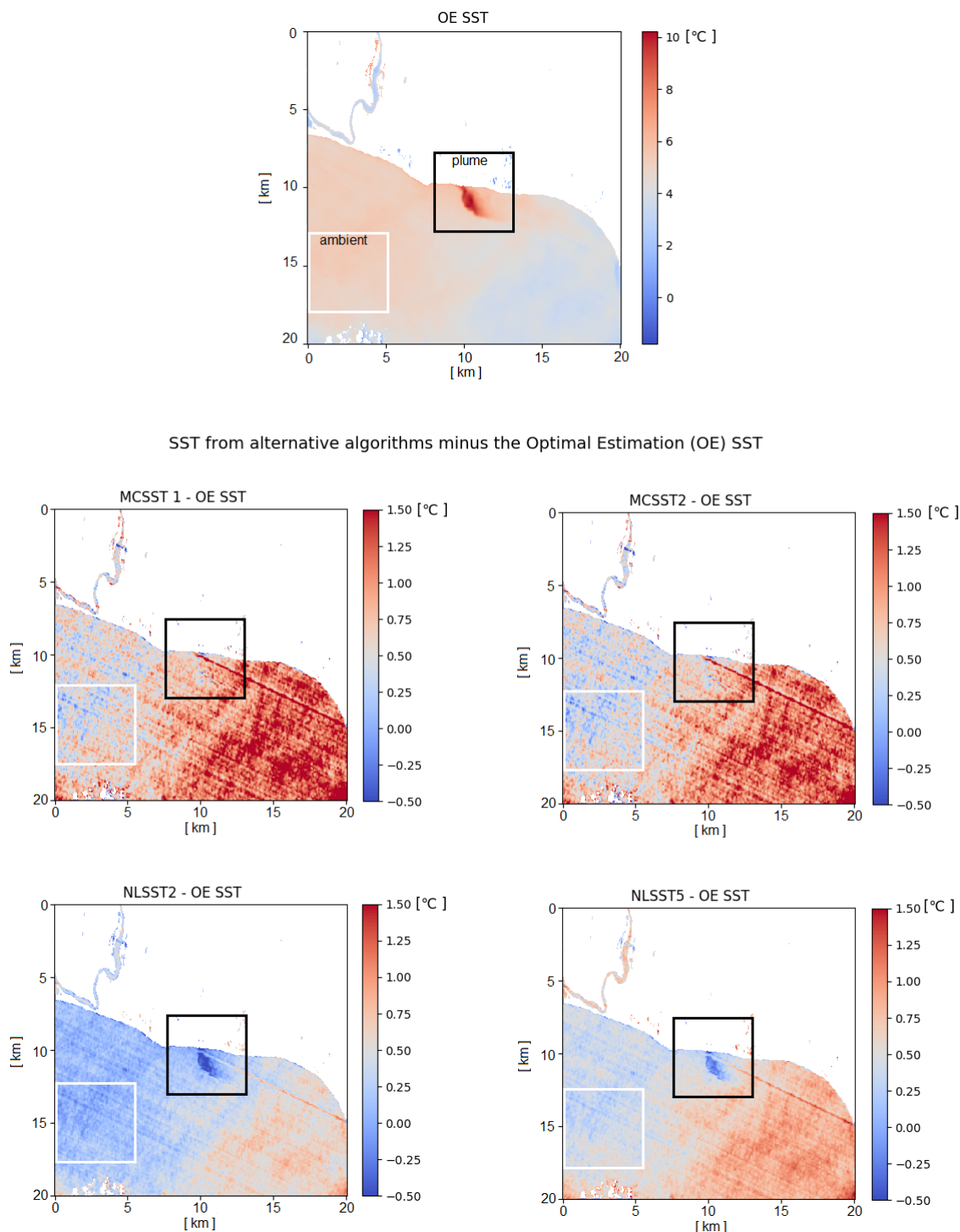


Figure 2.8: Differences in SST across an example Sizewell scene for different retrieval algorithms, Multi-Channel SST (MCSST) in middle panel and Non-Linear SST (NLSST) in bottom panel, compared to SST retrieved using Optimal Estimation (OE) in top panel. Land and clouds are masked in white. Black box indicates the location of the thermal plume and white box indicates the box of ambient waters. Largest positive SST differences are highlighted by dark red colour and large negative SST differences are in dark blue.

I compared the differences in retrieved SST for other scenes (see Figure 2.9). All retrieval algorithms yielded ambient SST ranging within $-1.2\text{ }^{\circ}\text{C}$ to $+3.3\text{ }^{\circ}\text{C}$ compared to the prior SST. I compared the average SST across the scene to the prior SST. The prior SST does not get very close to the coast and is more representative of the SST 20 km offshore and therefore would not capture temperature increases caused by the thermal plume dispersing close to the coast. On average, SSTs retrieved using NLSST algorithms were the closest to the prior values with differences of $\pm 1\text{ }^{\circ}\text{C}$. This is somewhat expected as in the absence of sufficient information from other sources, they will return the prior. The OE algorithm was in most cases furthest away from the prior SST, suggesting that they capture variations in the SST across the scene.

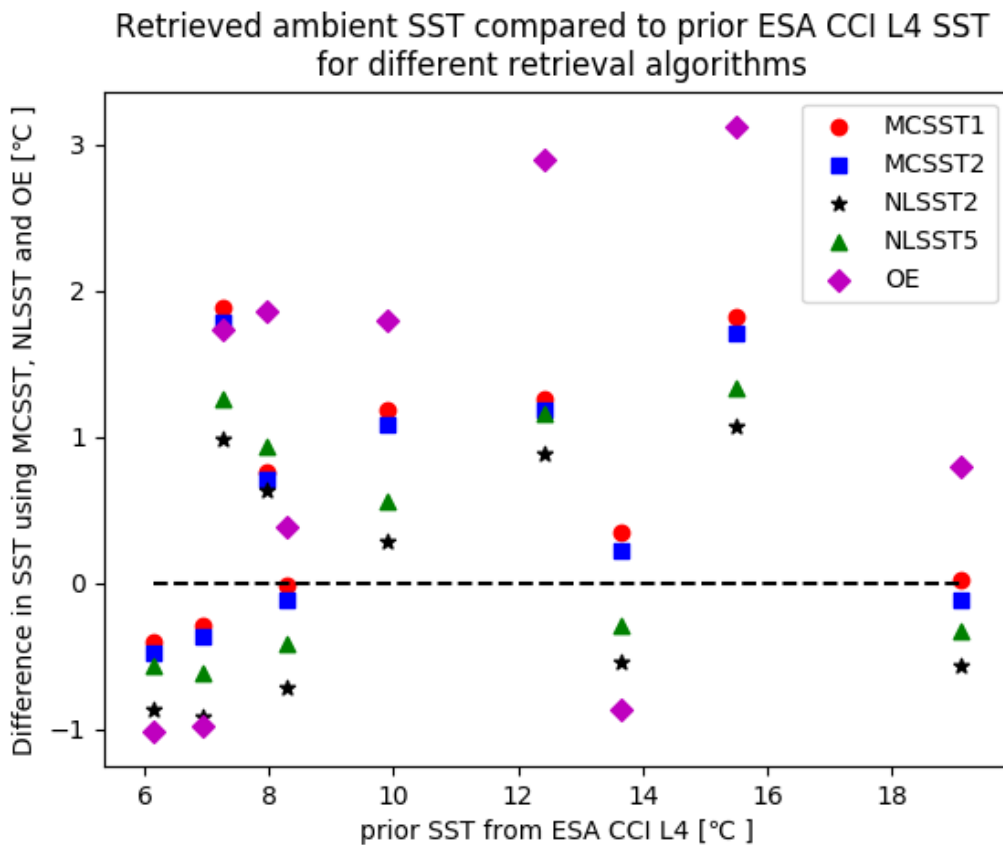


Figure 2.9: Differences in ambient SST compared to prior SST from ESA CCI L4 for different retrieval algorithms. The values of prior SST are on the x axis. SST differences Multi-Channel SST (MCSST) algorithms are marked by red circles and blue squares, Non-Linear SST (NLSST) algorithms are marked by the black stars and green triangles, Optimal Estimation (OE) algorithm is marked as magenta diamond.

Tables 2.5 and 2.6 show the differences in the average temperature across the plume and the ambient temperature. The ambient temperature chosen for comparison of the retrieval methods comes from the same region in each image (bound by a white box in Figure 2.8). That region was chosen to represent ambient waters because it was not obscured by clouds in any of the scene and the SST distribution was not influenced by the plume. The MCSST and NLSST algorithms differed from the OE SST from - 3.31 °C and +1.63 °C when looking at the thermal plume and -1.93 °C to +1.28 °C when looking at the ambient SST, suggesting that the biggest discrepancies occurred in the region with elevated temperatures caused by the plume. The thermal plume was cooler in the NLSST algorithms, compared to OE, when the temperature difference between the ambient waters and the plume was 3°C. For only two scenes the OE yielded a cooler plume than the plumes derived using other algorithms and for both of those cases the temperature difference between the plume and the ambient water was below 3 °C. The larger the temperature gradient across the plume, the more underestimated it was by the MCSST and NLSST algorithms (see Table 2.5). The NLSST algorithms were underestimating the ambient and the plume temperature more compared to the MCSST (see Tables 2.6 and 2.5). The thermal contrast between the ambient SST and the surface plume temperature was also smaller in the NLSST algorithms. This suggests that the NLSST retrieval algorithms are less likely to capture locally raised temperatures, which would result in a lower thermal contrast between the ambient waters and warmer plume.

A study looking into NLSST algorithms applied to the Advanced Very High Resolution Radiometer (AVHRR) data found that the non-linear algorithms are less sensitive to temperature variations across the scene and even a 1 °C increase in the SST could alter the retrieved NLSST by 0.5 °C [Merchant *et al.*, 2009]. The analysis presented in this section shows that the NLSST algorithms for Landsat 8 are less sensitive to SST variations across the scene and tend to underestimate the temperature difference caused by the plume. Optimal Estimation (OE) is more capable of capturing the differences and was therefore kept as the SST retrieval algorithm throughout this work.

Table 2.5: Differences in surface temperature of the thermal plume for different retrieval algorithms compared to OE. First column shows the date of the satellite observation, the second column is the maximum gradient across the plume, the third column is the average temperature of the plume for OE retrieval, the latter columns are the differences in the plume average temperature using MCSST and NLSST algorithms compared to OE. Highlighted in orange is the data for Figure 2.8.

date	$\max \nabla T_{plume} / 50 \text{ m}$	$T_{plume} \text{ OE}$	$\Delta T_{plume} \text{ MCSST1 - OE}$	$\Delta T_{plume} \text{ MCSST2 - OE}$	$\Delta T_{plume} \text{ NLSST2 - OE}$	$\Delta T_{plume} \text{ NLSST5 - OE}$
2013-10-30	0.98°C	15.51°C	1.63 °C	1.47°C	0.27°C	0.52 °C
2015-12-23	0.91°C	13.97°C	-0.31°C	-0.45°C	-1.78°C	-1.51°C
2016-02-16	0.90°C	9.75°C	1.44°C	1.30 °C	-0.45 °C	-0.16 °C
2016-09-11	1.56°C	25.24°C	-0.91°C	-1.08°C	-1.96°C	-1.75°C
2014-01-02	1.42°C	11.54°C	-0.02°C	-0.15°C	-1.41°C	-1.14°C
2014-02-03	1.12°C	8.20°C	1.31°C	1.20 °C	-0.04°C	0.25°C
2015-06-30	1.68°C	24.82°C	-2.22°C	-2.26°C	-3.31°C	-3.17°C
2017-03-15	0.89°C	11.22°C	0.60°C	0.30°C	-0.70°C	-0.36°C
2017-05-25	1.34°C	19.00°C	-0.95°C	-1.13°C	-2.23°C	-1.81°C
2015-04-18	1.05 °C	14.62°C	-1.01 °C	-0.89°C	-1.55°C	-1.46°C

Table 2.6: Differences in surface temperature of the ambient waters for different retrieval algorithms compared to OE. First column shows the date of the satellite observation, the second column is the maximum gradient across the plume, the third column is the average temperature of the ambient waters (chosen 5 km × 5 km area) for OE retrieval, the latter columns are the differences in the average ambient temperature using MCSST and NLSST algorithms compared to OE. Highlighted in orange is the data for Figure 2.8.

date	$\max \nabla T_{plume} / 50 \text{ m}$	$T_{ambient} \text{ OE}$	$\Delta T_{ambient} \text{ MCSST1 - OE}$	$\Delta T_{ambient} \text{ MCSST2 - OE}$	$\Delta T_{ambient} \text{ NLSST2 - OE}$	$\Delta T_{ambient} \text{ NLSST5 - OE}$
2013-10-30	0.98°C	12.57°C	1.25°C	1.12°C	0.37°C	0.62°C
2015-12-23	0.91°C	11.85°C	0.59°C	0.48°C	-0.31 °C	-0.04 °C
2016-02-16	0.90°C	5.23°C	0.50°C	0.43°C	0.08°C	0.38°C
2016-09-11	1.56°C	19.69°C	-0.74°C	-0.87°C	-1.31°C	-1.01°C
2014-01-02	1.42°C	9.02°C	-0.01°C	-0.09°C	-0.69°C	-0.40°C
2014-02-03	1.12°C	6.00°C	-0.15°C	-0.23°C	-0.77°C	-0.48°C
2015-06-30	1.68°C	18.18°C	-1.23°C	-1.34°C	-1.94°C	-1.68°C
2017-03-15	0.89°C	8.94°C	1.28°C	1.18°C	0.37°C	0.65 °C
2017-05-25	1.34°C	14.98°C	0.95°C	0.95°C	0.57°C	0.85 °C
2015-04-18	1.05°C	9.56°C	-0.38°C	-0.43°C	-0.51°C	-0.21°C

2.6 Thermal plume detection

For the daytime SST images and with MNDWI algorithm applied and the nighttime scenes with statistical land mask and manual cloud mask, I have then extended the mask by 2 pixels (100 m) using morphological dilation. This process is known in image processing as an operator in mathematical morphology. It allows for adding pixels to the boundaries of an object in the image, which results in expanding of the specific area, in this case the land and cloud mask. In order to be able to expand an area, a second set of coordinate points, called a structuring element, is superimposed on top of the image. Expanding the land mask was a vital step, as it allowed to mask out very warm, shallow waters close to the coast, which could be mistakenly interpreted as a thermal plume due to their raised temperature.

Next, warm water regions had to be differentiated from the surrounding waters, which was achieved using a threshold value above ambient water temperature. A consistent area of 5 km by 5 km was chosen for each place as the region representing ambient waters. The ambient waters were chosen in a way that they were not too far offshore, yet not affected by the thermal plume or any puddles of warm water. Then, the threshold value above ambient temperature was applied, leaving only regions of SST that fulfilled this criteria. From those contiguous regions, the thermal plume was chosen based on the distance from the power station. A limitation of such approach is that the highlighted area of the plume is dependent on the threshold value. Setting a higher threshold temperature might result in not detecting more dilute parts of the plume, whilst too low threshold would be within the natural SST variability in the ROI and lead to observing spots of warmer SSTs not related to the discharged plume.

The threshold to distinguish between the thermal plume and ambient waters suggested in literature was 0.5 C [[Langford, 1990](#)]. However, the threshold chosen to detect plumes in the satellite data was raised to 1.5 °C in the light of instrument uncertainty, described in Sections 2.1.2. and 2.1.3., and the uncertainty in the prior SST from ESA CCI L4 SST (Section 2.5.) . The uncertainty associated with the RTM is assumed to be 0.15 - 0.17 K for IR channels [[Saunders et al., 2018](#)]. The error propagation into the SST product was assumed to be a linear combination of errors in BT from each channel and the coefficients used in the retrieval [[Bulgin et al., 2016](#)].

2.7 Summary

High resolution satellite data provides good opportunity to create an observational dataset to detect industrial thermal plumes. Due to the large domain of a single satellite observation ($185 \text{ km} \times 180 \text{ km}$ for Landsat 8 and $60 \times 60 \text{ km}$ for ASTER) it is essential that any satellite observations are subsampled to the ROI and regrided onto a uniform grid to compare information from different sensors. This should be applied also to other satellites that would possibly be used for the purpose of thermal plume observation since the thermal plumes are local phenomena. The choice of common grid should be based on the spatial resolution of the observations to ensure the real resolution of the observations will not be reduced on the new grid. In case of Landsat 8 and ASTER data resolution of 50 m was reasonable to differentiate between the water and land in the coastal regions. Since most coastal locations are inter-tidal areas with dynamically changing land-sea boundary, a water detection algorithm, like MNDWI or NDWI, should be chosen. The water detection algorithms are constructed from the visible and NIR / SWIR data, hence the daytime satellite images can only be used for reflectance-based water detection. The nighttime scenes can only be used for regions with no tidal flats provided that there is an existing land mask and appropriate cloud screening. Cloud screening for the nighttime scenes in this project was threshold-based. A threshold-based method cannot guarantee that all clouds will be masked and requires validation through eye examination. In this case it was possible as the number of scenes was low. In case of a larger number of nighttime scenes, a more reliable cloud screening method should be established. Unmasked clouds will impact the surface temperature retrieval and result in cooler SSTs. In order to retrieve the SST the chosen instrument should provide data from at least one available thermal channel. The choice of SST retrieval algorithm will depend on the specifications of the used instrument as well as user's knowledge of the instrument. The presented technique of plume delineation from the ambient waters can be applied to data from other sensors while adapting the temperature threshold accordingly. The chosen threshold of 1.5°C above ambient SST is sufficient to detect the majority of the discharged thermal plume but it is likely to not capture more diluted parts of the plume at the plume boundary. However, the choice of threshold will depend on the uncertainties associated with the instrument and the retrieval process and will be unique for the instrument chosen.

Chapter 3:

Satellite observations of industrial thermal plumes

3.1 Statement of publication status

The material in this chapter has been published in Remote Sensing Journal on the 13 September 2019. I am the lead author of the manuscript. All figures were generated by me and I led and finalised the conceptualisation and scientific writing. I take full responsibility for the results. Other authors listed on this publication helped in discussions of the methods and provided feedback on the results. The reference for the manuscript is as follows:

Faulkner, A., Bulgin, C. E., Merchant, C. J. (2019). Coastal Tidal Effects on Industrial Thermal Plumes in Satellite Imagery. *Remote Sensing*, **11(18)**, 2132. doi 10.3390/rs11182132

The content of this chapter differs from the published article in the following ways:

- For consistency with the thesis structure, the numbers of the section headings equations and figures are updated and minor format changes are applied;
- The word "paper" has been substituted to "chapter" to keep consistency with thesis structure;
- The published results on Heysham and Sizewell are expanded by addition of other EDF Energy locations: Dungeness, Hartlepool, Hinkley, Hunterston and Torness;
- The published discussion and conclusions were included in this chapter's sections under the same name and expanded with the additional information.

Note that the published introduction and methods included in this chapter contain

minor overlaps with Chapter 1 and Chapter 2, but are included in their original form for completeness.

3.2 Abstract

Coastal tidal effects on thermal plumes are investigated, exploiting remote sensing of the major coastal industrial installations. The installations use sea water as a coolant, which is then released back into coastal environments at a higher-than-ambient temperature, allowing the plume to be delineated from the ambient waters. Satellite-based thermal sensors observing the Earth at spatial resolutions of 90 and 100 m are used. It is possible to identify coastal features and thermal spatial distributions. This chapter presents coastal tidal effects on detected plumes for two published case studies: an intertidal embayment and open water exposure, and expands by including additional power stations located on the coast of the UK. I correlated the behaviours of thermal plumes using remotely sensed high resolution thermal imagery with tidal phases derived from tide gauges. The results show very distinct behaviours for the flood and ebb tides. The detected surface plume location was dependent on flow switching direction for the different types of tide. The detected surface area was dependent on the strength of the currents, with the largest area observed during the strongest currents. Understanding the dispersion of the plume is essential to influence understanding of any potential ecological impacts.

3.3 Introduction

Coastal zones are sensitive ecosystems providing valuable habitats for varied flora and fauna, as well as economic benefits including tourism and leisure. Coastal areas are constantly changing due to interactions with weather and coastal waters, climate change effects, sea-level changes, land-use impacts, and human-made infrastructures [Islam *et al.*, 2016; Peponi *et al.*, 2019]. Tourism, maritime traffic, fishing, human-made coastal installations, etc. act as anthropogenic stressors on the coastal environment and may affect the distribution of marine species. Impacts vary spatially and temporally [Harik *et al.*, 2017]. Therefore, it is important to monitor those zones, providing a basis for resolving stresses in space and time [Harik *et al.*, 2017] and supporting sustainable coastal zone management [Islam *et al.*, 2016].

Coastal regions remain challenging areas for Earth observation due to dynamic land-

water boundaries and enhanced variability in shallow water regions. Field campaigns often don't get very close to the coast, limiting the investigated areas to regions offshore deep enough for the survey vessels. Tide observations from routine monitoring, coming from an extensive national network, are limited to point measurements. Numerous studies have used different modelling techniques in order to understand coastal dynamics [Mei and Liu, 1993; Klevanny et al., 1994; De Vriend, 1991; Dalrymple and Rogers, 2006; Durán-Colmenares et al., 2016]. In addition to the models, the use of high resolution remote sensing data can contribute to better understanding of the coastal zone [Alesheikh et al., 2007; Paduan and Rosenfeld, 1996; Dabuleviciene et al., 2018; Abascal Zorrilla et al., 2018]. Despite the temporal trade-off associated with the satellite repeat-time coverage, remote sensing information has the advantage of high spatial resolution observations.

In this chapter, satellite imagery is used to look at the coastal tidal effects on industrial thermal plumes. We use Landsat 8 and Advanced Spaceborne Thermal Emission and Reflection Radiometer (ASTER) products with the focus on the British coastal areas, in the vicinity of power stations using sea waters for cooling purposes. The outflow coolant water has temperature higher than ambient waters, enabling us to investigate coastal zones and gain understanding of surface water behaviour. We will refer to this coolant water outflow as a thermal plume throughout the remainder of this chapter.

Previous studies have focused on understanding the nature of thermal plumes by integrating in-situ measurements with thermal imagery from satellites [Huang et al., 2014] and portable thermal cameras [Muthulakshmi et al., 2013], using high-resolution imagery to study SST distribution around power stations [Dai et al., 2016; Ma et al., 2017; Tang et al., 2003; Ahn et al., 2006], investigating consistency between different sensors in thermal plume detection [Xu et al., 2014]. The spatial extent of the surface thermal plume was identified by comparison with observations taken during the same months prior to the power station operation, focusing on three locations: the bay [Dai et al., 2016; Ma et al., 2017], the harbour [Dai et al., 2016] and the open water [Dai et al., 2016]. For all regimes, the areas of the most significant temperature rise were limited close to the power stations and dissipated along the coast.

Thermal plumes have been used to study coastal dynamics in Daya Bay, on the coast of South China Sea. During the winter months, the plume is limited to small area westward of the power station, whereas in summer months plume area reaches 40-100 km² to the south-eastward of the bay [Tang et al., 2003]. The distinct seasonality of the thermal plume was attributed to strong mixing of the water column during the winter

months, dispersing the warm water throughout the water column. During the summer months, with stratified waters, the less saline waters disperse close to the surface. Sudden drops in temperature in the thermal plume region have been attributed to strong mixing of the plume with ambient waters [*Muthulakshmi et al.*, 2013].

Ahn et al. [2006] have investigated thermal plumes in Younggwang coastal areas, Korea. They have found that the occurrence of strong coastal currents and winds during winter and summer monsoons often results in a high rate of thermal dispersion in the southern and northern parts of the Younggwang coast. *Anupkumar et al.* [2005] drew similar conclusions in his field campaign with CTD probes in the Bay of Bengal, attributing the plume direction and distribution to the prevailing currents.

For two power stations located on the northern coast of Taiwan, the plume area and temperature difference were related to tidal regimes [*Huang et al.*, 2014]. In both cases, the highest temperature rises covered a bigger area during flood tides than during ebb tides, although the overall plume area was larger during ebb tides. This suggested quicker spreading of the thermal plume during ebb tides as well as advection offshore.

Research into thermal plumes in Europe has focused on thermal pollution of rivers and river estuaries [*Zoran*, 2011], making the coastal regions a good opportunity for further investigation. Major power generation facilities around the coast of Great Britain provide a range of case studies, including bays, channels and open water. I focus in this study on two installations: Heysham, located on the western coast of the UK in the Morecambe Bay adjacent to the extensive geological area of Heysham sands (Fig. 1), and Sizewell, located on the eastern coast in Suffolk and discharging waters to the North Sea (Fig. 2).

The purpose of this chapter is to use remote sensing imagery to investigate tidal effects on industrial plumes. Coastal bathymetry and tides both influence the dispersion of thermal plumes from industry. This chapter focuses on the extent to which remote sensing imagery can reveal the impact of tides on thermal plume dispersion. I use Landsat 8 and ASTER imagery of two regions near two industrial power stations. I detect thermal plumes in the region of interest (ROI) using a combination of water detection, mask expansion and thresholding techniques. I relate the detected plumes to calculated phase of tide based on the National Tide Gauge Network (NTNG) measurements. Finally, I create conditional probability maps of detected plumes occurrence. These results provide new spatial understanding for tidal effects along the British coast. This chapter proceeds as follows: Section 2 describes the methodology, Section 3 presents the results, Section 4

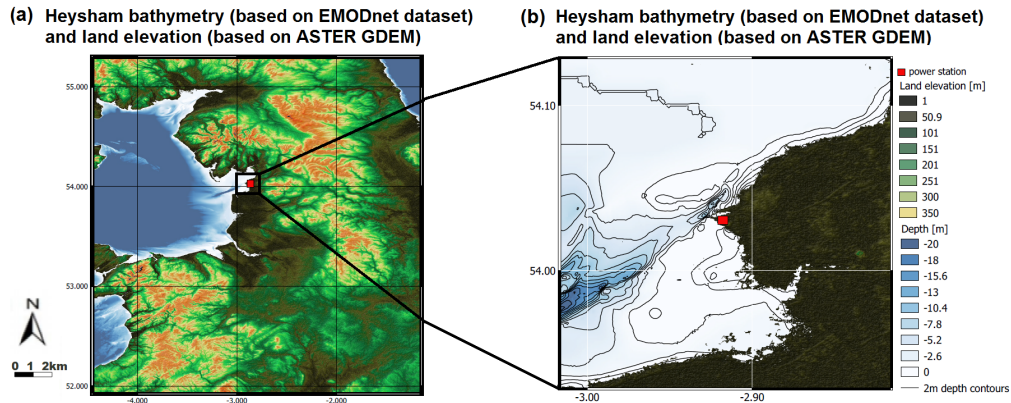


Figure 3.1: (a) Location of Morecambe Bay, with Heysham power plant marked as a red square, with land elevation obtained from ASTER GDEM and bathymetry obtained from EMODnet datasets. (b) Close-up of the ROI, with detailed bathymetry with contours at 2 m depth intervals obtained from EMODnet dataset. Lighter colours represent shallower waters and darker colours deeper waters.

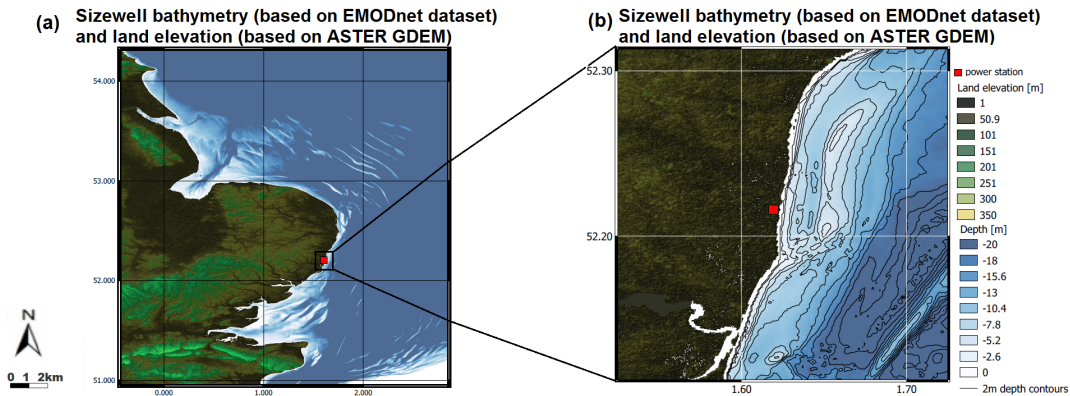


Figure 3.2: (a) Location of East Anglia, with Sizewell power plant marked as a red square, with land elevation obtained from ASTER GDEM and bathymetry obtained from EMODnet datasets. (b) Close-up of the ROI, with detailed bathymetry with contours at 2 m depth intervals obtained from EMODnet dataset. Lighter colours represent shallower waters and darker colours deeper waters.

provides the discussion of the results and Section 5 summarizes our findings.

3.4 Methods

I use high-resolution infrared and visible observations from the Operational Land Imager (OLI) and the Thermal Infrared Sensor (TIRS) on-board Landsat 8 and from ASTER on-board Terra. Landsat 8 is a satellite launched by the National Aeronautics and Space Administration (NASA) in collaboration with the United States Geological Survey (USGS). It has been operational since 11 February 2013. It has a return time of 16 days, providing high resolution data over land and ocean across a swath of 185 km.

The two push-broom instruments on-board, OLI and TIRS, cover visible, near-infrared (near-IR), short wave infrared (SWIR) and thermal infrared (TIR) wavelengths of the electromagnetic spectrum. Visible, near-IR and SWIR bands measure at 30 m resolution. The TIR wavelengths have resolution of 100 m, which is resampled using cubic convolution onto the 30m grid prior to dissemination. Cloud cover information is provided, used here to identify clear-sky observations required for the purpose of the study.

ASTER is an instrument on-board the Terra satellite that has been in operation since December 1999 in a joint operational mission between NASA and Japan's Ministry of Economy, Trade and Industry (METI). ASTER has three instruments: visible and near-infrared (VNIR), SWIR and TIR measuring at 15, 30 and 90 m resolution respectively. With the same revisit time as Landsat 8, ASTER coverage is not as complete as it acquires data on a tasked basis. Typically I find most acquisitions of ASTER data in locations of interest are at night.

I extract satellite data centered on the power station location over a ROI with a spatial extent of $0.2^\circ \times 0.2^\circ$. The data are regridded from their 30 m raster resolution onto a fixed degree grid at 0.0005° in order to obtain all ASTER, OLI and TIRS data on a common grid whilst minimising sampling issues. TIR bands for ASTER come at the resolution of 90 m and are resampled using nearest neighbour methods, with gaps filled by linear 2D interpolation, onto our grid. A grid resolution of about 50 m is adequate to investigate coastal features and distinguish between land, beach, cloud and water regions.

Coastal regions are typically characterized by variable land-water boundaries and in some cases the presence of inter-tidal flats, requiring correct identification of the water line for each image. The water line is the boundary between the sea and a non-water object (land, beach, mud flats, etc.). For daytime images I detect water using the Modified Normalised Difference Water Index (MNDWI) (Eq.1) [Xu, 2006], an extension of the Normalised Difference Water Index (NDWI) [McFeeters, 1996] shown to perform better in coastal regions [Kelly and Gontz, 2018; Pardo-Pascual et al., 2018] and mixed pixels [Xu, 2006]. Since the MNDWI uses visible and SWIR bands in the equation, it is impossible to apply the same algorithm for the scenes retrieved at night. Therefore to mask out land pixels in the nighttime scenes I have used a statistical land mask derived from a set of daytime MNDWI imagery. Nighttime imagery, with applied expanded statistical land mask derived from daytime images, has undergone thresholding to remove cold clouds and beaches. I apply a threshold of 276 K to band 13 of ASTER's data (10.2-10.9 μm), classifying every pixel with value below 276 K as contaminated by cold clouds

or beach, and everything above that threshold as water. This enables masking of cold clouds, but does not fully mask the exposed beach regions. However, this has not been an issue in plume detection since the thermal features of the industrial plume are of higher temperature than the beaches. As nighttime scenes are limited, the cloud detection could be verified visually to ensure that no obvious warm cloud features were evident in the region of the plume.

$$MNDWI = \frac{Green - SWIR}{Green + SWIR} \quad (3.1)$$

I retrieve sea surface temperature (SST) using optimal estimation [Merchant *et al.*, 2008]. Optimal estimation (OE) is an inverse method to estimate the state variables, given an initial estimate and simulations of the observations. The state variables retrieved are SST and atmospheric humidity. The simulations are run for a prior state obtained from numerical weather prediction (NWP) atmospheric profiles. The prior SST is daily gridded global sea surface temperature (level 4 SST) data from the European Space Agency Climate Change Initiative (ESA CCI) programme [Merchant *et al.*, 2019]. For each state vector there exists an "ideal, synthetic measurement" vector, and OE requires simulation of measurements as part of the retrieval process. Clear-sky observations are simulated using RTTOV [Saunders *et al.*, 2013; Hocking *et al.*, 2014] and ERA Interim profiles to represent the atmospheric state at the time of observation [Dee *et al.*, 2011]. Given the actual measurements, the simulations and the prior state, OE returns the most probable state variables vector. CCI level 4 SST is not adapted to the feature resolution required for coastal zones, but rather reflects temperatures ~ 20 km offshore [Merchant *et al.*, 2014]. Since there is only one prior SST value per acquired satellite scene, it does not include the temperature variations across the scene, including those caused by the thermal plume. We therefore assign the uncertainty in our prior SST to be the biggest temperature difference across the scene (i.e. biggest difference between the plume and ambient waters in each scene) and after investigation this is set to 8 K.

Having retrieved SST for the coastal regions, all masked land and beach regions in the image are expanded using morphological dilation [Gonzalez *et al.*, 2002] to exclude warm shallow coastal waters that could mistakenly be interpreted as thermal plumes. Next, possible plumes are detected through identifying contiguous areas that pass given thermal thresholds of 1.5 K warmer than a chosen box of ambient temperature of surface waters. The box of ambient waters is chosen for each image as a square area 5 km by 5 km of coastal waters at least 5 km offshore and not contaminated by the thermal plume

or warm shallow waters. By examining the satellite imagery in which the plume region is evident, I could find a consistent offshore region, common across all scenes that was outside of the plume extent. I calculate the average temperature in that box for each scene and treat it as surface ambient temperature for the whole image. The plume detection then compares the temperature of every water pixel to the ambient temperature. If the pixel was > 1.5 K warmer than the ambient temperature, it was classified as a potential plume. The thermal threshold of 1.5 K was chosen after considering the uncertainty associated with the instruments and SST retrieval method. The TIRS instrument onboard Landsat 8 had radiometric errors of -2.1 K and -4.4 K at 300 K for Band 10 (10.6-11.2 μm) and Band 11 (11.5-12.5 μm) respectively and high error variability, due to stray light artifacts after launch. In 2017, a new calibration process has reduced the residual variability to 0.51 K at 300 K for Band 10 and 0.84 K at 300 K for Band 11 [Barsi *et al.*, 2017]. The TIR subsystem for ASTER instrument has the signal-to-noise temperature difference of 0.3 K at 300 K. The radiometric accuracy of the retrieval varies between 1-3 K depending on the BT range [Abrams *et al.*, 2002]. Moreover, during summer and early autumn months, very shallow waters close to the coast can warm significantly during the day and applying a lower thermal threshold could mistakenly include those waters in the plume analysis, obscuring the results.

From the pixels identified as warmer than ambient I then use our algorithm to detect the plume itself. Small clusters of warm pixels (not more than two) that pass the threshold are masked out as noise. From the remaining aggregates of warm water pixels, the detected plume is identified as the object nearest to the power station, discarding other aggregates and treating them as ambient waters.

For each observation I identify the phase of the tide at the ROI. Tide measurements used in this study come from the National Tide Gauge Network (NTNG). The NTNG provides extensive monitoring of the tides in 44 point locations around the UK coast. I relate the satellite imagery to the tidal measurements to provide new insight into flow dynamics around the British coast. Figure 3.3 presents the data used and methods applied throughout the analysis process.

Since tidal measurements resemble a continuous periodic function, with measurements every 15 minutes, tidal data for the period of 3-7 days (including the date of the satellite overpass as the central day) has been fitted to a sine function (Eq. 2), where $H(t)$ is the height of water at satellite overpass time, \bar{H} is average height of water, A is the water height amplitude, f is frequency, t is time and ϕ is the phase offset.

All the observations have been sorted based on the phase of the tide, θ (Eq. 3). Values of θ range from 0 to 360 ° where 0-90 and 270-360 ° are periods of rising water levels, and 90-270 ° is the period of receding water.

$$H(t) = \bar{H} + A\sin(2\pi ft + \phi) \quad (3.2)$$

$$\theta = 2\pi ft + \phi \quad (3.3)$$

After sorting the satellite observations and detected plumes based on the phase of tide, I create probability density maps. The method used is as follows: I first apply the plume detection to every image. I then sum all plumes detected in images for specific phase of tide (i.e. all plumes detected in flood tide imagery and all plumes detected in ebb tide imagery) for a given location and divide by the total number of observation during the specific phase of tide (i.e. all images during flood tide or during ebb tide) used for the site, presenting the data as probabilities.

To distinguish between ebb and flood currents, I use Norwegian Meteorological Institute (MET Norway) operational ocean model data. The Norwegian MET operational ocean model covers the area of -28.556 to 79.801 ° E and 46.563 to 87.686 ° N with a grid spacing of 4 km. The model uses the atmospheric forcing from European Centre for Medium-Range Weather Forecasts (ECMWF) 0.125 °, vertical boundary conditions from Arctic-20km, and tides from a series of fully-global models of ocean tides. The currents available from the MET Norway include tides and wind-driven currents as well. There are two model runs a day and the hourly forecasts can be provided for up to 5 days. The ebb (flood) tides are in a southerly (northerly) direction for Sizewell and north-easterly (south-westerly) for Heysham. The strengths of currents vary, with weaker currents being observed during the beginning and end of each tide phase, and strongest around the middle of the tide phase. We have superimposed the example direction of the sea currents from the MET Norway data associated with the tide phase on our probability maps.

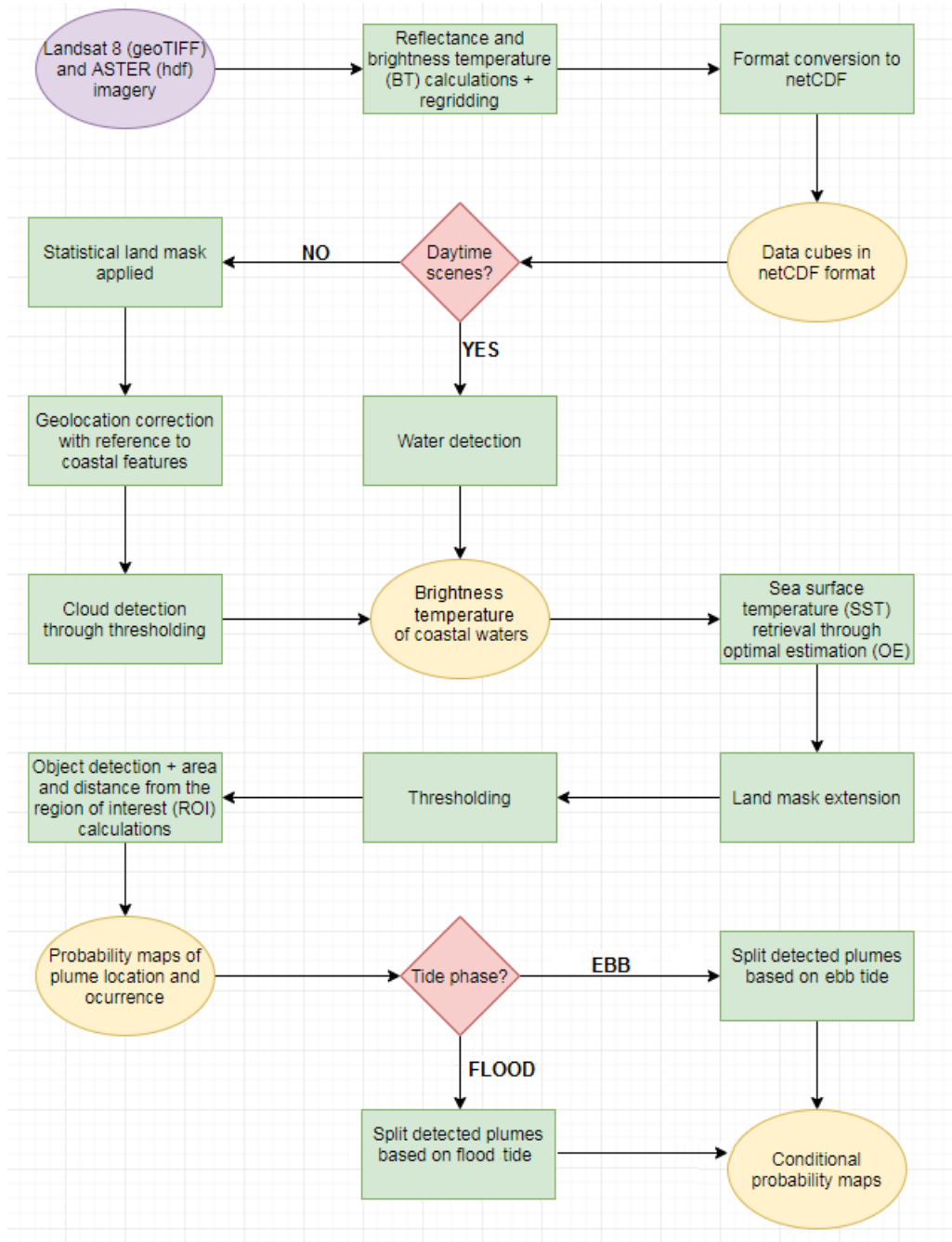


Figure 3.3: Workflow plan. Data used are presented in the oval shapes. Yellow ovals represent generated products, purple ovals - existing datasets. Methods applied are presented as green rectangles and decisions as red diamonds. netCDF data format mention in the plan is the Network Common Data Form.

3.5 Results

3.5.1 Heysham as example of intertidal embayment

Morecambe Bay is the largest macro-tidal embayment in north-west England with very dynamic intertidal area [*Mason et al., 2010*]. Our ROI is centred next to Heysham Sands and surrounded by tidal flats formed by mud or wet sand deposited by tides. The durations of the tides are unequal with the ebb tide lasting longer than the flood tide by around 40 minutes [*Coomber and Hansom, 1994*]. Heysham water height, measured at the tide gauge point, ranges between just 1-3 m during ebb tide and between 7-10 m during flood tide. The location as well as the extent of the thermal plume are highly dependent on the phase of the tide.

During the ebb tide, the regions of Heysham Sands near the ROI are exposed (Fig. 4b). The plume is easy to detect (Fig. 4a), starting at the end of the two pipelines coming out of the power station and moving with the currents associated with the ebb tide (Fig. 4b). Other warm water puddles are localised very close to the exposed sand bank areas and do not extend. The plume stretches in the direction of the open ocean, exiting the Morecambe bay (Fig. 4a) along the deep water channel stretching south-westward. This can be seen in the bathymetry maps (Fig. 4a). The detected plume covers a narrow, elongated region. In most cases the plume length does not exceed 5km and is confined to a narrow belt. However, on a few occasions, the plume's length reaches over 7 km extending further towards the deep water channel (Fig. 4a). Such behaviour was noticed during the middle phase of the ebb tide, when the currents were the strongest.

During the flood tide, the intertidal flats are hidden with waters rising, and the thermal plume is trapped close to the coastline (Fig. 4c), which is associated with the direction of the currents during the flood tide (Fig. 4d). There are two scenarios, where currents cause the plume to spread south east towards the river estuary, or northwards and recirculate into the Heysham Harbour. Where the thermal plume is advected towards Heysham Harbour, the flood tide is in the beginning or middle phase. In the first case, following the lowest water level, when the sand banks were still exposed and the currents have just changed the direction, flowing north-eastwards. This causes the plume to move northwards of the outlet pipes along the still exposed sand banks. During mid-flood, the sand banks are beginning to be covered with sea water and the north-eastwards currents are picking up, flowing into the bay. Strong currents cause the plume to move north-eastwards into the bay. In later phases of the flood tide, with currents decreasing in

strength and no exposed sandbanks, the plume is located south and south-east off the discharge pipes close to the coastline. In most cases (18 out of 23 images), the detected plume seems to be restricted to an area between the coast and 3.5 - 4 km offshore, suggesting good mixing of the waters. Mixing would cause further dispersion of the actual plume, however, as the detected plume needs to fulfill the criterion of 1.5 K above ambient temperature, a restricted area is indicative of a good mixing.

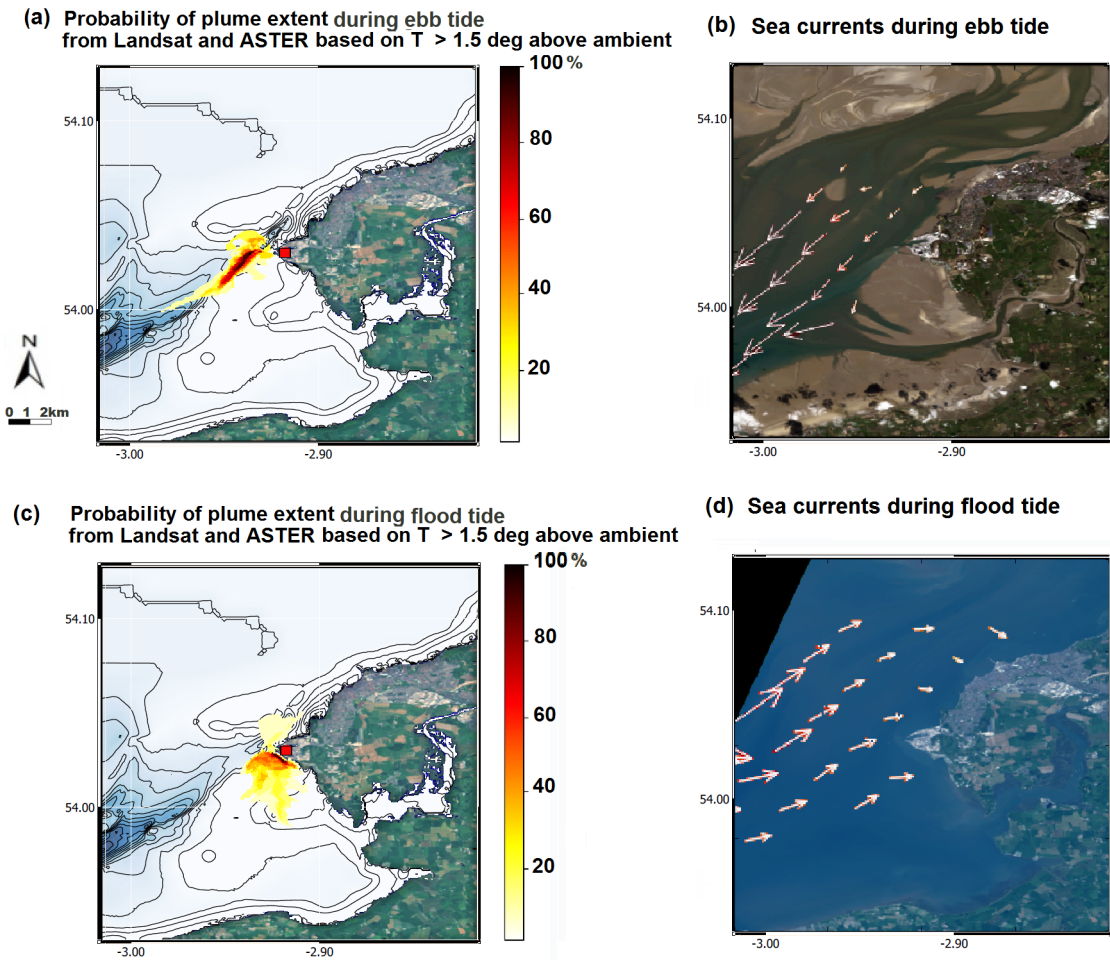


Figure 3.4: (a) Probability density map of thermal plume location and reach during ebb tide with darker colours presenting higher probability and lighter colours lower probability. On some occasions the sands are exposed (see b), while on other occasions the sands are not exposed to the same extent. The plume follows the same direction, along the deeper water channel, independent of the amount of sands exposed. (b) Corresponding RGB composite of an example daytime scene during ebb tide with waters visible in dark blue and green colour, exposed sands visible in light brown colour, land in dark green, and harbour and built-up areas in white. The arrows represent the currents based on the data from MET Norway. During the ebb tide, weaker flow is represented by smaller arrows and stronger flow is represented by bigger arrows. (c) Probability density map of thermal plume location of reach during flood tide with darker colours presenting higher probability and lighter colours lower probability. (d) Corresponding RGB composite depicting example daytime scene during flood tide with waters visible as dark blue colour, land in dark green, and harbour and built-up areas in white. The arrows represent the direction of flow during flood tide with weaker flow being represented by smaller arrows and stronger flow being represented by bigger arrows.

3.5.2 Sizewell as example of open water exposure

Suffolk coast is an example of open water exposure with Sizewell-Dunwich Banks located offshore, parallel to the coast, close to the ROI. These naturally-occurring structures are relatively narrow (around 2 km in width) underwater sand banks, over 10 km in length [Lees, 1983] and were created by wave energy, currents and sediment transport and they reduce wave energy. A few studies have shown that the growth of the banks (especially the Dunwich bank) has altered the direction and the height of approaching waves. The 20-year data record of annual average wind data indicates that the predominant winds are south-westerly with transport directed towards the north-east [Pye and Blott, 2006]. There are no sand or mud banks large enough to be captured by the satellite imagery as exposed during different tidal phases. However, Sizewell is located about 100 km away from the amphidromic point in the southern part of the North Sea [Sinha and Pingree, 1997], which is a point where the tidal constituent amplitude is zero. This influences the pattern of tidal currents, which consists of flow nearly parallel to the coast (Fig. 5b, 5d) reflected by the thermal plume forming an elongated area of warm water parallel to the coastline alternately north-east and south-west directions (Fig. 5a, 5c). The location of the detected plume is highly dependent on the phase of the tide.

During the ebb tide, the tidal streams run northwards, which can be observed by the direction of the plume dispersion (Fig. 5a). This flow direction is consistent throughout the ebb tide, with plume length varying between 3.5 km and 7 km. During the beginning and end of ebb tide, when the currents are weaker, the plume stays closer to the coast, reaching a maximum width of around 2 km. During the middle phase of the ebb tide when currents are stronger, the plume drifts slightly away from the coast and covers a larger area. In both cases, the plume area does not extend beyond the underwater banks, which can be noticed on the bathymetry maps as two shallow water regions 5 km off the coast (Fig. 5a).

During the flood tide, the tidal stream offshore runs southwards which is very well indicated by the plume direction (Fig. 5c). Again, this type of flow is consistent throughout the flood tide. The plume flows closer to the coast than during the ebb tide.

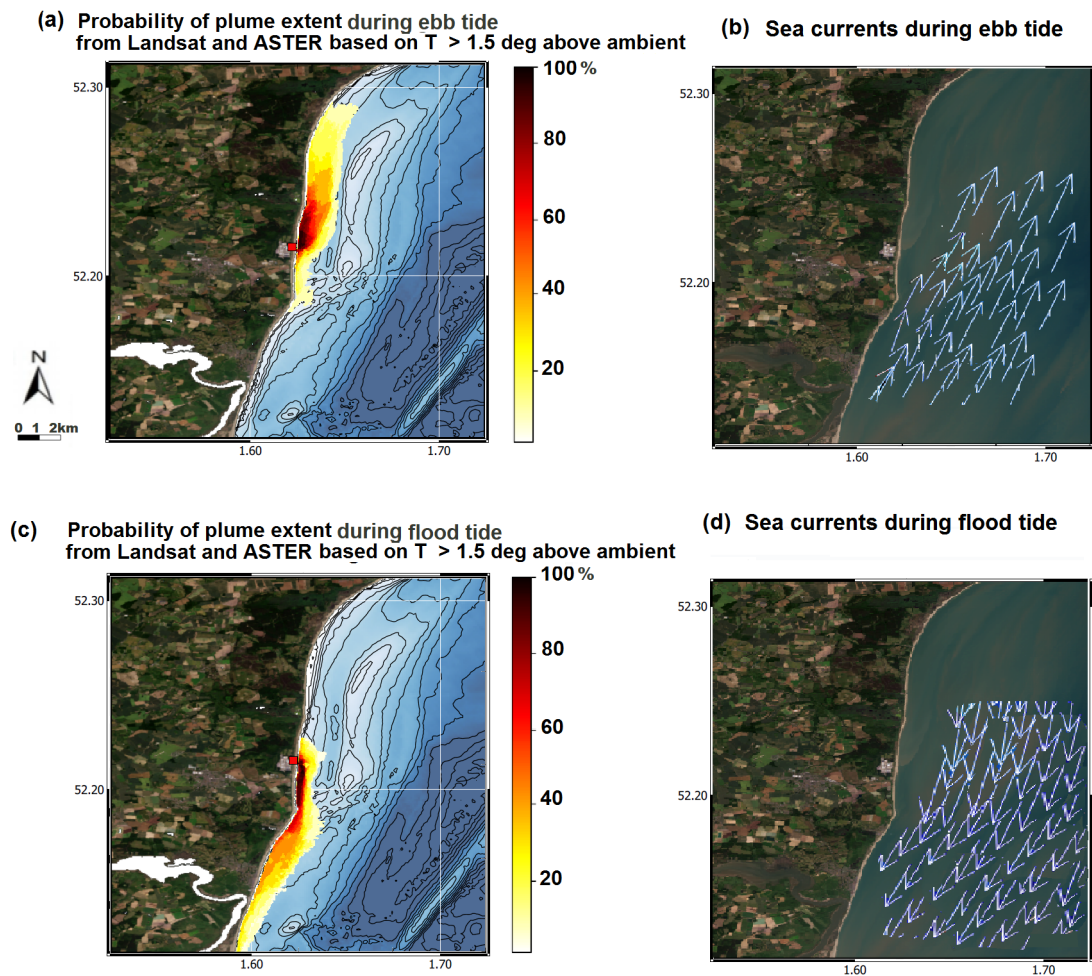


Figure 3.5: (a) Probability density map of thermal plume location and reach during ebb tide with darker colours presenting higher probability and lighter colours lower probability. (b) Corresponding RGB composite of an example daytime scene during ebb tide with waters visible in dark blue and green colour, exposed sands visible in light brown colour, land in dark green, and harbour and built-up areas in white. The arrows represent the currents based on the data from The Norwegian Meteorological Institute. (MET Norway). During the ebb tide, weaker flow is represented by smaller arrows and stronger flow is represented by bigger arrows. (c) Probability density map of thermal plume location of reach during flood tide with darker colours presenting higher probability and lighter colours lower probability. (d) Corresponding RGB composite depicting example daytime scene during flood tide with waters visible as dark blue colour, land in dark green, and harbour and built-up areas in white. The arrows represent the direction of flow during flood tide with weaker flow being represented by smaller arrows and stronger flow is represented by bigger arrows.

3.6 Extended results

This section extends the results of satellite-based observations of thermal plumes for other EDF Energy power stations: Hinkley, Torness, Dungeness, Hunterston and Hartlepool. The findings on the plume location have been based on the plumes detected in the Landsat 8 and ASTER imagery. Table 3.1 presents a concise summary of the characteristics of the thermal plumes observed for each power station. For 6 out of 7 sites (including Heysham and Sizewell) the tidal currents are the main driver of the plume dispersion. The plume follows the tidal currents and its direction of dispersion depends on the direction of the tidal stream. During the ebb tide, 4 out of 5 sites discussed in this section observed the plume dispersing westward, while during the flood tide the plume was dispersing eastward (see Table 3.1). The plume ejected by the Hartlepool power station does not exhibit clear tidal dependence in 80% of the observed cases and rather stays close to the discharge point. Such plume behaviour was related to the strength of the sea currents, which in the vicinity of the Hartlepool power station is very small (under 0.1 m s^{-1}) and therefore does not influence plume dispersion as significantly as in other sites discussed here.

Table 3.1: Summary of findings on the thermal plume characteristics for different power stations based on Landsat 8 and ASTER imagery.

Location	Hinkley	Torness	Dungeness	Hunterston	Hartlepool
Number of images during ebb tide	24	18	29	21	21
Number of images during flood tide	16	31	23	22	20
Plume influenced by the tides	yes	yes	yes	yes	no
Plume direction during ebb tide	westward	north-westward	westward	south-westward	no clear direction
Average plume extent during ebb tide	2.5 km	1.5 km	3 km	1.7 km	1 km
Max plume extent during ebb tide	4.3 km	3.2 km	9 km	4 km	1.5 km
Plume direction during flood tide	eastward	south-eastward	eastward	north-eastward	no clear direction
Average plume extent during flood tide	3 km	1 km	3.5 km	2 km	1.2 km
Max plume extent during flood tide	9 km	2.5 km	5 km	5.5 km	2 km

The detailed results have been presented as probability density maps of the location of the surface thermal plume for each site (Sections 3.6.1 - 3.6.5). All probability density maps in the following Sections have been presented in the same style, which to avoid repetition is described here. For locations with conditional probability as a function of tide, the left subplot presents probability of the thermal plume location during the ebb tide and the right subplot presents probability of the plume occurrence during the flood tide. Dark red colours represent higher probability and yellow colours represent lower probability of the plume occurrence. Land has been marked in green and bathymetry shaded in blue. The location of each power station is indicated by the red square.

3.6.1 Hinkley as example of location within an estuary

Hinkley power station, further described in Chapter 1 (Section 1.10.4.), is located in south west England. The bathymetry in the vicinity of the power station is shallow, with depths not exceeding 6 m. The seabed gently slopes into deeper waters around 8 - 10 km north-west from the power station. *Uncles* [1984] notes that the tidal currents are the main driver of the circulation, with asymmetric flood and ebb current magnitudes caused by semi-diurnal tides. The sea currents flow westward, towards the mouth of the channel, during the ebb tide and eastward, inland, during the flood tide. The strength of the tidal currents varies, with strongest currents present inland and tidal current strength decreasing towards the open sea [EDF Energy, 2010b]. The mean height of the water during flood tide is 11.5 m and during ebb tide it is 0.8 m [EDF Energy, 2010b]. The dominant waves approach from west and north-west [EDF Energy, 2010a].

The thermal plume ejected from the Hinkley power station was detected in 40 images. Figure 3.6 shows the probability map of the plume extent during ebb and flood tides. During ebb tide, the plume is very limited in area and stays very close to the coast. The spread of the plume is related to the tidal currents, which are weaker in the seaward direction and therefore don't stretch the plume far away from the discharge during the ebb tide. The currents are stronger during the flood tide, which increases the surface spread of the plume.

The findings from high resolution satellite imagery are in agreement with thermal plume modelling study [Fernard *et al.*, 2011] that was carried out in relation to building plans of Hinkley Point C power station in the future. The modelling study was run for an example year, assuming that the current and the future power stations were both in operation. Since the model outputs represent an averaged yearly situation, there is no distinction in plume location during different tide phases. However, even on the averaged 1 year model run, the plume disperses less westward staying closer to the coast line, and spreads further eastward, which can be observed during the flood tide in the satellite imagery.

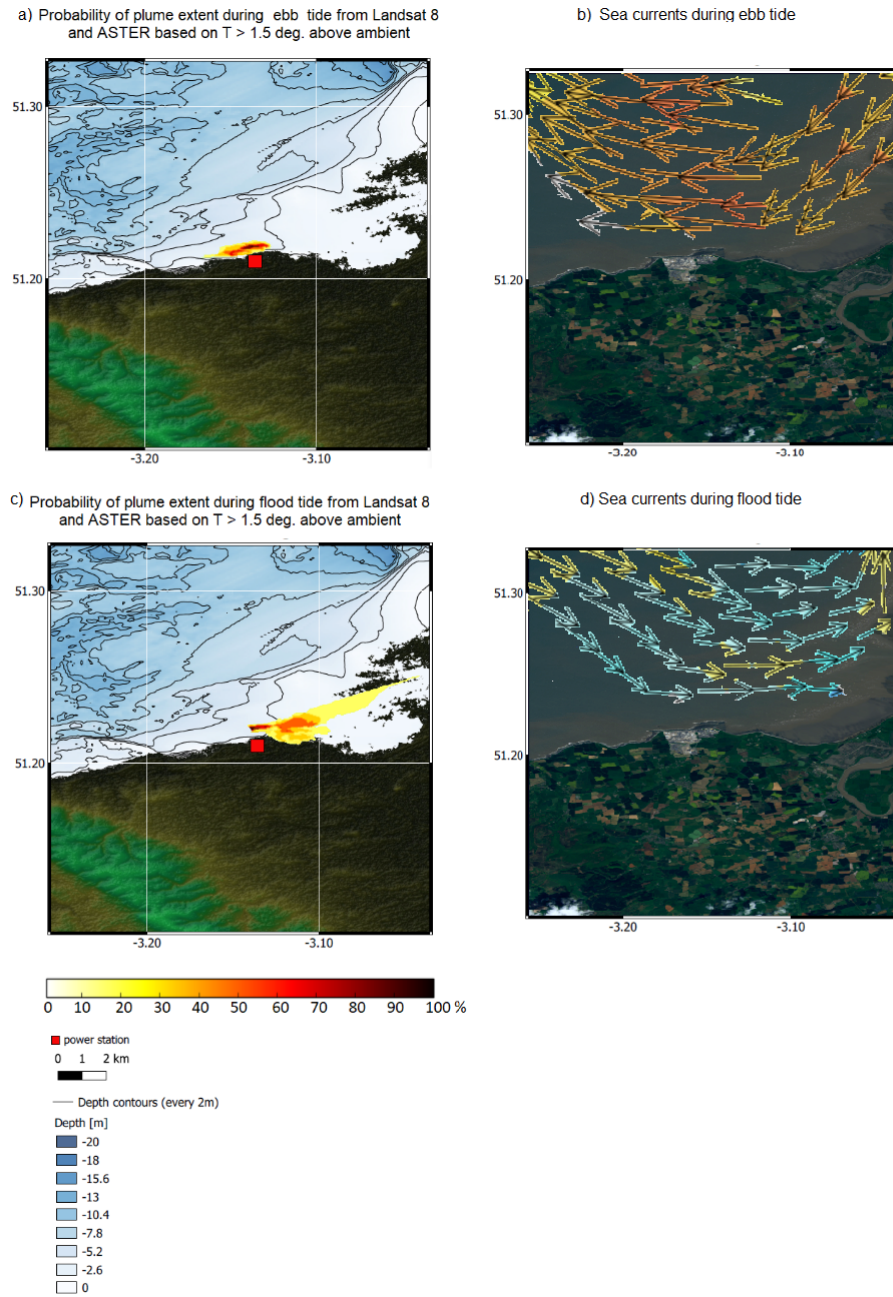


Figure 3.6: (a) Probability density map of thermal plume location and reach during ebb tide with darker colours presenting higher probability and lighter colours lower probability. (b) Corresponding RGB composite of an example daytime scene during ebb tide with waters visible in dark blue and green colour, land in dark green. The arrows represent the currents based on the data from The Norwegian Meteorological Institute. (MET Norway). During the ebb tide, weaker flow is represented by smaller arrows and stronger flow is represented by bigger arrows. Strongest flow is highlighted as yellow arrows. (c) Probability density map of thermal plume location of reach during flood tide with darker colours presenting higher probability and lighter colours lower probability. (d) Corresponding RGB composite depicting example daytime scene during flood tide with waters visible as dark blue colour, land in dark green. The arrows represent the direction of flow during flood tide with weaker flow being represented by smaller arrows and stronger flow is represented by bigger arrows.

3.6.2 Torness as example of open water exposure

Torness power station is located on the east coast of Scotland. The local bathymetry is sloping gently into the deep basin. The rocky seabed is temporarily exposed during low water events and underwater during flood and high water events [[Davies and Neves, 2012](#)]. Further description was included in Chapter 1 (Section 1.10.7.).

The thermal plume ejected from the Torness power station was detected in 49 images. The thermal plume is located close to the coast and does not extend beyond 1.5 km on both sides of the discharge point (see [Figure 3.7](#)). During the ebb tide, the plume stretches out from the outfall pipe forming a band of warm water dispersing along the coastline. 7 out of 18 images captured the plume dispersing up to 1.5 km away from the outfall pipes, while 11 images capture the plume within 500 m away from the outfall pipe. However during the flood tide, the detected plumes form a circular area of warm water, rather than an elongated band like in the ebb case. In 80% of the ebb cases the plume does not disperse further than 1 km away from the discharge point.

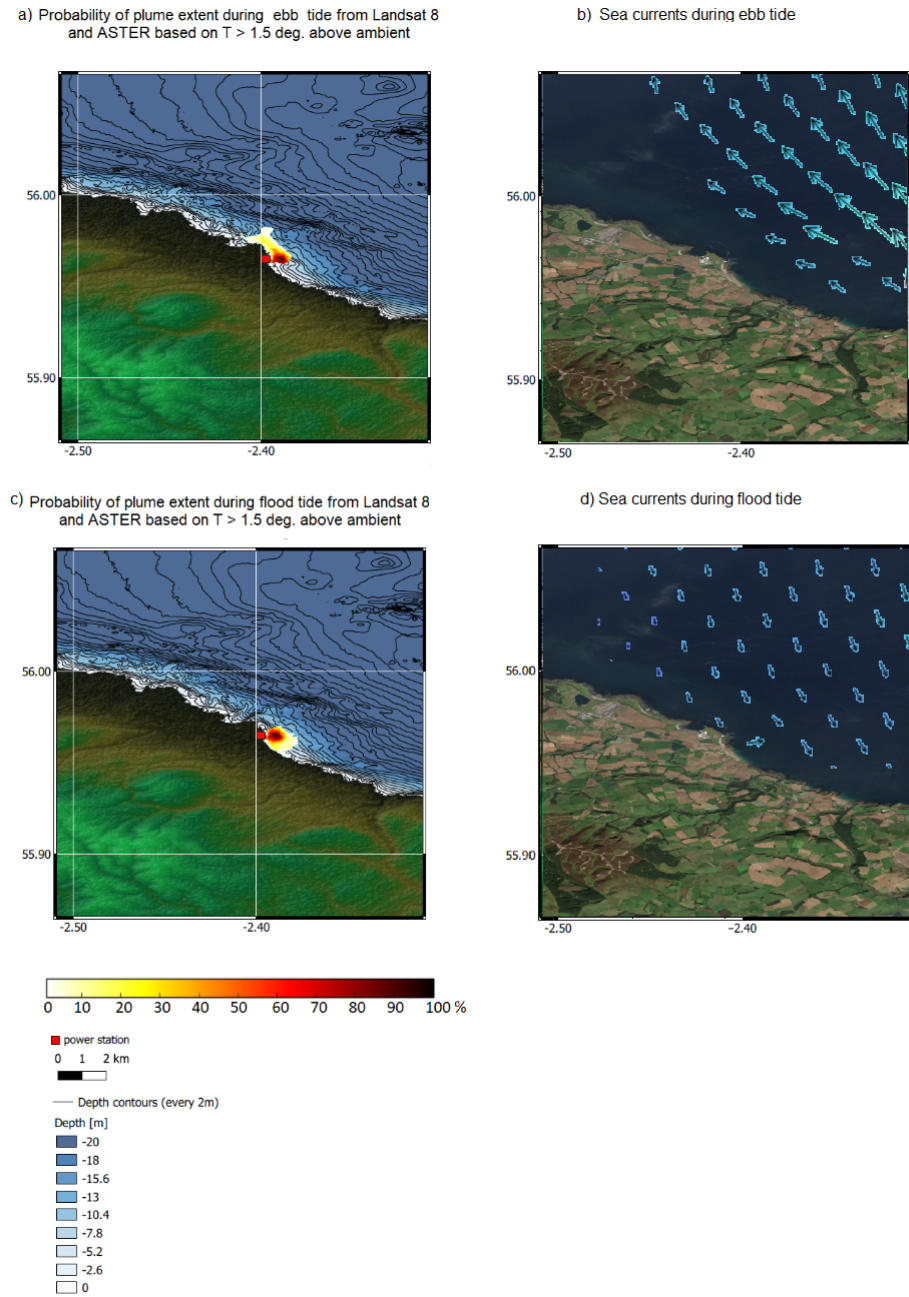


Figure 3.7: (a) Probability density map of thermal plume location and reach during ebb tide with darker colours presenting higher probability and lighter colours lower probability. (b) Corresponding RGB composite of an example daytime scene during ebb tide with waters visible in dark blue and green colour, land in dark green. The arrows represent the currents based on the data from The Norwegian Meteorological Institute. (MET Norway). During the ebb tide, weaker flow is represented by smaller arrows and stronger flow is represented by bigger arrows. (c) Probability density map of thermal plume location of reach during flood tide with darker colours presenting higher probability and lighter colours lower probability. (d) Corresponding RGB composite depicting example daytime scene during flood tide with waters visible as dark blue colour, land in dark green. The arrows represent the direction of flow during flood tide with weaker flow being represented by smaller arrows and stronger flow is represented by bigger arrows.

3.6.3 Dungeness as example of cusped foreland

Dungeness is located in the south east England. The triangular foreland extends south eastward [Lewis, 1932] with shallow waters located on both sides, which can be seen in Figure 3.8. Almost perpendicularly to the tip of the foreland there is a shelf, where the bathymetry drops down at a steep gradient, which is shown by the densely concentrated depth contours. Detailed description of the place was already included in Chapter 1 (Section 1.10.1.).

The thermal plume ejected from the Dungeness power station was detected in 52 images. This is the highest number of observations compared to the other power stations, because other locations had more images with clouds obscuring the discharged plume. 28 scenes collected between September 2018 and September 2019 were excluded from the analysis, since the power station was out of operation in that time period due to maintenance. Hence no thermal plume has been detected during that period.

The plume forms a narrow band, staying in the shallow water region and hugging the coast (see Figure 3.8). The outer edge of the plume is almost following the 8 m depth contour, making the plume's width vary from 200 m to 600 m. During the flood tide, the plume does not disperse far from the coast and rather stays limited to the shallow waters (see Figure 3.8). The observed plume is more limited in areal size than during the ebb tide, with 80% cases not extending beyond the deep water shelf and dispersing only in the shallow water close to coast.

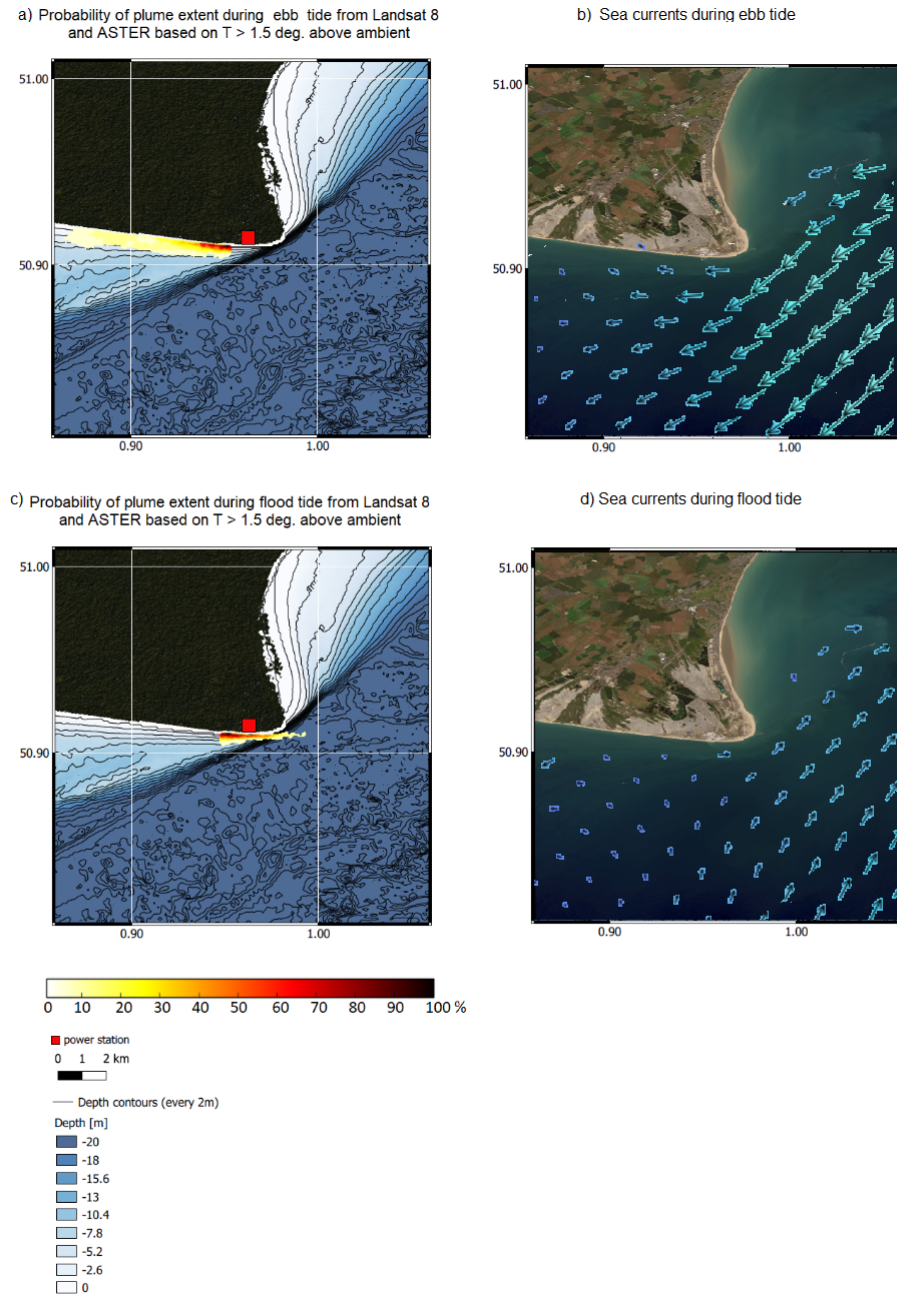


Figure 3.8: (a) Probability density map of thermal plume location and reach during ebb tide with darker colours presenting higher probability and lighter colours lower probability. (b) Corresponding RGB composite of an example daytime scene during ebb tide with waters visible in dark blue and green colour, land in dark green. The arrows represent the currents based on the data from The Norwegian Meteorological Institute. (MET Norway). During the ebb tide, weaker flow is represented by smaller arrows and stronger flow is represented by bigger arrows. (c) Probability density map of thermal plume location of reach during flood tide with darker colours presenting higher probability and lighter colours lower probability. (d) Corresponding RGB composite depicting example daytime scene during flood tide with waters visible as dark blue colour, land in dark green. The arrows represent the direction of flow during flood tide with weaker flow being represented by smaller arrows and stronger flow is represented by bigger arrows.

3.6.4 Hunterston as example of area surrounded by islands

Hunterston power station, introduced in Chapter 1 (Section 1.10.5.), is located in the Firth of Clyde, Scotland. The area directly off the coast is called Hunterston Sands and is comprised of shallow waters with water depth not exceeding 10 m. During summer time, Hunterston sands, which are exposed during low water events, become hot due to solar radiation and transfer part of that heat to the water incoming during the flood tide [Davies and Neves, 2012]. The water over the sands warms up and forms a band along the shoreline. Davies and Neves [2012] indicated that those local spots of warm water will impact thermal plume dispersion from the power station. Beyond the Hunterston Sands there is a steep drop in the seabed depth up to 50 m into the deep channel [Davies and Neves, 2012]. The area is surrounded by islands, called Little Cumbrae Islands, around which the bathymetry gets shallow again (see Figure 3.8).

The thermal plume ejected from the Hunterston power station was detected in 43 images. The plume is extending both north-east and south off the discharge point along the Hunterston channel. Even for the largest observed plume, its extent is limited by the presence of the islands. A field survey of the plume in 2008 [Briggs, 2008] suggested that the plume is embedded in the tidal stream and follows tidal currents. As much as this plume behaviour was seen in the satellite imagery, it was pronounced only for 25% of cases during the flood and the ebb tide (see Figure 3.9). In 29 out of 43 images the observed plume resembles a circular pool of warm water rather than an elongated band, and is located within 1.5 km from the power station discharge (see Figure 3.9). The field survey that characterised the plume was carried over one tidal cycle through a series of point measurements, with the amount of measurement points decreasing with distance away from the discharge point. Therefore it is possible that it did not capture the plume location completely.

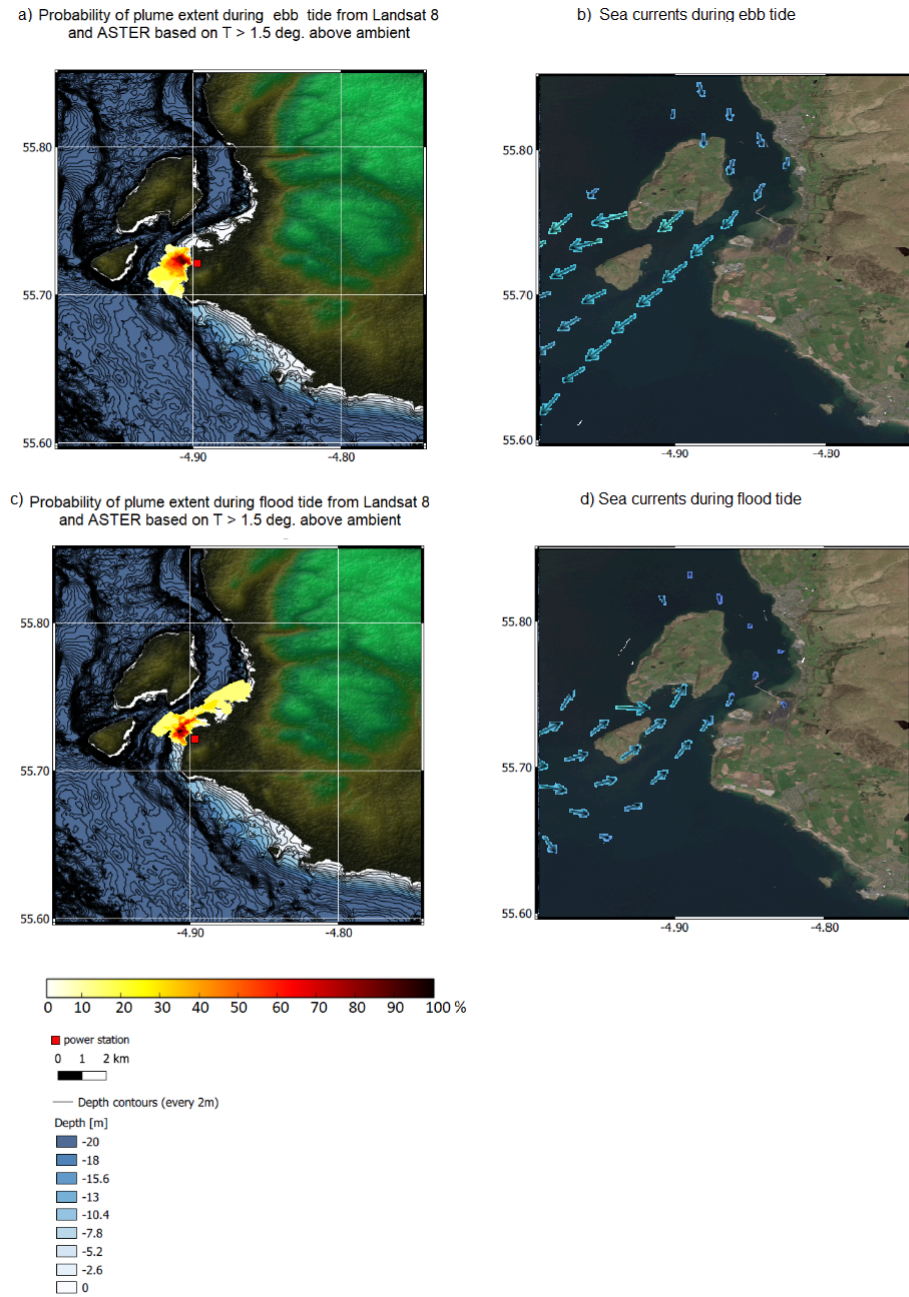


Figure 3.9: (a) Probability density map of thermal plume location and reach during ebb tide with darker colours presenting higher probability and lighter colours lower probability. (b) Corresponding RGB composite of an example daytime scene during ebb tide with waters visible in dark blue and green colour, land in dark green. The arrows represent the currents based on the data from The Norwegian Meteorological Institute. (MET Norway). During the ebb tide, weaker flow is represented by smaller arrows and stronger flow is represented by bigger arrows. (c) Probability density map of thermal plume location of reach during flood tide with darker colours presenting higher probability and lighter colours lower probability. (d) Corresponding RGB composite depicting example daytime scene during flood tide with waters visible as dark blue colour, land in dark green. The arrows represent the direction of flow during flood tide with weaker flow being represented by smaller arrows and stronger flow is represented by bigger arrows.

3.6.5 Hartlepool as example of estuary location

Hartlepool power station, introduced in Chapter 1 (Section 1.10.2), is located in the River Tees Estuary, north east England. The waters are shallow and gently sloping into deep basin from -2 m to -20 m over a distance of 10 km. The intake of the cooling water is located in the river estuary and the the plume is ejected back into the shallow coastal waters, left of the mouth of River Tees.

The thermal plume was detected in 41 images. In general the thermal plume seems to be confined to a small area in comparison to other locations. The observed surface plume does not spread far away from the outfall pipes and in 80% cases it stays within an 1 km radius from the outfall point (see Figure 3.10). In 8 images the observed plume extended 300 - 500 m further north and south off the discharge point, depending on the tidal currents. Despite the sea currents changing direction and flowing north-eastward during the flood tide and south-westward during the ebb tide, the probability of the plume location was not split between the two scenarios. The strength of the sea currents, based on the MET Norway dataset, in that region is very under 0.1 m s^{-1} so the plume is not stretched by the tidal stream as significantly as in other locations.

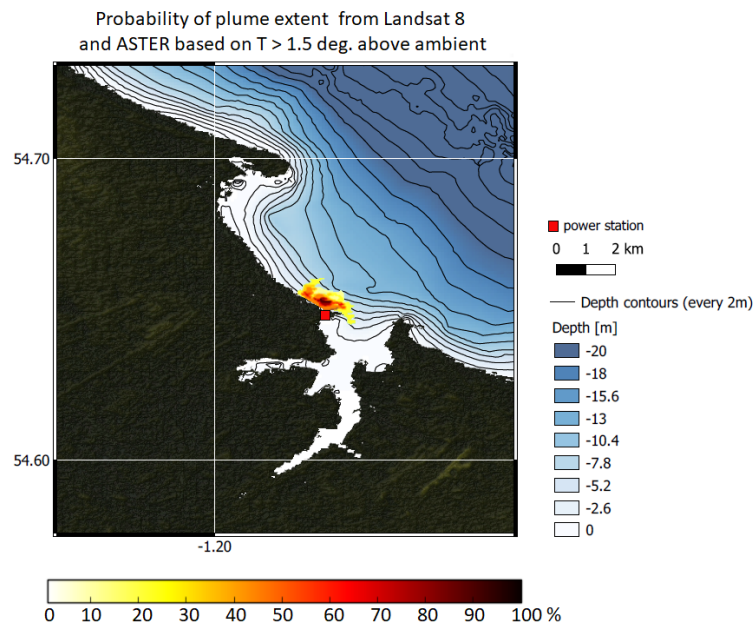


Figure 3.10: Close-up of the Hartlepool power station (marked as red square), with detailed bathymetry with contours at 2 m depth intervals obtained from EMODnet dataset. The probability density map of thermal plume location and reach is overlaid on top of the bathymetry. Darker colours present higher probability and lighter colours lower probability of the plume location.

3.7 Discussion

The probability density maps of the plume distribution presented above are based on clear-sky thermal imagery from ASTER and Landsat 8 TIRS with low cloud cover. Over the operational time of both instruments, the acquired number of images is not sufficient to monitor the thermal plume on a daily basis. It is, however, appropriate to use those images for detailed characterisation in the context of tidal effects on plume dispersion.

Detecting the plume based on thermal thresholds proves useful in understanding the plume behaviour associated with the tidal regimes. One difficulty with detecting plumes in remote sensing observations is the proximity of the observed plume to the warm water puddles. When the plume is extending towards the open water and the warm water puddles are localised very close to the exposed sand bank areas or land and are not extensive, it is easier to delineate the plume from the rest of the waters. However, under certain circumstances, it can be more complicated to delineate the plume properly and use the imagery for further analysis. When the thermal plume is trapped close to the coastline, during summer periods where the bathymetry is shallow, the plume and the warmer shallow coastal waters can have similar SST values. In those situations it is challenging to distinguish the plume from those warm shallow waters very close to the land. This issue has been addressed through land mask expansion, automatically excluding a narrow belt of warm coastal waters. This expansion does not cause the plume to be mistakenly missed, as in all images, the detected plume has width greater than the added mask expansion and continues to disperse offshore. However, it is possible that for other shallow water locations with a plume limited in area or trapped close to the coast, such mask expansion could exclude a part of the detected plume.

This technique of plume detection can be applied to data from other sensors while adapting the temperature threshold accordingly. [Langford \[1990\]](#) proposed as a definition of a thermal plume to be the water that is warmer by 0.5 K than the temperature of the ambient waters. This threshold, however, depends on the definition of the ambient waters and will not always allow accurate plume detection and when choosing the thermal threshold one should include the uncertainty associated with the chosen sensors and retrieval method. In case of using other sensors, the sensor should have at least one TIR channel for temperature retrieval. A combination of green (0.53 μm - 0.59 μm) and near-IR (0.85 μm - 0.88 μm) or green (0.53 μm - 0.59 μm) and SWIR (1.57 μm - 1.65 μm) channels would also be desirable in order to apply the water detection algorithm prior to

the plume detection, otherwise a combination of techniques would have to be applied to exclude land and cloud pixels before detecting the plume.

I consider my findings in comparison with other studies, which include field campaigns and modelling. The findings on the plume location were compared to field campaigns for the Heysham and Hunterston power stations. The satellite observations are consistent with the field campaigns carried out by EDF Energy [*Briggs and Taylor, 2008; Briggs, 2008*]. The direction of the detected plumes captured by the satellite imagery is in agreement with the boat surveys for both types of tide at both locations. For Heysham, the detected plume spatial extent observed during the flood tide is greater in the direction offshore from the satellite imagery than the boat survey. This is because the coastal waters near the shore were too shallow for the research vessel, which restricted access and therefore limited the investigated area. For Hunterston, the satellite-derived probability density maps suggested that the plume observed during the boat survey does not capture the full extent or variability of the plume.

The findings on plume dispersion were compared to modelling studies for the Sizewell and Hinkley power stations. The observations of the plume switching direction in the Sizewell area are consistent with a study, which used a hydrodynamic model and infrared images collected during different tidal phases to investigate the plume direction and surface area as a function of tide [*Elliott, 2011*]. Both the direction and the extent of the plume observed in the satellite imagery is consistent between [*Elliott, 2011*] study and this work. The findings for Hinkley area are also in agreement with a modelling study by *Fernard et al. [2011]*, which simulated plume dispersion throughout the year for currently operating and new-built power stations. The modelling study did not distinguish between different tidal conditions, so the satellite observations provide more detail into the possible plume location as a function of tides.

Tides are mainly influenced by the moon, with its influence in causing the tide being 2.16 times that of the sun. Hence, in most locations, the tide is said to be controlled by the lunar tide-generating forces and only modified by solar influence.

An important thing to bear in mind is that Landsat 8 is a sun-synchronous satellite, which means that it collects data over the same region around the same time. This will impact the tidal components, making the principal solar component, S2, more pronounced. At each location a solar-synchronous satellite pass will always occur at the same part of the S2 cycle, which could potentially distort the understanding of the tidal phases by the satellite observing the ebb tides only during the neap tide and the flood tides only

during the spring tide.

The sun and moon tide-generating forces aligned during the new moon and full moon phases. When the high tides of both the solar and lunar envelope occur simultaneously the height of the composite high tides is increased and similarly, when the low tides of the solar and lunar envelope align this brings about a decrease in the composite low tides [Hicks, 2006]. As a result, a larger than average tidal range occurs which is referred to as spring tides.

On the other hand, neap tides, when the tidal range is smaller than average, occur during the first and third quarters of the moon's phases. This is due to the tide generating forces of the sun being at right angles to that of the moon. The low tides of the solar envelope occur simultaneously to the high tides of the lunar envelope. This results in a smaller height of the composite high tide and larger height of the composite low tide [Hicks, 2006]. As a result, smaller tidal ranges occur during those periods, called neap tides.

In addition to the changes in the tidal range, the spring-neap tide phenomenon has an effect on when the high and low tide phases of the lunar tide occur. As the moon transitions away from the New or Full Moon phase into the first or third quarter, the solar envelope lags behind that of the lunar envelope such that the composite tide is hindered. This event is called priming and means that the high and low composite tides occur earlier than they would with just the lunar influence [Hicks, 2006].

Alternatively, the solar envelope is ahead of the lunar when the moon transitions from the first or third quarter into the Full or New Moon phase advancing the composite tide. As the earth spins and the high and low composite tides occur after that of the just lunar one [Hicks, 2006]. This event is known as lagging.

Having collected satellite observations over a period of almost 10 years, it is unlikely that every low tide observation occurred during the first and third moon phase and every high tide observation was captured during the second and fourth moon phase. The moon phase changes every 7 days (New Moon – first quarter – Full Moon – third quarter, while Landsat 8 revisit time over each location is 16 days. Some of the Landsat observations cannot be used due to cloud contamination, which can reduce the time between observations to 32 days or over a month.

In this chapter I am interested in observations of the plume itself. However, combining those satellite observations with a hydrodynamic model would be a good tool to describe coastal tidal dynamics [Davies *et al.*, 1985]. The observations could be used to validate the

three dimensional (3-D) simulations of the plume. Modelling would enable investigation of sub-surface processes that influence plume dispersion. Having a full understanding of the plume dynamics through a hydrodynamic model is important for recognising potential ecological impacts [*Carniello et al., 2014*]. This in turn will enable better information to be developed for facilities such as: industrial power stations, local communities, leisure facilities, and the centres for biodiversity of marine species.

3.8 Conclusions

Satellite imagery provides valuable additional information that contributes to better understanding of the impact of tides on the plume dispersion. The number of clear-sky images (on average 9 scenes per year depending on the location) is too low for day-to-day monitoring of a thermal plume, but it is adequate for detailed characterisation in the context of tidal effects on detected plumes. Industrial plumes are released from a point source and due to higher-than-ambient temperature reveal the direction of the surface water currents. Conditional probability maps of detected plumes are produced using multiple observations from different platforms, expanding the data from 2000 to 2019 sample with daytime and nighttime imagery across different seasons and years. The direction and the size of detected thermal plumes depend on: the phase of the tide and the strength of the surface currents. For Heysham as example of an intertidal embayment, the detected plume was resembling a narrow, elongated region of 5 - 7 km in length flowing south-westward during the ebb tide and a restricted pool of warmer-than ambient water reaching 3.5 - 4 km offshore during flood tide. For Sizewell as example of open water exposure, the detected plume was an elongated area of water ranging 3.5 - 10 km in length in the same direction as the tidal currents (southward for the flood tide and northward for the ebb tide). For Hartlepool as example of a very shallow estuary, the tidal currents were too weak to impact the direction of plume dispersion. The plume was staying close to the coast and did not disperse beyond 1.5 km on any occasion. Satellite remote sensing analysis, compared to traditional methods that use field campaigns, can cost-effectively inform the power stations of the surface plume behaviour during certain conditions and indicate the area of thermal contrast. With a lot of satellite data from various sensors freely available through online platforms such observations might prove useful compared to expensive one day campaigns. Understanding the dispersion of the plume is also essential to aid understanding of any potential ecological impacts.

Chapter 4:

Simulations of thermal plumes

4.1 Statement of publication status

The material in this chapter, together with part of the material in Chapter 5, has been accepted for publication in *Environmental Research Communications* on the 22 March 2021. I am the lead author of the manuscript. All figures were generated by me and I led and finalised the conceptualisation and scientific writing. I take full responsibility for the results. Other authors listed on this publication helped in discussions of the methods and provided feedback on the results. The provisional reference for the manuscript is as follows:

Faulkner, A., Bulgin, C. E., Merchant, C. J. (2021). Characterising industrial thermal plumes in coastal regions using 3-D numerical simulations. *Environmental Research Communications*

- The content of this chapter differs from the published article in the following ways:
- For consistency with the thesis structure, the numbers of the section headings equations and figures are updated and minor format changes are applied;
 - The word "paper" has been substituted to "chapter" to keep consistency with thesis structure;
 - The published description of the FLOW-3D set-up has been expanded and description on the governing equations in this chapter.
 - The published results on Heysham are expanded by the addition of discussion on the density-temperature equation considering the salinity and its potential impact;
 - The published discussion and conclusions were included in this chapter's sections under the same name and expanded with the additional information;
 - The published discussion also contains material from Chapter 5 of this thesis.

4.2 Abstract

Coastal power stations use sea water as a coolant, releasing it back into coastal environments at a higher-than-ambient temperature. Due to the possible ecological impacts on sensitive coastal zones, thermal plume formed by warmer coolant waters needs to be monitored, which is typically done through field campaigns. This chapter assesses the use of simulations and remotely sensed observations as complimentary methods to characterise plume behaviour for a chosen coastal power station located within an inter-tidal embayment. Simulations of the thermal plume for two main tide phases and associated sea current conditions are validated against the high-resolution satellite observations. Simulated plume temperatures are higher than the observed values, with the biggest difference of 2°C. The direction of the simulated plume dispersion is in agreement with observations and depends on the strength and direction of sea currents associated with the phase of the tide. The plume stretches most at the surface with limited impact on the benthic temperatures.

4.3 Introduction

As mentioned in previous chapters, nuclear power stations, located next to large rivers or on the coasts, use river or sea water as a coolant for their installations. The effluent water released back into the environment at a higher temperature than the ambient intake water forms a thermal plume.

Some aquatic organisms have narrow temperature tolerances and an increase in water temperature can impact the habitats, cause deformation in fish species [[Hung et al., 1998](#); [Fang et al., 2004](#)] or force them to relocate to colder regions.

In order to ascertain that the released thermal plume will not break any environmental requirements, industrial power plants complete plume characterisation studies prior to the power plant operation and continue to monitor thermal discharges during the life of the power plant. Once in operation, thermal plumes have traditionally been characterised through field campaigns, which involve a survey vessel taking point measurements in the vicinity of the power plant outfall pipes. Such campaigns are expensive and can only be carried out during certain months.

High-resolution remote sensing observations are another way of characterising thermal plumes as they provide good insight into spatial distributions of the SSTs in the

vicinity of the industrial power stations [*Faulkner et al., 2019; Tang et al., 2003; Davies and Mofor, 1993; Ahn et al., 2006*]. Satellite observations allow us to resolve thermal stresses in space and time and are good for understanding the driving surface processes. However, satellite observations are not representative of the development of the thermal plume below the surface or its 3-D nature. In order to understand possible impacts of industrial thermal plumes on the benthic habitats, high-resolution observations can be integrated with thermal plume simulations.

Modelling of thermal discharges into aquatic environments allows us to gain understanding of the thermal plume behaviour sub-surface and hence its 3-D nature. Numerical simulations of the thermal plumes can be divided into several groups: reproducing a specific example of a thermal discharge [*Durán-Colmenares et al., 2016; Issakhov, 2018*], exploring various scenarios of the thermal plume dispersion [*Cardoso-Mohedano et al., 2015; Salgueiro et al., 2015; Thai and Tri, 2017*], or simulating possible future thermal plume dispersions [*Dvornikov et al., 2017*].

Depending on the local environment, there are different driving factors of the plume dispersion. Thermal plumes released into stagnant environments tend to rise to the surface and spread at the surface driven by the volume outfall rate [*Ali, 2011*]. However, thermal plumes ejected into larger water bodies tend to be more reactive to winds [*Issakhov, 2016; Fossati et al., 2011*] and tides [*Fossati et al., 2011*] rather than operational capacity [*Issakhov, 2016*]. Simulations of industrial thermal plumes located in the coastal areas showed that the plume dispersion is highly dependent on the height of water and the strength and direction of the tidal currents associated with the tide phase [*Suh, 2001*].

To understand plume dispersion in 3-D when released into a changing environment, running a set of simulations with varying conditions is of advantage. Modelling studies usually focus on the main driving factor, depending on the location, such as: discharge speed and direction [*Ali, 2011*], power station operational capacities [*Issakhov, 2016; Ali, 2011*], tidal and current conditions [*Fossati et al., 2011; Abbaspour et al., 2005*], wind speed and direction [*Fossati et al., 2011; Issakhov, 2016; Abbaspour et al., 2005*] and seasonal changes in circulation [*Hamrick and Mills, 2000; Suh, 2001*] as factors influencing thermal plume dispersion.

In order to assume that the simulations are producing accurate results, of either current power station set up or future scenarios, it is vital to compare the output to observations or laboratory experiments. Most simulations are compared against field measurements [*Lowe et al., 2009; Suh, 2001; Hamrick and Mills, 2000*], thermal sensor

observations [Ali, 2011] or experimental data [Issakhov, 2016]. Validating thermal plume simulations against observations is essential for ensuring their usefulness [Abbaspour et al., 2005], because in some cases simulation results can disagree with observations [Ali, 2011; Hamrick and Mills, 2000], particularly in regions further away from the discharge point [Suh, 2001].

The purpose of this chapter is to report means of characterising industrial thermal plumes in the coastal regions other than traditional boat surveys. I use high resolution remote sensing imagery combined with a computational fluid dynamics (CDF) model. I detect thermal plumes in the high-resolution satellite imagery [Faulkner et al., 2019] and create 3-D simulations for selected days, simulating the tidal conditions during the satellite overpass. I use skill scores to compare the plume at the surface obtained through numerical simulations with the plume observed by the satellite sensor. I then assess any possible impact on surrounding sensitive habitats. This chapter proceeds as follows: Section 2 describes the methodology, Section 3 presents the results, Section 4 provides discussion and limitations, Section 5 summarizes my findings.

4.4 Methods

4.4.1 Satellite observations of thermal plumes to validate simulations

I used high-resolution infrared and visible observations from the Operational Land Imager (OLI) and the Thermal Infrared Sensor (TIRS) on-board Landsat 8 focused on our Region of Interest (ROI), the environs of Heysham. Heysham power station (54.0302 ° N, 2.9153 ° W) is located in Heysham, on the west coast of the UK, in the Morecambe Bay. This is one of the largest macro-tidal embayments in the UK with regularly exposed sandbanks and mudflats. I have chosen this ROI due to the bay's tidal regime and its associated dynamic land-water boundary.

Landsat 8 provides high-resolution observations from February 2013 until the time of writing, with a return time of 16 days. The number of observations is further limited by cloud cover, since only observations with clear sky or low cloud cover are useful in this application. I detected the extent of water using the Modified Normalised Water Difference Index (MNDWI) [Xu, 2006] due to the dynamic land-water boundary and presence of intertidal flats. In order to investigate thermal contrasts in the imagery, I retrieved sea surface temperature (SST) over the water regions in every image using Optimal Estimation [Merchant et al., 2008]. I applied a plume detection algorithm on

the SST scenes using a combination of cloud and land mask expansion, thresholding and area and distance calculation. Full details of these steps can be found in Faulkner et al (2019) [[Faulkner et al., 2019](#)]. I obtained 46 clear-sky images over our region of interest for the time period 2013-2019. From the 46 Landsat 8 satellite scenes, we chose two cases that fitted different scenarios: mid-ebb tide and mid-flood tide.

4.4.2 FLOW-3D software for flow simulations

FLOW-3D is one of the commercial computational fluid dynamics (CFD) software packages, which is used by energy and environmental industries that need to model spillways, any hydraulic features or water flow processes. One of the companies that uses FLOW-3D for the purpose of modelling thermal effluents in EDF (Energie de France) in France, the "mother" company of EDF Energy.

As a CFD package, FLOW-3D simulates the flow using discretised Navier-Stokes and continuity equations, which are solved for each computational cell on a structured rectangular grid in three dimensions [[Flow Science Inc., 2018](#)]. The Navier-Stokes equations are time-averaged in the form of the Reynolds-averaged Navier-Stokes (RANS) equations. Finite-difference method is used to calculate the numerical solutions and the free surface is tracked using the volume of fluid (VOF) [[Flow Science Inc., 2018](#)]. The VOF method allows for assigning a value to each computational cell ranging from 0.0 to 1.0 (0.0 for void regions and 1.0 for cells completely filled with fluid). Each cell is evaluated in terms of fluid fraction averaged over a control volume [[Barkhudarov, 2004](#)]. The solid geometry, such as land, river- or sea-bed, outfall pipes are represented using FAVOR formulation for Fractional Area/Volume Obstacle Representation Method [[Flow Science Inc., 2018](#)].

The software allows to set both hydrostatic approximation or keep the non-hydrostatic model. The choice of fluid is also determined by the user and can be chosen from an existing list (covering fluids such as air, water, oil). Depending on the simulation scenario, the RANS equations are solved for an incompressible flow (e.g. simulations of sediment scour or water flow through a tool) or a compressible flow, where the density change in the fluid is directly related to the temperature of that fluid [[Flow Science Inc., 2018](#)]. In this thesis, the RANS equations were chosen for the latter one, as the model was set up to simulate ejection of a buoyant thermal plume. Due to the very high resolution of the model and small cell size, there is no hydrostatic assumption and the momentum equations are used for all three dimensions without the simplification to a 2-D model.

All simulations are set in a Cartesian coordination plane (x, y, z). Due to using

FAVOR method to represent fluid / obstacle, all equations are expressed with area and volume porosity functions. The mass continuity equation used is:

$$V_F \frac{\partial \rho}{\partial t} + \frac{\partial}{\partial x}(\rho u A_x) + R \frac{\partial}{\partial y}(\rho v A_y) + \frac{\partial}{\partial z}(\rho w A_z) + \xi \frac{\rho u A_x}{x} = R_{DIF} + R_{SOR} \quad (4.1)$$

where V_F is the fractional volume open to flow, ρ is the fluid density. The three velocity components (u, v, w) are related to the three coordinate directions (x, y, z). A_x is the fractional area open to flow in the x-direction, A_y in the y-direction and A_z in the z-direction. Because the simulation is set up in the Cartesian coordinates plane, the R element is set to unity and ξ is set to zero. The terms on the right hand-side are as follows: R_{DIF} is a turbulent diffusion term and R_{SOR} is a density source term.

The turbulent diffusion term can be described as:

$$R_{DIF} = \frac{\partial}{\partial x}(v_p A_x \frac{\partial \rho}{\partial x}) + R \frac{\partial}{\partial y}(v_p A_y R \frac{\partial \rho}{\partial y}) + \frac{\partial}{\partial z}(v_p A_z \frac{\partial \rho}{\partial z}) + \xi \frac{\rho v_p A_x}{x} \quad (4.2)$$

where the coefficient v_p is equal to $cp\mu/\rho$, with μ being the coefficient of momentum diffusion (the viscosity) and cp is a constant (it's reciprocal is usually referred to as the turbulent Schmidt Number). This type of mass diffusion is used for turbulent mixing processes in fluids having a non-uniform density, like in the case of a buoyant thermal plume released into ambient waters. Because the simulated flow is compressible and the density within the fluid changes, they require solving of the full density transport equation [4.1](#).

The momentum equations used to model the fluid velocity components are, as mentioned previously, based on the Navier-Stokes equations:

$$\frac{\partial u}{\partial t} + \frac{1}{V_F} \left\{ u A_x \frac{\partial u}{\partial x} + v A_y R \frac{\partial u}{\partial y} + w A_z \frac{\partial u}{\partial z} \right\} - \xi \frac{A_y v^2}{x V_F} = -\frac{1}{\rho} \frac{\partial p}{\partial x} + G_x + f_x - b_x - \frac{R_{SOR}}{\rho V_F} (u - u_w - \delta u_s) \quad (4.3)$$

$$\frac{\partial v}{\partial t} + \frac{1}{V_F} \left\{ u A_x \frac{\partial v}{\partial x} + v A_y R \frac{\partial v}{\partial y} + w A_z \frac{\partial v}{\partial z} \right\} - \xi \frac{A_y u v}{x V_F} = -\frac{1}{\rho} \left(R \frac{\partial p}{\partial y} \right) + G_y + f_y - b_y - \frac{R_{SOR}}{\rho V_F} (v - v_w - \delta v_s) \quad (4.4)$$

$$\frac{\partial w}{\partial t} + \frac{1}{V_F} \left\{ u A_x \frac{\partial w}{\partial x} + v A_y R \frac{\partial w}{\partial y} + w A_z \frac{\partial w}{\partial z} \right\} = -\frac{1}{\rho} \frac{\partial p}{\partial z} + G_z + f_z - b_z - \frac{R_{SOR}}{\rho V_F} (w - w_w - \delta w_s) \quad (4.5)$$

where G_x, G_y, G_z are body accelerations, f_x, f_y, f_z are viscous accelerations, b_x, b_y, b_z are flow losses in simulations, which include porous media or porous baffle plates. Because the simulations of thermal plume injections do not include porous media or baffle zones, those terms are discarded. The last term on the right hand-side represents the mass injection at the source, including the source's geometry component. In the last term, the u_w, v_w, w_w stand for the velocity of the source component and u_s, v_s, w_s stand for the fluid velocity at surface, relative to the source itself. The pressure component is assumed to be static ($\delta = 1.0$), with no extra pressure needed to force the fluid movement. The fluid velocity is calculated from the mass flow rate prescribed at the source and the surface area of the source.

The for the non-turbulent flow, the viscosity of the two fluids is evaluated at each simulation grid point (mesh cell) as the volume fraction weighted average of two molecular constants assigned for each fluid. In case of a turbulent flow, the viscosity is evaluated as the sum of molecular and turbulent values.

Since the simulations of thermal flows are done for compressible fluids, the internal energy equation is:

$$\begin{aligned} V_F \frac{\partial}{\partial t} (\rho I) + \frac{\partial}{\partial x} (\rho I u A_x) + R \frac{\partial}{\partial y} (\rho I v A_y) + \frac{\partial}{\partial z} (\rho I w A_z) + \xi \frac{\rho I u A_x}{x} = \\ -p \left\{ \frac{\partial u A_x}{\partial x} + R \frac{\partial v A_y}{\partial y} + \frac{\partial w A_z}{\partial z} + \xi \frac{u A_x}{x} \right\} + R I_{DIF} + T_{DIF} + R I_{SOR} \end{aligned} \quad (4.6)$$

where I is the macroscopic mixture internal energy.

Energy is assumed to be linearly related to the temperature of fluid:

$$I = CV1 \cdot T + (1 - f_s) \cdot CLHT1 \quad (4.7)$$

where $CV1$ is the specific heat of the fluid 1 at a constant volume, f_s is the solid fraction, evaluated in each mesh cell and $CLHT1$ is the latent heat of fluid 1 associated with melting or freezing of the fluid.

In Equation 4.6, the $R I_{SOR}$ is the energy source component, which can be associated with the mass source R_{SOR} or heat sources within the fluid. The $R I_{DIF}$ and T_{DIF} are

representing turbulent diffusion of I and heat conduction respectively. They can be defined as:

$$RI_{DIF} = \frac{\partial}{\partial x} \left(v_I A_x \frac{\partial \rho I}{\partial x} \right) + R \frac{\partial}{\partial y} \left(v_I A_y R \frac{\partial \rho I}{\partial y} \right) + \frac{\partial}{\partial z} \left(v_I A_z \frac{\partial \rho I}{\partial z} \right) + \xi \frac{v_I A_x \rho I}{x} \quad (4.8)$$

$$T_{DIF} = \frac{\partial}{\partial x} \left(k A_x \frac{\partial T}{\partial x} \right) + R \frac{\partial}{\partial y} \left(k A_y R \frac{\partial T}{\partial y} \right) + \frac{\partial}{\partial z} \left(k A_z \frac{\partial T}{\partial z} \right) + \xi \frac{k A_x T}{x} \quad (4.9)$$

where v_I is equal to $c_I \mu / \rho$ and c_I is the reciprocal turbulent Prandtl number. The k represents thermal conductivity and can be defined as $k = \mu C_v / C_T$, where C_T is the Prandtl number.

For compressible flows, the equations of state are assumed to be:

$$\rho = \rho(p, T) \quad (4.10)$$

For thermally buoyant flows, like in the case of a thermal plume injection, fluid densities are evaluated as temperature-only functions or temperature and fluid fraction functions. In most cases the buoyant flows in the FLOW-3D software are solved using incompressible fluid model with included evaluation of buoyant forces. In this case density will be evaluated as temperature-only function. However, there is an option for thermally buoyant which allows for switching the compressible fluid model on, in which case the density will become evaluated by temperature and fluid fraction for each cell:

$$\rho = F \cdot \rho_1(T) + (1 - F) \cdot \rho_2(T) \quad (4.11)$$

where F is fluid fraction and T is temperature. This option was chosen for the thermal plume simulations.

To account for turbulence in the model, the Renormalised Group (RNG) model is advised to be chosen. The RNG framework was developed by *Yakhot et al.* [1992] to renormalise the Navier-Stokes equations and account for the small-scale motion effects. This turbulence model resembles the $k - \epsilon$ turbulence model in its approach. However, the equation constants in the $k - \epsilon$ model are found empirically while in the RNG model they are derived explicitly.

4.4.3 Setting up thermal plume simulations

My thermal plume simulations address clear-sky images obtained on 08/12/2017 and 17/03/2016. I performed the simulations for two different tide scenarios using FLOW-3D software [*FLOW-3D, Santa Fe, NM: Flow Science, Inc., 2019; Barkhudarov, 2004*]. Setting up simulations under the same conditions as the observations required the information on phase of the tide, which was obtained from National Tide Gauge Network (NTNG). For each observation and its tidal phase, I required an estimation of ambient sea currents associated with the tide. For this, I accessed sea current data from the Norwegian Meteorological Institute (MET Norway) [*Norwegian Meteorological Institute, 2019*].

In order to reproduce the local topography, I obtained the bathymetry from European Marine Observation and Data Network (EMODNet) and land elevation from ASTER Global Digital Elevation Model (ASTER GDEM). Land elevation was merged with the bathymetry and cropped to the area corresponding to the ROI using QGIS software [*QGIS Development Team, 2009*] and converted into a 3-D object using Rhinoceros software [*McNeel R. & Associates, 2018*]. The 3-D object was then set up as the area's geometry for the simulations.

Next, details such as outfall pipes were added to the geometry elements. The cooling water from Heysham Power Station is ejected through two parallel channels into the coastal waters. The information on the location and dimensions of the outfall channels is available through Google Maps open source software [*Google n.d., 2019*]. The narrower channel is 514 m in length and 15 m in diameter. The wider channel is 747 m long and 41 m wide. The two channels are built 208 m away from each other. Because of the large tidal variations in the height of the surface water level and the water retreating during the ebb tide for a couple of hundred meters away from the shoreline, the outfall channels are dug deep and long enough to make sure that the ejected plume reaches the ambient coastal waters under any conditions.

In order to be computationally cost-effective the simulation domain was limited for each plume simulation, depending on where the observed plume was located in the Landsat 8 imagery (Figure 4.1). For the ebb tide the thermal plume always disperses southwestward off the discharge pipes, which allowed us to position the active simulation domain in that region. For the flood tide, the simulation domain was positioned northwards of the discharge pipes, based on the plume location observed in the satellite imagery.

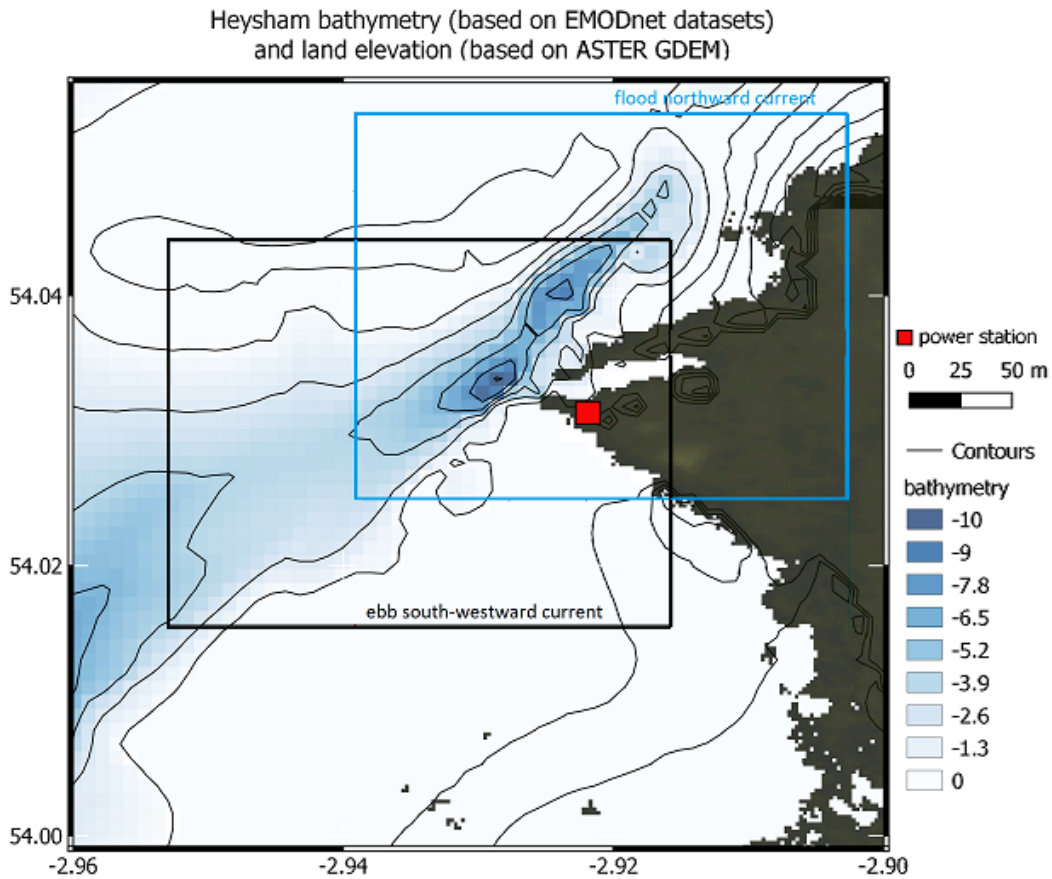


Figure 4.1: Bathymetry for the region of Heysham, eastern part of the Morecambe Bay based on a dataset from European Marine Observation and Data Network (EmodNET). Darker colours mark deeper regions and lighter colours correspond to shallower bathymetry. Land is represented by the dark green colour with the power station marked as a red square. Simulation domains are marked as black and blue rectangles for ebb and flood simulations respectively.

The computational mesh specifies the 3-D region for which the simulation will be performed, the domain outside the mesh is not included in the simulations. The mesh was comprised of $5\text{ m} \times 5\text{ m}$ cells in the horizontal (x and y dimension) and the smallest cell size in the z direction that is allowed by the software solver, i.e. 2 m cell size for ebb simulations and 1.4 m for flood simulations. The smaller cell size in the z direction for flood domain was essential to get the best possible depth resolution in the very shallow regions present north of the power station (identified by the blue box in Figure 4.1).

Once the geometry in the simulation domain was representing real life conditions, I added the ambient fluid, which as default for hydrodynamic simulations in FLOW-3D, is water at $20\text{ }^\circ\text{C}$. In this study I was practically constrained to use the default ambient fluid. We specified the water surface elevation in the simulation based on the tidal observations.

First, simulations were run to establish a flow of the ambient water through the domain. Values of the velocities associated with the tidal currents, obtained from the Norwegian Meteorological Institute (MET), were prescribed at the boundaries of the simulation mesh, where the flow was entering the domain. This means that the velocities were prescribed at the upper and the right boundary of the mesh for the ebb flow and at the lower and the left boundary of the mesh for the flood tide. The other two mesh boundaries in the simulations were set to enable the flow to enter and leave the domain, which in turn removes any possible effects of the shear velocity associated with the solid wall boundary. The flow simulations were run until the solution was close to reaching steady state with respect to those boundary conditions, and thereby approximating the dynamic flow for the corresponding phase of tide. The simulations were then continued with thermal plume injection prescribed at the location of the outfall pipes. The thermal plume injection represented the outfall volume rates and the temperatures of the outfall plume, information provided by the power station operators.

To address the constraint that the ambient water temperature was 20 °C, in the simulations the outfall temperatures were scaled to obtain the same density contrast as that between measured outfall water and the observed ambient water temperature (Figure 4.2).

First, I calculated corresponding densities for the observed ambient temperatures and the temperatures measured at the outfall pipes using an equation after McCutcheon et al. (1993):

$$\rho = 1000[1 - (T + 288.9414) \div (508929.2(T + 68.12963)) \cdot (T - 3.9863)^2] \quad (4.12)$$

where ρ is density and T is temperature of water.

Then, I calculated the density difference for the ejected plume with respect to ambient water density, as shown by:

$$\delta\rho = \rho_o - \rho_a \quad (4.13)$$

where ρ_o is the density of water measured at the outfall pipes and ρ_a is the density of observed ambient waters averaged over an area of 1 km km. Next, the density of simulated ambient water at 20 °C was calculated using Equation 4.12. The density difference $\delta\rho$ was then added onto the density of simulated ambient water density:

$$new \rho_o = \rho_{sa} + \delta\rho \quad (4.14)$$

where $\delta\rho$ is the density difference between observed ambient waters and the outfall pipes and ρ_{sa} was the density of simulated ambient water at 20 °C. By doing this I ensured that the density difference between ambient water and the outfall thermal effluent was consistent between observations and the simulation.

After the simulations have finished running, I used the density difference information to turn the simulations into a temperature field that can be compared with observations. For all simulation cells, where $\delta\rho = 0$ I assigned the observed ambient temperature values. For all other simulation cells, temperature values were recalculated based on density difference from the observed ambient values.

The caveat of this approach is that the relationship between temperature and density for water is not linear, hence the same density difference will correspond to different temperature differences. Figure 4.2 shows an example scenario, where the observed ambient temperature and measured temperature of the outfall water are both colder than 20 °C. The difference in the temperature between the ambient waters, 5.6 °C, and the measured outfall waters, 17.0 °C, is 11.4 °C. The corresponding density difference is 1.17 kg m⁻³. To obtain the same density difference in the simulations, with the constraint of ambient waters being 20 °C, the outfall water temperature is set to 25.05 °C. Even though the density difference remains the same between the observed and the simulated temperatures, the gradient representing the change in density will be different (see Figure 4.2). Because the observed ambient temperature on both days was lower than 20 °C, it is probable that as a result the temperature differences are under-estimated in the simulations, which as default use 20 °C as ambient temperature.

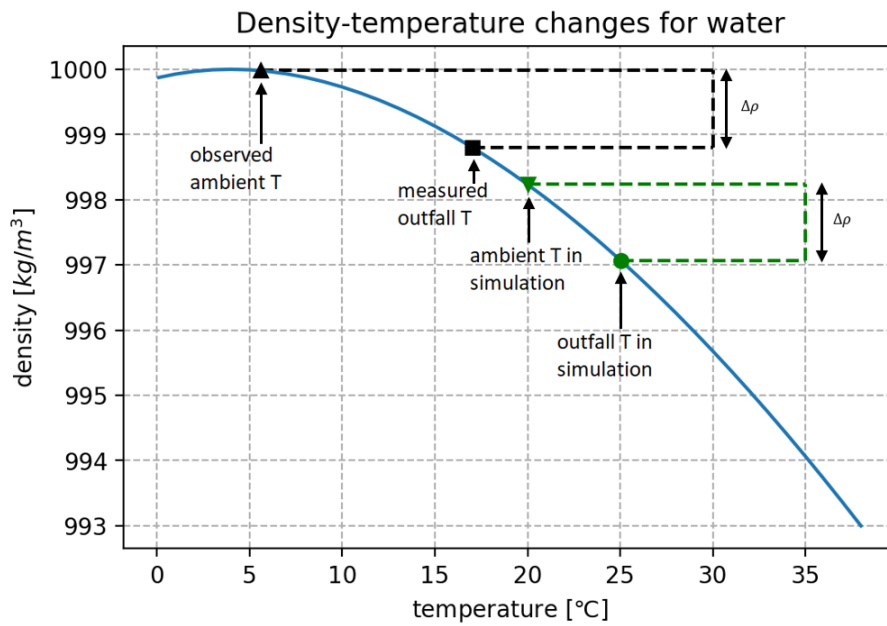


Figure 4.2: Changes in water density (y axis) with rise in temperature (x axis) based on the McCutcheon et al. (1993).

4.4.4 Density as function of temperature-only vs density evaluated as function of temperature and salinity

Since the density in FLOW-3D modelling software is evaluated as temperature-only function, Equation 4.12 was chosen. It is, however, a slightly out-dated equation and does not represent the real situation in the estuary location like Heysham. Therefore, in this part, the relationship between the temperature and density for non-saline water, which was used for the purpose of the simulations is compared with the more recent standard, Thermodynamic Equation Of Seawater - 2010 (TEOS-10) [McDougall and Barker, 2011] available at www.teos-10.org. TEOS-10 is a standard for calculating thermodynamic properties of seawater. It is based on a Gibbs formula from which thermodynamic properties, such as density can be derived in a thermodynamically consistent manner. In terms of describing and allowing for derivation of thermodynamically consistent properties of seawater, TEOS-10 supersedes the old standards used before and hence it has become the primary way of estimating properties of seawater [Pawlowicz, 2010].

Using TEOS-10 density was evaluated as a function of temperature and salinity. The average water salinity was chosen to be 32, as it was reported that mean annual salinity values between the Solway Firth and the Liverpool Bay are one of the lowest for that part of the country, under 32.5 [Howarth, 2005]. Since TEOS-10 no longer uses the unitless

practical salinity, it allows for recalculation of the salinity into absolute salinity with units gkg^{-1} . Absolute salinity can be defined as:

$$S_A = S_R + \delta S_A \quad (4.15)$$

where δS_A is the correction factor, which can be looked up in the global atlas for the open ocean or in the absence of other information can be assumed to be 0. The latter is often used when describing coastal regions [Pawlowicz, 2010]. The S_R is the reference salinity and can be defined as:

$$S_R/(gkg^{-1}) = \frac{35.16504}{35} \times S_P \quad (4.16)$$

where S_P is the practical salinity.

Figure 4.3 shows the changes in density for non-saline waters computed using *McCutcheon et al.* [1992] compared to the density changes for coastal saline waters computed using TEOS-10 [McDougall and Barker, 2011] for the same temperature range. Looking at the lines, it can be noticed that the saline waters have higher density than the non-saline waters (as seen on the right-side vertical scale). Moreover, the relationship between the density and temperature for the saline waters resembles a more linear one compared to the one for non-saline waters. Because the relationship between the temperature and density is more linear, the density gradients associated with the temperature changes (discussed on page 88) would be more consistent. For the same example, as discussed previously, the observed ambient water at 5.6 °C and the temperature measured at outfall water at 17.0 °C yields an 11.4 °C temperature difference. The corresponding density difference for the saline waters is 2.014 kg m⁻³. For the simulations, where the simulated ambient water is always 20 °C, the simulated outfall water temperature would then be 27 °C. This would result in the temperature difference between the simulated ambient water and simulated outfall waters to be 7 °C, which is closer to the observed differences.

Since the buoyant force is directly proportional to the density as:

$$F_B = \rho V g \quad (4.17)$$

where ρ is the density, V is the volume of the displaced fluid and g is the gravitational acceleration. Because salty sea water has higher density, it will have also higher buoyancy. Higher density difference between the ambient waters and the released thermal plume in the simulations would make the plume more buoyant and hence rising to the surface.

Not including salinity in the density evaluation for saline waters would impact the

simulation results, as the simulated waters are less buoyant than when salinity is included. For the aforementioned example, the difference in the buoyant forces solely due to the differences in density (for the same ambient waters, with the same volume outfall rate $82 \text{ m}^3 \text{ s}^{-1}$ and gravity assumed to be 9.81 m s^{-2}) is 20,104 N for every second worth of the volume discharged, which corresponds to 2,050 kg of water being displaced.

When thinking about the mixing, estuaries can be classified into: well mixed, partially mixed and stratified [*Stoker, 1992*]. The local material dispersion is affected by the turbulent mixing (happening on the length scales of the estuary or less and time scales shorter than the tidal cycle) and larger-scale motions, such as tides [*Fischer, 1976*]. The mixing characteristics are influenced by water density, tides, discharge and wind [*Stoker, 1992*]. Although increased tidal currents would strengthen the vertical mixing, in estuaries with strong stratification the vertical mixing is reduced to some degree [*Fischer, 1976; Hong and Shen, 2012; Scully et al., 2005*]. Furthermore, studies have suggested that the increases of vertical transport would be more linked to changes in the stratification than by the tidal changes [*Hong and Shen, 2012; Scully et al., 2005*].

The mixing efficiency for buoyancy driven mixing can depend on the density of the fluid and the size of the domain [*Wykes et al., 2015*]. For a less stratified estuary, in a well-mixed saline environment, more buoyancy-driven mixing would be expected in saline coastal estuarine water than for the presented non-saline waters in the simulations. On the other hand, for a more stable, stratified estuary, the vertical mixing would be hindered, despite the impact of tides. That could result in potentially higher temperatures at the seabed due to hindered vertical exchange.

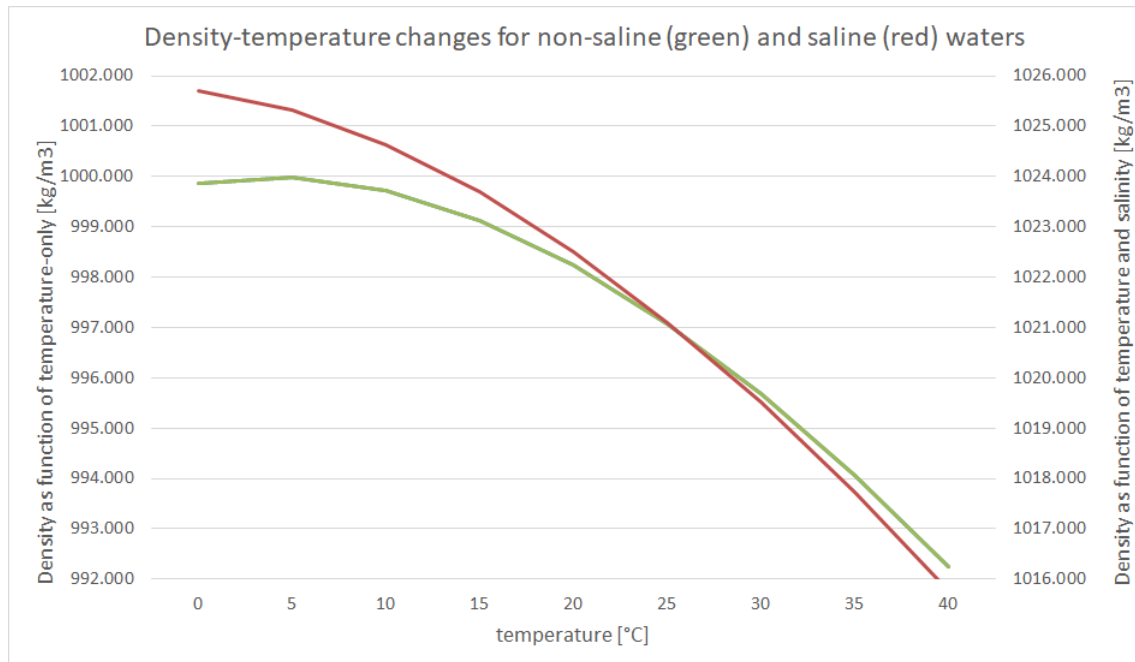


Figure 4.3: Changes in water density (y axis) with rise in temperature (x axis) based on the McCutcheon et al. (1993) represented by the green line and on the TEOS-10, with average water practical salinity chosen as 32, represented by the red line.

4.5 Results

In sections below, I discuss my results for the fully developed simulated plumes during the ebb tide on 17/03/2016 (Figure 4.4) and the flood tide on 08/12/2017 (Figure 4.5). Land in the figures is shaded by the dark grey colour with ambient water regions in blue colour. The plume is marked by the black solid line. The contour lines within the plume represent the temperature gradation. In order to compare the simulations of the surface plume to the observations, the simulation results were regridded onto observation grid (50 m × 50 m) by taking an average over all simulation points that fall into one observation grid. The simulated plume was defined as ambient temperature + 1.5 °C, to keep the criterion consistent between detected plumes in Landsat 8 observations and simulations. This criterion was first used for plume detection in the satellite imagery and was chosen in view of the uncertainty associated with the satellite instruments and the sea surface temperature retrieval method [Faulkner et al., 2019].

4.5.1 Simulations of thermal plume dispersion for ebb tide

Figure 4.4 presents horizontal cross sections of the simulated plume during ebb tide for: the water surface, -3.0 m, -5.0 m and -7.0 m depth contours. The plume is dispersing in the south-westward direction, which is consistent with the sea currents during ebb tide.

At the time of the observation, the tide was in the mid-ebb phase, which means that the tidal currents were the strongest and consistently moved in the same direction. The tidal current velocity estimated during the observation time was 0.65 m s^{-1} .

The simulated plume at the surface (Figure 4.4 top left) disperses as a narrow band of 2.2 km in length and approximately 0.3 km in width. The plume does not disperse much laterally in the ambient waters, which is indicated by the steep temperature gradients along the length of the plume. The area, over which the temperature is elevated over $5 \text{ }^{\circ}\text{C}$ higher than ambient, is spread south-westward up to 1 km away from the outfall pipes. The highest temperature noted in the simulation is $17.5 \text{ }^{\circ}\text{C}$, which is $7 \text{ }^{\circ}\text{C}$ higher than ambient, and is located within 0.3 km of the outfall pipes. There is a small circular area in the south-east part of the plume, where a slight temperature rise of $3 \text{ }^{\circ}\text{C}$ warmer than ambient is noted (Figure 4.4). Comparing the simulation results with the bathymetry map in Figure 4.1, the same circular feature can be observed. This circulation feature is not shown in the -3.0 m cross section. The plume thus follows the bathymetry and does not disperse into shallow-water regions.

The simulated plume is dispersing along the deep water channel and the extent of the plume at depth is limited by the bathymetry, which can be seen on the cross sections at -3.0 m (Figure 4.4 upper right), -5.0 m (Figure 4.4 lower left) and -7.0 m (Figure 4.4 lower right). There is a similar temperature distribution at -3.0 m depth 1.2 km away from the outfall pipes suggesting good vertical mixing within the water column. For -5.0 m depth, the plume area is limited to 0.4 km in length and located very close to the outfall pipes.

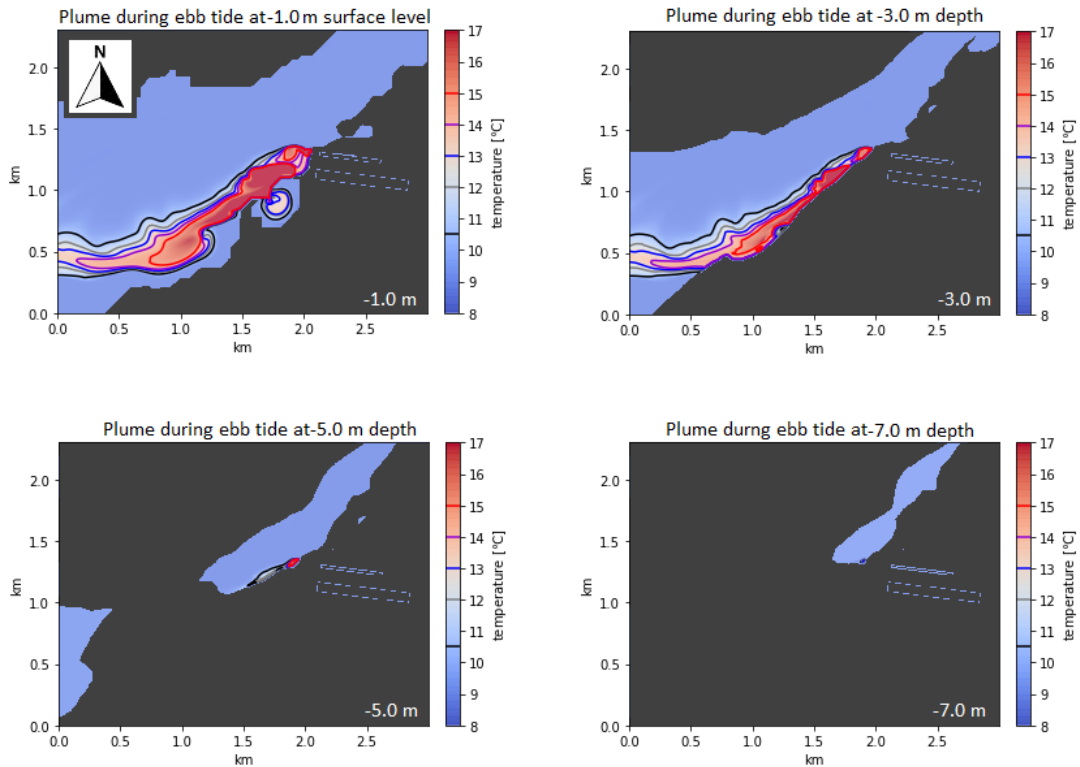


Figure 4.4: Horizontal cross sections of the simulated thermal plume during ebb tide at different depths. Land is marked in dark grey. The area of the plume is marked by the black line, with other coloured lines signifying different temperature contours within the plume. Higher temperatures are shown in red.

4.5.2 Simulations of thermal plume dispersion for flood tide

Figure 4.5 presents horizontal cross sections of the simulated plume during flood tide for: the water surface, -0.9 m, -3.7 m and -6.5 m depth contours. The depths are different to ebb tide due to the different vertical resolution. The plume is dispersing in the north-eastward direction, which is consistent with the sea currents related to flood tide phase. During the observation time, the tide was in the mid-flood phase, with the current velocity during the observation time being 0.8 m s^{-1} .

The plume observed at the surface (Figure 4.5 top left) disperses as a narrow band of 2 km in length and approximately 0.4 km in width. The plume is mixing well with the ambient waters with distance away from the source due to the strong currents, which can be observed by the temperature gradient within the plume with highest temperatures located close to the outfall pipes and plume temperature decreasing away from the outfall pipes. The area of highest temperature rise (over $5.5 \text{ }^\circ\text{C}$ higher than ambient) is limited to 0.4 km away from the outfall pipes. The highest temperature noted in the simulation results is $15.2 \text{ }^\circ\text{C}$, which is $9.6 \text{ }^\circ\text{C}$ higher than ambient. The temperature difference

between the ambient water and the plume in the simulation is higher than in the ebb case, which is related to higher outfall temperatures relative to the ambient waters recorded during 08/12/2017. The area with the highest temperature rise is limited to 0.1 km away from the outfall pipes.

The simulated plume is hugging the coastline and the extent of the plume is limited by the bathymetry in the shallow regions, which can be seen on the cross sections at -0.9 m (Figure 4.5 upper right), -3.7 m (Figure 4.5 lower left) and -6.5 m (Figure 4.5 lower right). The region of highest temperature rise is located close to the outfall pipes and its area decreases with depth, suggesting that the plume rises to the surface and spreads more at the surface. For -3.7 m and -6.5 m depth, the plume's area is limited to 1 km and 0.4 km in length respectively, with warmest temperatures not exceeding 4.4 °C from ambient water temperature.

The plume is well mixed and the plume temperatures further from the outfall pipes are lower. The mixing is caused by the strong north-eastward tidal currents. There is a small recirculation area, where the south-east part of the plume enters the Heysham harbour. The coolant water intake point is located in the harbour, so this could cause potential challenges with intake of warmer plume waters for cooling purposes. However, the part of the plume entering the harbour is very narrow and the temperature rise in the harbour is only 1.5 °C warmer than ambient, which is on the threshold of plume detection. At deeper levels, no plume recirculation into the Heysham harbour is present.

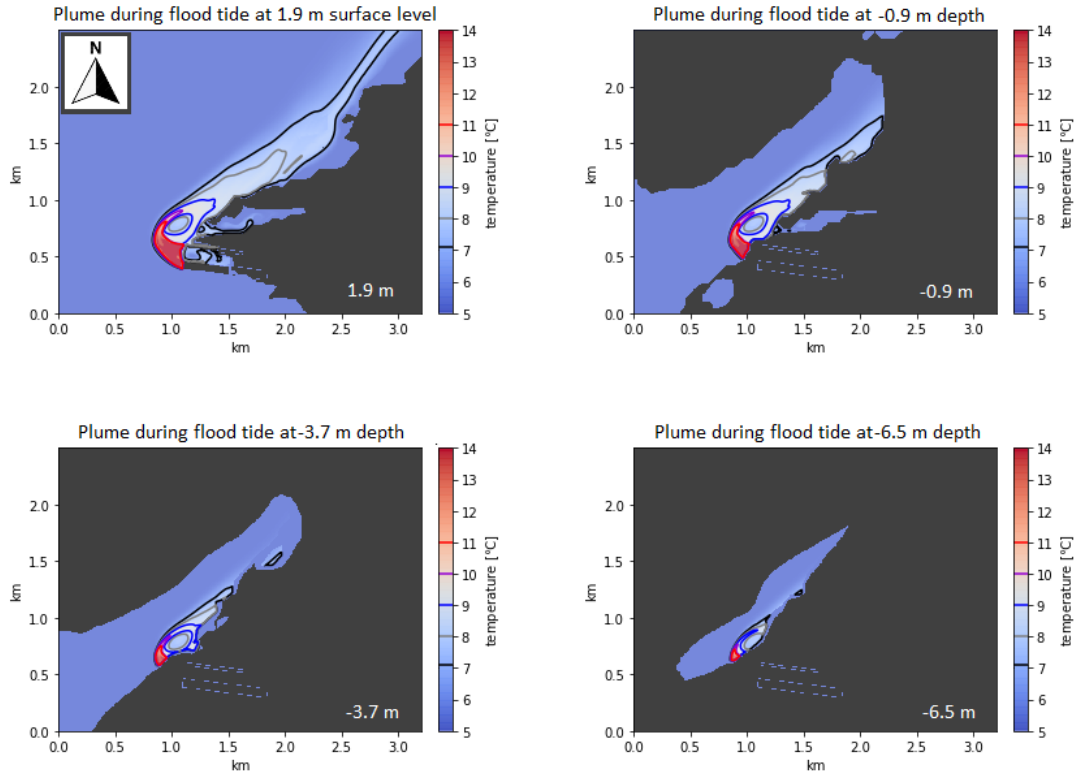


Figure 4.5: Horizontal cross sections of the simulated thermal plume during flood tide at different depths. Land is marked in dark grey. The area of the plume is marked by the black line, with other coloured lines signifying different temperature contours within the plume. Higher temperatures are shown in red.

4.5.3 Simulations with assumed maximum volume discharge

Power station operating capacity varies on a daily basis depending on the demand to the national grid. In order to control possible impact on the environment, each power station has laws describing the allowed maximum outfall rate and temperature difference from the ambient. Apart from simulating two scenarios for the ebb and the flood tide using observations and measurements carried out by the power station, I have also done simulations for the same days using maximum outfall specified by those regulations. Simulating worst case scenarios of highest volume flow rates or temperatures allow power station operators to characterise the thermal effluent and its impact on surrounding temperatures under critical conditions. I have chosen to run simulations for the maximum volume outfall and measured temperatures. This choice was based on observations provided by the Heysham power station, which included timeseries of measured volume outfalls and temperatures at outfall. Looking at the data, it could be concluded that volume outfall rates were inversely proportional to outfall temperatures (i.e. effluent at lower temperature was released at higher volume rate and effluent at higher temperature

was released at lower volume rate). Hence a scenario with both maximum outfall rates and maximum temperatures is improbable to happen in real life.

The simulation set up for the maximum volume outfall rates was similar to previous simulations, with only difference being the specified outfall rate at the end of the outfall pipes. First, a flow through the domain was established, identical to the flow in simulations for the 17/03/2016 (ebb tide) and 08/12/2017 (flood tide). Once the flow has reached steady state, the thermal plume was ejected from the ends of the outfall pipes at a maximum allowed discharge rate, which is $33 \text{ m}^3 \text{ s}^{-1}$ for one discharge channel and $49 \text{ m}^3 \text{ s}^{-1}$ for the other outfall pipe [Briggs and Taylor, 2008]. The temperature of the plume stayed the same as in previous simulations, related to the observed temperatures.

Figure 4.6 show cross sections of the plume observed during the ebb tide, in a scenario where the power station would be operating on full capacity, discharging thermal plume at highest possible outfall rate. Figure 4.7 shows a scenario where the plume is ejected at a maximum discharge during the flood tide. The contours within the plume symbolise different temperatures within the plume, and were unchanged from previous simulations to allow easier comparison between the observed scenario and the maximum discharge scenario.

The plume captured in Figure 4.6 is dispersing south-westward, same as the plume captured by the simulations with observed outfall rates on that day (Figure 4.4). The simulated plume is not more spread out laterally, but is stretching more in the direction of the sea currents. Plume's area of temperature above $15 \text{ }^\circ\text{C}$ is stretching over 1.8 km, which is further away from outfall pipes compared to the simulation with conditions on that day. Warmer parts of the plume spread away from the outfall pipes not only at the surface, but also at depth, which is visible in the top right and bottom left panels in Figure 4.6. There is a circular feature visible at the surface, which disappears in the cross section at -3.0 m depth. The plume thus follows the bathymetry and does not disperse into shallow-water regions. The temperatures within the plume are slightly higher in the maximum discharge scenario, on average $1 \text{ }^\circ\text{C}$ across the plume. This suggests that higher continuous discharges of warmer water, hinder the plume cooling through mixing with ambient waters.

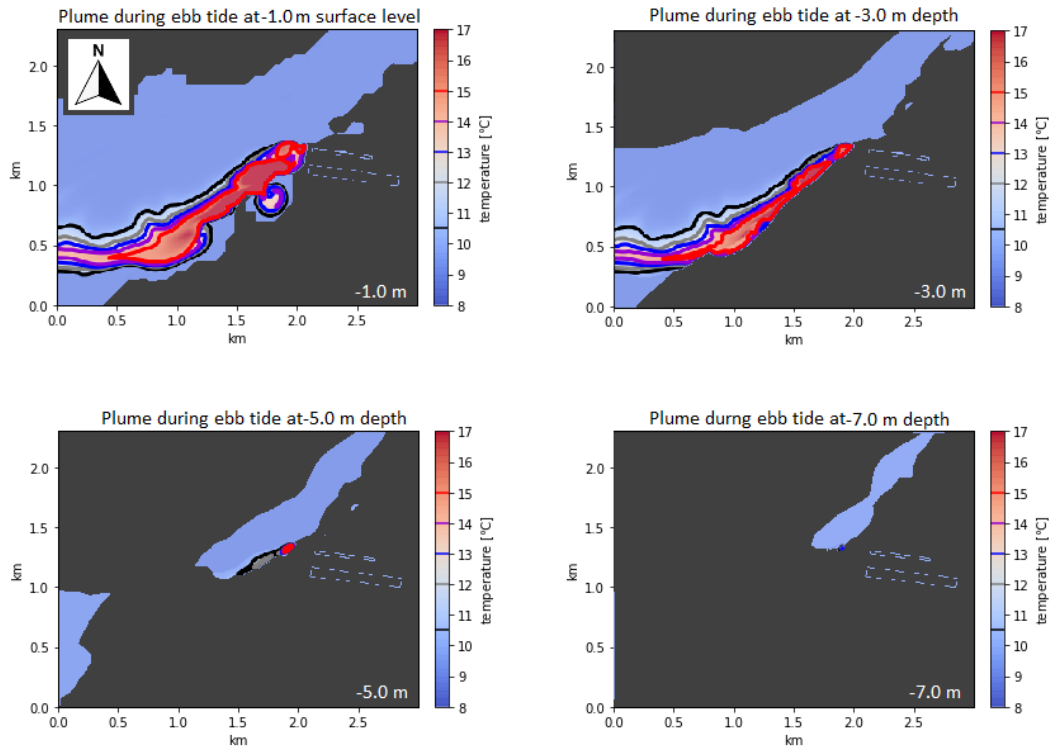


Figure 4.6: Horizontal cross sections of the simulated thermal plume during ebb tide for maximum volume outfall at different depths. Land is marked in dark grey, while water in blue colours. Plume’s area is marked by the black line, with other coloured lines signifying different temperature regions within the plume. Higher temperatures are in light and dark red.

The plume captured in Figure 4.7 is dispersing north-eastward, same as the plume captured by the simulations with observed outfall rates on that day (Figure 4.5). The simulated plume is more elongated, stretching more in the direction of the sea currents. Looking at the temperatures within the plume, areas with temperature rise $2.4\text{ }^{\circ}\text{C}$ and $3.4\text{ }^{\circ}\text{C}$ spread further away from outfall pipes compared to the simulation with prescribed outfall rates from that day. Looking at the top left panel in Figure 4.7, it can be noticed that there is a small circular area, where the south-east part of the plume enters the Heysham harbour introducing waters $2.5\text{ }^{\circ}\text{C}$ higher than ambient. However, the area of the highest temperature rise ($11\text{ }^{\circ}\text{C}$ and warmer) is limited close to the discharge pipes, similar to the simulation with observed outfall rates. Simulated plume spreads further away from the outfall pipes not only at the surface, but also at depth, which is visible in the top right and bottom left panels in Figure 4.7. The temperatures within the plume are slightly higher in the maximum discharge scenario, on average $1\text{ }^{\circ}\text{C}$ across the plume.

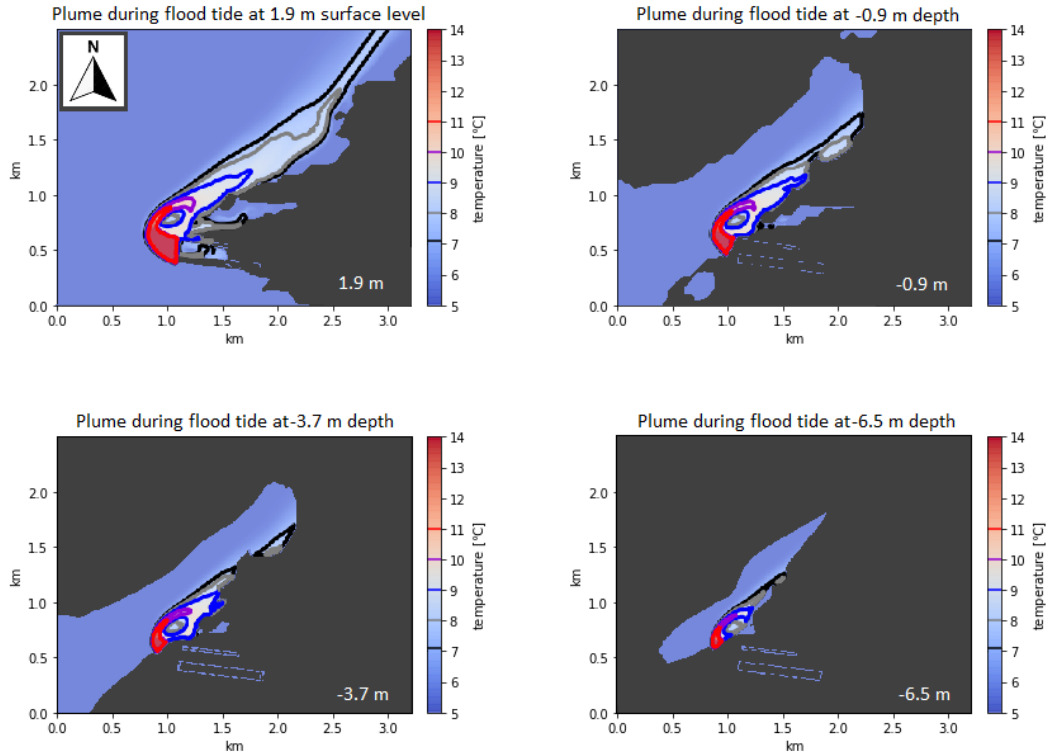


Figure 4.7: Horizontal cross sections of the simulated thermal plume during ebb tide for maximum volume outfall at different depths. Land is marked in dark grey, while water in blue colours. Plume's area is marked by the black line, with other coloured lines signifying different temperature regions within the plume. Higher temperatures are in light and dark red.

4.5.4 Comparing surface SST distribution from simulations with satellite observations

In order to assess the simulations, we compared the simulated surface thermal plume with the corresponding Landsat 8 observations for ebb (Figure 4.8) and flood (Figure 4.9) tides. The exposed sand banks are marked in light brown and the land in dark green with the power station as a red square. For both ebb and flood tide, there is good agreement between the observations and simulations in the direction of the plume dispersion (see Table 4.1), suggesting that the plume is embedded in the tidal currents. The temperature distribution within the plume is similar between the observations and the simulations. However, the absolute temperature values are higher in the simulations than the observations, suggesting that the temperatures overestimate the temperature (see Table 4.1).

For the ebb tide (Figure 4.8), the difference in the plume area between the simulations and observations is greater than for the flood tide (Figure 4.9). The observed plume is more laterally dispersed in the observations, having approximate width of 0.9 km. The

simulated plume is narrower with warmer temperatures highly concentrated over an area approximately 0.3 km wide. The area of highest temperature rise (≥ 15 °C) is similar in both observations and simulations, however, the maximum temperature values are higher in the simulations by 2.3 °C compared to the observed maximum of 15.2 °C. The simulated plume is constrained by the bathymetry and the location of the coastline, however, it turns westward further away from the outfall pipes, which is not observed in the satellite image. The plume turning away from the bathymetry further south is not caused by boundary effects, since the currents were prescribed only at two boundaries. However, the flow development in the simulation is limited to the area filled with water, which is represented by a channel widening to the west (see Figure 4.4 top left), and the velocity vectors redirect towards the west from their prescribed south-westward flow.

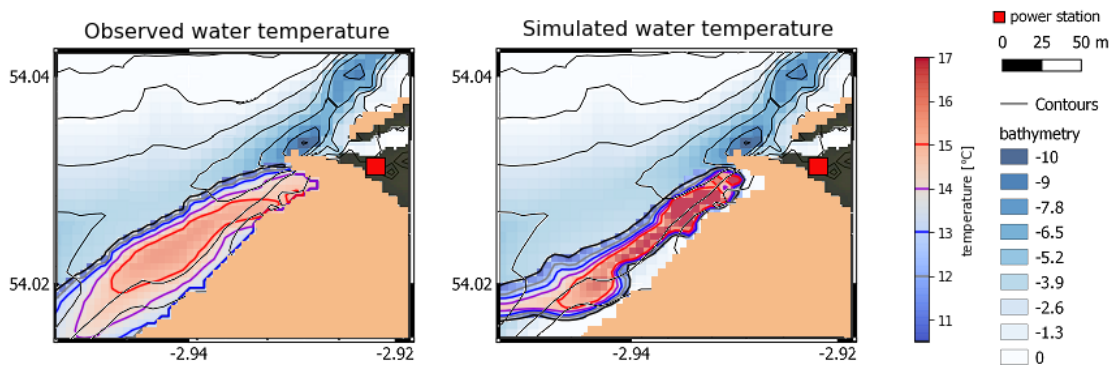


Figure 4.8: Observed (left) and simulated (right) surface plume during mid-ebb tide for Heysham. The exposed sand banks are represented by the light brown colour and land by the dark green with the power station marked as a red square. Bathymetry is marked in thin black lines. The plume's temperature contours are thick lines marked also on the colour bar.

Looking at the thermal plume direction for the flood tide (Figure 4.9), the simulations and observations are in good agreement. The plume is dispersing as a narrow band north-eastward, reaching over 2 km in length. The simulated plume is narrower than the observed plume and the difference is greatest further away from the outfall pipes. A possible explanation is that at the time of the satellite overpass the wind was blowing north-westward at 8.5 m s^{-1} , and the influence of wind stress was not included in the simulations. The temperature distribution within the simulated surface plume resembles the one of the observed plume, with highest temperatures located close to the outfall pipes (0.3 km away from the outfall pipes in the observations and 0.2 km in the simulations). The highest temperature in the observed plume is 13.0 °C, while in the simulations the maximum temperature within the plume is 15.2 °C. The highest temperature region is

limited in area and further away from the source the surface plume the temperatures are cooler, which is caused by stronger tidal currents.

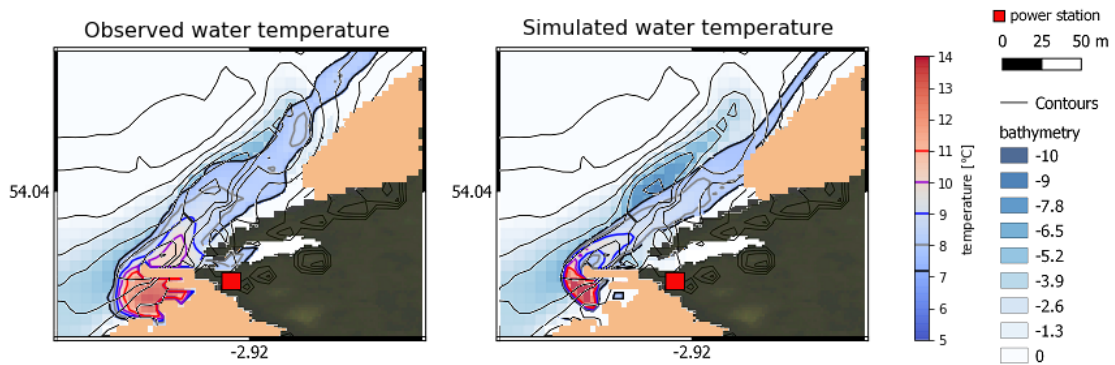


Figure 4.9: Observed (left) and simulated (right) surface plume during mid-flood tide for Heysham. The exposed sand banks are represented by the light brown colour and land by the dark green with the power station marked as a red square. Bathymetry is marked in thin black lines. The plume's temperature contours are thick lines marked also on the colour bar.

Table 4.1: Summary of plume characteristics from the ebb time and flood tide simulations

	max temperature of the plume	max temperature difference from ambient	plume direction	plume width	plume length
08/12/2017 simulated	15.2 °C	9.6 °C	north eastward	0.4 km	2 km
08/12/2017 observed	13.0 °C	7.4 °C	north eastward	0.6 km	2 km
17/03/2016 simulated	17.5 °C	7.0 °C	south westward	0.3 km	2.2 km
17/03/2016 observed	15.2 °C	4.7 °C	south westward	0.9 km	2.2 km

In order to compare the surface plume between the simulations and the observations we have used skill scores. Skill scores are a common measure used to measure the degree of accordance between the observations and the prediction, usually achieved through a model or simulation. Skill scores used in this chapter are: Hit Rate, which indicates % of simulated plume agreeing with the observed plume, False Alarm Rate, which indicates % of simulated plume falling outside of the observed plume, and Misses, which show % of observed plume, which is absent in the simulations. All skill scores are summarised in Table 2.

In case of the ebb tide (Figure 4.10 a), the simulated plume area is located almost completely within the observed plume area, with 13% of the simulated plume not coincident with the observed plume. However, the simulated plume area is almost two times narrower, resulting in 55% of the observed plume lying outside the simulated. For the flood tide (Figure 4.10 b), the simulated plume is dispersing slightly closer to the coast than the observed plume, with 19% of the simulated plume not consistent with the observed plume. As in the previous case, the simulated plume has a smaller area, resulting

in 54% of the simulated and observed plume being in agreement and 46% of the observed plume being missed in the simulations.

The simulations capture the direction of the plume dispersion, but underestimate the areal extent at the surface (Figure 4.10). Because the plume is ejected to an already steady state flow, it will continue dispersing in the same direction. In reality, the plume is dispersing constantly into a changing tidal environment and during transition phases it is forced away from the coast and disperses horizontally. It is possible that due to the history of the plume over time, the plume will be more spread out at the surface in observations than in the simulations, which assume only equilibrium state.

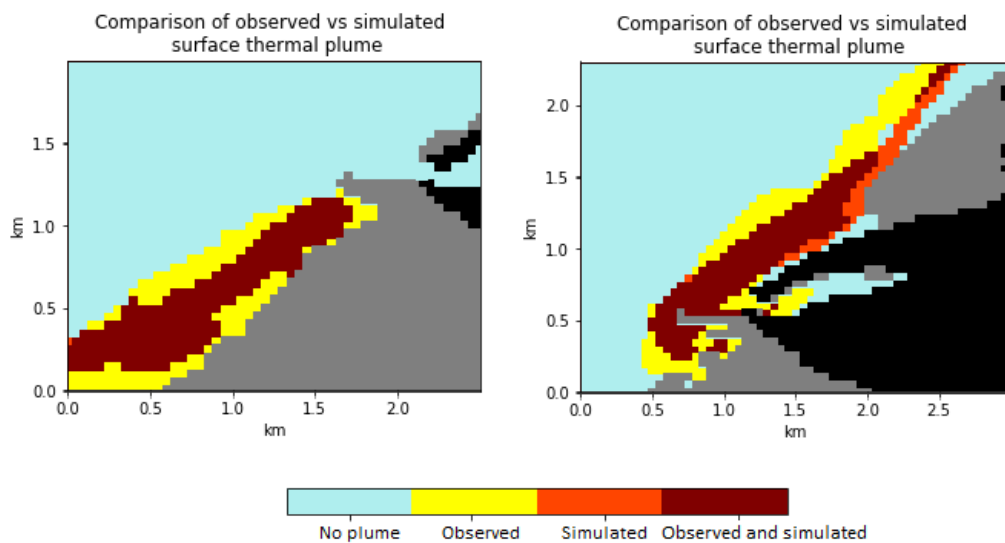


Figure 4.10: Simulated (marked in red) and observed (marked in yellow) thermal plume dispersing during mid-ebb tide (left panel) and mid-flood (right panel) for Heysham. The exposed sand banks are represented by the dark grey colour and land by the black colour. The common area, where the plume appears in the observations and the simulations is marked in dark brown.

Table 4.2: Summary of skill scores for the chosen ebb tide and flood tide days

	Hit Rate	False Alarm Rate	Misses
08/12/2017	54 %	19 %	46 %
17/03/2016	45 %	13 %	55 %

4.6 Discussion

Our choice of simulation mesh size permits most bathymetry features to be resolved, especially in the deeper regions. Discrepancies between the actual seabed and the simulated seabed will only occur in the very shallow regions, where the depth difference across

an area is smaller than 1.4 m. The simulated geometry of the domain will influence the flow development, for which velocity vector directions and strengths are prescribed at boundary as prior. This can be seen during the simulated ebb tide, when the water is diverging slightly westward in further parts of the plume, however, the main axis across the most part of the plume in both cases is within a few degrees. This shows that for the complicated bathymetry, like Heysham, the simulations are able to capture most seabed features and simulate the flow sensibly.

Idealised simulations do not fully reproduce the actual conditions on the observed day. The plume and ambient temperature are based on density difference rather than actual observed values. Conversion between the temperature and density was possible due to FLOW-3D density evaluation, in which density is a function of temperature only. However, as shown in the Methods Section, the relationship between density and temperature is not linear. This means that the observed density difference will correspond to a different range of simulated temperatures during the simulation time. Moreover, the simulated densities were calculated for non-saline waters, which impacts the buoyancy and the efficiency of the plume mixing. In presented simulations the density difference is lower than for saline waters, resulting in smaller buoyant forces and lower rate of mixing.

Table 4.3 below summarises the conditions for both days, for which the simulations were carried out. For the ebb tide simulation (17/03/2016) the ambient water temperature was 10.5 °C, the average temperature rise within the plume was 15.5 °C, the air temperature was 7.0 °C and the wind speed measured closest to the satellite overpass was 1.0 m s⁻¹. For the flood tide observations the ambient water temperature was 5.6 °C, the area of significant temperature rise within the plume was 11.1 °C, the air temperature was 3.0 °C and the wind speed measured closest to the satellite overpass was 8.5 m s⁻¹.

Table 4.3: Summary of conditions for the chosen ebb tide and flood tide days

	air temperature	ambient water temperature	average temperature across the plume	wind at 10 m
08/12/2017	3.0 °C	5.6 °C	11.1 °C	8.5 m s ⁻¹
17/03/2016	7.0 °C	10.5 °C	15.5 °C	1.0 m s ⁻¹

In order to investigate the differences in the plume's temperature between the simulations and the observations, I looked into heat transport within the water body and the heat exchange between the water and the air. A limitation of the simulations is that heat transfer is occurring between the ambient waters and the discharged plume through turbulent diffusion and advection of the plume. The simulations do not include air-sea heat exchange, since they are performed for a single fluid (i.e. water) and hence surface heat loss is not captured. Surface heat loss between the water and the atmosphere occurs through radiative heat fluxes, latent heat fluxes and sensible heat fluxes, none of which are included in the simulations. I looked into the rate of heat loss associated with each of those fluxes and calculated the excess rate of heat loss associated only with the thermal plume. I calculated the excess fluxes to assess the effect the injection of the thermal plume has on the surface heat loss compared to a scenario including only ambient water and no thermal effluent.

The radiative heat flux is related to the body's temperature and can be parametrised as:

$$Q_R = \varepsilon_s \sigma T_s^4 - \varepsilon_a \sigma T_a^4 \quad (4.18)$$

where ε_s is the emissivity of the water surface (we used the value of 0.97), T_s is the sea surface temperature, ε_a is the broadband effective emissivity of the atmosphere assumed to be 0.75 after [Vallis \[2012\]](#), T_a is the pressure-weighted average atmosphere temperature and σ is the Stefan-Boltzman constant.

In order to calculate the excess radiative heat flux, I modified the above equation to get the difference between the radiative flux over the plume and the radiative flux over ambient water:

$$Q_{R'} = (\varepsilon_s \sigma T_p^4 - \varepsilon_a \sigma T_a^4) - (\varepsilon_s \sigma T_w^4 - \varepsilon_a \sigma T_a^4) \quad (4.19)$$

which yields:

$$Q_{R'} = \varepsilon_s \sigma T_p^4 - \varepsilon_s \sigma T_w^4 \quad (4.20)$$

where $Q_{R'}$ is the excess radiative heat flux caused by the presence of the thermal plume, T_p is the average temperature across the plume and T_w is the ambient water temperature.

We looked into the rate of heat loss associated with each of the heat fluxes and calculated the excess rate of heat loss associated only with the thermal plume. We calculated the excess fluxes to assess the effect the injection of the thermal plume has on the surface heat loss compared to a scenario including only ambient waters present. Understanding how long it would take the system to go back to equilibrium, after being distorted by the

additional heat injection in the form of a thermal plume, is essential to assess whether there will be some remaining thermal plume still dispersing from previous tidal phase once the tidal currents start changing direction. In such a scenario the plume would be more spread out by the changing tidal currents. For this purpose, the background air-sea interactions are not the main focus, but the time it would take to put the system back into equilibrium after injecting warmer waters.

The excess radiative heat flux caused by the excess heat from the thermal plume for the ebb tide on 17/03/2016 was 25.51 W m^{-2} . The excess radiative heat flux value calculated for the flood tide on 08/12/2017 was 26.71 W m^{-2} .

I also calculated sensible and latent heat fluxes, which describe the energy being released from the Earth's surface and absorbed in the atmosphere. Sensible heat flux is related to changes in temperature by heating an object directly, while latent heat flux is related to changes in phase associated in this case with evaporation. Sensible heat flux, Q_S , is dependent on wind speed and temperature [*Marshall and Plumb, 2008*] as:

$$Q_S = \rho c_p c_s U_{10}(T_s - T_a) \quad (4.21)$$

where c_s is the stability dependent bulk transfer coefficient, U_{10} is the wind at 10 m height, T_s is the SST and T_a is the temperature of the air at 10 m height. For c_p I used $1004.83 \text{ J kg}^{-1} \text{ K}^{-1}$. For c_s I used a typical value of 0.00175 after *McPhee [2008]*.

In order to calculate the excess sensible heat flux, I modified the above equation to:

$$Q_{S'} = (\rho c_p c_s U_{10}(T_p - T_a)) - (\rho c_p c_s U_{10}(T_w - T_a)) \quad (4.22)$$

which yields:

$$Q_{S'} = \rho c_p c_s U_{10}(T_p - T_w) \quad (4.23)$$

where $Q_{S'}$ is the excess sensible heat flux caused by the presence of the thermal plume, T_p is the average temperature across the plume and T_w is the ambient water temperature.

The calculated excess sensible heat flux for the ebb tide was 10.86 W m^{-2} . For the flood tide the excess sensible heat flux was higher (112.72 W m^{-2}), which is related to much stronger winds recorded during that time (see Table 4.3).

Latent heat flux, Q_E , is related to wind fluxes and differences in specific humidity,

using bulk aerodynamic parametrisation, as:

$$Q_E = -l \rho C_E U_{10}(\bar{q}_a - \bar{q}_s) \quad (4.24)$$

where C_E is the bulk transfer coefficient for water vapour, U_{10} is the wind speed at 10m, q_a is the near surface air-specific humidity, q_s is the air-specific humidity just at the air-ocean interference.

In order to calculate the excess latent heat flux, I modified the above equation to:

$$Q_{E'} = (-l \rho C_E U_{10}(\bar{q}_a - \bar{q}_w)) - (-l \rho C_E U_{10}(\bar{q}_a - \bar{q}_p)) \quad (4.25)$$

which yields:

$$Q_{E'} = -l \rho C_E U_{10}(\bar{q}_p - \bar{q}_w) \quad (4.26)$$

where $Q_{S'}$ is the excess sensible flux caused by the presence of the thermal plume, q_p is the air-specific humidity across the plume and q_w is the air-specific humidity over ambient water.

For the ebb tide the excess latent heat flux was 33.67 W m^{-2} . For the flood tide the excess latent heat flux was 118.18 W m^{-2} . Higher values of the excess latent heat flux for 08/12/2017 compared to 17/03/2016 are, like in the case of sensible heat flux, related to much stronger winds observed on that day (see Table 4.3).

Next, I looked into the excess rate of cooling related to the presence of the thermal plumes. I related the net rate of heating out of the water column to the rate of change of heat content by:

$$F \times A = (\rho A h) c_p \frac{\partial T}{\partial t} \quad (4.27)$$

where F is the sum of the fluxes out of the water column, A is the area, ρ is the density of water, h is the height of the water column, c_p is the specific heat capacity of water, $\frac{\partial T}{\partial t}$ is the temperature change with time. After rearranging, the above equation yields:

$$\frac{\partial T}{\partial t} = \frac{F}{\rho h c_p} \quad (4.28)$$

I used $4184 \text{ J kg}^{-1} \text{ K}^{-1}$ as specific heat capacity of water and assumed an average depth of 5 m. The sum of excess heat fluxes for the ebb tide on the 17/03/2016 was 70.04 W m^{-2} , leading to the excess cooling associated with the plume for the ebb tide being equal to $3.35 \times 10^{-6} \text{ K s}^{-1}$. For the flood tide on the 08/12/2017 this was 257.61 W

m^{-2} , which translated into an excess cooling of $1.23 \times 10^{-5} \text{ K s}^{-1}$. Over the period of 3 hours, during which the tidal currents are flowing steadily in the same direction, the excess cooling caused by the thermal plume is 0.04 K and 0.13 K for the ebb tide and the flood tide respectively. The simulation domain is of small aerial size and the calculated heat fluxes are of a low order of magnitude (see Table 4.4), hence not including the heat fluxes in the simulation will not impact the results substantially.

Table 4.4: Summary of excess surface heat fluxes for the simulated ebb and flood tides caused by the thermal plume

	radiative heat flux	sensible heat flux	latent heat flux	summed fluxes	rate of cooling
08/12/2017	$26.71 \text{ W m}^{-2} \text{ }^\circ\text{C}$	112.72 W m^{-2}	118.18 W m^{-2}	256.61 W m^{-2}	$1.23 \times 10^{-5} \text{ K s}^{-1}$
17/03/2016	$25.51 \text{ W m}^{-2} \text{ }^\circ\text{C}$	10.86 W m^{-2}	33.67 W m^{-2}	70.04 W m^{-2}	$3.35 \times 10^{-6} \text{ K s}^{-1}$

My simulation set up works well for domains, where the driving factor for heat dispersion are the sea currents. The effect of air-sea heat exchange for a small and shallow domain plays a much smaller role compared to diffusivity of the plume within the ambient water and therefore can be neglected. The simulations capture the plume evolution and dispersion in the ambient waters well and provide information on the vertical structure of the temperature and plumes impact on the seabed temperatures. Such analysis is useful for environmental monitoring the plume.

In the future, setting up a simulation with varying tidal and sea currents conditions would be an improvement. In reality the plume is ejected constantly into a changing environment and capturing the history of the plume over a changing tidal cycle would be more sophisticated. However, for operational characterising purposes, the simplified simulation is a good approximation.

4.7 Conclusions

I have simulated the dispersion of the thermal plume at Heysham for two predominant, reoccurring scenarios: flood and ebb tide. In order to validate the simulation outputs, I have used Landsat 8 thermal imagery and sea currents reanalysis dataset from Norwegian Meteorological Institute. The simulations were run separately for each tidal scenario. The main driver of the heat dispersion were the sea currents, with the air-sea heat exchange playing a minor role. Simulations of thermal plume ejection into the coastal environment, validated by high-resolution observations, can be used as a good approximation for plume characterisation.

The simulations provide knowledge on plume development from the start of the

operation until the simulation reaches steady state for each tide type. This includes specifying the main direction of the plume dispersion under different tidal conditions and possible extent of the plume. Performing simulations in 3-D provides information on subsurface dispersion and the 3-D nature of the plume. Such information can be used in understanding possible ecological impacts on the close-to-coast and benthic regions, and ensuring environmental requirements are met.

For small domains, like Heysham, idealised simulations driven by the tidal currents present a sensible solution compared to single-day field surveys. An advantage of simulations of thermal plumes over field campaigns is that the simulations enable investigating multiple scenarios for plume dispersion. Simplified simulations are a cost-effective way of understanding plume behaviour during different outfall rates and varying tidal conditions. A one day boat survey is only able to capture the plume only during specific atmospheric and hydrologic conditions and thermal plume outfall rates.

Lastly, simulations open a possibility of exploring scenarios with highest permitted outfall temperatures and volume outfall rates without the need for those worst case scenarios to occur in real life. Setting up simulations for maximum flow rates during different tidal conditions is useful in assessing areas at risk of being influenced by the thermal plume and explore potential ecological impacts on neighbouring sensitive habitats. Understanding possible impacts of the thermal stress on the temperature sensitive aquatic ecosystems in the vicinity of the power station is important from an environmental and sustainability point of view, to ensure the operation of the power station does not have a negative impact on the biodiversity.

Chapter 5:

Comparing remotely sensed observations to traditional field campaigns

5.1 Statement of publication status

Part of the material in this chapter, together with the material in Chapter 4, has been accepted for publication in *Environmental Research Communications* on the 22 March 2021. I am the lead author of the manuscript. All figures were generated by me and I led and finalised the conceptualisation and scientific writing. I take full responsibility for the results. Other authors listed on this publication helped in discussions of the methods and provided feedback on the results. The provisional reference for the manuscript is as follows:

Faulkner, A., Bulgin, C. E., Merchant, C. J. (2021). Characterising industrial thermal plumes in coastal regions using 3-D numerical simulations. *Environmental Research Communications*

The content of this chapter differs from the published article in the following ways:

- For consistency with the thesis structure, the numbers of the section headings equations and figures are updated and minor format changes are applied;
- The word "paper" has been substituted to "chapter" to keep consistency with thesis structure;
- Only the text and figures considering the seasonality for the Heysham Power station have been included within the published results and the discussion;
- The remaining parts of this chapter have not been used as part of any publication.

5.2 Introduction

Traditionally, thermal plumes are characterised through field campaigns. Those usually consist of a boat survey and are carried out over a short period of time. The cost related to carrying out a field survey is a limiting factor in duration and repetitiveness of boat surveys. Therefore exploring new potential ways of characterising thermal plumes is of high value to existing power stations directors. Investigating thermal plumes using satellite observations and 3-D numerical simulations, compared to traditional methods, can provide new insight into plume characteristics through better spatial and temporal coverage. This allows for characterisation of the plume behaviour during the different conditions and indication of the area of thermal contrast. This chapter focuses on comparing traditional methods of characterising thermal plumes through field campaigns to high resolution satellite observations, presented in Chapter 3, and addressing gaps in knowledge with 3-D simulations, presented in Chapter 4. Understanding the distribution of thermal plumes is essential for identifying any potential ecological impacts and supporting sustainable coastal zone management, which is discussed in Sections 5.3.1.1 and 5.3.2.2.

5.3 Traditional ways of monitoring thermal plumes

Traditionally, after putting a power plant into operation, EDF Energy has been launching field campaigns in order to characterise the plume and investigate potential thermal impacts on the environment. The field campaign is organised as a boat survey and uses multiple profiling instruments to provide a detailed environmental survey. An experienced team of 2 - 3 people conducts multiple measurements and observations to characterise the temperature distribution in the vicinity of the power station as accurately as possible.

Field measurements are only conducted in good weather conditions, therefore most of the profiling campaigns happen during the summer season (June, July, August). Moreover, field campaigns are not carried out regularly but rather once for each power station. Carrying out a field campaign is expensive since the cost includes the hire of the boat and staff carrying out the field survey, transportation of the boat, mooring fees, acquiring and processing of the data. Each campaign costs at least £4000 - 5000 per day and the price is the factor limiting the duration and repetitiveness of the measurements. The measurements are usually undertaken during one day for the neap tide (when the differ-

ence between the ebb and flood tides is small) and one day for the spring tide (when the difference between the ebb and the flood tide is large). On rare occasions the campaign might be suspended after installing the instruments and postponed to a later date [*Briggs and Taylor, 2008*] until the weather conditions improve. This generates new expenses.

Once the campaign is set up, conductivity and temperature profilers are deployed in the vicinity of power station in various points away from the outfall pipes. Temperature and salinity measurements are collected by the profilers at different depths. In order to trigger data output, the profilers need to be submersed in the water and during the boat survey the vertical measurements are obtained at a regular 0.2 m depth interval. Conducting the temperature measurements through different depths builds a 3-D understanding of the thermal plume released from the outfall pipes. Sea currents are measured by an acoustic doppler current profiler every 5 seconds. It provides information on the direction and speed of the sea currents.

The network of measurements provides understanding of the behaviour of the thermal plume. Combining horizontal and vertical profiling gives an impression of how the plume is behaving with depth and the three dimensionality of the plume can be inferred. The data collected during a field campaign is then combined with the knowledge on special areas of conservation and commercially-sensitive species to create an in-depth report on a specific power plant and highlight possible areas of thermal stress for various aquatic species.

However, there are a few challenges with characterising thermal plumes through boat surveys. Because of the limited duration of a field campaign, the measurements capture one ebb and one flood tide for the spring and the neap tide. Having one set of measurements for each type of tide is more representative of the weakest currents (neap tide) and strongest currents (spring tide). Taking measurements over the whole day does not allow the boat survey to capture the instantaneous snapshot of the SST distribution during e.g. mid-ebb tide as the current strength and direction, which influences plume location, will be changing throughout the day. The plume behaviour captured during those tide phases is then extrapolated and it is assumed that the plume behaves similarly throughout the whole year.

Another possible issue is the uneven distribution of the sample of profiles, with more profilers concentrated in the vicinity of the power station and their density decreasing with distance away from the outfall pipes. Sparse distribution of the profilers increases the inaccuracy in plume characterisation, since the data is interpolated between the points.

In the region with fewer profilers some information on the plume extent is lost. Field campaigns are carried out in places deep enough for the survey vessel to move freely. This means that in areas close to the coast which are less than 0.5 m deep and sandbanks during low tide the boat with the profilers is not able to take any measurements. Lack of measurements in shallow regions close to the coast limits gaining full understanding of the plume extent.

5.4 Characterising thermal plume through satellite imagery

An alternative way to characterising thermal plumes, presented in this PhD thesis, is using high resolution remote sensing data to detect and characterise industrial thermal plumes. Imagery from Landsat 8 or ASTER is freely available through portals like USGS, generating no cost of acquiring data. Clear-sky satellite data at resolution 30 - 100 m collected over the observational lifetime of the satellite gives new insights into thermal plume characteristics by providing snapshots in time of the temperature distribution in the vicinity of the power station. Full details on satellite observations of thermal plumes are in Chapters 2 and 3.

Due to the large domain of each image, a single snapshot of clear-sky remotely sensed data provides information on the dynamic land-water boundary and surface temperature distribution over the whole region of interest during the same moment in time. This is crucial to understand the plume behaviour under certain conditions. The advantage of choosing remotely sensed information is that there is no change of tide or current between the points due to possible time delay like in case of point probing. With a long satellite record, remote sensing imagery provides information on plume behaviour during multiple tidal phases and varying sea currents, which enables observing plume evolution at different stages of a tidal cycle, i.e. high slack water, ebb tide, mid-ebb tide, low slack water, flood tide, mid-flood tide. Having a snapshot in time for each stage of the tidal cycle provides information on the tidal impact on the ejected thermal effluent.

5.5 Comparing thermal plumes characterised through traditional field campaigns and remote sensing of thermal plumes

In the section below, I compare results of thermal plume characteristics obtained through a field campaign and satellite observations. During this PhD project, I had access to results of two field surveys carried out in 2007 for Hunterston power station [Briggs, 2008] and Heysham power station [Briggs and Taylor, 2008]. The figures relating to the field surveys presented in the following sections are taken from the Heysham and Hunterston field reports, which I had access to. I did not have access to raw data so I was not able to process the data myself. This section provides a concise summary of the advantages and the disadvantages of the field campaigns and remote sensing observations as methods of thermal plume characterisation. Sections 5.3.1 and 5.3.2 present a comparison of the results for two EDF Energy power stations: Hunterston and Heysham.

Boat surveys provide a 3-D description of the thermal plume on the campaign day (see Tab. 5.1). The survey takes measurements over the course of > 10 hours per day, while it takes ~ 6 hours for the tide to change from high water to low water. The thermal plume is constantly changing, depending on power station volume outfall rates and the phase of tide, very often being embedded in the sea currents, which change their strength and direction throughout the day. This might not have a significant impact between measurements located close to each other, but it will affect the measurements in points located further away from each other and over the whole plume. Therefore field surveys are not an ideal way of monitoring, but rather characterising the thermal plume.

Remotely sensed observations are able to provide multiple observations over the course of satellite life span, which are collected all year round (see Table 5.1). Information on the sea surface temperature distribution collected over different seasons and tidal cycles provides better grounds for characterising thermal plumes compared to a single temperature field. However, satellite observations capture thermal plumes in 2-D and are not able to provide information on temperature distribution subsurface or closest to the seabed (see Table 5.1).

Table 5.1: Comparison of satellite observations and field campaigns to characterise thermal plumes.

	Satellite observations	Field campaigns
cost	freely available data	£ 4000 - 5000 per day
domain size	20 km × 20 km (or larger if necessary)	4 km × 4 km
spatial resolution (horizontal)	50 m	100 m - 300 m
spatial resolution (vertical)	no at-depth observations	0.2 m
repeatability	observation return time of 16 days (for Landsat 8)	no repetition of the field campaign
seasonality	collecting observations over the whole year	only in the summer months
constraints	quality observations constrained by the cloud cover	measurements carried out only during fair weather

5.5.1 Hunterston power station

Hunterston field survey has been carried out on two days: 14 September 2007 and 19 September 2007 to approximately represent the spring tide neap tide respectively. Spring tide is a period of strong tides, when flood tide results in slightly higher water than average and slightly lower water during ebb tide. Neap tide is a period of moderate tides, where the difference between flood and ebb water levels is smaller. During the field survey the station was running at around 60 % of their capacity with all four cooling pumps continuously discharging the water at the outfall volume outfall rate of $25.8 \text{ m}^3 \text{ s}^{-1}$ [Briggs, 2008]. The field survey consisted of three sets of measurements: horizontal mapping of the water temperature at 0.5 m below the surface, profiling in various points of the vertical cross section of the water column and fixed logger measurements.

The horizontal mapping of the plume was obtained through combining four separate field surveys conducted on the same day, which mapped different regions horizontally using a Vale-port MIDAS CTD drop probe. Each horizontal survey consisted of measurements of water temperature at 0.5 m depth along predefined horizontal lines. Distance between the measurement points was increasing with distance away from the outfall pipes. The ambient water was decided as the lowest temperature recorded during horizontal mapping during each of the four surveys. Any water $\geq 0.5 \text{ }^\circ\text{C}$ warmer than ambient was classed as thermal plume. Since the horizontal mapping occurred over the course of one day, it captured both ebb and flood tides, which is mirrored by the detected plume dispersing in

the south and the north direction.

Figure 5.1 shows the surface thermal plume during spring and neap tide captured by the boat survey. During the neap tide survey the plume formed a band stretching 3.2 km north-east and 2.2 km south-west off the discharge pipe. The plume was stretching between the Cumbrae Islands and the mainland. At its widest point (1.6 km) the plume does not reach the two islands and extends towards the rest of the channel. However, the southern part of the plume was stretched over the cooling water intake point and the field survey suggested possible recirculation of the thermal plume back as intake cooling water [Briggs, 2008]. During the spring tide the plume stretched similarly to the neap tide, however this time it formed a narrower band (1 km at its widest point) staying closer to the mainland coastline. The highest temperature gain measured at all points over the whole period of surveying during the spring tide was 8.0 °C, with the maximum temperature within the plume being 21.3 °C. During the neap tide survey the highest temperature gain across the plume was 5.5 °C, with the maximum temperature in that point being 19.9 °C. The surface spatial extent of the thermal plume was smaller during the spring tide and more spread out during the neap tide. This suggests that the plume during the neap tide was cooler as it was losing heat through mixing with the ambient waters.

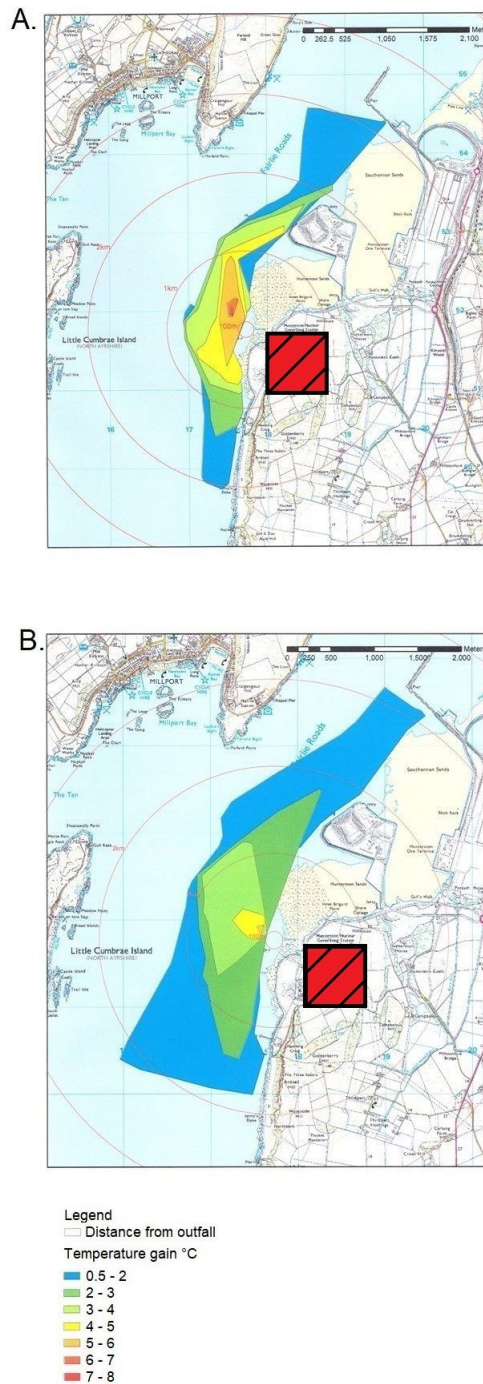


Figure 5.1: Horizontal plume mapping for Hunterston power station during spring tide (A) and neap tide (B) taken from *Briggs [2008]* (not publicly available). Temperatures within the plume are marked by green, yellow, orange and red polygons, with green being the lowest temperature gain (0.5 °C - 2 °C) and red bring the highest temperature gain (7 °C - 8 °C). Power station is marked as a red square with black stripes.

The field survey reported that the plume was not mapped in the shallow waters in the inter-tidal zone and therefore was not tracked towards the shore. Those gaps in surface thermal plume mapping can be filled in with available remote sensing imagery. Figure 5.2 shows the detected surface thermal plumes ejected from the discharge of the Hunterston power station during ebb and flood tides (described in detail in Chapter 3).

The plumes dispersing during the flood tide in satellite imagery are observed also in very shallow inter-tidal regions of Hunterston Sands, which provides new additional information to the field survey, which was not able to record temperatures in those areas due to the bathymetry being too shallow for the surveying vessel. The plumes dispersing during the ebb tide were found to be more laterally dispersed than what was observed in the field survey, possibly related to different tidal and wind conditions than during the field survey.

The length of the plume in the field surveys was similar to the 80% probability of the plume occurrence derived from the satellite observations, however on several occasions the plume was seen to disperse further away from the outfall pipes (8 out of 43 satellite observations). The areal size of the plume in the field surveys was smaller than observed by the satellites. The plume described by the field survey is forming a narrow band and staying close to the coastline. On the probability density maps it can be seen that the plume disperses further towards the Cumbrae Islands and is more laterally spread out. This is even more prominent for the ebb tide conditions with the plume dispersing southwards. The results from the satellite observations provide the plume location over an wider range of conditions.

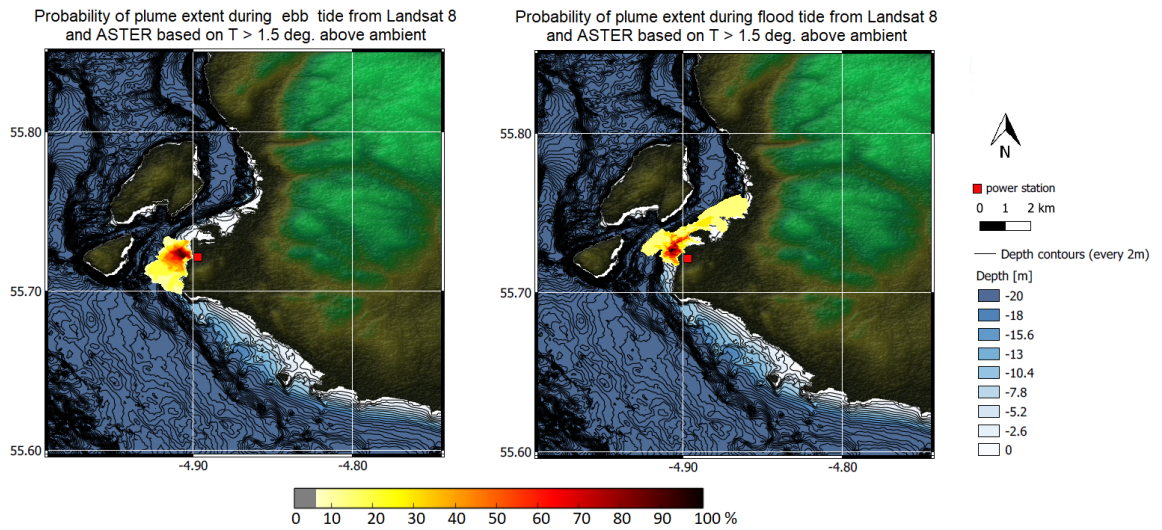


Figure 5.2: Close-up of the Hunterston power station (marked as red square), with detailed bathymetry with contours at 2 m depth intervals obtained from EMODnet dataset. The probability density map of thermal plume location during ebb tide (left) and flood tide (right) and reach is overlaid on top of the bathymetry. Darker colours present higher probability and lighter colours lower probability of the plume location.

The temperature distribution within the plume captured by the remote sensing observations was consistent with the field survey, with highest temperatures observed close to the discharge point and the temperatures decreasing with distance away from the power station. The maximum temperature difference between the ambient waters and the plume noted by the field survey ($5.5\text{ }^{\circ}\text{C}$ for the neap tide and $8.0\text{ }^{\circ}\text{C}$ for the spring tide) was similar to the maximum temperature gains during summer months observed by the satellites, which range from $4.7\text{ }^{\circ}\text{C}$ to $9\text{ }^{\circ}\text{C}$ (see Figure 5.3). Since satellite imagery provides multiple data points with observed SST, it is more representative of the surrounding ambient waters than a value measured in a single point. The thermal contrast between the plume and the ambient waters during summer months observed by the satellites is somewhat in agreement with the field observations, with highest temperature differences observed over the summer months (June, July, August). During other seasons, especially winter and autumn months, there's a smaller thermal contrast between the plume and the ambient waters (see Figure 5.3).

In the winter the power stations usually pump the cooling water using fewer pumps than in the summer (e.g. for Sizewell power station 3 pumps are used between October and May and 4 pumps between May and October). Lower number of pipes reduces the volume intake and outfall rates. It is most likely related to the intake water temperature, which during the winter months is the lowest. Hence, less water is needed to cool the

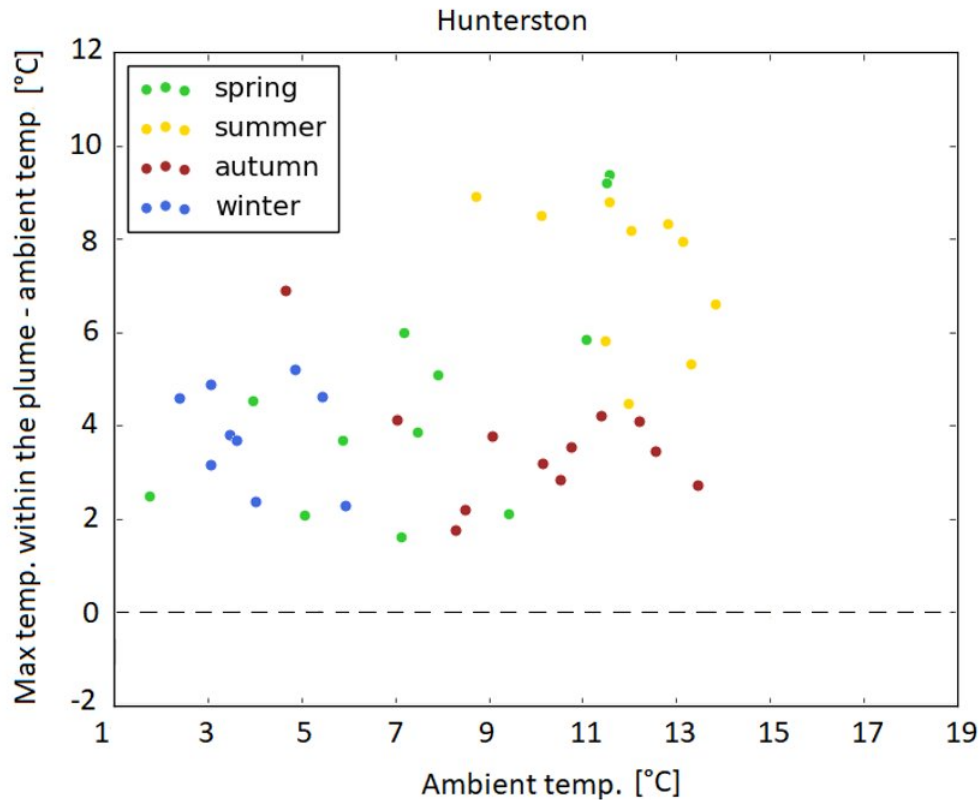


Figure 5.3: Maximum differences between the surface plume temperature and ambient SST for all satellite observations for Hunterston power station. The differences are grouped according to season with green dots representing differences in SST captured during March, April, May, yellow dots - during June, July, August, red dots - during September, October, November, blue dots - during December, January, February.

condensation plate (see Chapter 1, Section 1.2). There is a strong negative correlation between the volume flow rate and the temperature gain of the cooling water released as the thermal plume (see Figure 5.4). Higher outfall rates discharge the plume with a smaller temperature gain and lower outfall rates are correlated with higher temperatures at the discharge point. Power stations try to keep the temperature gain (ΔT) steady throughout the year (measured at the discharge point on the premises of the power station) and it oscillates usually between 10 °C and 13 °C. The ΔT at the discharge point is larger in the winter months, yet in the satellite data the ΔT between the observed plume and the ambient waters is smaller in winter months (see Figure 5.3). There are a few possible explanations to this:

- the plume released at depth is mixing with much colder waters, which causes it to lose part of the heat before it reaches the surface;
- in many satellite images the plumes observed during late autumn and winter months were more spread out, which can increase the heat loss through surface evaporation due

to the temperature difference between the released plume and the cold air;
- increased wind speeds during winter months will encourage more heat loss.

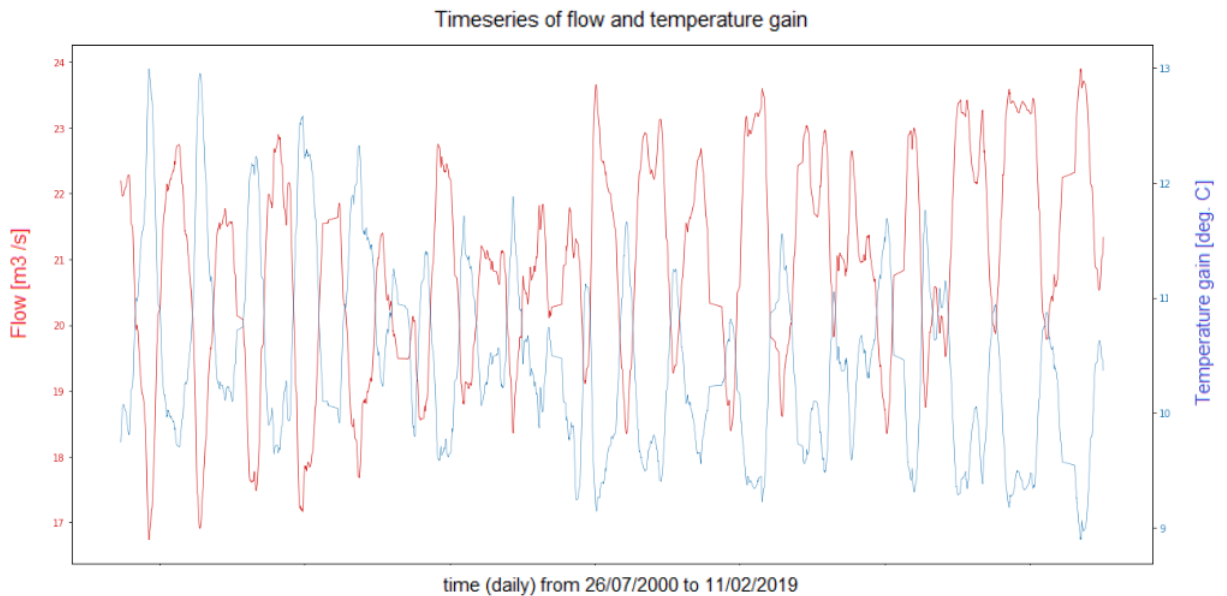


Figure 5.4: A timeseries of volume flow rates and temperature gains for the Heysham power station measured over the period of ~ 19 years by the Heysham power station. Same correlation is observed for other EDF Energy power stations.

Thermal plume discharged from the Hunterston power station has been studied before by *Davies and Mofor* [1993] and *Davies et al.* [1993] through a series of flights over the region of interest with an airborne thematic mapper on two days in 1987 (10 May and 22 July), during which both Hunterston A and B power stations were in operation. Previous studies of thermal plume dispersion suggest that the presence of the Cumbrae Islands has an effect on the spreading of the thermal plume, acting as a barrier. The main tidal flow direction is along the axis of Hunterston Channel, which runs between the main land and the two islands [*Davies and Mofor*, 1993]. *Davies et al.* [1993] has shown that the positively buoyant thermal plume rises and spreads at the surface. The plume spreads across the channel, with temperature decreasing away from the outfall pipe. Once the plume reaches the Cumbrae Islands, it is redirected back towards the shore as a secondary plume, which can cause warmer water to accumulate in the Hunterston channel along the shore. Their findings are in agreement with both the field survey and the remote sensing observations. The plume characterised by both methods was not extending beyond the islands and rather dispersing close to shore.

5.5.1.1 Assessment of the plume impact on the environment

Fry [1967] has divided the effects of raised temperatures on the environment into

three categories: lethal, controlling and directive. Lethal effects are the temperature rises that directly cause death of aquatic organisms. Controlling effects cause physiological or biochemical changes within the sensitive organisms. Directive effects result in behavioural changes in the organisms, such as migration to a colder environment. [Gibbons \[1976\]](#) added a fourth category called the indirect effects. Indirect effects are temperature raises that do not directly impact the aquatic organisms, but are related to another biochemical factor, which in turn affects local flora and fauna. This section discusses possible effects the thermal plume released at Hunterston power station has on its environs.

The Firth of Clyde is one of the largest estuaries in the UK and the largest estuary in Scotland, containing 38 Sites of Special Scientific Interest (SSSI) and 30 Geological Conservation Review Sites. The majority of the SSSI lie further away from Hunterston with 1 of the SSSI located within 5 km radius of the power station [[Briggs, 2008](#)]. Moreover, two Shellfish Areas are located in the vicinity of the power plant, a large one south of the power station and a small one located north east of the power station in the region of Hunterston Sands (see [Figure 5.5](#)). In those two areas according to the Shellfish Directive guidelines, the tolerable temperature gain should be less than 2 °C. The waters around the Cumbrae Islands, opposite the power station, are identified by Scottish Natural Heritage as Marine Consultation areas (see [Figure 5.5](#)) due to the quality of the environment and sensitivity of the habitats located there.

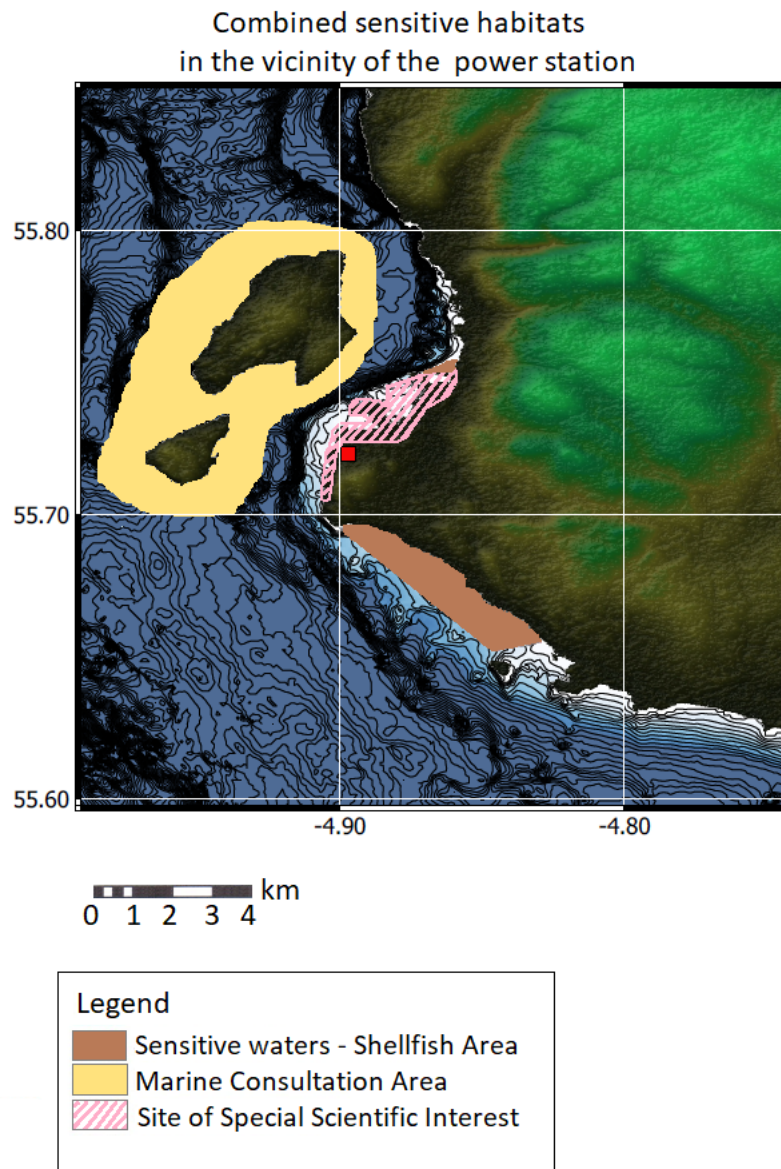


Figure 5.5: Location of sensitive habitats in the vicinity of the Hunterston power station. In yellow are marked Marine Consultation Areas around two Cumbrae Islands. In brown are marked sensitive waters, where the shellfish populations are located. Pink stripes represent a Site of Special Scientific Interest, which are the Hunterston Sands. Power station is marked as the red square.

Figure 5.6 shows example individual thermal plumes detected in satellite imagery during different tidal stages overlaid on top of sensitive environments of Hunterston. The plume does not reach Marine Consultation Areas in any of the tidal scenarios. During all presented tidal scenarios, the plume is located fully or partly over the SSSI of Hunterston Sands (marked as pink striped region). The impact of the plume is most pronounced during the slack water and flood tide, as during the ebb tide only the northern part of the plume is located in that area and the rest of the plume disperses further away (see

Figure 5.6). During the ebb tide, the end of the plume overlays a part of the Shellfish area south of the power station. However, the plume at this stage is very diluted and the temperature rise is between 1 - 1.5 °C, which is within the Shellfish Directive limits. During the flood tide, the plume does not disperse far enough to impact the other Shellfish Area, north of the power station.

The temperature distribution at the seabed measured during the field survey showed that the bottom temperature gains were observed within 1 km south of the discharge pipes during the ebb tide and 1 km north during the flood tide. The highest temperature rise caused by the thermal plume was 1.9 °C [Briggs, 2008]. The survey found that the surface plume temperatures were higher than the bottom plume temperatures with the largest difference of 5.1 °C [Briggs, 2008]. Since all recorded bottom temperatures were below 2 °C, they were not exceeding the Shellfish Directive limits.

The field survey concluded that during the operational time of both Hunterston A and Hunterston B power stations, the composition of the habitats in the intertidal areas neighbouring the power station has been altered [Briggs, 2008]. The Hunterston Sands are habitats of various species of lugworm casts (*Pygospio elegans*, *Capitella capitata*, *Lumbricillus sp* and *Paranais litoralis*) [Carse and O'Reilly, 2005] and dwarf eel-grass (*Zostera noltii*) [DH Ecological Consultancy, 2005]. *Zostera* is found to be tolerant and not sensitive to temperature changes and low intolerance of changes in oxygenation with high recoverability [Tyler-Walters, 2005]. Lugworm casts, similarly to eel-grass species, have low sensitivity to temperature rises and very high recoverability [Riley, 2005]. For *capitella capitata*, changes in temperature and salinity could result in decreased variability within the population or changes in breeding period, however, the species is found to tolerate temperature increases and adapt until the critical temperatures of ≥ 30 °C [Tillin, 2018].

The species inhabiting the shallow waters have high temperature tolerances, with the lethal temperature threshold ranging from 35.5 °C for *G. cineraria* to 44.3 °C for *semibalanus balanoides* [Evans, 1948; Southward, 1958], while for intertidal littorinidae species the lethal temperatures range between 44.3 °C up to 46 °C [Evans, 1948; Southward, 1958]. One of the groups belonging to littorinidae are sea snails. Littorinid snails were found to be one of the most invulnerable species to temperature rises and would survive prolonged periods of temperatures exceeding 37 °C without deterioration in the population [Suresh et al., 1993]. A particular species of sea snails, flat top shells (*Gibbula umbilicalis*), have been originally inhabiting the southern coasts of the UK. The migration of the snails north to the Scottish regions was associated with the raising water temperature in those

regions due to climate change [*Mieszkowska et al.*, 2006], which indicates that the species favours higher temperatures and may have high tolerance of raised temperatures due to thermal discharges.

Since the species found in the sub-tidal and intertidal zones in the vicinity of Hunterston have low sensitivity to temperature and oxygenation changes, the effects of the thermal plume on the surrounding habitats are in the non-lethal category. Possible effects might impact reproductive patterns of the aquatic species, such as alterations in reproductive cycle, longer breeding period [*Briggs*, 2008; *Barnett and Hardy*, 1984], increased larvae density or extended growing periods [*Briggs*, 2008]. The results of earlier breeding caused by the thermal plume cannot be claimed as completely positive or negative and rather will depend on the type of organism affected (planktonic or benthic) and their larvae dependence on food supply. For some crustaceans like copepods (*Asellopsis intermedia*) and molluscs like sea snails (*Nassarius reticulatus*) earlier start of reproduction and accelerated development rates due to raised temperatures were shown to be harmful. Higher temperatures in the vicinity of the power plant led to earlier spawning and quicker larvae growth, however, the low food supply (e.g. phytoplankton) early in the year caused the larvae to die of starvation [*Barnett*, 1972; *Hardy*, 1977]. Increased growth rates due to temperature rises cause alterations in shell morphology for some shellfish species, with increased shell growth in bivalve molluscs (*Tellina tenuis*) and thinner and lighter shells for sea snail (*Nassarius reticulatus*) [*Barnett*, 1972]. In contrast, some species (e.g. sand-burrowing amphipods (*Urothoe brevicornis*)) react very positively to raised temperatures as they feed on detrital rocks and their food supply is therefore not regulated by the time of the year. The amphipods reached larger final size due to a longer growing period [*Barnett*, 1971].

Apart from the statuary littoral species, the Firth of Clyde is also a migratory route for some fish species: wild salmon and sea trout [*Joint Marine Programme*, 2004]. A study in 2006 found that temperature increased by less than 4 °C do not have any effect on salmonid families and suggested it is the case for other species as well [*Turnpenny and Liney*, 2006]. Since the islands limit the spread of the plume, it is unlikely that the plume will disperse beyond the islands and into the estuary of the Clyde river affecting the migratory fish in that estuary [*Briggs*, 2008].

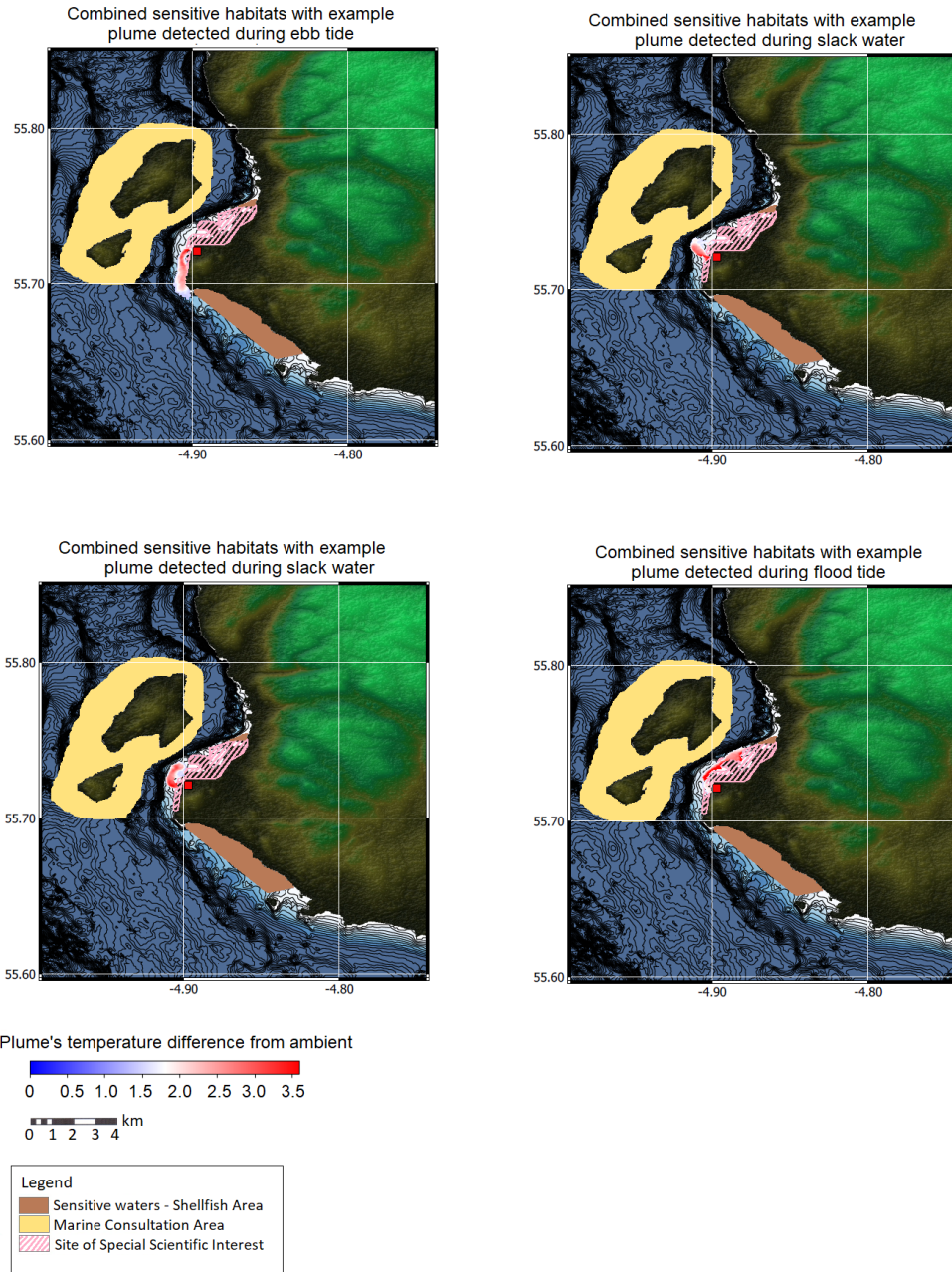


Figure 5.6: Location of sensitive habitats in the vicinity of the Hunterston power station with thermal plume detected in satellite imagery during different tidal stages. Plume dispersing during ebb tide is in top left, during slack water - top right, slack water changing into flood tide - bottom left and during flood tide - bottom right. Plume's temperature is described as difference from ambient water temperature.

5.5.2 Heysham power station

Heysham field survey has been carried out on two days: 10 July 2007 and 15 July 2007 for neap tide and spring tide respectively. During the field survey the two reactors at Heysham were working at more than 70 % of their capacity and discharging the thermal plume from two discharge channels at $67.17 \text{ m}^3 \text{ s}^{-1}$ [Briggs and Taylor, 2008]. The field survey consisted of three sets of measurements, the same as the ones described for the Hunterston survey. All point temperature measurements were categorised into four groups: 0.5 to 2.0, 2.0 to 5.0 and 5.0 to 8.0 °C warmer than ambient water, which again was chosen to be the lowest temperature recorded.

The horizontal mapping occurred over the course of one day for the neap and one day for the spring tide and captured both flood and ebb tides, which is mirrored by the detected plume dispersing both north-eastward and south-westward away from the discharge pipes (see Figure 5.7). Satellite imagery capture the dispersion of the thermal plume during a specific phase of tide instantaneously and therefore shows the distinction between the dispersion during the ebb and during the flood tide (see Figure 5.8).

The field survey showed that during the neap tide the northern part of the plume extends up to 1.5 km, whereas the south-western part of the plume extends up to 3 km away from the outfall pipes. Both northern and southern parts of the plume formed a narrow area along the deep water channel. Thermal gains of 2 °C - 5 °C were observed over most part of the plume, up to 1 km north and 3 km south of the discharge pipes. The results of the horizontal mapping indicated a small area of 2 °C warmer than ambient water recirculating into the Heysham harbour, where the intake of the cooling waters is located. It is worth pointing out that only one measuring point in the field survey was located within the Heysham harbour, which made it hard to properly assess the size of the plume entering the harbour. The area of highest temperature rise (8 °C or higher than ambient temperature) during the neap tide was limited in area and did not disperse further than 0.5 km south west away from the outfall pipes, with the highest temperature measured of 26.3 °C. Surface plume area recorded during spring tide was similar, however, areas of higher temperature gains (2 °C - 5 °C and 5 °C - 8 °C) were smaller compared to the neap tide survey, but the maximum temperature recorded was higher and was 26.6 °C (see Figure 5.7).

Vertical profiling happened on the same days as horizontal mapping of the plume. In order to map the plume at depth, 133 profiles of the water column were taken, with most profiles concentrated within 1 km of the of the discharge pipes and only 15 vertical

profiles were collected further than 1 km away from the discharge pipes.

The northern part of the plume, associated with the flood tide, recorded lower bottom temperature gains, which suggests that the waters were stratified and advected the plume to the surface [Briggs and Taylor, 2008]. During the period of slack water, between changing of the flood to the ebb tide, recorded temperature gains were low and limited in area, suggesting that the plume has undergone mixing and dilution in the shallow ambient water regions, where no measurements were conducted [Briggs and Taylor, 2008]. Southern part of the plume, associated with the ebb tide, showed highest temperature gains along the south-westward deep water channel. The corresponding bottom temperature gains were lower, suggesting that the plume was buoyant and advected to the surface [Briggs and Taylor, 2008]. The field survey states that highest temperature gains were recorded within 0.5 km and 1 km away from the discharge pipes, however, having collected only 15 vertical profiles further than 1 km over the course of two days does not provide a robust enough sample to characterise the thermal plume thoroughly.

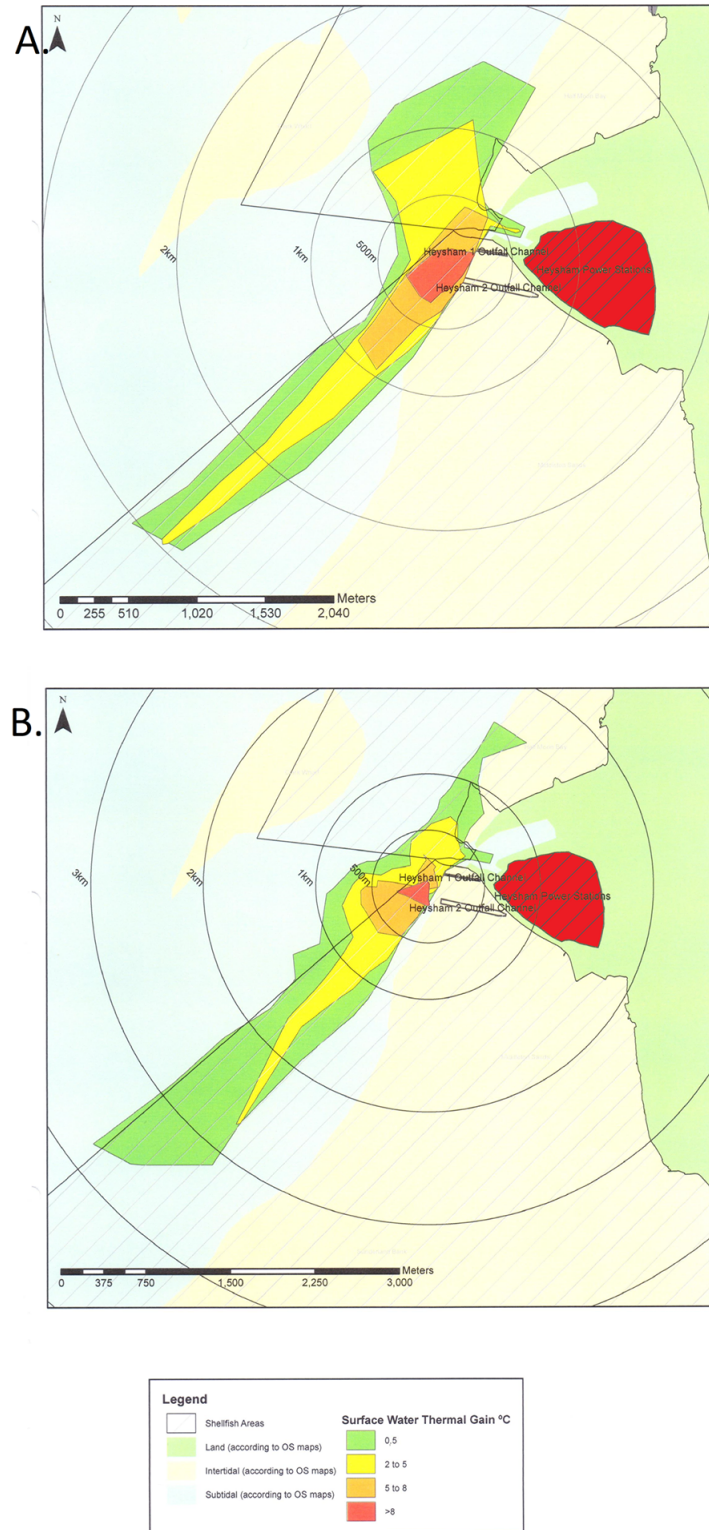


Figure 5.7: Horizontal plume mapping during neap tide (A) and spring tide (B) taken from *Briggs and Taylor* [2008] (not publicly available). Temperatures within the plume are marked by green, yellow, orange and red polygons, with green being the lowest temperature gain (0.5°C - 2°C) and red bring the highest temperature gain (above 8°C). The power station area is marked in red with black stripes.

The probability density maps (Figure 5.8) based on thermal plume detection in multiple images shows that the size and reach of the surface plume may vary, depending on the strength of sea currents as well as volume outfall rate from the discharge pipes. The plumes captured during the ebb tide extend from 1 km up to 5 km south westward along the deep water channel, the direction being consistent with the field survey. The plumes captured during the flood tide disperse up to 2.2 km north-eastwards, which is also in agreement with the horizontal mapping. The neap tide and spring tide surveys suggested that the plume spreads more in the northern part and forms a long narrow band in the south-western part. This is not true for the satellite imagery, where the plume dispersing north-eastwards also forms a long narrow band and disperses further away from the discharge pipes than measured by profilers. This might be related to sparse observations further away from the discharge point and not enough lines included in the horizontal mapping.

The survey suggested that parts of the plume located in the shallow waters north and south-east off the discharge pipes might have been missed by the survey, due to the depth constraints on the surveying boat. On a few occasions, during slack water period (see Figure 5.8 right), thermal plumes were detected south-eastward off the discharge pipes in the shallow water regions. This provides new information in thermal plume characterisation, since boat surveys were not able to survey those areas and provide information on the extent of thermal plume. In most cases the plume during slack water stays close to the coast and does not disperse much into the shallow waters, however, towards the end of slack water with strengthening ebb tide currents, the plume disperses further away from the discharge pipes into the shallow waters.

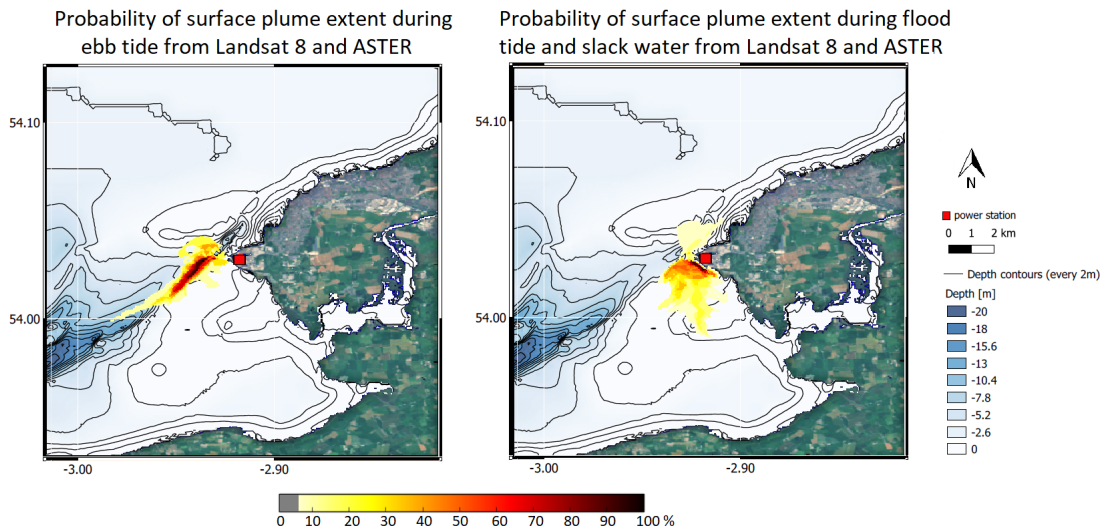


Figure 5.8: Probability density maps for the surface plume extent during ebb tide (left) and flood tide and slack water (right) based on Landsat 8 and ASTER imagery, with lighter color representing lower chance of plume extent and darker colours represent higher probability of plume extent. All plumes were detected based on criterion of 1.5°C warmer than ambient water temperature.

The largest temperature difference between the plume and the ambient waters noted by the field survey was $>8.0^{\circ}\text{C}$, with the plume maximum temperature of 26.3°C during the spring tide and 26.6°C during the neap tide. The highest temperature difference observed during the summer months through remote sensing ranges between 5.0°C and 8.7°C for ambient water temperature 11°C - 17°C (see Figure 5.9). The field measurements noted a slightly warmer maximum temperature within the plume compared to maximum temperature of the satellite observations, which was 23.7°C . There are two possible explanations of this. Firstly, the survey could have been recorded on a day with warmer ambient waters, which would result in warmer ambient plume. Secondly, the discrepancies could be related to the definition of ambient waters. In the observations the ambient water is derived as an average temperature over 25 km^2 of waters close to the ROI, but not affected by the thermal plume. In the field survey the coldest recorded value during the survey is set as the ambient temperature. Choosing the lowest temperature as the ambient could result in higher temperature difference between the ambient water and the plume. Looking at the maximum temperature gains caused by the thermal plume over other months, it can be noticed that during the winter and autumn months the temperature differences in the majority of satellite data were $\leq 5^{\circ}\text{C}$. A possible explanation to this is the seasonal working pattern of a power station, which was already explained in previous section for Hunterston.

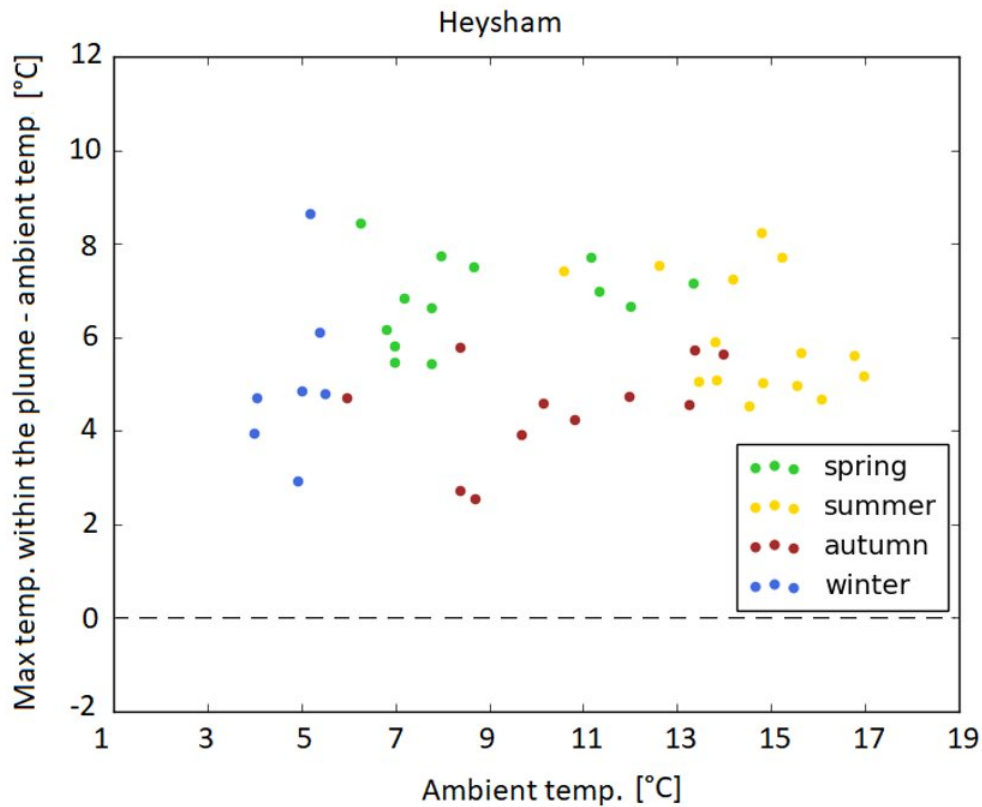


Figure 5.9: Maximum differences between the surface plume temperature and ambient SST for all satellite observations. The differences are grouped according to season with green dots representing differences in SST captured during March, April, May, yellow dots - during June, July, August, red dots - during September, October, November, blue dots - during December, January, February.

5.5.2.1 Integrating remote sensing information with 3-D simulations - example of Heysham

Due to time constraints of the simulation software free license, the sub-surface analysis could only be carried out for one power station and after discussions the location chosen was Heysham. Simulations of plume dispersion during ebb and flood tide on two chosen days were validated against satellite imagery and can plausibly characterise the sub-surface plume dispersal during other ebb and flood tides (described in detail in Chapter 4). The simulation results were similar to the results obtained through the vertical profiling during the field survey. The simulated thermal plume had highest temperatures at the surface, close to the outfall pipes with lower temperature gains further away from the discharge pipes. The extent of the plume was decreasing with depth and was very localised at seabed, not extending beyond 0.5 km in both scenarios, suggesting that the plume was advected to the surface. Detailed description of the simulation results can be

found in Chapter 4, Section 4.3.1-4.3.3. Integrating satellite observations with 3-D simulations is a feasible complimentary method of thermal plume monitoring to the traditional boat surveys. It provides an opportunity to understand thermal plume dispersion during varying tidal currents and volume discharge rates.

5.5.3 Assessment of the plume impact on the environment

Morecambe Bay is the meeting point of major estuaries: Kent, Leven, Lune, Wyre, and multiple smaller estuaries. Together they form the largest continuous intertidal area in the UK [*Joint Nature Conservation Committee (online), 2020*]. The whole of Morecambe Bay is under protection as the Special Area of Conservation (SAC) for habitats. The intertidal sandflats located in the shallow parts of the bay are part of the Special Protection Area (SPA) for bird species. This means that the bay area is valuable in terms of British wildlife and diverse habitats. Due to the high ecological importance and its location with respect to SAC and SPA, any future development proposals, outside the already existing energy generation, are likely to have constraints on type and scale of the project [*The Greater Manchester Ecology Unit, 2017*].

Two of the sensitive habitats located on the intertidal flats of Morecambe Bay are common mussel and cockle beds. Common mussels (*Mytilus edulis*) prefer shallow waters (up to 5 m depth) (see Figure 5.10) and have a large temperature tolerance, with a temperature range between 10 °C and 20 °C not impacting the species [*Bayne and Bayne, 1976*], with other studies suggesting even larger tolerance of 5 °C - 20 °C with upper sustained limit of 29 °C [*Walne et al., 1979*]. Common cockles (*Cerastoderma edule*) are widely distributed around the British coast, and similarly to mussels they are eurythermic, which means they have a wide range of temperatures they tolerate with an upper lethal limit of 35 °C after being exposed for 24 hours [*Ansell et al., 1981*]. The Marine Life Information Network (MarLIN) has assessed common mussel species to have high tolerance and common cockle species to have intermediate intolerance to short term changes in temperature and both species show high recoverability [*Tyler-Walters, 2008*].

Apart from the stationary habitats located in the bay, due to the presence of multiple estuaries, the bay is abundant in fish species, such as: plaice, flounder and dab. Moreover, it is also a vital fish nursery area and habitat for migratory fish species: salmon (*Salmo salar*), sea trout (*Salmo trutta*) and eels (*Anguilla anguilla*) [*Potts and Swaby, 1993*]. Optimal temperature ranges between 0 °C - 28 °C and 0 °C - 26 °C for salmon and trout respectively, with optimal growth temperature of 16 °C -17 °C [*Elliott and Elliott, 2010*].

For eels [Deelder \[1984\]](#) proposed that the European species can adapt to temperatures ranging from 0 °C to 30 °C. Another study mentioned a temperature range of 10 °C - 38 °C beyond which the feeding activity was stopped [[Sadler, 1979](#)].

During the field survey, the absolute temperatures within the plume were compared to the thermal death point of 33°C as stated in [Bamber \[1990\]](#). Thermal death point is a temperature which will lead to instantaneous death of organisms or over a finite period of time. On both occasions the maximum temperatures recorded within the plumes did not exceed 33 °C. Comparing the temperatures within the plume is a good approach in characterising thermal stress for aquatic organisms, however, providing more thermal thresholds would be more useful as different aquatic communities will have different thermal tolerances and experience stress at different thresholds (upper thermal limit for a common mussel is 29 °C [[Walne et al., 1979](#)] and lethal temperature for common cockle is 35 °C [[Ansell et al., 1981](#)], while for fish species it is below 30 °C).

In order to assess the impact of the plume on the aquatic organisms, I have integrated information collected during the field survey with bathymetry maps and knowledge of the surface plume area and location. [Figure 5.10](#) presents habitats of common mussel, common cockle, as well as boulder and cobble skear. The circular rings in the image present area with a radius ranging from 1 km to 5 km away from the outfall pipes. Mussel and cockle beds are widely distributed around the UK coast, preferring sandy bays and estuaries as their habitat. Moreover, Morecambe Bay is the location of large commercial mussel beds. Boulder and cobble skear in the Bay are habitats for such communities as serrated wrack, sponges, sea squirts and red seaweeds, as well as a good settlement for honeycomb worm (*Sabellaria alveolata*) reefs [[Marine Management Organisation \(online\), 2014](#)]. Honeycomb worm is an eurythermic organism and can survive in temperatures ranging from 5 °C up to 25 °C. Exposing species to a stepwise temperature increase from 15 °C to 25 °C indicated that the worm is able to undergo biological changes in phospholipids to acclimatise to higher temperature locally [[Muir et al., 2016](#)].

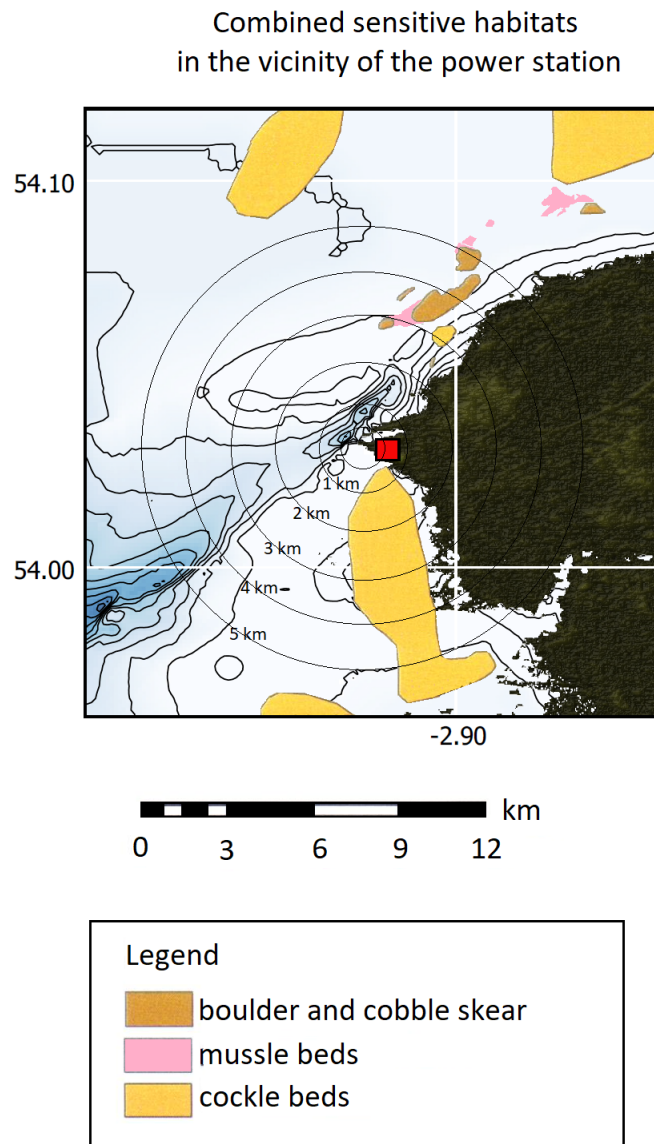


Figure 5.10: Location of sensitive habitats in the vicinity of the Heysham power station. Boulder and cobble skear is marked in brown, mussel beds in grey, cockle beds in yellow. Left panel shows location of all communities, middle panel - boulder and cobble skear and right panel mussel and cockle beds. Distance away from the outfall pipes is marked by different sized circles with the radius written for each circle, ranging from 1 km to 5 km.

Figure 5.11 presents example individual thermal plumes detected in satellite imagery during different tidal stages overlaid on top of sensitive environments of Heysham. Most of the vulnerable habitats are located in shallow water regions and do not follow the south-western deep water channel. Hence thermal plume ejected during the ebb tide will not impact those communities, even when dispersing further away from the discharge pipes (see Figure 5.11). Since the plume ejected during ebb tide follows the deep water channel, dispersing towards the ocean (see Figure 5.11), it will not reach any of the Morecambe

Bay estuaries, which are known as nurseries and habitats of various fish species. The plume dispersing during the flood tide is limited in area and does not disperse much beyond 3 km. However, on some occasions the tail of the plume could reach the mussel and cockle beds located north, within 4 km off the discharge pipes. It is important to note that the tail of the plume has already undergone substantial mixing and dilution and the temperature gain is much lower than in the main part of the plume, usually between 1.5 °C - 2 °C. Looking at the MarLIN report, such temperature rise should not impact either species. It is, however, important to be aware of potential impacts in that area related to reoccurring raised temperatures, which might change reproductive patterns of (*Mytilus edulis*) mussels or increase larval densities [[Tyler-Walters, 2008](#)]. The largest impact of the thermal plume will be observed during slack water periods on boulder and cobble skear communities such as the honeycomb worm. With weak and changing sea currents, the thermal plume is dispersing south eastwards of the discharge pipes, in the direction of a large area of boulder and cobble in the shallow waters. In most cases the plume stays localised close to the coast, however, on some occasions the plume disperses further south and east spreading in the shallow water.

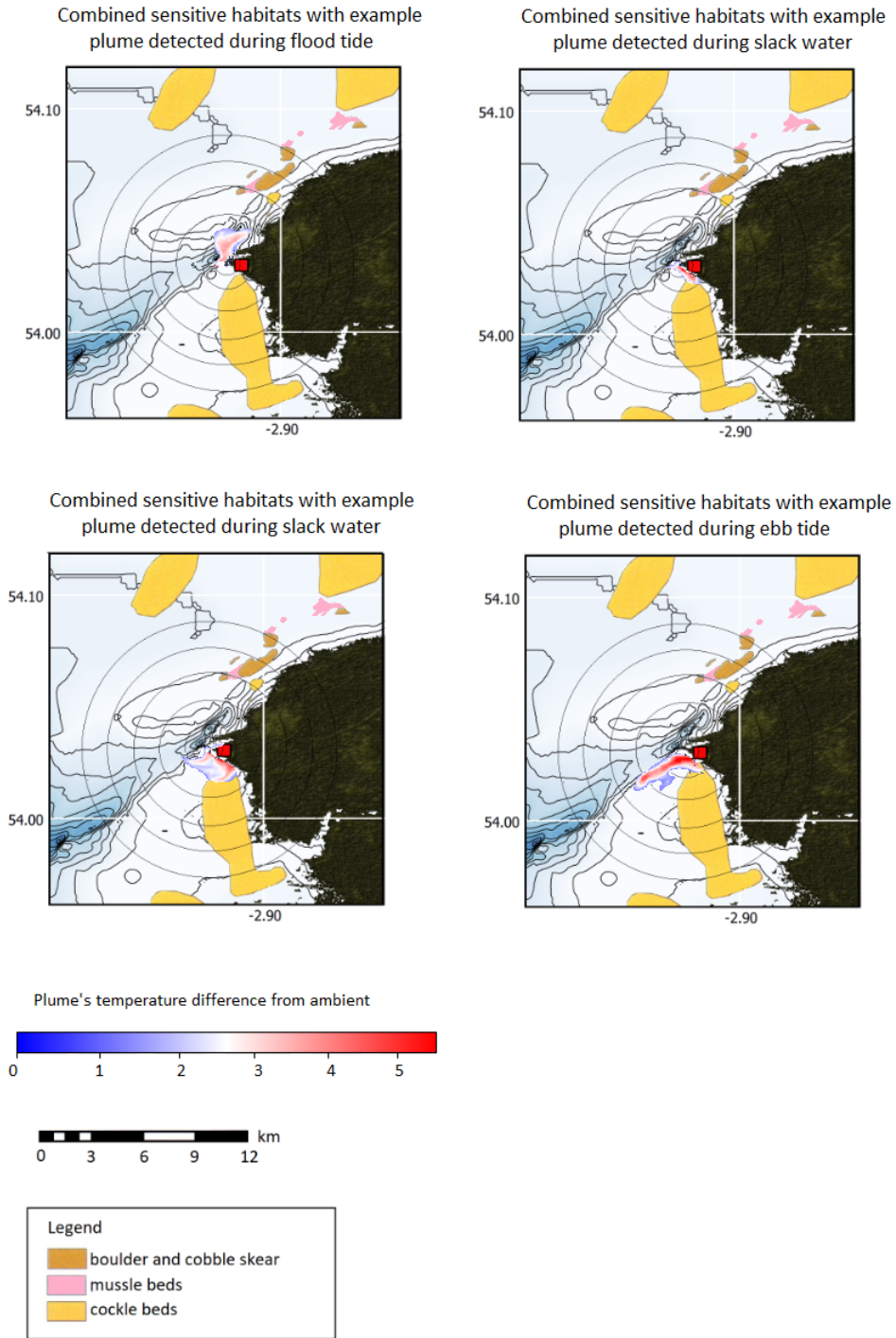


Figure 5.11: Location of sensitive habitats in the vicinity of the Heysham power station with thermal plume detected in satellite imagery during different stages. Plume dispersing during flood tide is in top left, during slack water - top right, slack water changing into ebb tide - bottom left and during ebb tide - bottom right. Plume's temperature is described as difference from ambient water temperature. Distance away from the outfall pipes is marked by different sized circles with the radius written for each circle, ranging from 1 km to 5 km.

5.6 Conclusions

Observing or establishing a monitoring system of the thermal plumes is important to determine that with further operation of the power station no vulnerable habitats are endangered. Field campaigns provide a comprehensive way of characterising thermal plumes at surface and at depth. Since the plume dispersion is dependent on the tides, capturing the plume during one complete tidal cycle plausibly informs of the plume location during other tidal cycles. The repeatability of the measurements is constrained by the high cost of each campaign, which makes it infeasible for monitoring purposes. The use of high resolution satellite observations is a useful and cost-effective method to extend the observations of the thermal plumes and possibly monitor thermal plumes at surface. Remote sensing observations do not provide enough information on their own to replace traditional boat surveys, but can be used as a continuation of the thermal plume observation after the field campaign.

Chapter 6:

Conclusions and future work

6.1 Conclusions

A good monitoring system of the industrial thermal plumes from power stations is a valuable source of understanding of the variability in plume location and thermal impact, which helps in the decision-making process to fulfill environmental requirements. To explore the potential and evaluate capabilities of alternate and complimentary methods to traditional plume characterisation surveys, the primary objectives of this thesis were to determine the extent and quality of information available from satellites and a chosen 3-D model and to assess how we can bridge the gaps in plume characterisation using a combination of those methods. Three science questions were posed:

- *Science question 1. What remote sensing methodology enables us to characterise thermal plumes quantitatively?*
- *Science question 2. What complimentary information can 3-D simulations provide in characterising thermal plumes?*
- *Science question 3. Do satellite observations and 3-D simulations provide a feasible complimentary method to traditional ways of thermal plume monitoring?*

These questions have been addressed in Chapters 3, 4 and 5 of this thesis. The key conclusions, set in a broader context, as well as answers to the questions above are presented in the remaining parts of this section.

Science question 1. What remote sensing methodology enables us to characterise thermal plumes quantitatively?

High resolution remote sensing, collecting data at 90 - 100 m (such as Landsat 8 or ASTER), is more adequate for detecting thermal plumes than moderate resolution observations from satellites such as the Advanced Very High Resolution Radiometer (AVHRR) with pixel resolution 1.1 km. High spatial resolution is necessitated by the size of an industrial thermal plume, which varies between 0.15 km² and 1 km², and the temperature differences within the plume can be observed on a scale of several hundreds meters. Hence, coarser spatial resolution will either not be able to detect the thermal plume or not capture the temperature variability within the detected plume. High spatial resolution also allows for most features (e.g. river estuaries, harbours) to be resolved and a large spectral resolution ranging from visible through shortwave infra-red (SWIR) to thermal infra-red (TIR) channels provides enough information to successfully retrieve temperature only over the water regions. The ability to use the Modified Normalized Water Difference Index (MNDWI) as the water detection algorithm in each image is desirable due to the dynamic land-water boundary and frequent presence of inter-tidal flats in the coastal regions.

Since only data with sufficiently low cloud cover or clear skies can be used to observe thermal plumes, the amount of data appropriate for this use will be limited. Long observational record and availability of all images collected over the scheduled repeat cycle of Landsat 8 provided huge advantage in the amount of available data over the Region of Interest (ROI) compared to ASTER, which downloads the data to the ground segment only on demand. ASTER imagery can be used as additional information, but in order to establish thermal plume monitoring system, a satellite with a reoccurring data collection should be chosen. A decade worth of observations with sufficiently clear skies for thermal plume detection resulted in around 40 to 50 observations per ROI. Despite the number of available observations being a limitation, a collection of satellite images provided enough information on thermal distributions during different tide phases, seasons, power station operational capacity and volume outfall rates. The obtained high resolution observation data set is adequate to get estimates of the plume distribution in the ROI through probability density maps, further described in Chapter 3. Probability density maps can be used to depict the possible reach of the thermal plume during two main tidal states. Such maps form a valuable basis in thermal plume characterisation as they include thermal plume images captured during a chosen tidal period, but with varying sea current strengths and

power station discharge volumes related to operational capacity.

While a single thermal image indicates temperature distribution within the plume at a given point in time, an available long observation record allows for exploration of variability in the ambient SST and plume temperature over seasons. The whole data set of thermal plume observations can be arranged according to the phase of tide during the satellite overpass to see thermal plume as a function of tide. This is important information for shallow coastal areas, where the flow is mainly driven by tidal currents and the dispersion of the thermal plume ejected into coastal environments is embedded within the flow. A series of consecutive satellite images placed in order of increasing phase of tide is a sufficient tool for indicating main direction of dispersion and plausible reach of the plume at surface across the whole tidal range. Since the flow in the coastal areas tends to be turbulent and the ejected plume evolves with time, such animated tools provide informative aid to power station operators in understanding changing plume behaviour.

Science question 2. What complimentary information can 3-D simulations provide in characterising thermal plumes?

While satellite observations can quantify the extent, intensity and dynamics of the surface thermal plume dispersion, the 3-D characterisation of the plume is not fully determined by the surface signature. 3-D simulations may better describe plume dispersion subsurface and hence deduce the impact on the bottom temperatures and benthic organisms. Since the spread of the plume is not homogeneous through the water column, using 3-D simulations is a useful improvement to 2-D simulations of thermal plumes, which has been used in previous studies. Moreover, because the bathymetry will influence spreading of the plume, 3-D simulations respecting terrain morphology are necessary for reasonable results. While the direction of the plume dispersion and its size will depend on prior known conditions, models are able to generate spatially and temporally complete data showing plume development in three dimensions. Ability to set high resolution of the model is crucial in properly resolving the bathymetry of a given location, since it will impact local flow vectors, which was the case for Heysham model.

Two main tidal regimes, the ebb tide and the flood tide, were modelled by extracting information on water flow direction and speed on two chosen days from the Norwegian MET. These simulation outputs were first high-resolution 3-D thermal plume results discussed for a UK coastal power station in terms of tidal impact. Previous studies focused on 2-D modelling and a couple of 3-D studies provided only 2-D results output.

The simulated plume length at depth was almost six times shorter than at the surface and the plume area at seabed was covering a substantially smaller area, with the area of highest temperature rise over 10 times less, compared to the surface signatures. The patterns were unique for the Heysham power station, but were found to be in agreement with the results from the previous field campaign, where bottom temperature gains were limited close to the source and thermal plumes were dispersing further at surface. The simulations at the surface were sufficiently validated by the observations with over 80% of the simulated plume located inside the observed plume and the dominant direction of the modelled plume at the surface was found to be consistent with satellite observations collected on the same day.

The simulated plume was not as dispersed laterally as in the satellite-derived product. The difference in the areal size of the plume is most likely caused by idealising the flow in the simulations to a steady flow in one prescribed direction, while in real life the thermal plume is ejected into a constantly changing environment. Since the lifetime of the plume is longer than the duration of a tide phase, which was demonstrated by the excess heat loss in Chapter 4, there will be a history of a changing plume not portrayed in the simulations. This could be refined by setting up a model with thermal plume ejected into a changing flow.

Science question 3. Do satellite observations and 3-D simulations provide a feasible complimentary method to traditional ways of thermal plume monitoring?

Traditional field surveys focus on characterising thermal plumes through a series of point measurements at surface and at depth conducted over one full neap tide cycle and one full spring tide cycle. Due to the high cost associated with each field survey, exploring alternative ways of describing thermal plumes is of value. The utility of the extracted information from the high resolution observations and simulation runs has been demonstrated, and presents a feasible complimentary method for thermal plume monitoring to traditional boat surveys. For newly operating power stations, a detailed field survey is beneficial in characterising thermal plume since there will be very few or no remote sensing observations available. Over the operational lifetime of a power station carrying over methods presented in this thesis can prove more cost-effective assuming availability of necessary software within the company.

Remotely sensed images capture a complete temperature distribution over the whole

area at a single point in time and are not limited by areas of shallow seabed since the observations are taken from space. This provides additional information to the field surveys, which are unable to take measurements in regions shallower than 0.5 m and have to interpolate between point measurements. In case of no access to the modelling software for environmental sensitivity assessment, the information on the SST distribution could be extrapolated down to the seabed as the upper limiting scenario. However, this would suggest a larger plume at the bottom to have impact on the benthic organisms than in a real-life scenario when the positively buoyant plume is advected to the surface. In order to provide a more plausible analysis of the plume impact on the environment, the plume-related rise in the bottom temperatures on a given day can be achieved using a 3-D simulation given prior known outflow rates and tidal state. Combining satellite observations with a 3-D simulation, provides a unique opportunity for a comprehensive characterisation of the thermal plume at surface and at depth.

Satellite-derived information and simulations overlaid on maps of sensitive habitats and special protection zones provide indication of the conditions under which the plume may affect the aquatic habitats. It is important to understand organisms' responses to raised temperatures and know thermal thresholds resulting in lethal response. Eurythermic organisms can adapt locally in the vicinity of the power station outfalls if the temperature rise caused by the discharged plume will not exceed their tolerable range. More sensitive organisms, which cannot alter biologically as a response to higher temperatures, will be forced to relocate to areas not affected by the thermal plumes.

6.2 Future Work

This work could be taken further by:

- refining the remote sensing observations of thermal plumes
- including drone remote sensing over a power station or using sea gliders for plume surveying
- setting up more complex simulations, closer to resembling real-life tidal scenarios

Those points are discussed further in the text below.

Refining thermal plume detection in the remote sensing observations

We can achieve a successful identification of thermal plumes in satellite images based on proposed 1.5 °C threshold. The thermal plume threshold used in Chapter 3 is higher

than the value of 0.5 °C higher than ambient suggested by *Langford* [1990]. The difficulties in setting the lower threshold are that it would make it challenging to distinguish between natural variability of the coastal SSTs and a lower threshold might not account for the uncertainty in the retrieved SST. Landsat continues to revisit the calibration of each thermal channel by implementing the stray light correction algorithm, which was also included in this thesis. Recently there have been updates to the radiometric calibration of TIRS, which has not been implemented in the early part of this thesis. Landsat 8 Level 2 data collected from March 2020 includes the updated radiometric calibration. This should allow revisiting temperature retrievals for Landsat 8 and exploring possibilities of a more sensitive thermal threshold allowing for a better characterisation of the thermal plume extent by detecting more diluted parts of the plume.

In the future using a Copernicus Land Surface Temperature Monitoring (LSTM) mission, which is currently in preparation for the new Copernicus generation as "expansion" mission, might be of advantage. Copernicus LSTM, which will cover coastal zones, will aim at total uncertainty in retrieved surface temperature to be less than 1 K and noise equivalent delta temperature (NEDT) for thermal channels to be within 0.1 K for a reference BT at 300 K. Moreover, the launch of Landsat 9 satellite in 2021 could potentially result in having a greater temporal density of observations capturing thermal plumes while both Landsat satellites are in orbit and extending the length of the time series after Landsat 8 retires. Extending the observational data set by continuing to collect images with detected thermal plumes could lead to reduced uncertainties in the mapped probabilistic distributions of plume occurrence. Operational monitoring of the thermal plumes using only satellite observations may not be fully achievable as there might happen thermal pollution events, which would not be captured by the satellite sensors due to the satellite return time.

Including drone remote sensing over a power station or using sea gliders for plume surveying

Since there are no freely available field measurements of the thermal plumes, except the reports from the single boat survey, in the future including drone observations of the thermal discharges would open up new opportunities. Drones present a relatively cost-effective way of extending the observations of surface thermal plumes. Every drone campaign would have to be scheduled beforehand and agreed with the power station as there are no-fly zones in the vicinity of the power stations. Scheduling a drone campaign to

take repeated observations at specified times would give a complete picture by capturing thermal plume discharges over one full tidal cycle at high temporal and spatial resolution. Collecting continuous observations using a visible channel instrument (providing RGB imagery over the tidal coastal regions) and a thermal camera collecting surface BTs at different thermal wavelengths over the ROI would allow capturing the transition from mid-flood to mid-ebb, or mid-ebb to mid-flood. The collection of images could then be used as validation of more complex simulations with varying tidal conditions.

Moreover, since Landsat 8 repeat time is 16 days, it is possible to calculate future days of the satellite overpass over the power station location and schedule a drone campaign around the Landsat 8 overpass. Provided that the weather conditions would be favourable (i.e. low percentage of cloud cover over the ROI), thermal imagery from both sensors could be compared. The comparison should include the size and location of the thermal features as well as absolute surface temperature values. A precisely calibrated drone with well described instrument uncertainty could be used as a validation check to the satellite imagery. High spatial resolution of drone images (from 7.5 cm [*Chianucci et al., 2016*] to 2 cm [*Banu et al., 2016*]) compared to the resampled 30 m spatial grid of Landsat 8 could potentially present a more detailed characterisation of the surface plume and temperature variations within the plume.

Using drones for surface thermal plume mapping also opens up new possibilities of surveying the plume during cloudy conditions. Since the limit of the drone fly height is 120 m, its viewing instruments will not be obscured by clouds and therefore will be able to capture the SST distribution around the power station on days where the satellite images do not provide enough information due to cloud contamination. Images of the surface thermal plumes on cloudy days could be used to extend the available data set of thermal plume observations. Even though no previous projects have used drones to characterise thermal plumes in coastal environments, studies have used drone information in the past for quantifying river temperature heterogeneity [*Dugdale et al., 2019*], characterising geothermal areas at a high spatial resolution [*Harvey et al., 2016*] or characterising terrestrial discharges into coastal environments [*Ferrara et al., 2017*]. Those studies have proven the feasibility and usefulness of high-resolution sampling using visible and near-IR cameras to capture the temperature distributions of the region of interest. Thus, including drones in the spatial mapping of thermal plumes seems like a feasible additional characterisation method.

Another possibility is using sea gliders for surveying the ROI. Sea gliders an un-

manned under-water instruments, which require almost no human involvement. Those instruments are able to collect data on the temperature, density, salinity and sea current information [Griffiths *et al.*, 2007; Rudnick *et al.*, 2004]. The collected data can be then fed into the processing unit on the shore. Due to the low speed ($< 0.5 \text{ m s}^{-1}$) they are able to sample the ROI in detail and provide in-depth information on the physical characteristics of the ROI at a relatively low cost [Griffiths *et al.*, 2007]. Previous studies were able to use the data from sea gliders to validate their models [Rudnick, 2016], which suggests that this technique (combined with the numerical modelling) could provide a feasible alternative solution to the expensive field campaigns.

Setting up more complex simulations, closer to resembling real-life tidal scenarios

Simulations presented in Chapter 4 were based on simplified tidal scenarios. The simulations were set up for various volume discharges during the two tidal states and were claimed satisfactory for operational plume characterisation. However, the plume was ejected from the discharge pipes into a steady flow environment representing mid-ebb or mid-flood scenario, which does not capture full tidal variation. In inter-tidal coastal areas, simulations over a full tidal cycle would permit capturing changes in the location of the thermal plume embedded within constantly changing, unsteady flow.

As the results from the simulation runs have been processed, there were discrepancies in the shape of the plume and the areal size of the surface plume in the simulations was found to be around two times smaller than the observed one. The differences were investigated in terms of air-sea heat exchanges related to the excess cooling of the plume. Based on the heat flux calculated in Chapter 4, the plume lifetime based on the heat loss is longer than the time it takes for the tidal currents to change and shift the plume. It was suggested that the discrepancies in plume size and shape arose because the plume was discharged from the outfall pipes into an already steady flow and therefore the simulations did not capture full impact of the tides on the plume.

In order to simulate the discharges as close to real life as possible, the thermal plume in the simulations should be released into a changing flow. Such set up would include the changing height of water, direction and strength of the tidal currents. Instead of prescribing tidal currents at simulation domain boundaries, those values would be set as variables changing over time. This would open up possibilities of tracking the thermal plume in changing conditions and see how the history of the plume influences its extent.

Such analysis could be useful for power stations prior to operation to analyse potential impact of future thermal plume discharges and investigate whether they would conform with provided environmental permits. In order to assess the simulation outputs, simulated surface plumes should be compared against field measurements, thermal remote sensing or drone observations. Observational methods presented in this thesis would form a suitable source for validation of the simulations at surface.

6.3 Closing remarks

Given the need to decarbonise economic activity and the role that nuclear power stations may have in complementing renewable energy supplies, there will likely be an on-going need for methods of assessing environmental impacts and compliance from thermal plumes. The work presented here shows that remote sensing and simulation can be informative and cost-effective approaches to this need, and directions for further development have been proposed.

REFERENCES

- Abascal Zorrilla, N., V. Vantrepotte, E. Gensac, N. Huybrechts, and A. Gardel, The Advantages of Landsat 8-OLI-Derived Suspended Particulate Matter Maps for Monitoring the Subtidal Extension of Amazonian Coastal Mud Banks (French Guiana), *Remote Sensing*, 10(11), 1733, 2018.
- Abbaspour, M., A. Javid, P. Moghimi, and K. Kayhan, Modeling of thermal pollution in coastal area and its economical and environmental assessment, *International Journal of Environmental Science & Technology*, 2(1), 13–26, 2005.
- Abrams, M., S. Hook, and B. Ramachandran, ASTER user handbook, Version 2, [Available online under: https://asterweb.jpl.nasa.gov/content/03_data/04_Documents/aster_user_guide_v2.doc], 2002.
- Ahn, Y.-H., P. Shanmugam, J.-H. Lee, and Y. Q. Kang, Application of satellite infrared data for mapping of thermal plume contamination in coastal ecosystem of Korea, *Marine environmental research*, 61(2), 186–201, 2006.
- Alesheikh, A. A., A. Ghorbanali, and N. Nouri, Coastline change detection using remote sensing, *International Journal of Environmental Science & Technology*, 4(1), 61–66, 2007.
- Ali, J., Modelling of thermal plume discharge into shallow and still water, Ph.D. thesis, University of Huddersfield, [Available online under <http://eprints.hud.ac.uk/id/eprint/11118/>], 2011.
- Ansell, A., P. Barnett, A. Bodoy, and H. Massé, Upper temperature tolerances of some European molluscs, *Marine Biology*, 65(2), 177–183, 1981.
- Anupkumar, B., T. Rao, V. Venugopalan, and S. Narasimhan, Thermal mapping in the Kalpakkam Coast (Bay of Bengal) in the vicinity of Madras atomic power station, *International journal of environmental studies*, 62(4), 473–485, 2005.
- Bamber, R., Environmental impact assessment: the example of marine biology and the UK power industry, *Marine Pollution Bulletin*, 21(6), 270–274, 1990.
- Banu, T. P., G. F. Borlea, and C. Banu, The use of drones in forestry, *Journal of Environmental Science and Engineering B*, 5(11), 557–562, 2016.
- Barkhudarov, M. R., Lagrangian VOF Advection method for FLOW-3D, *Flow Science Inc*, 1(10), [Available online under: <https://citeseerx.ist.psu.edu/viewdoc/download?doi=10.1.1.585.3265&rep=rep1&type=pdf>], 2004.
- Barnett, P., Some changes in intertidal sand communities due to thermal pollution, *Proceedings of the Royal Society of London. Series B. Biological Sciences*, 177(1048), 353–364, 1971.
- Barnett, P., Effects of warm water effluents from power stations on marine life, *Proceedings of the Royal Society of London. Series B. Biological Sciences*, 180(1061), 497–509, 1972.
- Barnett, P., and B. Hardy, Thermal deformations., 1984.
- Barreto, Á., M. Arbelo, P. A. Hernández-Leal, L. Núñez-Casillas, M. Mira, and C. Coll, Evaluation of surface temperature and emissivity derived from ASTER data: A case study using ground-based measurements at a volcanic site, *Journal of Atmospheric and Oceanic Technology*, 27(10), 1677–1688, 2010.

- Barsi, J. A., J. R. Schott, S. J. Hook, N. G. Raqueno, B. L. Markham, and R. G. Radocinski, Landsat-8 thermal infrared sensor (TIRS) vicarious radiometric calibration, *Remote Sensing*, 6(11), 11,607–11,626, 2014.
- Barsi, J. A., B. L. Markham, M. Montanaro, A. Gerace, S. J. Hook, J. R. Schott, N. G. Raqueno, and R. Morfitt, Landsat-8 TIRS thermal radiometric calibration status, in *Earth Observing Systems XXII*, vol. 10402, p. 104021G, International Society for Optics and Photonics, 2017.
- Bayne, B. L., and B. Bayne, *Marine mussels: their ecology and physiology*, vol. 10, Cambridge University Press, 1976.
- Boschetti, M., F. Nutini, G. Manfron, P. A. Brivio, and A. Nelson, Comparative analysis of normalised difference spectral indices derived from MODIS for detecting surface water in flooded rice cropping systems, *PloS one*, 9(2), 2014.
- Briggs, A., Thermal Plume and Habitat Sensitivity Study, Hunterston Nuclear Power Station, [Not publicly available. To request access, contact EDF Energy.], 2008.
- Briggs, A., and J. Taylor, Thermal Plume and Habitat Sensitivity Study, Heysham Nuclear Power Station, [Not publicly available. To request access, contact EDF Energy.], 2008.
- Bulgin, C. E., O. Embury, G. Corlett, and C. J. Merchant, Independent uncertainty estimates for coefficient based sea surface temperature retrieval from the Along-Track Scanning Radiometer instruments, *Remote Sensing of Environment*, 178, 213–222, 2016.
- Caratelli, E., F. Dentale, and F. Reale, On the effects of wave-induced drift and dispersion in the deepwater horizon oil spill, *Monitoring and Modeling the Deepwater Horizon Oil Spill: A Record-Breaking Enterprise, Geophysical. Monograph Series*, 195, 197–204, 2011.
- Cardoso-Mohedano, J., R. Bernardello, J. Sanchez-Cabeza, A. Ruiz-Fernández, R. Alonso-Rodríguez, and A. Cruzado, Thermal impact from a thermoelectric power plant on a tropical coastal lagoon, *Water, Air, & Soil Pollution*, 226(1), 2202, 2015.
- Carniello, L., S. Silvestri, M. Marani, A. D’Alpaos, V. Volpe, and A. Defina, Sediment dynamics in shallow tidal basins: In situ observations, satellite retrievals, and numerical modeling in the Venice Lagoon, *Journal of Geophysical Research: Earth Surface*, 119(4), 802–815, 2014.
- Carse, L., and M. O’Reilly, Marine Biology Summary Report No. 02/07. Hunterston Shore Survey - Sep - 2002, 2005.
- Chen, C., P. Shi, and Q. Mao, Application of remote sensing techniques for monitoring the thermal pollution of cooling-water discharge from nuclear power plant, *Journal of Environmental Science and Health, Part A*, 38(8), 1659–1668, 2003.
- Chianucci, F., L. Disperati, D. Guzzi, D. Bianchini, V. Nardino, C. Lastri, A. Rindinella, and P. Corona, Estimation of canopy attributes in beech forests using true colour digital images from a small fixed-wing uav, *International journal of applied earth observation and geoinformation*, 47, 60–68, 2016.
- Chuang, Y.-L., H.-H. Yang, and H.-J. Lin, Effects of a thermal discharge from a nuclear power plant on phytoplankton and periphyton in subtropical coastal waters, *Journal of Sea Research*, 61(4), 197–205, 2009.

- Cloern, J. E., A. D. Jassby, T. S. Schraga, E. Nejad, and C. Martin, Ecosystem variability along the estuarine salinity gradient: Examples from long-term study of San Francisco Bay, *Limnology and Oceanography*, *62*(S1), S272–S291, 2017.
- Coomber, D. P. M., and J. D. Hansom, Estuaries Management Plans: Coastal Processes and Conservation, Morecambe Bay, [Available online under: <http://eprints.gla.ac.uk/100064/>], 1994.
- Crippen, R. E., S. J. Hook, and E. J. Fielding, Nighttime ASTER thermal imagery as an elevation surrogate for filling SRTM DEM voids, *Geophysical Research Letters*, *34*(1), 2007.
- Cunningham, W. P., T. H. Cooper, E. Gorham, and M. T. Hepworth, *Environmental encyclopedia*, Gale Research, 1998.
- Dabuleviciene, T., I. Kozlov, D. Vaiciute, and I. Dailidienė, Remote Sensing of Coastal Upwelling in the South-Eastern Baltic Sea: Statistical Properties and Implications for the Coastal Environment, *Remote Sensing*, *10*(11), 1752, 2018.
- Dai, X., Z. Guo, Y. Chen, P. Ma, and C. Chen, Monitoring of thermal plume discharged from thermal and nuclear power plants in eastern China using satellite images, in *2016 IEEE International Geoscience and Remote Sensing Symposium (IGARSS)*, pp. 7659–7662, IEEE, 2016.
- Dalrymple, R. A., and B. Rogers, Numerical modeling of water waves with the SPH method, *Coastal engineering*, *53*(2-3), 141–147, 2006.
- Davies, A., J. Sauvel, and J. Evans, Computing near coastal tidal dynamics from observations and a numerical model, *Continental Shelf Research*, *4*(3), 341–366, 1985.
- Davies, P., and L. Mofor, Remote sensing observations and analyses of cooling water discharges from a coastal power station, *International journal of remote sensing*, *14*(2), 253–273, 1993.
- Davies, P., L. Mofor, and Y. Jiao, Foam lines generated by a spreading buoyant plume, *International Journal of Remote Sensing*, *14*(14), 2647–2663, 1993.
- Davies, P. A., and M. V. Neves, *Recent research advances in the fluid mechanics of turbulent jets and plumes*, vol. 255, Springer Science & Business Media, 2012.
- De Vriend, H. J., Mathematical modelling and large-scale coastal behaviour: part 1: physical processes, *Journal of hydraulic research*, *29*(6), 727–740, 1991.
- Dee, D. P., et al., The era-interim reanalysis: Configuration and performance of the data assimilation system, *Quarterly Journal of the royal meteorological society*, *137*(656), 553–597, 2011.
- Deelder, C. L., *Synopsis of biological data on the eel, Anguilla anguilla (Linnaeus, 1758)*. *2*, 1984.
- Delpey, M., F. Ardhuin, P. Otheguy, and A. Jouon, Effects of waves on coastal water dispersion in a small estuarine bay, *Journal of Geophysical Research: Oceans*, *119*(1), 70–86, 2014.
- DH Ecological Consultancy, Nationally scarce plant survey and woodland national vegetation classification survey of Portencross SSSI, North Ayrshire, 2005.

- Donlon, C., P. Minnett, C. Gentemann, T. Nightingale, I. Barton, B. Ward, and M. Murray, Toward improved validation of satellite sea surface skin temperature measurements for climate research, *Journal of Climate*, 15(4), 353–369, 2002.
- Donlon, C. J., M. Martin, J. Stark, J. Roberts-Jones, E. Fiedler, and W. Wimmer, The operational sea surface temperature and sea ice analysis (OSTIA) system, *Remote Sensing of Environment*, 116, 140–158, 2012.
- Dugdale, S. J., C. A. Kelleher, I. A. Malcolm, S. Caldwell, and D. M. Hannah, Assessing the potential of drone-based thermal infrared imagery for quantifying river temperature heterogeneity, *Hydrological Processes*, 33(7), 1152–1163, 2019.
- Durán-Colmenares, A., H. Barrios-Piña, and H. Ramírez-León, Numerical modeling of water thermal plumes emitted by thermal power plants, *Water*, 8(11), 482, 2016.
- Dvornikov, A. Y., S. D. Martyanov, V. A. Ryabchenko, T. R. Eremina, A. V. Isaev, and D. V. Sein, Assessment of extreme hydrological conditions in the Bothnian Bay, Baltic Sea, and the impact of the nuclear power plant “Hanhikivi-1” on the local thermal regime, *Earth System Dynamics*, 8(2), 265–282, 2017.
- EDF Energy, Environment Impact Assessment Scoping Report Hinkley Point C Pre-Application Consultation—Stage 1, [Available online under <https://www.edfenergy.com/file/2312/download>], accessed: 15.05.2020, 2010a.
- EDF Energy, Hinkley Point C Pre-Application Consultation—Stage 2. Environmental Appraisal: Volume 2, [Available online under <https://www.edfenergy.com/file/1827/download>], accessed: 15.05.2020, 2010b.
- Elliott, J., and J. Elliott, Temperature requirements of Atlantic salmon *Salmo salar*, brown trout *Salmo trutta* and Arctic charr *Salvelinus alpinus*: predicting the effects of climate change, *Journal of fish biology*, 77(8), 1793–1817, 2010.
- Elliott, M., Thermal standards for cooling water from new build nuclear power stations, *British Energy Estuarine & Marine Studies*, 2011.
- Encyclopaedia Britannica, Encyclopaedia britannica, [Available online under <https://www.britannica.com/science/rip-current>], accessed: 15.01.2021, 2007.
- Ernst, W. G., and W. G. Ernst, *Earth systems: processes and issues*, Cambridge University Press, 2000.
- Evans, R. G., The lethal temperatures of some common British littoral molluscs, *The Journal of Animal Ecology*, pp. 165–173, 1948.
- Fang, T.-H., J.-F. Chen, Y.-Y. Tu, J.-S. Hwang, and W.-T. Lo, Hydrographical studies of waters adjacent to nuclear power plants I and II in Northern Taiwan, *Journal of Marine Science and Technology*, 12(5), 364–371, 2004.
- Faulkner, A., C. E. Bulgin, and C. J. Merchant, Coastal tidal effects on industrial thermal plumes in satellite imagery, *Remote Sensing*, 11(18), 2132, 2019.
- Fernard, L., T. Silva, J. Bacon, and S. van Leeuwen, Hinkley Point; Thermal Plume Modelling: GETM Stage 3a Results with the Final CW Configuration, [No longer available online. In order to request access contact EDF Energy.], 2011.
- Ferrara, C., M. Lega, G. Fusco, P. Bishop, and T. Endreny, Characterization of terrestrial discharges into coastal waters with thermal imagery from a hierarchical monitoring program, *Water*, 9(7), 500, 2017.

- Fischer, H. B., Mixing and dispersion in estuaries, *Annual review of fluid mechanics*, 8(1), 107–133, 1976.
- FLOW-3D, Santa Fe, NM: Flow Science, Inc., ® version 12.0 [computer software], <https://www.flow3d.com>, [Available only to users with a valid software license.], 2019.
- Flow Science Inc., Flow-3d version 12.0 users manual (2018). flow-3d [computer software], <https://www.flow3d.com>, [Available only to users with a valid software license.], 2018.
- Fossati, M., P. Santoro, S. Urrestarazu, and I. Piedra-Cueva, Numerical study of the effect of a power plant cooling water discharge in the Montevideo Bay, *Journal of Applied Mathematics*, 2011, 2011.
- Fry, F. J., Responses of vertebrate poikilotherms to temperature, *Thermobiology*, pp. 375–409, 1967.
- Gerace, A., and M. Montanaro, Derivation and validation of the stray light correction algorithm for the thermal infrared sensor onboard Landsat 8, *Remote Sensing of Environment*, 191, 246–257, 2017.
- Giarrusso, C., E. P. Carratelli, and G. Spulsi, On the effects of wave drift on the dispersion of floating pollutants, *Ocean engineering*, 28(10), 1339–1348, 2001.
- Gibbons, J., Thermal alteration and the enhancement of species populations, *Tech. rep.*, 1976.
- Gonzalez, R. C., R. E. Woods, et al., *Digital image processing*, Prentice hall. Upper Saddle River, NJ, 2002.
- Google n.d., [Google Maps image of Heysham Power Plant with the outfall pipes, Morecambe Bay, UK], <https://www.google.com/maps/place/Heysham/@54.0301019,-2.9279105,1555m/data=!3m1!1e3!4m5!3m4!1s0x487b6032d1b5ffc1:0x30c7ed43b99179d7!8m2!3d54.04199!4d-2.894475>, accessed: 01.09.2019, 2019.
- Griffiths, G., C. Jones, J. Ferguson, and N. Bose, Undersea gliders, *Journal of Ocean Technology*, 2(2), 64–75, 2007.
- Haas, K. A., and I. A. Svendsen, Laboratory measurements of the vertical structure of rip currents, *Journal of Geophysical Research: Oceans*, 107(C5), 15–1, 2002.
- Hamrick, J. M., and W. B. Mills, Analysis of water temperatures in Conowingo Pond as influenced by the Peach Bottom atomic power plant thermal discharge, *Environmental Science & Policy*, 3, 197–209, 2000.
- Hardy, B. L. S., The effects of a warm water effluent on the biology of the sand-dwelling harpacticoid copepod *Asellopsis intermedia* (T. Scott)., Ph.D. thesis, University of Glasgow, [Full text unavailable online. To request access contact the University of Glasgow library.], 1977.
- Harik, G., I. Alameddine, R. Maroun, G. Rachid, D. Bruschi, D. A. Garcia, and M. El-Fadel, Implications of adopting a biodiversity-based vulnerability index versus a shoreline environmental sensitivity index on management and policy planning along coastal areas, *Journal of environmental management*, 187, 187–200, 2017.
- Harvey, M., J. Rowland, and K. Luketina, Drone with thermal infrared camera provides high resolution georeferenced imagery of the Waikite geothermal area, New Zealand, *Journal of Volcanology and Geothermal Research*, 325, 61–69, 2016.

- Hicks, S. D., *Understanding tides*, US Department of Commerce, National Oceanic and Atmospheric Administration, 2006.
- Hillman, R. E., N. W. Davis, and J. Wennemer, Abundance, diversity, and stability in shore-zone fish communities in an area of Long Island Sound affected by the thermal discharge of a nuclear power station, *Estuarine and Coastal Marine Science*, 5(3), 355–381, 1977.
- Hocking, J., P. Rayer, D. Rundle, R. Saunders, M. Matricardi, A. Geer, P. Brunel, and J. Vidot, RTTOV v11 Users Guide, NWP-SAF report, Met, Office: Exeter, UK, [Available online under https://nwpsaf.eu/oldsite/deliverables/rtm/docs_rttov11/users_guide_11_v1.4.pdf], 2014.
- Hong, B., and J. Shen, Responses of estuarine salinity and transport processes to potential future sea-level rise in the Chesapeake Bay, *Estuarine, Coastal and Shelf Science*, 104, 33–45, 2012.
- Howarth, M., Hydrography of the Irish Sea, *Tech. rep.*, Citeseer, [Available online under https://www.google.com/search?q=hydrography+of+the+irish+sea&sxsrf=ALeKk01ygxtZLWH6NDLctElvsQ1NofVwWg%3A1617643829123&ei=NULrYMTtBvSH9u8P566e4Ao&oq=hydrography+of+the+irish+sea&gs_lcp=Cgdnd3Mtd2l6EAMyCAghEBYQHRAeOgcIIxCwAxAnOgcIABBHELAD0gQIIxAnOgoILhDHARCvARBDOgQIABBD0sclient=gws-wiz&ved=0ahUKEwiE3Lru00fvAhX0g_OHHWeXB6wQ4dUDCA0&uact=5#], 2005.
- Huang, F., Y. Lin, and C. Wang, Marine elements associated with siting of coastal nuclear power plants, in *2016 5th International Conference on Civil, Architectural and Hydraulic Engineering (ICCAHE 2016)*, Atlantis Press, 2016.
- Huang, G., and W.-K. A. Law, The dispersion of surface contaminants by Stokes drift in random waves, *Acta Oceanologica Sinica*, 37(7), 55–61, 2018.
- Huang, S.-J., J.-T. Lin, Y.-T. Lo, N.-J. Kuo, and C.-R. Ho, The coastal sea surface temperature changes near the nuclear power plants of northern Taiwan observed from satellite images, in *OCEANS 2014-TAIPEI*, pp. 1–5, IEEE, 2014.
- Hulley, G., and S. Hook, A new methodology for cloud detection and classification with ASTER data, *Geophysical research letters*, 35(16), 2008.
- Hung, T.-C., C.-C. Huang, and K.-T. Shao, Ecological survey of coastal water adjacent to nuclear power plants in Taiwan, *Chemistry and Ecology*, 15(1-3), 129–142, 1998.
- Islam, M. A., D. Mitra, A. Dewan, and S. H. Akhter, Coastal multi-hazard vulnerability assessment along the Ganges deltaic coast of Bangladesh—A geospatial approach, *Ocean & Coastal Management*, 127, 1–15, 2016.
- Issakhov, A., Mathematical modeling of the discharged heat water effect on the aquatic environment from thermal power plant under various operational capacities, *Applied Mathematical Modelling*, 40(2), 1082–1096, 2016.
- Issakhov, A., Mathematical modeling of the hot water discharge effect on the aquatic environment of the thermal power plant by using two water discharge pipes, *International Journal of Energy for a Clean Environment*, 19(1-2), 2018.
- Issakhov, A., and Y. Zhandaulet, Numerical simulation of thermal pollution zones' formations in the water environment from the activities of the power plant, *Engineering Applications of Computational Fluid Mechanics*, 13(1), 279–299, 2019.

- Jang, J.-C., and K. Park, High-resolution sea surface temperature retrieval from Landsat 8 OLI/TIRS data at coastal regions, *Remote Sensing*, 11(22), 2687, 2019.
- Janin, J., F. Lepeintre, and P. Pechon, Telemac-3D: A finite element code to solve 3D free surface flow problems, in *Computer modelling of seas and coastal regions*, pp. 489–506, Springer, 1992.
- Jiang, S., and J. Hou, The impact analysis for marine environment which caused by the thermal discharge of power plant, in *2015 International Forum on Energy, Environment Science and Materials*, Atlantis Press, 2015.
- Joint Marine Programme, *The tangle of Clyde. Why we must reform the management of Scotland's marine environment.*, The Joint Marine Programme, Scotland, 2004.
- Joint Nature Conservation Committee (online), Morecambe Bay, Designated Special Area of Conservation (SAC), [Available online under <https://sac.jncc.gov.uk/site/UK0013027>], accessed: 10.06.2020, 2020.
- Kelly, J. T., and A. M. Gontz, Using GPS-surveyed intertidal zones to determine the validity of shorelines automatically mapped by Landsat water indices, *International journal of applied earth observation and geoinformation*, 65, 92–104, 2018.
- Klevanny, K., G. Matveyev, and N. Voltzinger, An integrated modelling system for coastal area dynamics, *International Journal for Numerical Methods in Fluids*, 19(3), 181–206, 1994.
- Langford, T., *Ecological effects of thermal discharges*, Springer Science & Business Media, 1990.
- Laws, E. A., *Aquatic pollution: an introductory text*, John Wiley & Sons, 2017.
- Lees, B. J., Observations of tidal and residual currents in the Sizewell-Dunwich area, East Anglia, UK, *Deutsche Hydrografische Zeitschrift*, 36(1), 1–24, 1983.
- Levy, R., J. Barsi, and B. Markham, Landsat 8 OLI and TIRS calibration updates and trends for the period of 4 years of operation, [Available online under <https://digitalcommons.usu.edu/calcon/CALCON2017/All2017Content/7/>], 2017.
- Lewis, W., The formation of Dungeness foreland, *The Geographical Journal*, 80(4), 309–324, 1932.
- Liang, S., *Comprehensive Remote Sensing*, Elsevier, 2017.
- Liu, Y., P. Song, J. Peng, and C. Ye, A physical explanation of the variation in threshold for delineating terrestrial water surfaces from multi-temporal images: effects of radiometric correction, *International Journal of Remote Sensing*, 33(18), 5862–5875, 2012.
- Lohmar, F. J., World geodetic system 1984—geodetic reference system of GPS orbits, in *GPS-Techniques Applied to Geodesy and Surveying*, pp. 476–486, Springer, 1988.
- Lowe, S. A., F. Schuepfer, and D. J. Dunning, Case study: three-dimensional hydrodynamic model of a power plant thermal discharge, *Journal of Hydraulic Engineering*, 135(4), 247–256, 2009.
- lpdaac.usgs.gov, LP DAAC - Land Processes Distributed Active Archive Center, ASTER Scenes Reassessed for Cloud Cover, [Available online under <https://lpdaac.usgs.gov/news/aster-scenes-reassessed-for-cloud-cover/>], accessed: 19.12.2017, 2017.

- Ma, P., X. Dai, Z. Guo, C. Wei, and W. Ma, Detection of thermal pollution from power plants on China's eastern coast using remote sensing data, *Stochastic environmental research and risk assessment*, 31(8), 1957–1975, 2017.
- Madden, N., A. Lewis, and M. Davis, Thermal effluent from the power sector: an analysis of once-through cooling system impacts on surface water temperature, *Environmental Research Letters*, 8(3), 035,006, 2013.
- Marine Management Organisation (online), High risk inshore european marine sites and features and sub-features, https://assets.publishing.service.gov.uk/government/uploads/system/uploads/attachment_data/file/314322/redsitelist.pdf, accessed: 15.06.2020, 2014.
- Markandya, A., and P. Wilkinson, Electricity generation and health, *The lancet*, 370(9591), 979–990, 2007.
- Marshall, J., and R. Plumb, *Atmosphere, ocean, and climate dynamics: an introductory text, volume v. 93*, Elsevier Academic Press, Amsterdam, 2008.
- Mason, D., T. Scott, and S. Dance, Remote sensing of intertidal morphological change in Morecambe Bay, UK, between 1991 and 2007, *Estuarine, Coastal and Shelf Science*, 87(3), 487–496, 2010.
- McCutcheon, S. C., J. L. Martin, T. O. Barnwell Jr, et al., Water quality., in *Handbook of hydrology.*, pp. 11–73, McGraw-Hill Inc, 1992.
- McDougall, T. J., and P. M. Barker, Getting started with TEOS-10 and the Gibbs Seawater (GSW) oceanographic toolbox, *SCOR/IAPSO WG, 127*, 1–28, [Available online under http://www.teos-10.org/pubs/gsw/v3_04/pdf/Getting_Started.pdf], 2011.
- McFeeters, S. K., The use of the Normalized Difference Water Index (NDWI) in the delineation of open water features, *International journal of remote sensing*, 17(7), 1425–1432, 1996.
- McNeel R. & Associates, Rhino 6.6.18323.1, <https://www.rhino3d.com/download/Rhino/6.0/release>, [Available only to users with a valid software license.], 2018.
- McPhee, M., *Air-ice-ocean interaction: Turbulent ocean boundary layer exchange processes*, Springer Science & Business Media, 2008.
- Mei, C. C., and P. Liu, Surface waves and coastal dynamics, *Annual review of fluid mechanics*, 25(1), 215–240, 1993.
- Merchant, C., P. Le Borgne, A. Marsouin, and H. Roquet, Optimal estimation of sea surface temperature from split-window observations, *Remote Sensing of Environment*, 112(5), 2469–2484, 2008.
- Merchant, C., A. Harris, H. Roquet, and P. Le Borgne, Retrieval characteristics of non-linear sea surface temperature from the Advanced Very High Resolution Radiometer, *Geophysical Research Letters*, 36(17), 2009.
- Merchant, C. J., et al., Sea surface temperature datasets for climate applications from Phase 1 of the European Space Agency Climate Change Initiative (SST CCI), *Geoscience Data Journal*, 1(2), 179–191, 2014.
- Merchant, C. J., et al., Satellite-based time-series of sea-surface temperature since 1981 for climate applications, *Nature Science Data*, 2019.

- Mieszowska, N., M. Kendall, S. Hawkins, R. Leaper, P. Williamson, N. Hardman-Mountford, and A. Southward, Changes in the range of some common rocky shore species in Britain—a response to climate change?, in *Marine Biodiversity*, pp. 241–251, Springer, 2006.
- Muir, A. P., F. L. Nunes, S. F. Dubois, and F. Pernet, Lipid remodelling in the reef-building honeycomb worm, *Sabellaria alveolata*, reflects acclimation and local adaptation to temperature, *Scientific reports*, 6, 35,669, 2016.
- Muthulakshmi, A., U. Natesan, V. A. Ferrer, K. Deepthi, V. Venugopalan, and S. Narasimhan, A novel technique to monitor thermal discharges using thermal infrared imaging, *Environmental Science: Processes & Impacts*, 15(9), 1729–1734, 2013.
- NASA JPL, asterweb.jpl.nasa.gov, Obtaining ASTER Data (online), [Available online under: https://asterweb.jpl.nasa.gov/obtaining_data.asp], accessed: 19.12.2017, 2017.
- Norwegian Meteorological Institute, Nordic 4 km model, [Available online under <https://thredds.met.no/thredds/fou-hi/nordic4km.html>], accessed: 01.09.2019, 2019.
- Paduan, J. D., and L. K. Rosenfeld, Remotely sensed surface currents in Monterey Bay from shore-based HF radar (Coastal Ocean Dynamics Application Radar), *Journal of Geophysical Research: Oceans*, 101(C9), 20,669–20,686, 1996.
- Pardo-Pascual, J., E. Sánchez-García, J. Almonacid-Caballer, J. Palomar-Vázquez, E. Priego De Los Santos, A. Fernández-Sarría, and Á. Balaguer-Beser, Assessing the accuracy of automatically extracted shorelines on microtidal beaches from Landsat 7, Landsat 8 and Sentinel-2 Imagery, *Remote Sensing*, 10(2), 326, 2018.
- Pawlowicz, R., What every oceanographer needs to know about TEOS-10 (The TEOS-10 Primer), [Unpublished manuscript. Available online under www.TEOS-10.org], 2010.
- Peponi, A., P. Morgado, and J. Trindade, Combining artificial neural networks and GIS fundamentals for coastal erosion prediction modeling, *Sustainability*, 11(4), 975, 2019.
- Poornima, E., M. Rajadurai, T. Rao, B. Anupkumar, R. Rajamohan, S. Narasimhan, V. Rao, and V. Venugopalan, Impact of thermal discharge from a tropical coastal power plant on phytoplankton, *Journal of Thermal Biology*, 30(4), 307–316, 2005.
- Potts, G., and S. Swaby, Review of the status of estuarine fishes. Final report to English Nature (Contract No. F72-12-54)(Being an assessment of the fishes of twenty-two estuaries and coastal ecosystems carried out between December, 1992 and February, 1993), [No longer available online.], 1993.
- Punetha, M., Thermal pollution: Mathematical modelling and analysis, in *Environmental Contaminants*, pp. 409–431, Springer, 2018.
- Pye, K., and S. J. Blott, Coastal processes and morphological change in the Dunwich-Sizewell area, Suffolk, UK, *Journal of Coastal Research*, pp. 453–473, 2006.
- QGIS Development Team, QGIS geographic information system, <http://qgis.osgeo.org>, [Freely available software.], 2009.
- Reniers, A. J., J. MacMahan, E. Thornton, T. P. Stanton, M. Henriquez, J. Brown, J. Brown, and E. Gallagher, Surf zone surface retention on a rip-channeled beach, *Journal of Geophysical Research: Oceans*, 114(C10), 2009.

- Riley, K., *Capitella capitata*. Gallery worm. Marine Life Information Network: Biology and Sensitivity Key Information Sub-Programme, <https://www.marlin.ac.uk/habitats/detail/106>, accessed: 01.07.2020, 2005.
- Rodgers, C. D., *Inverse methods for atmospheric sounding: theory and practice*, vol. 2, World scientific, 2000.
- Roy, D. P., et al., Landsat-8: Science and product vision for terrestrial global change research, *Remote sensing of Environment*, 145, 154–172, 2014.
- Rudnick, D. L., Ocean research enabled by underwater gliders, *Annual review of marine science*, 8, 519–541, 2016.
- Rudnick, D. L., R. E. Davis, C. C. Eriksen, D. M. Fratantoni, and M. J. Perry, Underwater gliders for ocean research, *Marine Technology Society Journal*, 38(2), 73–84, 2004.
- Sadler, K., Effects of temperature on the growth and survival of the European eel, *Anguilla anguilla* L., *Journal of Fish Biology*, 15(4), 499–507, 1979.
- Salgueiro, D., H. de Pablo, R. Nevesa, and M. Mateus, Modelling the thermal effluent of a near coast power plant (Sines, Portugal), *Revista de Gestão Costeira Integrada-Journal of Integrated Coastal Zone Management*, 15(4), 533–544, 2015.
- Saunders, R., J. Hocking, D. Rundle, P. Rayer, M. Matricardi, A. Geer, C. Lupu, P. Brunel, and J. Vidot, Rttov-11 science and validation report, *NWP-SAF report, Met Office, UK*, 2013.
- Saunders, R., et al., An update on the RTTOV fast radiative transfer model (currently at version 12)., *Geoscientific Model Development*, 11(7), 2018.
- Scully, M. E., C. Friedrichs, and J. Brubaker, Control of estuarine stratification and mixing by wind-induced straining of the estuarine density field, *Estuaries*, 28(3), 321–326, 2005.
- Sinha, B., and R. Pingree, The principal lunar semidiurnal tide and its harmonics: baseline solutions for M2 and M4 constituents on the North-West European Continental Shelf, *Continental Shelf Research*, 17(11), 1321–1365, 1997.
- Southward, A., Note on the temperature tolerances of some intertidal animals in relation to environmental temperatures and geographical distribution, *Journal of the Marine Biological Association of the United Kingdom*, 37(1), 49–66, 1958.
- Stoker, Y. E., Salinity distribution and variation with freshwater inflow and tide, and potential changes in salinity due to altered freshwater inflow in the Charlotte Harbor Estuarine System, Florida. United States Geological Survey, *Water Resources Investigations Report*, pp. 92–4062, 1992.
- Suh, S., A hybrid near-field/far-field thermal discharge model for coastal areas, *Marine pollution bulletin*, 43(7-12), 225–233, 2001.
- Suresh, K., M. Ahamed, G. Durairaj, and K. Nair, Impact of power plant heated effluent on the abundance of sedentary organisms, off Kalpakkam, East coast of India, *Hydrobiologia*, 268(2), 109–114, 1993.
- Szabó, S., Z. Gacsi, and B. Balázs, Specific features of NDVI, NDWI and MNDWI as reflected in land cover categories, *Acta Geographica Debrecina Landscape & Environment*, 10(3-4), 194–202, 2016.

- Tang, D., D. R. Kester, Z. Wang, J. Lian, and H. Kawamura, AVHRR satellite remote sensing and shipboard measurements of the thermal plume from the Daya Bay, nuclear power station, China, *Remote Sensing of Environment*, 84(4), 506–515, 2003.
- Teixeira, T. P., L. M. Neves, and F. G. Araújo, Effects of a nuclear power plant thermal discharge on habitat complexity and fish community structure in Ilha Grande Bay, Brazil, *Marine Environmental Research*, 68(4), 188–195, 2009.
- Teixeira, T. P., L. M. Neves, and F. G. Araújo, Thermal impact of a nuclear power plant in a coastal area in Southeastern Brazil: effects of heating and physical structure on benthic cover and fish communities, *Hydrobiologia*, 684(1), 161–175, 2012.
- Telesh, I. V., and V. V. Khlebovich, Principal processes within the estuarine salinity gradient: a review, *Marine Pollution Bulletin*, 61(4-6), 149–155, 2010.
- Thai, T. H., and D. Q. Tri, Modeling the effect of thermal diffusion process from nuclear power plants in vietnam, *Energy and Power Engineering*, 9(08), 403, 2017.
- The Greater Manchester Ecology Unit, Preliminary Desk Top Ecological Assessments. Energy Sites (Heysham), [Available online under [https://www.lancaster.gov.uk/assets/attach/3335/Prelim%20Desktop%20Ecological%20Assess%20-%20Potential%20Allocated%20Sites%20\(Energy\).pdf](https://www.lancaster.gov.uk/assets/attach/3335/Prelim%20Desktop%20Ecological%20Assess%20-%20Potential%20Allocated%20Sites%20(Energy).pdf)], accessed: 10.06.2020, 2017.
- The United States Geological Survey, Landsat 8 long term acquisition plan, [Available online under <https://www.usgs.gov/core-science-systems/nli/landsat/landsat-8-long-term-acquisition-plan>], accessed: 30.08.2020, 2020.
- The United States Geological Survey, What does the term UTM mean? Is UTM better or more accurate than latitude/longitude?, [Available online under https://www.usgs.gov/faqs/what-does-term-utm-mean-utm-better-or-more-accurate-latitude-longitude?qt-news_science_products=0#qt-news_science_products], accessed: 15.01.2021, 2021.
- Tillin, H., *Capitella capitata*, *Thyasira* spp. and *Ophryotrocha dubia* in organically-enriched offshore circalittoral mud or sandy mud, *Marine Biological Association of the United Kingdom*, 2018.
- Turnpenny, A., and K. Liney, Review and development of temperature standards for marine and freshwater environments, *Unpublished Jacobs report to SNIFFER and UKTAG*, [Available online under <https://infrastructure.planninginspectorate.gov.uk/wp-content/ipc/uploads/projects/EN010001/EN010001-005189-HPC-NNBPEA-XX-000-RET-000200%201.pdf>], 2006.
- Turnpenny, A., J. Coughlan, B. Ng, P. Crews, R. Bamber, and P. Rowles, Cooling water options for the new generation of nuclear power stations in the UK, *Environment Agency, Evidence Directorate SC070015/SR3, Bristol, UK*, 2010.
- Tyler-Walters, H., *Zostera Noltii*. Dwarf eelgrass. Marine Life Information Network: Biology and Sensitivity Key Information Sub-Programme, [Available online under <https://www.marlin.ac.uk/species/detail/1409>], accessed: 01.07.2020, 2005.
- Tyler-Walters, H., *Mytilus edulis*. Common mussel, [Available online under <https://www.marlin.ac.uk/species/detail/1421>], accessed: 01.07.2020, 2008.
- Uncles, R., Hydrodynamics of the Bristol Channel, *Marine Pollution Bulletin*, (2), 1984.

- Vallis, G. K., *Climate and the Oceans*, Princeton University Press, 2012.
- Van Den Bremer, TS and Breivik Ø, Stokes drift, *Philosophical Transactions of the Royal Society A: Mathematical, Physical and Engineering Sciences*, 376(2111), 2018.
- Vaz, N., and J. M. Dias, Hydrographic characterization of an estuarine tidal channel, *Journal of Marine Systems*, 70(1-2), 168–181, 2008.
- Walne, P. R., et al., *Culture of bivalve molluscs: 50 years' experience at Conwy.*, Ed. 2, Fishing News Books Ltd., 1979.
- Wang, D., D. Pan, J.-A. Wei, F. Gong, Q. Zhu, and P. Chen, Monitoring thermal discharge from a nuclear plant through landsat 8, in *Remote Sensing of the Ocean, Sea Ice, Coastal Waters, and Large Water Regions 2016*, vol. 9999, p. 99991E, International Society for Optics and Photonics, 2016a.
- Wang, S., F. Chen, and W. Zhang, Numerical investigation of temperature distribution of thermal discharge in a river-type reservoir, *Polish Journal of Environmental Studies*, 28(5), 3909–3917, 2019.
- Wang, X., X. Wang, J. Fan, S. Wen, J. Zhao, and X. Su, Comparison of different spatial resolution thermal infrared data in monitoring thermal plume from the Hongyanhe nuclear power plant, in *2016 IEEE International Geoscience and Remote Sensing Symposium (IGARSS)*, pp. 4649–4652, IEEE, 2016b.
- Wu, J., E. Buchak, J. Edinger, and V. Kolluru, Simulation of cooling-water discharges from power plants, *Journal of environmental management*, 61(1), 77–92, 2001.
- Wykes, M. S. D., G. O. Hughes, and S. Dalziel, On the meaning of mixing efficiency for buoyancy driven mixing in stratified turbulent flows, [Available online under <https://www.repository.cam.ac.uk/handle/1810/248964>], 2015.
- Xu, H., Modification of normalised difference water index (NDWI) to enhance open water features in remotely sensed imagery, *International journal of remote sensing*, 27(14), 3025–3033, 2006.
- Xu, J., L. Zhu, J. Jiang, J. Li, S. Zhao, L. Yuan, et al., Monitoring thermal discharge in Daya Bay plant based on thermal infrared band of HJ-1B and TM remote sensing data., *China Environmental Science*, 34(5), 1181–1186, 2014.
- Yakhot, V., S. Orszag, S. Thangam, T. Gatski, and C. Speziale, Development of turbulence models for shear flows by a double expansion technique, *Physics of Fluids A: Fluid Dynamics*, 4(7), 1510–1520, 1992.
- Zanter, K., Landsat 8 (L8) data users handbook, *Landsat Science Official Website*, [Available online under <http://dl.icdst.org/pdfs/files/2512b7ec8c34f3a7330e7fa339792e5e.pdf>], 2016.
- Zanter, K., Landsat 8 (18) data users handbook, *Landsat Science Official Website*, [Available online under <https://www.usgs.gov/media/files/landsat-8-data-users-handbook>], 2019.
- Zoran, M., Nuclear power plant's water thermal plume assessment by satellite remote sensing data, in *Proceedings of the Global Conference on Global Warming*, pp. 11–14, 2011.